A Study of Optical Propagation in Polymer Liquid Crystal Nanocomposites for Photolithography Applications

A Thesis

Submitted to the Faculty

of

Drexel University

by

Anna E. Fox

in partial fulfillment of the

requirements for the degree

of

Doctor of Philosophy

July 2009

Acknowledgments

I would like to start by acknowledging my research advisor Dr. Adam Fontecchio for completely unwavering support over the past five years. Dr Fontecchio and Drexel University have afforded me opportunities unknown to the usual graduate student. My research advisor's complete trust in my ability has paved the way for me to pursue outside collaborations and find personal motivation for my work. Without this support I would not have earned multiple fellowships and awards that have enabled me to move forward into a National Research Council Postdoctoral Fellowship at NIST.

I would like to thank my committee consisting of Dr. Tim Kurzweg, Dr. Gary Friedman, Dr. Alisa Morss-Clyne, and Dr. Moses Noh for constructively critiquing my work and providing invaluable feedback. I appreciate their feedback and acknowledge that their input refines my work.

I would also like to acknowledge the Drexel University Nanophotonics Group graduate students including David Delaine, Dr. Hemang Shah, Sameet Shriyan, Ben Pelleg, Jared Coyle, and Kashma Rai in addition to countless undergraduate students including Marie Cosgrove-Davies, Vince Zaccone, Kyle Dooley, Courtney Kokser, Liz Plowman, Bill Hicks, and Alyssa Bellingham. Each of these graduate and undergraduate students have assisted me in one way or another.

I would like to thank Dr. Gregory Crawford and his students at the Display Laboratory at Brown University for their time and the use of their equipment. I acknowledge the Materials and Manufacturing Directorate of the U.S. Air Force Research Laboratory at Wright-Patterson Air Force Base for their time and the use of their equipment.

I offer my gratitude to collaborators for helpful discussion and insights about my

research from the Dartmouth College Ultrafast Optics group led by Dr. Ulf Österberg with students Dr. David Lukofsky, Dr. Colleen Fox, Dr. Armin Ellis, and Naval Research Laboratory collaborator Dr. Marc Currie. Thank you to Dr. Elsa Garmire and Dr. Mun Choi for mentoring me as I proceed to my next career step.

Finally I would like to acknowledge my financial support from the NASA New Investigator program and through the National Research Foundation Graduate Research Fellowship Program.

Table of Contents

List of Tables

List of Figures

Abstract

A Study of Optical Propagation in Polymer Liquid Crystal Nanocomposites for Photolithography Applications

Anna E. Fox

Adam K. Fontecchio, Ph.D.

Technology devices today are rapidly growing in complexity while shrinking in physical size as exemplified by the ultra slim laptops and music players currently available on the market. With the downsizing of packaging and the increase in components, innovative new lithography techniques designed to push the density limit of the digital functions on a chip are becoming more available. Though many different forms of lithography exist, all with individual benefits, there currently exists no photolithography tool that can completely eliminate alignment error over a series of exposures; a tool that can bring the industry into the next phase of nanometer photo-patterning. The device that can achieve this goal is designed using digitally adaptable polymer light-valve films to spatially control exposure transmission creating a photomask with an arbitrary and dynamically adjustable pattern.

This thesis presents the fundamental engineering behind the design of this novel photomasking application that uses a nanostructured composite. The material used is holographically-formed polymer-dispersed liquid crystal (H-PDLC) film and it is a photosensitive material formed with an interference pattern to contain layers of liquid crystal molecules held in a polymer matrix. With control over individual regions of film in a patterned electrode configuration, areas can be user defined as opaque or transmissive to resist exposing light. When used in a photomasking application, the light and dark fields can be real-time adjusted for rapid mask debugging, mask testing, and multiple exposures with no realignment. To truly understand the microscopic optical behavior of this device, aspects of propagation through the nanos-

tructured film are investigated. Diffractive and edge interference effects are simulated and measured. In addition to this study, transmissive wavefront, scattering, coherence, intensity, and absorption are examined to assess factors limiting imaging due to transmission through the nanostructured thin film. To this point, there have been no investigations into imaging through an H-PDLC as it pertains to patterning photoresist, and limited studies regarding optical propagation within the film. Shown in this work is compelling evidence not only of the practicality of a liquid crystal adaptable photomask but also a study of the optical transmission properties within this type of thin film.

Chapter 1. Scope of the Thesis

1.1 Introduction

Advances in lithography, or the science of transferring a pattern onto a substrate, are integrally important to the continuously evolving and shrinking world of nanotechnology. From the first experimentation of pattern transfer around 1796, when Aloys Senefelder discovered that Bavarian limestone treated with certain oils caused a change in the surface hydrophobicity of the stone affecting the adhesion of the ink [1], lithography has proved to be an irreplaceable tool in art and science. Photolithography, a specific subset of the lithographic technique that involves masking a photosensitive substrate and patterning using light, was discovered in a similar manner by Nicéphore Niépce in the 1820's when he observed that after several hours in sunlight, exposed bitumen hardened while a shaded neighboring region dissolved in turpentine [1]. Though photolithography was essentially invented by Niépce, this great man is more well known as the inventor of photography [2]. Today various lithographic techniques are used to fabricate printed circuit boards (PCBs), integrated circuits (ICs), microelectromechanical systems (MEMS), nanoelectricalmechanical systems (NEMS), and many other practical structures and devices. These structures and devices are the platform for many forms of cutting edge science, engineering, and nanotechnology research.

Lithographic technique comes in many flavors. Serial patterning methods such as the electron beam (e-beam) or x-ray lithography have their place in achieving high resolution patterns at the cost of extremely low throughput and high expense. Parallel processing such as photolithography, on the other hand, yields high production numbers at the price of lower resolution, and is currently the industry standard for

most high throughput manufacturing. A master chrome and quartz glass mask is usually fabricated once using a serial technique, and patterned repeatedly using the parallel process. As a result of this type of fabrication being so widely used in research and industry and the demand for small scale mass produced structures growing, photolithography technology is improving resolution by using shorter wavelengths and better optical systems. Mask technology is a quickly growing field in which high levels of research effort is being invested. Despite these advancements, there does not exist a photomask design that breaks the traditional chrome on glass mold and introduces the wavelength selective electro-optic properties of polymer composites for brand new mask functionality. These improved masks are no longer a passive part of the fabrication process, but a living, adapting, and constantly changing controllable pattern that can be further optimized to satisfy a growing photolithographic demand.

In this thesis, we discuss the development of a cutting edge type of photomask that replaces the traditional chrome and quartz glass mask with an electro-optically controllable polymer film. The polymer composite used in this application has unique optical properties including greater than 50% reflectance of a narrow band of wavelengths due to the microstructure and composition of the film. This type of polymer film also possesses electrical control over the optical properties, meaning application of a time varying bias across the film causes a shift in the microstructure that allows transmission of the selected narrow wavelength band. Using the film as a photomask implies that the reflecting portion of the film acts as the dark or chrome field while the transmissive portion acts as the light field. Through spatial control of the biased regions of the film, this photomask element offers functionality that no binary photomask has ever been able to perform: real-time pattern reconfiguration, partial masking or grayscale masking, potential phase masking control, and dynamic halftone masking. Figure 1.1 is a schematic representation of the device developed in this thesis. We will elaborate on each of the components of this figure, and discuss the

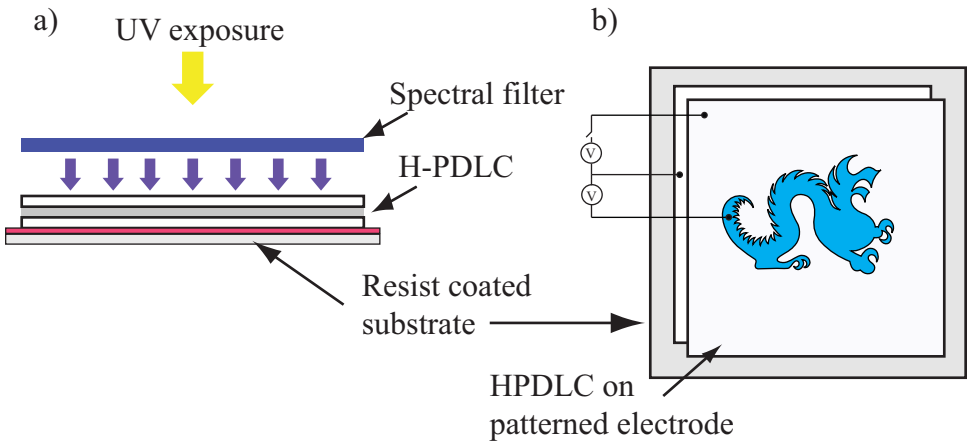

Figure 1.1: Schematic of the reconfigurable photomask device developed in this work. In a), a cross sectional view of the device is shown indicating UV light, a spectral filter, polymer film, and patterning substrate. In b) we show a top down illustration indicating the polymer film with electrically isolated regions above the patterning substrate.

optical properties of each of the transmission layers.

Using electrically controllable thin films in photolithography is the primary application and the topic of this thesis, however photopatterning is a complicated science and requires much more than simply imaging a mask pattern. Optical propagation through a binary mask is not simply the study of pattern formation but also the examination of interference, diffraction, coherence, proximity, and spatial filtering effects. Though propagation through a quartz and chrome mask is well understood, introducing a periodically modulated nanostructure to function as both the dark and the clear parts of the mask introduces a whole new dimension of complexity for optical propagation. The end pattern formed in photoresist is virtually 100% dependent on the properties and the quality of the light that reaches the photosensitive layer, and many factors determine this. In a sense, and not to subtract from the importance of the photolithography application, the science of this thesis is a study of pattern or image formation from light propagating inside a nanostructure using photosensitive

resist as an image plane or an image capturing substrate. Once imaging is fully understood in resist, functions can be built up layer by layer using standard lithographic etch and deposition tools, but before any of that can happen, fundamental optical patterning must be fully examined and comprehended.

The work done in this study investigates both the optical propagation and the photolithography application, and has innovate aspects in both science and device engineering. Though lithography as a technique has many forms, and there have been several other types of mask-reconfigurable photolithography patterning systems, this work is the only that proposes using a wavelength selective holographically-formed polymer-dispersed liquid crystal (H-PDLC) thin film as an adaptable photomask. Currently this is the only photolithography technique that can real-time adapt, be retrofitted into existing stepper or reticle systems, offer bias-linear transmission, scalability, phase control functionality, and operation into the UV. This device offers a brand new technique for fabrication of MEMS devices, printed circuit boards, and photoalignment masks as well as functioning as an invaluable tool for techniques such as inverse lithography and diffraction compensation testing. The innovative science investigated in this thesis, as discussed earlier, relates to optical propagation through this nanostructure and its effect on pattern generation at the image plane. Understanding imaging on the resist layer is fundamental to developing an optimized patterning tool, and also allows us to examine some of the future usages of the device. In both simulation and measurement, we examine diffraction, interference, coherence, scattering, wavefront, dose intensity variation, and resolution to visualize the nanostructure's effect on the exposure light, and the altered exposure light's effect on the photoresist.

A summary of the contributions presented in this thesis includes:

1. Development of the application

- Patterning of resist using a holographically formed polymer dispersed liquid crystal (H-PDLC) mask.
- Wet and dry etching of features patterned using the H-PDLC mask.
- Illustration of multiple patterns by reconfiguring the same mask.
- Demonstration of passively addressed arrays formed using the H-PDLC mask.
- Proof of resist and substrate quality after patterning using the thin film mask in comparison to a binary mask.
- Illustration of decreasing sized features reaching the predicted resolution limit.

2. Investigation into the fundamental optical properties as applied to this periodic nanostructure

   - Simulation showing predicted diffraction effects with comparison to the transmitted image captured in resist.
   - Simulation showing interference occurring due to phase shifting in adjacent regions of H-PDLC with different bias. The simulation results are compared to experimental resist interference patterns.
   - Transmissive intensity and its relation to the image formation on the image plane.
   - The light source is examined for differences in image quality as a function of varying levels of spatial coherence.
   - A study of scattering modes was performed, and their effect on image formation discussed.
   - Transmissive wavefront was characterized to determine the relation to image formation.

- Absorption, in particular UV absorption of liquid crystals and films is discussed and its effect in relation to image formation examined.

- Simulation of field fringing outside an H-PDLC and its effects on partial switching. Partial switching outside of electrode regions is dimensioned and related to imaging.

1.2 Thesis Outline

This thesis is organized to enable the reader to first understand the important fundamentals of the materials used, followed by discussion of process, literature review, data presentation, and analysis. We start in Chapter 2 by discussing thermotropic liquid crystals, why they are unique and important for this work, and the details of their properties. Outlined are the properties of the various types of thermotropics, in this work we mainly use nematic, but in the literature review several techniques that rely on chirals and smectics are discussed. For completeness, lyotropic, discotic, and polymer liquid crystals are mentioned, but not elaborated on. More information about these materials can be found in Refs [3–5].

The natural molecular arrangement and structure of the nematic liquid crystal is the reason it works so well in this application, and its composition has unique optical properties. To understand image formation through a nanostructure of liquid crystals, we must examine the molecular and dielectric responses when placed in an electric field. So the second half of Chapter 2 thoroughly reviews polarization and dielectric function of uniaxial materials and is followed with a summary of real and imaginary dielectric constants that determine the material's off-resonance absorption and dispersion. The molecular structure of a nematic can be analyzed and broken down into sets of available electronic transitions, whereby the optical resonances can be determined.

In Chapter 3, a review of liquid crystal films is performed with their governing equations, formation mechanisms, material sets, characterization technique, and a discussion of many useful published applications.

Photolithography is the main application, and the means by which we are capturing image formation. In Chapter 4, the benefits and the process of photolithography is outlined. An important section exists in this chapter on system resolution and the origin of patterning minimum feature size definitions. Understanding the optical limitations defined by the Rayleigh criterium is an important first step in designing this optical imaging system.

After that, in Chapter 5, we review several different types of photolithography techniques that use an adaptable method. Lithography has a vast number of available techniques, most have benefits in either speed or resolution but usually not both. Since we are proposing a photomasking application, we limit the review to methods that are considered photolithography and have a reconfigurable quality to the mask itself. The exception made in this review is discussion of a maskless technique that uses laser projection from a MEMS spatial light modulator because of its recent growth and importance in the field of real time pattern generation.

This point marks the conclusion of background and the beginning of new work. To visualize light propagation inside this layered nanostructure, grating simulations were performed and summarized in Chapter 6. Incorporated into these simulations is 1) propagation of light in a periodically index modulated medium and 2) experimental properties measured using SEMs of H-PDLCs used for this study. The resulting simulation shows good likeness to a grating fabricated in our labs, and confirms that we have mathematical understanding of the structure we are using.

Next, in Chapter 7, the development of our proof of concept photolithography device is developed. Its principles of operation are discussed and some initial patterning is presented. Characterization of patterned resist and substrate is compared to that

patterned using a binary mask. Initial resist edge slope data is presented and wet and dry etching of the underlying substrate is shown.

The results from a miniaturization study are shown next in Chapter 8. A test mask was obtained with features designed to push the resolution and patterning limit of the device. First, the approach to the predicted resolution limit of contact lithography for this system is shown. After that the dynamic quality of the mask is shown by patterning several features using a single mask. Then arrays of passively addressed 100 μm and 50 μm square are presented. An analysis of pattern generation on exposure dose is then shown.

Analysis of pattern generation starts with a simulation of Fresnel diffraction and its corresponding relation to images captured using this system is summarized in Chapter 9. Next interference pattern imaging is analyzed with data and a simulation. We examine transmission and wavefront quality to determine if transmission in the nanostructure introduces aberration. Finally, any effect that field fringing has is simulated.

The photolithography application developed in this thesis would not be possible without understanding the underlying science of light propagation through the H-PDLC nanostructure. We provide the macroscopic development of the application stage and the microscopic examination of the fundamental optical properties of the film. With this understanding, we not only show a brand new device with interesting applications but also optical theory that has never been applied to this type of nanostructure previously.

Chapter 2. Liquid Crystal Electrical and Optical Properties

Since their discovery in 1888, liquid crystals have been shown useful in a wide span of applications from biological to optical technology. Materials ranging from cholesterol to DNA form a liquid crystal phase [6]. For the purpose of this thesis, the primary concern is thermotropic liquid crystals, or materials that form a liquid crystal phase as a function of temperature. This temperature related phase provides the electrically controllable birefringent properties for the application developed in this work. In this chapter, we review the different types of thermotropic liquid crystals while examining some of their important structural properties. Next we use a uniaxial dielectric model to examine the electrical and optical properties of this material. Finally, we discuss how these properties enable the technology presented in this thesis.

2.1 Thermotropic Liquid Crystals

Friedrich Reinitzer serendipitously discovered liquid crystals in 1888 while experimentally determining the chemical structure of cholesterol extracted from the roots of carrots. Reinitzer observed an interesting and unexpected color transition near the crystallization temperature in both cholesterol acetate and cholesterol benzoate, but more interesting was the double melting point of the latter crystal. Cholesterol benzoate exhibited an initial transition from solid to opaque liquid at 145.5 °C and then a sudden transition from cloudy to a clear liquid at 178.5 °C. Work with cholesterol benzoate was continued by Otto Lehmann who microscopically examined this substance near it melting points and discovered its ability to rotate polarized light [7–9].

The three properties observed in these experiments, multiple melting points, colorful reflection of light, and rotation of polarized light are some of the major properties

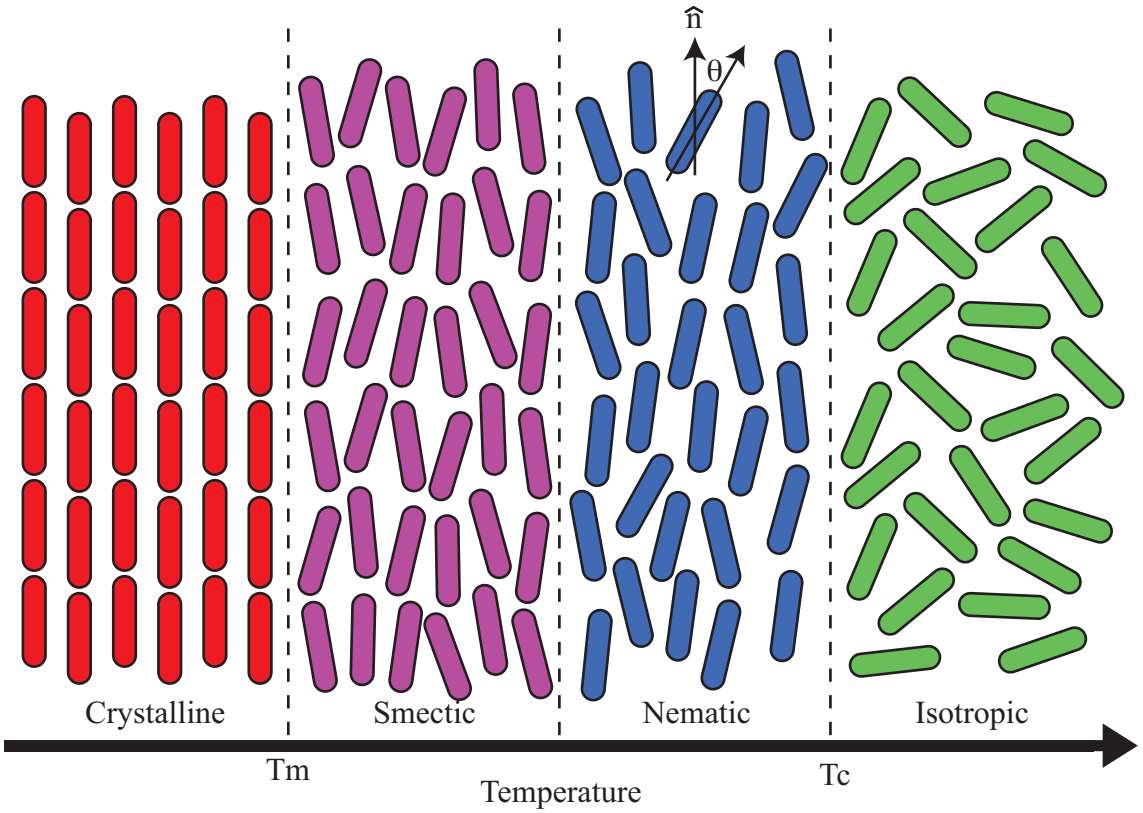

Figure 2.1: Illustration of rod-like liquid crystal molecules exhibiting different levels of orientational and positional order in the crystal, smectic, nematic, and isotropic phases as a function of increasing temperature with melting and clearing points noted. Figure recreated from P. Collings [Princeton University Press, 1990, pg. 9]

of a thermotropic liquid crystal material, and properties that differentiate it from ordinary substances that do not exhibit this special phase in between solid and liquid phases. The liquid crystal phase can be identified visually as taking the form of a cloudy liquid over the temperature range in which it is in that phase. Microscopically, the phase can be described as a substance possessing a level of molecular orientational order, but lacking molecular positional order. This differs from a crystalline state in which the substance possesses both orientational and positional order, while the liquid phase possesses neither [3]. Figure 2.1 is an illustration showing the molecular positional and orientational order as a function of increasing temperature across several

phases. Smectic and nematic are phases that possess orientational but not positional order. Visual observances that correspond with phase can be attributed to the differences in molecular order; the cloudy appearance is related to light scattering as a result of average of orientational order within the anisotropic substance. The transition point between the liquid crystal phase and isotropic phase is called the clearing point because it is marked with a sudden change in appearance from cloudy to a clear liquid. This effect is the result of a loss of orientational order and an overall averaging of molecular direction [10].

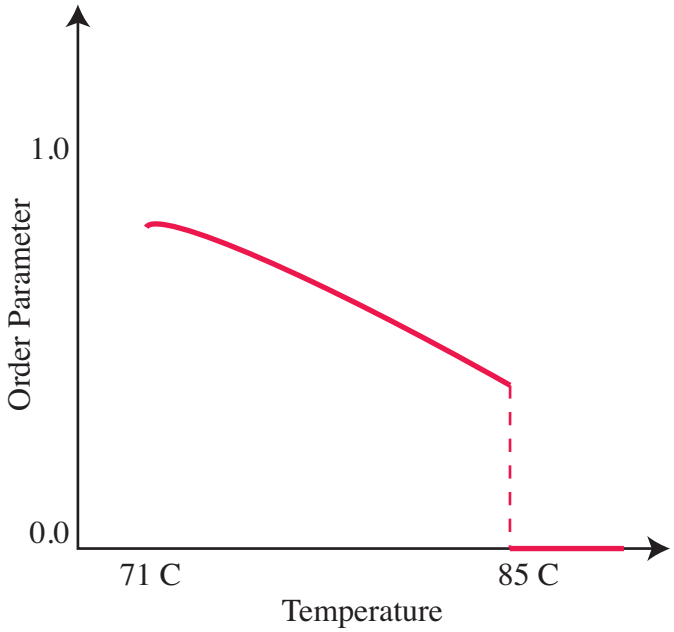

Figure 2.2: Typical order parameter plot of a thermotropic liquid crystal, cholesterol myristate, as a function of temperature showing a melting temperature of 71 °C and a clearing temperature of 85 °C. [P. Collings, Princeton University Press, 1990, pg. 11]

Order parameter is the quantitative measurement of the orientational organization of a liquid crystal sample at a given time. Each rod-like thermotropic molecule appears at an angle with respect to the favored direction of the liquid crystal long

axes, or the director shown as $\hat{n}$ in Figure 2.1. Rather than simply averaging the molecular angle, it is common to calculate the order parameter, S, which itself is an average over all of the present molecules. The equation governing order parameter is

$$S = \frac{1}{2}\langle 3\cos^2\theta - 1\rangle \tag{2.1}$$

with θ as the angular offset from the director. An order parameter of 1 implies an average angle of 0° or complete orientational order while an order parameter of 0 indicates the lack of orientational order representing the solid and isotropic phases on either side of the temperature spectrum. The liquid crystal phase yields intermediate values that typically vary with temperature as shown in Figure 2.2 [3]. Note the discontinuity at the clearing point temperature representing the sudden change from cloudy to clear liquid. This phase change is usually not a continuous transition, but a sudden and reversible jump. The purpose of observing order parameter is to understand that although a liquid crystal maintains a degree of orientational order, the molecules are angularly offset from the director normal and vary with time and temperature.

2.2 Types of Liquid Crystals

Thermotropic liquid crystals form four primary phases: nematic, chiral nematic, smectic, and discotic. For the purpose of a complete review, each phase is discussed, but the primary focus of this thesis is the nematic phase.

2.2.1 Nematic Liquid Crystals

The liquid crystal phase is characterized by molecular orientational alignment along a director axis, but this can occur in several forms with differing physical properties. The most common type of thermotropic liquid crystal formed is the nematic

phase which is described by an average orientational order along the director axis and no positional order. Figure 2.1 shows the nematic phase with rod-like molecules partially aligned in the vertical direction. Nematic liquid crystals have been considered the most ideal phase to observe both the liquid and crystalline features of this unique state because they exhibit director alignment but can flow due to the lack of positional order [4, 11]. A common application of nematic liquid crystals is the liquid crystal display (LCD) in which nematics are used as electrically controlled light valves. Holographically formed polymer dispersed liquid crystal films, the polymer dispersion used in this thesis, is also an application of nematic liquid crystals.

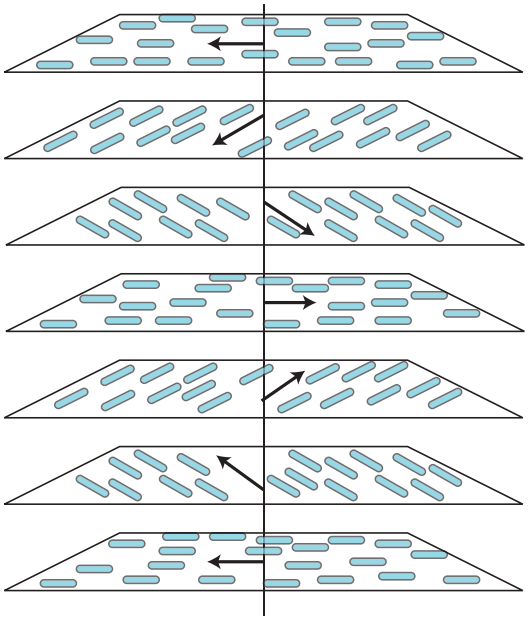

Figure 2.3: Helical orientation of the director in the chiral nematic liquid crystal phase twisting around the optic axis. Recreated from Chandrasekhar [Cambridge University Press, 1992, pg. 5]

2.2.2 Chiral Nematic Liquid Crystals

Thermotropic liquid crystals can form a phase known as chiral nematic that differs from nematic in the orientation of the director axis. Liquid crystals in a chiral nematic

phase on average align in a helical orientation as shown in Figure 2.3. The chiral nematic phase is physically identical to the nematic phase less the helical orientation of the director which rotates around a center axis. Pitch is defined as the length required for the director to rotate 360° and when this value is equal to a wavelength of visible light, through interference, that wavelength is reflected [11]. This optical activity is one of the important properties of this phase and the reason the discoverers of the liquid crystal phase observed the low temperature colorful transition in cholesterol benzoate [7] and one of the reasons that this type of liquid crystal is often used in temperature sensing devices.

2.2.3 Smectic Liquid Crystals

No material has been shown to exhibit both a nematic and a chiral nematic phase, but a material can exhibit a nematic and a smectic phase. A smectic liquid crystal possesses not only orientational order, but an amount of weak positional order differentiating it from the nematic phase. Smectic molecules tend to align along the axis of a director, similar to nematics, but also tend to form layers as shown in the smectic column of Figure 2.1. Smectic phases tend to occur at a lower temperature than the nematic phase yet maintain their characteristic fluidity due to the weak positional order. At least nine different smectic phases have been identified to date with defining characteristics including the amount of positional order within a layer and the direction of the director axis [3, 11, 12].

2.2.4 Discotic Liquid Crystals

To this point in this thesis, liquid crystal molecules have been regarded as rod-like in shape and structure. In 1977, a disc-like molecule was discovered to form a liquid crystal phase [13], now known as a discotic liquid crystal. Discotic liquid crystals

form several phases similar to their rod-like counterpart including a nematic and a columnar. Nematic discotic liquid crystals contain the orientational order of all the molecules aligned along a common director axis, where that axis is perpendicular to the plane of the molecule. The discotic nematic phase is shown in Figure 2.4a. The columnar phase contains an increased amount of positional order along with the orientational order in that the molecules form stacks. This phase is shown in Figure 2.4b. The columnar phase can form stacks anchored in a hexagonal pattern as shown in the figure, but it can also form stacks with different anchoring such as a rectangular pattern. Discotic liquid crystals have been suggested as potential materials for organic photovoltaics because of their large surface area [14].

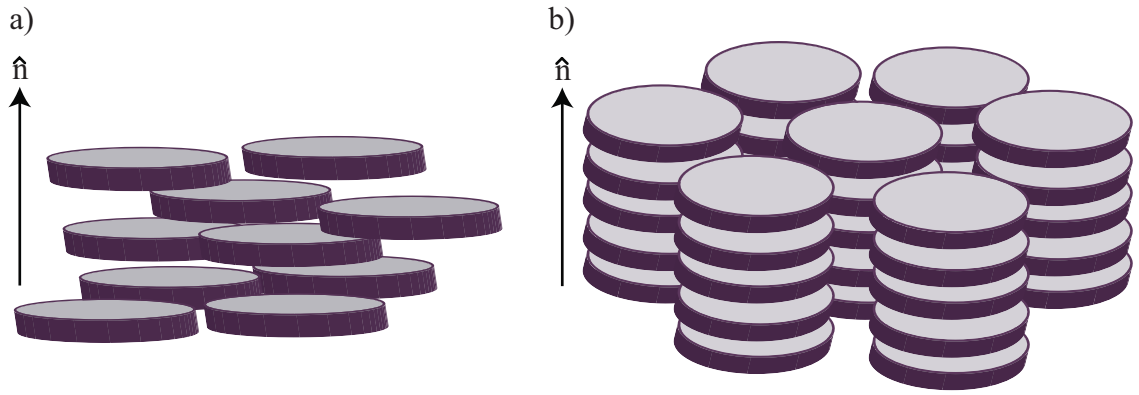

Figure 2.4: Two phases of discotic liquid crystals. a) Nematic phase, b) Columnar phase. Recreated from Chandrasekhar [Cambridge University Press, 1992, pg.10]

2.2.5 Lyotropic Liquid Crystals

Certain materials exhibit the orientational order of a liquid crystal phase as a function of concentration rather than temperature. Lyotropic liquid crystals are formed from molecules with differing end group properties, the classic example being hydrophilic and hydrophobic molecules aligning in water. These molecules are free and lack posi-

tional order, but orient themselves according to their end group preferences forming the orientational order phase. Soap is a common example of a hydrophilic/hydrophobic solution that forms a lyotropic liquid crystal phase [3], as does DNA [6], and carbon nanotubes prepared in certain solutions [15]. Surfactants and phospholipids also form a lyotropic liquid crystal phase.

2.2.6 Polymer Liquid Crystals

Polymers can exhibit the orientational order of a liquid crystal phase as well. Certain polymer materials composed of rod-like rigid mesogens connected either end to end or from the side are considered liquid crystals. Main chain polymer liquid crystals are mesogens connected end to end with a flexible bridge in between. Side chain polymer liquid crystals consist of mesogens connected to a flexible main chain as side chains. The flexible connecting bridges provide the lack of positional order while the mesogens tend to maintain alignment with respect to one another. This effect adds the orientational order required to form a liquid crystal phase [3, 11].

The scope of this thesis pertains mainly to nematic liquid crystals, but it is evident in this review that liquid crystal materials come in many varieties with many structures and applications.

2.3 Electrical Properties of Nematic Liquid Crystals

Uniaxial liquid crystals in the nematic phase possess a physical anisotropy that effects the electrical, magnetic, mechanical, and optical properties of the molecule. As a result of the unique shape and molecular ordering, liquid crystal materials react strongly with external forces, more so than isotropic matter. Here we will discuss electrical and optical properties of this anisotropic material and thoroughly examine the molecular properties that contribute to anisotropic index, absorption bands, and

birefringence.

2.3.1 Anisotropy

Isotropy is a structural property of a material stating that its reaction to external impulse is directionally independent. Fundamental material properties such as optical and electrical characteristics are identical regardless of orientation, part of the material definition of all gasses and liquids except liquid crystals. Before the discovery of liquid crystals, anisotropy was a characteristic unique to solids. Although not all solids are anisotropic, no liquids or gasses possess the structural property. Liquid crystals, on the other hand, exhibit anisotropy due to their orientational direction preference and the general shape of the molecule. It is the anisotropy that causes liquid crystals to be very sensitive to external forces, and exhibit strong directionality within the electrical, magnetic, optical, and mechanical properties.

2.3.2 Dielectric Function and Field Effects

Dielectric material is defined by the amount of bound charge contained within the atomic structure. Ideal dielectrics contain no free charge, but bound charges in the material have the ability to polarize with external forces applied. Liquid crystal materials are dielectrics that exhibit structural changes as a result of polarization of charge. Dielectrics in general can be modeled using the Lorentz Model of matter and from this theory, the dielectric properties and optical properties of isotropic and anisotropic material can be derived. Lorentz theorized that matter can be modeled as oscillating masses on springs with driving forces equivalent to external electric fields. Consider a volume of masses m with charge e, attached to springs each with constant K. Each spring suffers from damping constant b and external electric driving force

E. The equation of motion for a single spring in one dimension is

$$m\ddot{\mathbf{x}} + b\dot{\mathbf{x}} + K\mathbf{x} = e\mathbf{E} \tag{2.2}$$

Assuming a time harmonic electric field of frequency ω, we can solve for the oscillatory part of the displacement solution which is

$$\mathbf{x} = \frac{(e/m)}{\omega_0^2 - \omega - i\gamma\omega} \tag{2.3}$$

where resonant frequency $\omega_0^2 = K/m$ and $\gamma = b/m$. The consequences of this result show that the relationship between dielectric displacement and driving force is complex and therefore will have a phase difference. Depending on the frequency of the driving force with respect to ω_0 the displacement and field will show varying phase difference [16].

Considering a volume of oscillators behaving under these conditions where $\mathcal{N}$ is the number of oscillators per unit volume and dipole moment, $\mathbf{p}$, is defined as $e\mathbf{x}$. Polarization, or the number of dipoles per unit volume is therefore defined as

$$\mathcal{N}\mathbf{p} = \mathcal{N}e\mathbf{x} \tag{2.4}$$

Substituting equation 2.3 into the definition of the number of dipoles per unit volume, the polarization $\mathbf{P}$ is derived

$$\mathbf{P} = \frac{\omega_p^2}{\omega_o^2 - \omega^2 - i\gamma\omega}\epsilon_0\mathbf{E} \tag{2.5}$$

$$\omega_p^2 = \mathcal{N}e^2/m\epsilon_0 \tag{2.6}$$

The above equation can be rewritten $\mathbf{P} = \chi\epsilon_0\mathbf{E}$ which defines electric susceptibility or a material's predisposition to polarizing bound charges. Continuing to operate

under the assumption that this is a linear isotropic dielectric material, the electric flux density can be defined as

$$\mathbf{D} = \epsilon_0 \mathbf{E} + \mathbf{P} \tag{2.7}$$

$$= \epsilon_0 \epsilon_r \mathbf{E} = \epsilon \mathbf{E} \tag{2.8}$$

where ϵ is the complex dielectric function [16].

Understanding the fundamental behavior of electric susceptibility and electric displacement of dielectric materials will enable derivation of current flux to visualize a molecule's reaction to an electric field, and will eventually enable us to derive the optical constants. But before we can derive the effects of more external forces, we consider anisotropic material. Up to this point, we have been working under the assumption of linear isotropic material. Consider now a model with masses and springs in three dimensions. Fundamentally, each axis behaves as stated previously, but behavior among axes may differ. Complex dielectric function ϵ is no longer a scalar constant, but a tensor with values in three dimensions. The constitutive equation becomes $\mathbf{D} = \epsilon_0 \bar{\epsilon} \cdot \mathbf{E}$ where

$$\bar{\epsilon} = \begin{pmatrix} \epsilon_1 & 0 & 0 \\ 0 & \epsilon_2 & 0 \\ 0 & 0 & \epsilon_3 \end{pmatrix} \tag{2.9}$$

Since the rod-like liquid crystals we study are uniaxial crystals, the dielectric tensor can be broken into parallel and perpendicular components to represent the appropriate degrees of freedom. Note that dielectric function is still a complex expression

$$\bar{\epsilon} = \begin{pmatrix} \epsilon_\perp & 0 & 0 \\ 0 & \epsilon_\perp & 0 \\ 0 & 0 & \epsilon_\parallel \end{pmatrix} \tag{2.10}$$

A typical liquid crystal will have dielectric function defined for the parallel and perpendicular axis. Notice that two of the axes in the uniaxial crystal have a common dielectric function. A material with positive dielectric anisotropy will have $\epsilon_{\parallel} > \epsilon_{\perp}$ which is typical for the nematics we use [11] and illustrated in Figure 2.5 [3]. This graph is a representation of parallel and perpendicular dielectric function of a positive dielectric in the liquid crystal phase converging to a single dielectric function at the clearing temperature. The rod-like liquid crystal will also have a parallel and perpendicular induced current densities due to this anisotropy. When in the presence of an electric field, the expected build up of charge through polarization causes a director reorientation into the field direction. This effect does not change the amount of natural orientation or order parameter of the material, only the preferred direction of the molecules [3]. This is the defining characteristic that makes nematic liquid crystal an electrically controllable material suitable for light valve applications, and the fundamental property used in this thesis.

Since electric and magnetic fields are fundamentally related, magnetic field effects on liquid crystal molecules are strikingly similar. Anisotropic materials have perpendicular and parallel magnetic susceptibilities that mimic the electric susceptibility graph in Figure 2.5. Liquid crystals have dual magnetic susceptibilities while in the liquid crystal phase, and convergence of susceptibility at the clearing point. Placing liquid crystal molecules in a magnetic field will cause reorientation of the preferred alignment direction along field lines, but will not change the order parameter of the molecules [3].

2.4 Optical Properties

Light interaction with liquid crystal molecules experiences a similar anisotropy to other external forces. Birefringence is one of the more exploited optical properties of

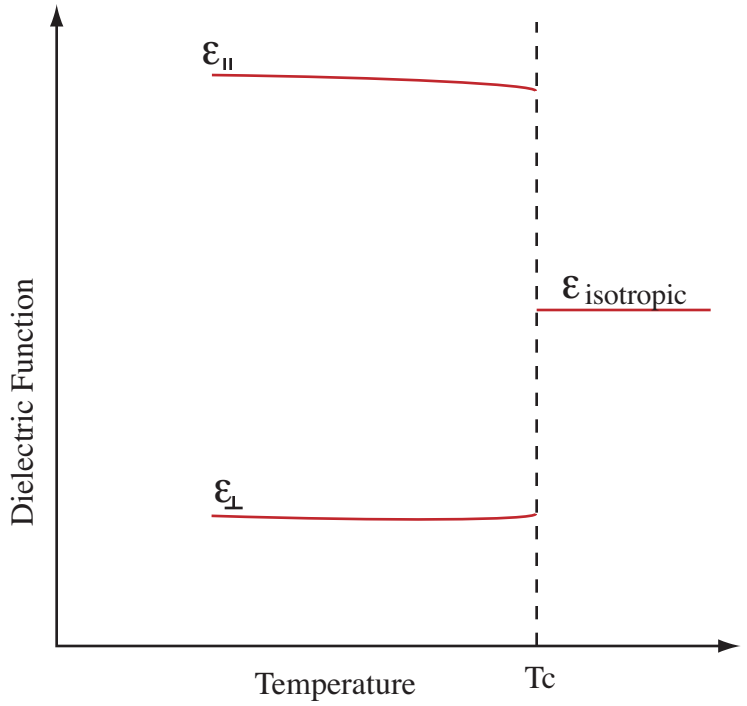

Figure 2.5: Graphical illustration of the dielectric function of a liquid crystal showing its dual functions in the liquid crystal phase. Dielectric function converges in the isotropic phase. [P. Collings, 1990, pg. 43]

liquid crystals due to their anisotropic nature and the ability to control the director with electric and magnetic fields. This property is defined by a material having different refractive indices corresponding with different directions, for the nematics we are studying, the birefringence will be defined on the parallel and perpendicular axes similar to dielectric function and magnetic susceptibility. A sample of molecules will possess a dual refractive index as long as it is in the liquid crystal phase and converge to a common index at the clearing point. The major impact of this property and its effects on propagating light occurs when interacting with polarized light. Depending on the preferred direction of the liquid crystal molecules in which linearly polarized light is incident, axis independent phase delay can cause a circular or elliptical polarization. Only when the linearly polarized light is at 0° or at 90° will the linear

polarization be unaffected by the anisotropic medium due to the fact that it is only interacting with a single axis. Liquid crystals are commonly used in optical devices as phase retarders and polarizers, but this effect is probably most commonly employed in a liquid crystal display (LCD). An LCD operates with a polarizer and an analyzer orthogonal to one another. Incident light is linearly polarized as it passes through the polarizer. A layer of liquid crystals aligned in a certain direction and controlled by an external electric field either rotate the polarization so that the light passes through the analyzer, or does not effect the polarization in which case the light is blocked by the analyzer. This light valve application is probably one of the most commonly known applications of liquid crystals today.

The anisotropic index is directly related to the dual dielectric function a uniaxial crystal exhibits. It was mentioned earlier that the dielectric function tensor is a matrix of complex numbers associated with the parallel and perpendicular directions. In fact, index of refraction n is defined as the square root of real part of the dielectric function. Recalling Equation 2.5 from above, the complex dielectric function for a single axis of a uniaxial crystal is

$$\epsilon = \frac{\omega_p^2}{\omega_o^2 - \omega^2 - i\gamma\omega} \tag{2.11}$$

where ω_p^2 or plasma frequency is related to the number of oscillators in a one dimensional plane, charge on an electron, mass, and permittivity of free space. This function can be broken into its real and imaginary components to better differentiate the parts that represent dielectric absorption and dispersion.

$$\epsilon^{'} = 1 + \frac{\omega_p^2(\omega_0^2 - \omega^2)}{(\omega_0^2 - \omega^2)^2 + \gamma^2\omega^2} \tag{2.12}$$

$$\epsilon^{''} = \frac{\omega_p^2\gamma\omega}{(\omega_0^2 - \omega^2)^2 + \gamma^2\omega^2} \tag{2.13}$$

Important observations from the real and imaginary components of the dielectric function include the significant dependence of both dispersion and absorption on spectral frequency of the driving force from the oscillator model. Additionally, each component shares a dependence on resonant frequency and damping constant. It is these components that ultimately determine the response of a molecule with particular construction to a wave of optical frequencies. In other words, the optical properties of any dielectric being perturbed with an optical frequency will respond based on these equations and the resonance determined by the material composition [16]. Applying this to a uniaxial crystal, we can assume that there is a unique real and imaginary dielectric component for parallel and perpendicular axes with unique resonant frequency and damping constant. It can also be shown that for a liquid crystal, parallel and perpendicular dielectric function will be dependent on polarizability with respect to the long axis, order parameter, and aspect ratio of the molecule [17].

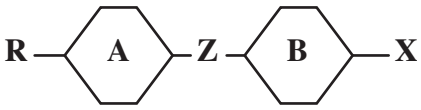

Figure 2.6: General structure of a rod-like liquid crystal molecule showing two aromatic rings, a side chain group R, a linking group Z, and a terminal group X. Figure recreated from I. C. Khoo [World Scientific, 1993, pg. 6]

The construction of the liquid crystal molecule determines many of the specific optical properties, absorption bands, and resonant frequencies as thoroughly discussed in Ref. [17]. The structure also determines the thermal properties such as melting and clearing points. Rod-like liquid crystals have the molecular form shown in Figure 2.6 with two aromatic rings, a linking group, a side chain group, and a terminal group. A and B represent the aromatic rings, Z is the linking group, and R and X are the side chain and terminal group respectively. The side chains often observed are alkyl

and alkoxy groups effecting the material properties with length and flexibility. The side chain structure will determine which liquid crystal phase, if any, the molecule forms, and at what temperatures transitions between phases occur. Aromatic rings are usually represented as a cyclohexane or a phenyl group. Materials that form a liquid crystal phase contain a structure with at least one of these rings. Length and type of ring will determine the melting point and dielectric functions of the different phases that form. It is important to note that the ring contributes some of the electronic structure that effects the optical properties. For example the cyclohexane contributes σ-electrons while a phenyl ring has both π and σ-electrons [17]. A linking group of ester or ethylene causes an electronic structure that effects the optical absorption and contributes more π-electrons to the system. Finally, polar strength of the terminal group is a major factor in determining dielectric function and anisotropy of the molecule. For instance, a terminal group consisting of cyano, isocyanate, fluoro, and chloro contribute strong polarity creating large dielectric anisotropy while alkyl, alkoxy, or sulfide terminal groups provide a weak anisotropy [17].

Electronic transitions within the molecule primarily determine the optical properties. Each group in the molecule contributes a unique amount of σ and π electrons in which common excitation transitions that occur in liquid crystal structures are $\sigma \rightarrow \sigma^*$, $n \rightarrow \pi^*$, and $\pi \rightarrow \pi^*$. Transitions occurring as a result of saturated cyclohexane and unsaturated phenyl rings typically found in materials exhibiting a liquid crystal phase contribute significantly to resonant absorption and refractive index properties. Liquid crystal materials are known to have asymptotically high absorption in the deep UV wavelength range as a result of the resonant $\sigma \rightarrow \sigma^*$ excitation found in both aromatic ring types. In addition to $\sigma \rightarrow \sigma^*$ transitions, phenyl rings contribute a $\pi \rightarrow \pi^*$ transition, which has a resonant wavelength of approximately 180 nm. Though $n \rightarrow \pi^*$ transitions have a resonance wavelength of slightly greater than 200 nm, their contribution is weak [17].

Off resonant absorption occurs throughout the visible wavelength range but is significantly less than resonant absorption occurring in the deep UV. As a result of strong scattering observed in nematics because of director orientation, off resonance absorption measurements can be difficult. Experimental method proposed by Wu and Lim [Appl. Opt., 1987] measures off resonance absorption coefficient and scattering coefficient simultaneously by performing propagation extinction measurements as a function of path length in isotropic liquid crystal [18]. In the isotropic state, extinction due to absorption is significantly greater than that of scattering, and can be presumed to be the primary source of transmissive extinction at temperatures greater than the clearing point. Absorption is relatively insensitive to temperature variations and should be consistent over the isotropic/nematic transition. However scattering is extremely sensitive to the phase change and can be considered the primary extinction source in the nematic phase. Using these methods, this work concluded that off resonance, visible scattering coefficient varies with λ^{-4}, an expected relationship based on scattering center size and regime. It was also concluded that off resonant absorption coefficient varies with λ^{-2} and obeys the quantum mechanical treatment of equation 2.5 that incorporates multiple resonances, strength of individual resonance, and full-width half-maximum (FWHM) of the resonant band [18].

As resonant and off-resonant absorption are functions of the electronic transition bands that compose a liquid crystal compound, anisotropic index of refraction is a property also derived from electron excitations. Anisotropic index is both wavelength and temperature dependent. For uniaxial crystals, similar to those used in this work, the ordinary index in the visible region is 1.50 ± 0.04 and is not heavily related on electronic transitions. However, extraordinary index in the visible region can range from 1.5 to 1.9 and is highly dependent on molecular construction [19]. Several models have been used to relate band structure with anisotropic index and birefringence taking into consideration first average resonant wavelength and then more realistic

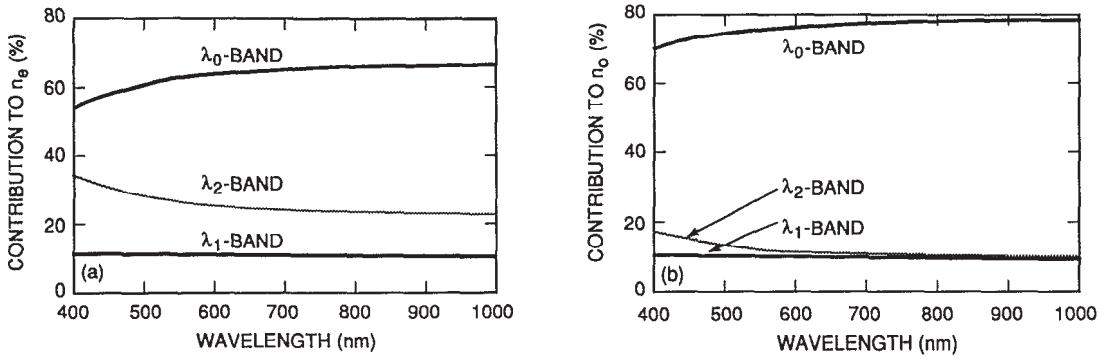

Figure 2.7: From Wu *et al.* [J. Appl. Phys, 1991] percent contribution to anisotropic index as a function of wavelength for each of the three significant electric transitions found in uniaxial liquid crystals, for 5CB at 20^o C. Reprinted with permission.

multiple resonance systems. The single band model represents anisotropic index to an average resonant wavelength and a mean oscillator strength

$$n_e(\lambda) \simeq 1 + g_{\parallel} \frac{\lambda^2 \lambda_{\parallel}^2}{\lambda^2 - \lambda_{\parallel}^2} \tag{2.14}$$

$$n_o(\lambda) \simeq 1 + g_{\perp} \frac{\lambda^2 \lambda_{\perp}^2}{\lambda^2 - \lambda_{\perp}^2} \tag{2.15}$$

where $\lambda_{\parallel}$ and $\lambda_{\perp}$ are mean resonant wavelength and $g_{\parallel,\perp}$ are the temperature dependent number of available transition electrons. Mean oscillator strength is incorporated into mean resonant wavelength. Uniaxial liquid crystals often have an extraordinary axis oscillator strength greater than that of the ordinary axis resulting in positive anisotropy [20].

The three band model expands on the single band model to incorporate the effects of three discrete electronic transitions commonly found in uniaxial liquid crystals. The closest to resonance, and the strongest transition originates from $\sigma \rightarrow \sigma^*$ excitations with a resonant wavelength of λ_0. $\pi \rightarrow \pi^*$ transitions provide two weaker contributions, at defined resonant bands λ_1 and λ_2. Expanding Equation 2.15 to take into

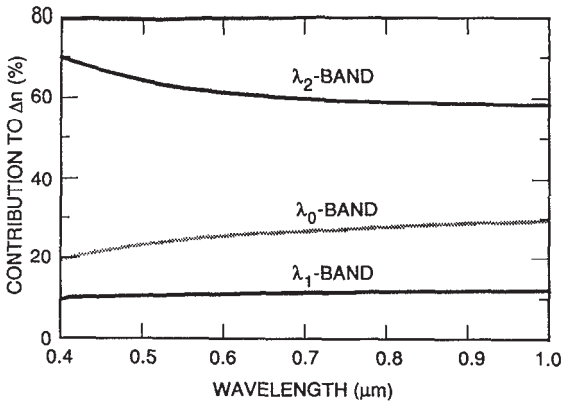

Figure 2.8: From Wu *et al.* [J. Appl. Phys, 1991] percent contribution of discrete bands to birefringence as a function of wavelength. Reprinted with permission.

consideration multiple discrete resonances results in

$$n_e(\lambda) \simeq 1 + g_{0,e}\frac{\lambda^2\lambda_0^2}{\lambda^2-\lambda_0^2} + g_{1,e}\frac{\lambda^2\lambda_1^2}{\lambda^2-\lambda_1^2} + g_{2,e}\frac{\lambda^2\lambda_2^2}{\lambda^2-\lambda_2^2} \tag{2.16}$$

$$n_o(\lambda) \simeq 1 + g_{0,o}\frac{\lambda^2\lambda_0^2}{\lambda^2-\lambda_0^2} + g_{1,o}\frac{\lambda^2\lambda_1^2}{\lambda^2-\lambda_1^2} + g_{2,o}\frac{\lambda^2\lambda_2^2}{\lambda^2-\lambda_2^2} \tag{2.17}$$

where g values are the number of available σ and π electrons for each respective term weighted by band oscillator strength. The important conclusions from these models allow us to determine individual band contribution to visible index and birefringence for both axes given any liquid crystal material. An example from Ref [20], redisplayed in Figure 2.7 shows the band contributions to ordinary and extraordinary index as a function of wavelength for 5CB. Clearly λ_0, the resonance for $\sigma \rightarrow \sigma^*$ transitions is the strongest oscillator and contributes the most to both indices where the $\pi \rightarrow \pi^*$ transitions play a lesser role.

On the other hand, referring to Figure 2.8, also an example from Ref. [20], $\pi \rightarrow \pi^*$ transitions contribute strongly to birefringence with $\sigma \rightarrow \sigma^*$ transition playing a less significant role. What can be concluded from these results is that $\sigma \rightarrow \sigma^*$ transitions

are stronger oscillators with a shorter wavelength resonance, but are isotropic in nature explaining the significant contribution to index. However $\pi \rightarrow \pi^*$ transitions absorb with large anisotropy providing birefringent characteristics.

Summarized in this chapter are the types of liquid crystals, focusing on nematics which are primarily used in this work, and the physical, electrical and optical properties that are associated with uniaxial materials. Anisotropic dielectric tensor is related to the Lorentz material model with absorption and dispersion described. Electronic transitions in rod-like liquid crystals are well understood, and their contributions to absorption and index is presented.

Chapter 3. Liquid Crystal Polymer Dispersions

Liquid crystal and polymer dispersions are the materials that make up the device used in this thesis. There exist two dispersions of particular interest specifically polymer-dispersed liquid crystal (PDLC) and holographically-formed polymer-dispered liquid crystal (H-PDLC) films. As a result of nanoscale material ordering, these thin film dispersions exhibit optical interaction properties that are dynamic under various biasing conditions. These films consist of liquid crystal molecules phase separated into droplets dispersed into a polymer matrix. H-PDLC has a more organized structure created by writing an interference pattern into the photosensitive monomer; PDLC is of a similar composition but consisting of randomly distributed liquid crystal droplets. The nanostructure and liquid crystal anisotropy contribute to the optical properties of the material and the liquid crystal property of field alignment contributes to the dynamic nature of the film. This type of film has recently had applications in display technologies, wavelength combing applications, and as different kinds of sensors because of its interesting material structure and dynamic optical properties. In this chapter, we discuss the structure, properties and applications of these two electro-optically active thin films.

3.1 Polymer-Dispersed Liquid Crystal Films

The concept of using liquid crystal molecules in a porous medium with electrode control over their orientation was introduced by Craighead [Appl. Phys. Lett, 1982] as a new type of display medium [21]. It was found that when the liquid crystal refractive indices differed from the substrate index in the direction of incident light, that light was strongly scattered by the liquid crystal molecules. When a bias of

$\sim 10^4$ V/cm was applied to the electrodes and across the porous substrate, the liquid crystal molecules aligned with the field lines and presented a uniform index equal to the substrate. In this state the material appeared optically transparent.

Doane *et al.* [Appl. Phys. Lett., 1986] were the first to encapsulate nematic liquid crystals into a matrix during a photoinitiated polymerization process [22]. Similar to work with nematic liquid crystals in a porous substrate, this material strongly scatters incident light when the liquid crystal areas are randomly aligned, and appear optically clear when bias is applied and the molecules align. The index mismatch between liquid crystal droplet regions and polymer areas exists as a result of the anisotropy of the LC molecule: anisotropic molecules in random orientations is interpreted by incident light as regions of differing index. Application of bias aligns the molecules and presents a uniform orientation and therefore a uniform index. With the index of the aligned molecules designed to be equal to the polymer matrix, the material appears transparent. Polymer concentration in PDLC is usually 30-40%, and the droplets that form as a result of phase separation are on the order of 1 μm. As a result of the large diameter of the droplets in a PDLC system, this material is an efficient scatterer of visible wavelengths [23]. These films have found various interesting applications including display technology, electrically controllable privacy windows [24], and spatial filtering [25].

PDLC is formed from a homogeneous mixture of polymer, initiator, and liquid crystal prepared in a spaced sample between indium-tin-oxide electrodes. The pre-polymer mixture is then cured with UV light supplied by a mercury arc lamp. Phase separation occurs and results in micron sized (ranging from 0.1 μm to 10 μm) spherical droplets of liquid crystal aggregating within the polymer binder [23]. Nematic liquid crystals are defined to have ordinary and extraordinary indices of n_o and n_e, which typically differ at most by 15% [26]. In an unaligned state, the overall index of the liquid crystal droplets is an average of its ordinary and extraordinary indices while

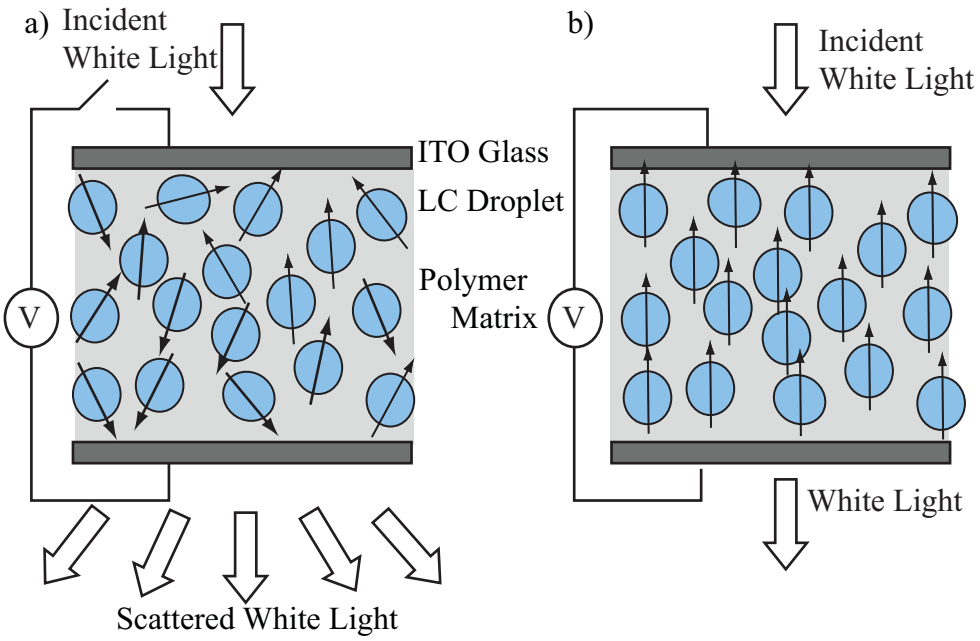

Figure 3.1: Schematic illustration of PDLC. a) PDLC in an unbiased state showing liquid droplets with directors aligned randomly. b)PDLC in a biased state shows an orientation of the liquid crystal droplet director

the index of the isotropic polymer binder is chemically designed to have n_p equal to either n_o or n_e. Application of bias allows matching of n_p to an aligned LC director. Figure 3.1 is a graphical description of the optical properties in unbiased and biased states. Figure 3.1a shows white light incident on the PDLC in its scattering state. Droplets with randomly oriented directors cause the index of the LC regions to be an average of the anisotropic indices. As a result of this index mismatch, light is strongly scattered. Figure 3.1b illustrates application of bias to the system which causes the directors to align and the average index of the LC regions become equal to the index of the polymer binder.

The liquid crystal droplets are aggregates of nematic LC molecules that have a unique director orientation. Each molecule is on average pointing in the direction of the director, but deviates by some angle defined by the order parameter equation.

Random fluctuation of the directors occur, but are considered negligible in comparison to scattering from droplet index differences [23]. Application of bias rotates the director, or the average orientation of the liquid crystal molecules. The molecules themselves continue to be defined by the order parameter equation.

3.2 Holographically-Formed Polymer-Dispersed Liquid Crystal Films

Holograms have been widely used in photonics to function as various optical elements such mirrors and lenses, and as a result of diffraction, wavelength selective elements such as spectral filters [27, 28]. Holography is a process of recording amplitude and phase of a field in a medium such as a photopolymer to create an optical element that has many benefits over conventional optics. Holographic optical elements (HOEs) can be lightweight and flexible unlike traditional glass optics, and can multiplex multiple functions into a single volume. Photopolymers have been used to record various types of HOEs including grating structures formed with an interference pattern. Recording an interference pattern is an efficient method of forming periodic refractive index variation. Passive HOEs have no ability to be externally adjusted once fabrication is complete; there is currently interest in an active HOE, or a diffractive element that can be externally controlled in real-time. The introduction of an index modulated material with the ability for external control over index variations to holography yields a new material known as holographically-formed polymer-dispersed liquid crystal. These volume gratings have properties including electro-optic modulation and strong index differentiation between layers.

HOEs can be formed as transmission or reflection gratings. Figure 3.2a shows the holography recording setup forming a transmission grating with the objective and reference beams on the same side of the sample. The grating lines form perpendicular to the recording beams. Figure 3.2b shows the holography setup for a reflection grating

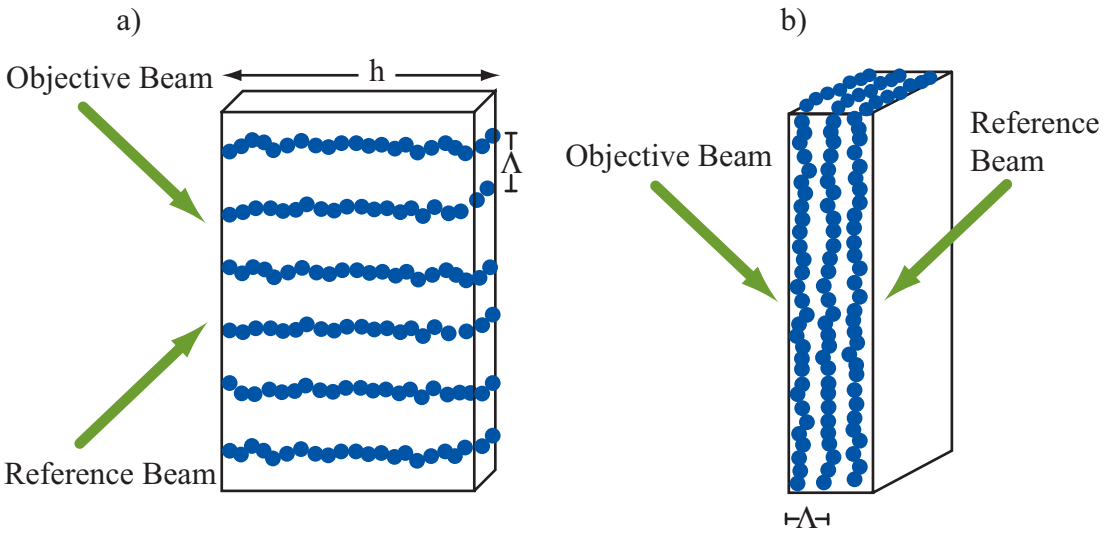

Figure 3.2: This schematic shows the transmission and reflection holographic writing orientations. h is the cell thickness and Λ is grating pitch a) Beam orientation for transmission grating. b) Beam orientation for reflection grating. Recreated from Bunning [Annu. Rev. Mater. Sci., 2000]. Reprinted with permission.

with the objective and reference beams incident on opposite sides of the recording medium. The grating lines form parallel to the incident beams. Combining this holographic recording technology with PDLC materials, the H-PDLC transmission and reflection gratings are realized. A sample of liquid crystal and photosensitive monomer is exposed to an interference pattern created by counter propagating laser beams either in a transmission grating or a reflection grating setup, that structure is permanently recorded into the photopolymer. The photosensitive monomer polymerizes rapidly in the bright fringes and forces the liquid crystal molecules to phase separate into droplets and diffuse into the dark regions of the interference pattern. The resulting H-PDLC structure has periodic layers of liquid crystal rich regions and polymer binder regions; the resulting material acts like a grating, but continues to possess the electro-optic modulation properties of PDLC. The optical properties of H-PDLC differs from PDLC in a variety of ways. Scatter is reduced because the

droplet sizes are between 100-200 μm differing from the micron sized droplets in PDLC. Second, coherent diffraction occurs because of the layered structure and enables transmission gratings to diffract ordered modes and reflection grating selectively reflect a band of wavelengths where PDLC simply scatters. Electro-optic properties remain similar; application of bias will rotate the directors and index match throughout the material. As scattering was reduced in PDLC with the application of bias, diffraction is reduced in H-PDLC.

Grating pitch of a reflection configuration grating recorded in photosensitive media is governed by the Bragg equation

$$\Lambda = \frac{\lambda}{2n \sin \theta} \tag{3.1}$$

where λ is the exposure wavelength, n represents the average index of refraction of the recording medium, and θ is the angle of the recording beam with respect to normal. Recording angle can be set or adjusted using a series of methods. Shown in Figure 3.3a is an interference recording setup using free space optics to capture counter propagating beams interfering at the sample. As a result of the beams entering the sample from opposing sides, the planes are formed parallel to the substrate which constitutes a reflection grating. The widths of the interference fringes can be made larger or smaller by varying the angle of propagation with normal.

When illuminated with white light, the equation governing the peak reflected wavelength λ_b or stop-band is

$$\lambda_b = 2n\Lambda \tag{3.2}$$

where n is the average index of the periodic structure and Λ is the grating period determined in recording. The index of an H-PDLC periodic structure in reflection mode is an average of liquid crystal indices and polymer index. Nematic liquid crystal

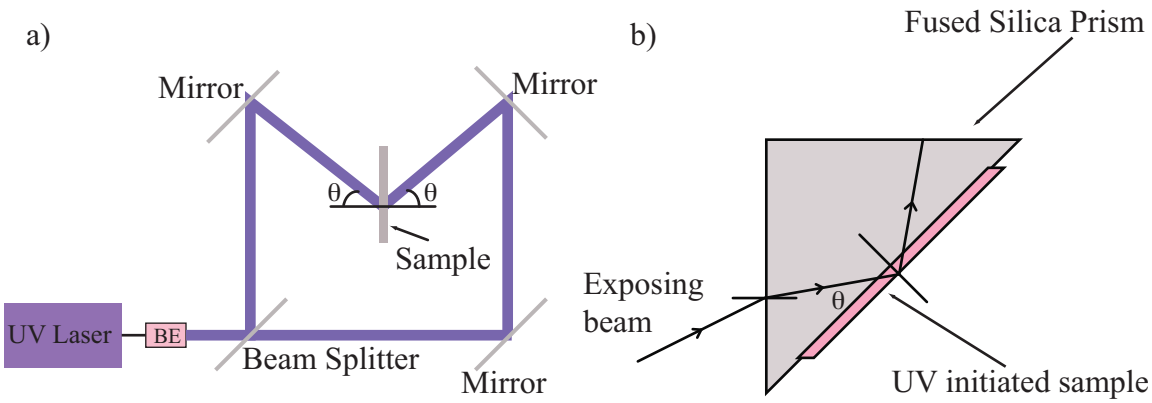

Figure 3.3: Counter propagating beam formation of a reflection grating and the single beam prism method formation of a reflection grating

index is approximated to be

$$n_{LC}^2 = \frac{(n_e^2 + 2n_o^2)}{3} \tag{3.3}$$

and should be averaged with the index of the isotropic polymer matrix to find the average index of the periodic structure. Writing a hologram with beams near normal will result in a reflection wavelength close to the wavelength of the exposing beam; the Bragg condition limits grating pitch such that it cannot reflect a wavelength less than the wavelength of the exposing beam. Increasing θ with yield larger interference fringes and a higher reflected wavelength. It can be seen from Figure 3.3a that increasing θ beyond a critical angle will result in total internal reflection inside the sample which ruins a standing interference pattern. Figure 3.3b is a recording setup that allows for higher angle interference to be achieved by using the total internal reflection inside the sample [29]. The recording light passes into the prism and bends inward, the interference pattern exists between the glass electrodes containing the sample. Adjusting the recording angle and reflected wavelength using this method is as simple as rotating the prism. With various material sets and exposure methods,

H-PDLC gratings have been recorded that reflect wavelengths spanning the visible and IR spectra.

Reconstructing a reflection-type of HOE requires illuminating with incident white light perpendicular to the layers of polymer and liquid crystal. By reconstructing the hologram using white light, a narrow band of light corresponding to the Bragg wavelength is reflected from the surface of the HOE. With the exception of light that is absorbed by the material or scattered by the subdomain spherical features, all other wavelengths of light are transmitted through the hologram. The center wavelength of the Bragg reflection was determined during the recording of the hologram and the intensity of the reflection is known as diffraction efficiency. Diffraction efficiency is determined by the total number of recorded polymer and liquid crystal layers and can be written from Kogelnik coupled wave theory as

$$\eta = \frac{1}{1 + (1 - \epsilon^2/\nu^2)/\sinh^2(\nu^2 - \epsilon^2)^{1/2}} \tag{3.4}$$

with

$$\nu = \frac{\pi \Delta n \Lambda}{\lambda_b} \tag{3.5}$$

and

$$\epsilon = \frac{2\pi \Delta\lambda \Lambda n_{ave}}{\lambda_b^2} \tag{3.6}$$

where $\Delta\lambda$ is the full-width half-maximum of the reflection spectrum, Δn is the refractive index difference, and n_{ave} is average index [30]. The baseline describes the amount of out-of-band light is transmitted through the HOE, ideally this is 100%, but very rarely does an H-PDLC exhibit 100% out-of-band transmission. Baseline is effected mainly by droplet scattering, but can also be effected by index mismatch in the air-glass interface on the surface and absorption within the HOE. Thin H-PDLC exhibits higher baseline but the trade-off is lower diffraction efficiency.

H-PDLC holographic optical elements are exciting not only because of their ability to phase separate into nanodomains related to recording intensity patterns but also because of their electro-optical properties. An element of switchability is introduced as a result of the liquid crystal response to electric field, and optical variation occurs because of liquid crystal anisotropy. During formation, the photosensitive monomer polymerizes in the bright fringes of the recording intensity map while the liquid crystal molecules are forced into the dark fringes. At this point of formation the volume fraction of liquid crystal molecules rapidly increases and forms droplets of random director orientations. It is this average of ordinary and extraordinary axes that enables the index mismatch with the polymer region and thus enables the Bragg reflection. Application of an electric field across the thickness of the film cases the randomly oriented directors to align with the field lines and liquid crystal rich regions take on the index of a single axis rather than the average of both axes. This results in index matching between polymer and liquid crystal regions and the disappearance of the Bragg reflection.

Figure 3.4 is a schematic representation of H-PDLC illustrating both its unbiased (a) and its biased states (b). In its unbiased state, the spherical droplets are shown to be aligned loosely in rows and held in place by the polymer matrix. The arrow in each droplet is to represent a director orientation of the group of molecules. Indium-tin-oxide (ITO) coated glass bounds the film on top and bottom, and each pair of layers is separated by approximately 100 nm. Optically, incident light is shown to have a Bragg reflection related to the index difference of the layers and the grating pitch. In Figure 3.4b, bias is applied across the thickness of the film and as a result, the director orientation of the droplet molecules aligns in the direction of the field. Even though a grating pitch exists, with minimal index mismatch in the layers incident white light transmits and the Bragg reflection is erased.

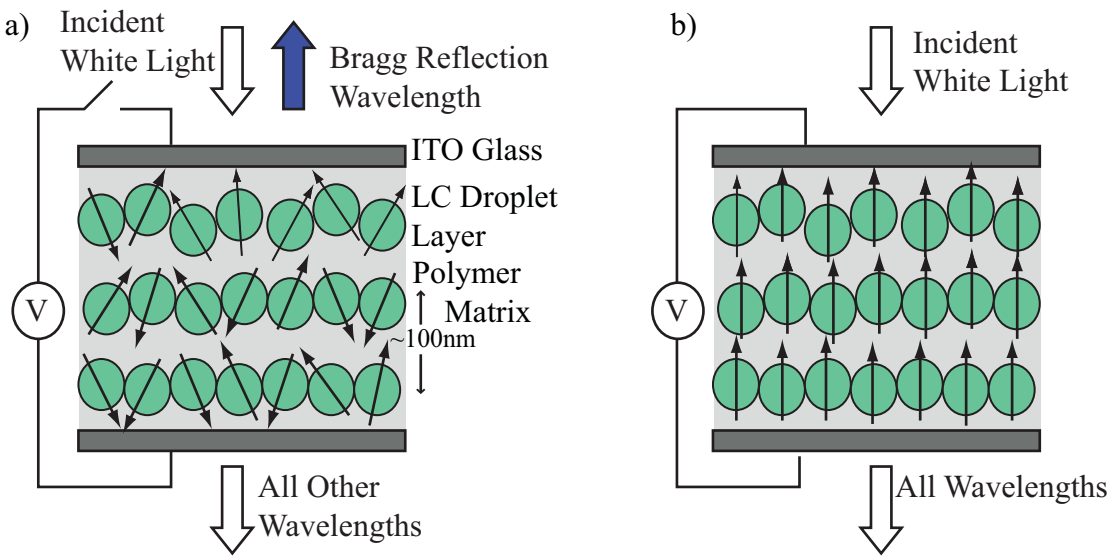

Figure 3.4: Schematic drawing of H-PDLC film showing the liquid crystal droplets and polymer layers. The grating spacing is marked as approximately 100 nm. (a)H-PDLC film is in its unbiased state, Bragg wavelength is reflected off the film surface. (b)H-PDLC film in its biased state. The liquid crystal droplets align along a common axis, the index mismatch disappears, and all the light transmits through the film

3.3 H-PDLC Material Sets

Fabrication process and recording angle are factors that strongly determine the center wavelength of the stop-band in a reflection grating; periodic index variation and layer density impact the reflectivity and bandwidth, the material sets that compose these gratings also impact the optical, electrical, and mechanical characteristics. The materials used to fabricate H-PDLCs include a monomer, a liquid crystal, photoinitiator, and in some cases surfactant. Each component has specific properties that make phase separation possible and the material sets are listed in Table 3.1.

Monomers used need to form a highly crosslinked network with a fast gelation rate in order to force the liquid crystal into small and ordered nanodomains. Multifunctional acrylate monomers crosslink in seconds using a free-radical addition polymerization reaction and are very suitable for high diffraction efficiency H-PDLC for-

Table 3.1: Acrylate and Thiolene Material Sets

Set Number	Monomer	Component	Percent
1	Visibly initiated thiolene	Rhodamine	0.30%
		Benzoyl Peroxide	4.00%
		n-vinyl-pyrrolidinone	2.70%
		BL038	25.00%
		NOA65	68.00%
2	Acrylate visible initiator	Rose Bengal	3.00%
		n-phenyl glycine	5.00%
		n-vinyl-pyrrolidinone	43.00%
3	Visibly initiated acrylate	Ebecryl 4833	25.00%
		Ebecryl 4866	25.00%
		BL038	36.00%
		Initiator	14.00%
4	UV initiated thiolene	Darocure 4265	5.00%
		BL038	30.00%
		NOA65	65.00%
5	UV initiated acrylate	Darocure 4265	5.00%
		Ebecryl 8301	27.50%
		Ebecryl 4866	27.50%
		BL038	40.00%

mation. Typical monomers used in this work are tri and hexafunctional urethane acrylate oligomer. N-vinyl pyrrolidinone (NVP) is often used when mixing urethane monomers to dilute and blend the constituents, though this additive is less reactive it has effects on droplet size [27, 31].

A second common monomer used in H-PDLC fabrication is commercially available as Norland Optical Adhesive (NOA), which contains multifunctional thiols. The gelation rate of thiol monomers is slower than that of acrylate and results in larger droplets, which is the reason NOA65 is commonly used for fabrication of PDLC. H-PDLC reflection gratings can be formed using high intensity exposure, and high diffraction efficiency has been obtained in gratings with larger pitch [27].

H-PDLCs fabricated for this work use two writing wavelengths: 365 nm sourced

from an Argon:Ion laser and 532 nm sourced from a diode laser. Photoinitiator is necessary for both monomer chemistries using either exposure sources to react with a co-initiator and produce a free radical to initiate the free-radical addition polymerization reaction. Desirable initiators have long lifetimes and high quantum yield in addition to good absorption at the recording wavelength. Rose bengal and rhodamine 6G, two traditional laser dyes, have been used successfully to initiate acrylate and thiolene chemistries because of their high quantum yield and absorption of 532 nm light. Co-initiators in these systems providing the free-radical are N-phenyl glycine and benzoyl peroxide. For UV, Ciba Darocure products have proven successful in initiating both chemistries because of its high absorption of 365 nm exposure light [27].

Desirable liquid crystal components are usually nematic with high anisotropy in order to maximize diffraction efficiency and minimize switching fields. The index of the liquid crystal ordinary axis should should match the index of the polymer to enable the film layers to match with applied bias. The liquid crystals used in this work are Merck BL series, which are composed of cyanobiphenyls [27]. BL038, the liquid crystal used predominately in this work has an anisotropy of 0.272 with n_o equaling 1.527. Index of refraction of cured NOA65 polymer is equal to 1.524, a close match with the ordinary axis index.

Finally, in some instances, mainly when working with visibly initiated acrylate systems a surfactant is added to reduce switching voltage by lowering surface anchoring between the liquid crystal molecules and the polymer matrix [27, 32]. The surfactant typically used was polysorbate 80, commercially known as Tween 80, which is composed of polyethoxylated sorbitan and oleic acid.

H-PDLC is fabricated on structural substrates for several reasons including support of the approximately 5-20 μm film and uniformity of that thickness . The substrate is not only used for structure but also to provide an electrically conductive

optically clear electrode to the H-PDLC. Antireflective coated Corning 1737 coated with index matched indium-tin-oxide (ITO) is common when fabricating visibly initiated H-PDLC however non AR coated Corning 1737 is used when fabricating in the UV. Minimizing index differences within the substrate layers ultimately minimizes transmission losses resulting from surface reflections. There is a desire to fabricate flexible H-PDLCs or films on flexible substrates, and glass in limiting in this respect. An alternative substrate, polyethylene terephthalate (PET) has been considered that provides flexibility for various applications.

3.4 H-PDLC Spectral Characterization

Characterization of an H-PDLC typically measures the optical, electrical, and temporal properties of the film. Optical properties that are of interest include diffraction efficiency, Bragg center wavelength, FWHM of the reflection band, wavelength uniformity across the area of the grating, scattering, transmissive wavefront aberration, diffraction efficiency and center wavelength shift as a function of incident angle, and baseline transmission. Many of these measurements are accomplished using a white light source and a fiber optic spectrometer; aberration analysis is characterized using a wavefront analyzer. Radial scattering is measured using a photodiode mounted on a rotation stage which is a device that does not record wavelength dependent scattering, only scattering intensity. Electrical characterization includes measurement of switching voltage in volts per micron to maximize transmission through the film. This is an analog function, so several biases should be examined spanning the full switching range. Mechanical characteristics can be measured using a scanning electron micrograph image, similar to Figure 3.5a, to analyze droplet diameter uniformity, spacing, and centerline offset. A profilometer can also be used to see important grating period details, like shown in Figure 3.5b. Finally, because the on-switch and the off-switch

are not functions of the same mechanism, on-switch is triggered by application of bias, off-switch is related to relaxation, it is common to analyze the time period for each.

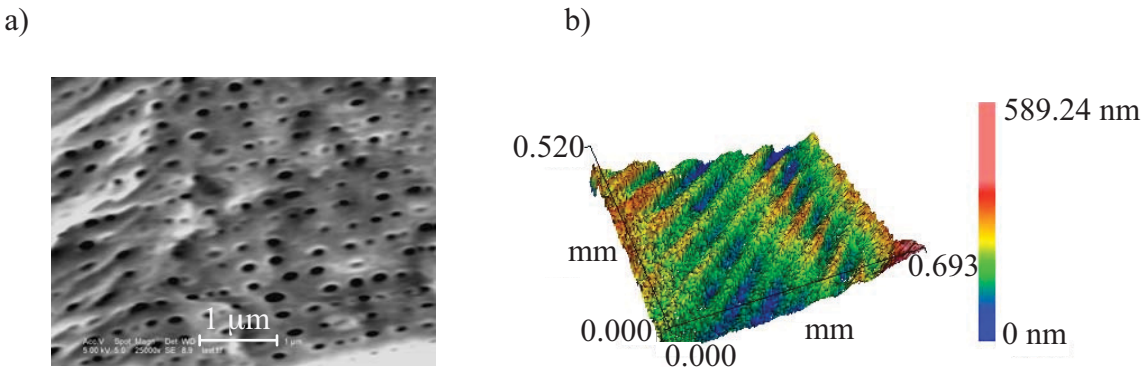

Figure 3.5: Experimental grating measured using the a) Scanning electron microscope and b) the profilometer

An important characterization typically performed on all gratings fabricated is a transmissive diffraction efficiency measurement. When performing this measurement, grating notch is measured using an Ocean Optics fiber-based spectrometer and white light source. Illuminating the grating with white light enables us to determine the stop-band wavelength, diffraction efficiency, baseline, and electro optic properties. There are several reasons we do not look at the sample in reflection mode, for one it is difficult and inaccurate to capture the reflection from the grating because of divergence. Figure 3.6 shows two sets of four gratings with varying pitch superimposed for a typical characterization measurement. Transmission baseline was characterized to be as high as 85% while diffraction efficiency was characterized as typically 55% to 65%. Losses in transmission baseline are attributed to scattered light from the liquid crystal droplets in the film.

Scattering is a known transmission extinction factor in H-PDLC. Nanostructured

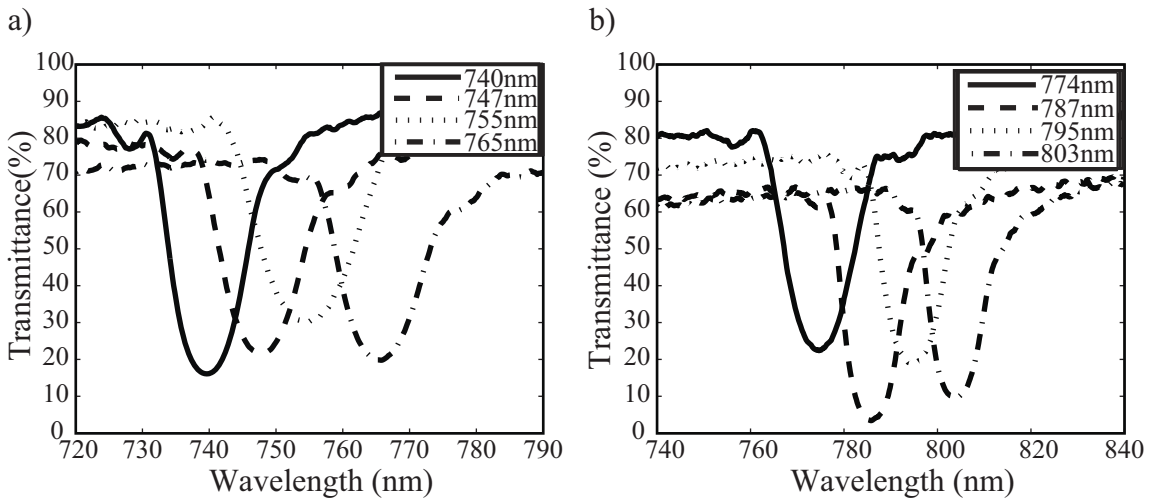

Figure 3.6: Example transmission notches of individual H-PDLC cells. H-PDLC transmission spectra was measured with no bias, and data was superimposed.

droplets comprising the modulation layers are of the size to cause Rayleigh regime scattering, which has a λ^{-4} attenuation relationship with wavelength. Scattering from this type of structure is also known to form modes, which means that its intensity can vary with rotation around the sample, and at some symmetrical angle fall to zero. Scattering of normally incident white light was measured by rotating a detector 180° around the center axis of a fixed H-PDLC sample. A measurement of scattered light was recorded every 5°. H-PDLC gratings were fabricated for this scattering measurement using the visibly initiated thiolene syrup to have a notch wavelength centered at 633 nm, and a He:Ne laser was used as a scattering probe. Cell widths of 5 μm, 10 μm, and 20 μm were compared. Scattering from H-PDLC films were compared with scattering from similar spaced cells of cured thiolene monomer (visibly initiated syrup with no liquid crystal added) and ITO glass spaced and adhered with optical adhesive. Results showed scattering modes formed approximately 75° from normal incidence in the H-PDLC samples. No scattering modes were observed for the samples of cured thiolene monomer or ITO glass adhered with optical adhesive. Scattering

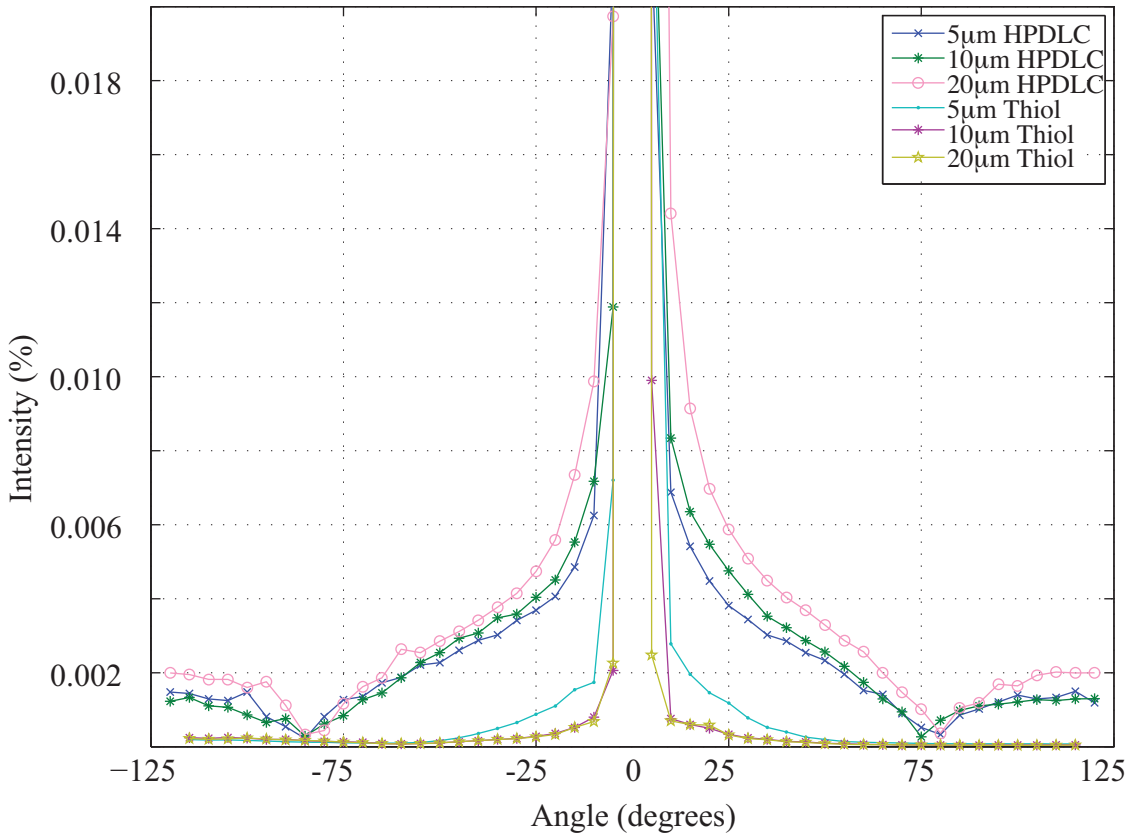

Figure 3.7: Scattering modes appearing at approximately $\pm 75^o$ with respect to normal incidence for samples of HPDLC. Samples of thiolene polymer show no scattering modes.

increased as a function of cell width in the H-PDLC samples. Measurements from the H-PDLC samples indicated higher scattering in the samples fabricated with LC than samples fabricated using only thiolene monomer and visible initiator confirming the conclusion that scattering loss in H-PDLC is due to the LC component of the film and not to the cured polymer or the ITO glass.

Another important characterization of H-PDLC is a droplet size, anisotropy, and centerline offset study that can be performed using an SEM of a portion of film. This characterization can be used to populate real-grating parameters in a simulation of

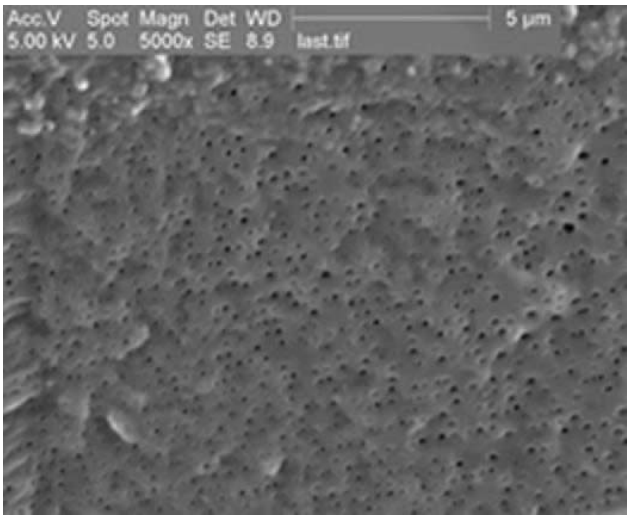

Figure 3.8: SEM image of the thiolene grating at 5000x magnification.

light transmission or to qualify some of the optical properties such as scatter. The attributed scattering from the liquid crystal component is due to nonuniform droplet size and distribution within the liquid crystal layer of the H-PDLC. Additionally, transmission losses due to scattering are attributed to refractive index variation between liquid crystal droplets [33]. Figure 3.8 is a scanning electron microscope image of a thiolene grating used in this study at 5000X magnification. The SEM image shows the polymer matrix with dark voids where liquid crystal droplets have been removed with acetone. The variation in droplet size and distribution can be clearly visualized in this micrograph. Statistical analysis of droplets in this SEM image shows an average long axis length of 164 nm with a standard deviation of 33 nm and an average short axis length of 82 nm with a standard deviation of 15 nm. Additionally, in the SEM micrograph, it is evident from the location of the liquid crystal droplet voids that they are not perfectly aligned in grating rows. Deviation from row centerline was analyzed and showed a distribution with standard deviation of 28 nm. On average, the droplets formed 3 nm below the row centerline again confirming the source of the scattering losses. These statistics are summarized in Table 3.2.

Table 3.2: Thiolene H-PDLC droplet distribution statistics

Parameter	Value
Average Long Axis Length (nm)	164
Long Axis Std (nm)	33
Short Axis Std (nm)	15
Average Short Axis Length (nm)	82
Centerline Row Deviation (nm)	28
Centerline Row Offset (nm)	3

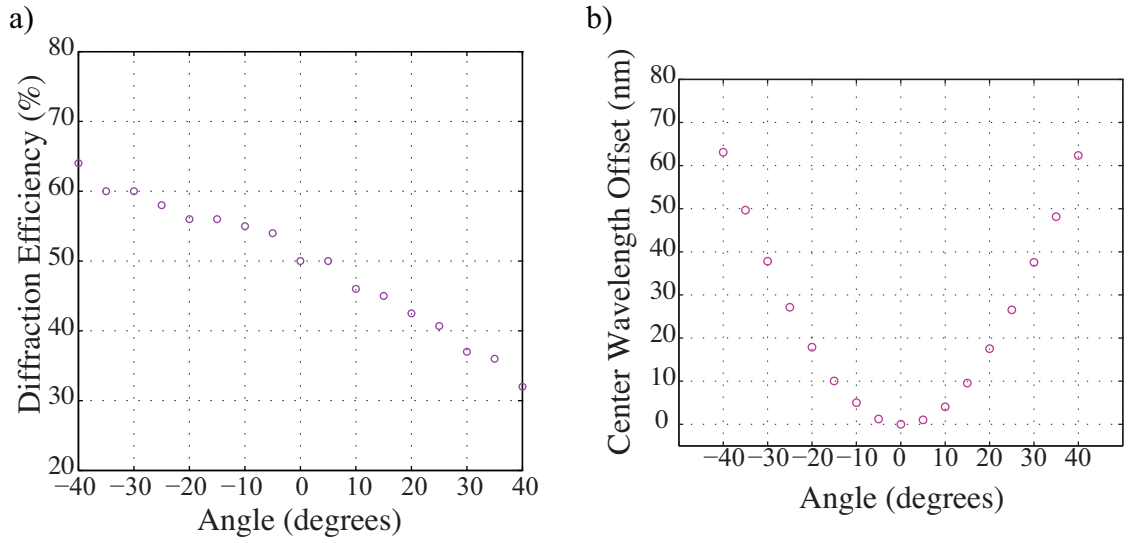

Figure 3.9: a) Diffraction efficiency as a function of incident angle. b) Notch center wavelength shift as a function of incident angle.

Blueshift is a characterization that enables us to see grating performance as a function of incident illumination angle. As the angle of light changes incident on the film, diffraction efficiency and center wavelength of the stop-band shifts. Figures 3.9a and 3.9b show a 50 % change in diffraction efficiency as the angle of incidence is varied ±40 degrees and center wavelength shifts symmetrically with change in incident angle.

3.5 H-PDLC Application Review

H-PDLCs have been developed into many useful applications. They were originally thought to be a promising solution to power consuming transmissive displays because of their innate color filtering and the elimination of the need for polarizers. Since then, these Bragg gratings have been explored for applications in telecommunications [34, 35], improving display technology such as conformal [36, 37] and reflective displays [38–41]. Stacking layers of H-PDLC films is useful for obtaining a broad reflection spectrum or multiple discrete reflection peaks. Stacked layers of H-PDLC material have also been reported to improve reflective display quality [42, 43]. Additionally, stacked H-PDLC films have been reported for application in a reflection-mode spectrometer [44]. H-PDLC has been used for applications in wavelength demultiplexing [45] and optical spectroscopy [46], an application published by the author and coworkers [Fox, Appl. Opt, 2007].

3.5.1 Photonic Structures and Lasing

A thorough application review is presented by Liu *et. al.* [Advan. OptoElec., 2008] with significant applications summarized here [47] . Photonic crystals are structures in which there exists a periodic dielectric variation in any direction, and as a result, a structure in which a band of optical wavelengths is prohibited from propagating. H-PDLC reflection gratings including the Bragg gratings fabricated for this work are

considered 1-dimensional photonic crystals because of the periodic material variation in a single direction. Using more than two intersecting beams at different angles, many 2D and 3D structures have been fabricated. Electrical switchability adds an interesting dynamic quality to H-PDLC photonic crystals. Tondiglia *et al.*[Adv. Mater., 2002] fabricated the first H-PDLC photonic crystal in 2002 [48], and since then structures such as face-centered cubic [49], transverse square [50, 51], orthorhombic [52], diamond and Penrose configurations [53, 54] have been realized. In addition, Escuti *et al.* [Opt. Eng, 2004] proved that five 2D and fourteen 3D Bravais lattices can be fabricated using multiple beams with precisely aligned incident angles [55].

H-PDLC has been realized as a lasing element because of its periodic structure and the usage of laser dye in formation, H-PDLC can be a resonant cavity and a gain-giving medium simultaneously. Applications that involve electrically controllable lasing include distributed feedback (DFB) lasing [56] and optimization of the lasing effect [57–61].

3.5.2 Sensors

H-PDLC has been developed into different types of sensors including a pressure sensor and a chemical vapor sensor. A reflection grating pressure sensor was realized to operate on the principle that changing the grating spacing results in a shift of reflected center wavelength therefore applying pressure perpendicular to the grating layers causes a detectable wavelength shift [62, 63]. Rai *et al.* [Mol. Cryst. Liq. Cryst., 2006] determined that pressure responsively is a function of polymer elasticity, which in turn is a function of initiator concentration. Measurable center wavelength shift increased several nanometers with a 5% to 21% initiator concentration [64].

A novel application was demonstrated by Hsiao *et al.* [Adv. Mater., 2005] who used an H-PDLC as a chemical vapor sensor. The operating principle of this type of

sensor relies on the porous nature of H-PDLC and the index change of the material upon absorption of a vapor. This group showed that absorption of various concentrations of acetone vapor into the polymer pores caused significant reflected wavelength shift, a shift large enough to be observed with the eye making it very applicable for visual detection of potentially dangerous vapor. [65].

3.5.3 Transmission Mode Spectrometer Application

An important and innovative application that uses stacked layers of liquid crystal polymer composite H-PDLC films as a component of a serial transmission-mode optical spectrometer was published by the author in *Applied Optics* [46]. Wavelength sensing devices such as spectrometers consist of a wavelength filtering component and an intensity sensing detector. The wavelength filtering component of the proposed spectrometer consists of four H-PDLC layers pressed between slides of antireflection (AR) and indium-tin-oxide (ITO) coated Corning 1737 glass. The optical path of this device involves transmitting the data signal through the four H-PDLC films serving as wavelength filters, each with the voltage-controlled ability to transmit or reflect a portion of the input signal's spectral content as shown in Figure 3.10. An energy sensing device, such as a CCD, photodiode or photomultiplier tube that serves as the optical path termination, is inline with the H-PDLC stack. Voltage control over each of the four H-PDLC samples enables precision wavelength detection on the terminating sensor by activating and deactivating the transmission notch, causing selective transmission or reflection of the signal's spectral content. Loss between H-PDLC layers is reduced by application of an index-matching material. Characterization of the spectral response of the four layer H-PDLC stack that functions as a wavelength filter allows for spectroscopic analysis.

Characterization of H-PDLC stacks included spectral analysis of the four serially

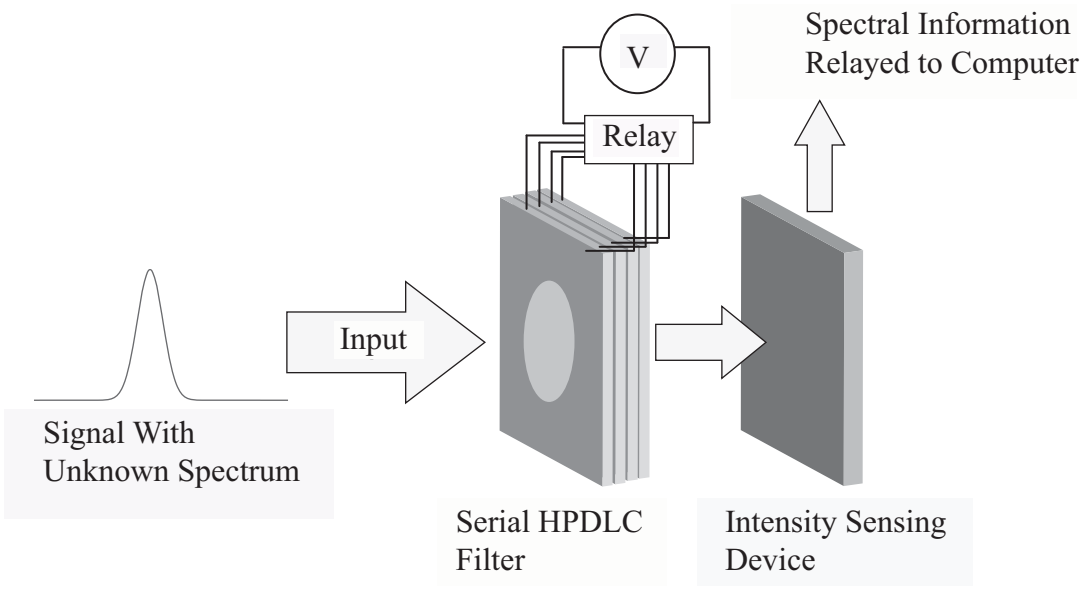

Figure 3.10: Schematic diagram of the proposed wavelength sensing device. The optical path is shown as an input signal of undetermined spectral content. The H-PDLC filter stack can selectively transmit and reflect a selected wavelength while the CCD or intensity detector relays wavelength dependent intensity information to a computer.

stacked cells with NOA65 (Norland Optical Products) functioning as index matching fluid (n=1.524) and optical adhesive at cell to cell interfaces. Spectral output of a white light test source appears as a broadband representation of the 10 nm spaced transmission notches of the stacked H-PDLC cells or an envelope spanning the spectral range of the individual cells' transmission notches. Upon application of voltage to one of the H-PDLC cells within the stack, the transmission notch of the biased cell increases, and the envelope line shape changes.

Spectral analysis was performed using an Ocean Optics white light source as an input signal to the filter set, and an Ocean Optics spectrometer was used to gather the spectral response data. Data was collected under several conditions, including zero bias and application of bias to each cell individually. The results of this spectral analysis is graphically shown in Figure 3.11a and Figure 3.11b. It can be observed

that in the zero bias state (curve labeled Envelope), the transmission envelope of the stack component represents a broadband outline of its constituent cells. With application of bias to the individual cells (curves labeled according to their center wavelengths), transmission of the notch wavelength of the cell under bias is increased by as much as 20% from the broadband envelope. Out of band transmission increase with switching was measured to be between 5% and 9%. This effect is clear in both sets of H-PDLC stacks in Figures 3.11a and 3.11b. Scattering loss from each cell causes a significant decrease in the percent of light that is transmitted to the detector after four layers of H-PDLC. Though a reduction in transmission loss due to scattering would significantly improve the performance of the proposed device, a sensitive intensity detecting device can detect the 20% increase in transmission as the H-PDLC switches states.

Signal to noise ratio (SNR) was characterized as a function of the number of cells in a stack. Figure 3.12a displays SNR data on a logarithmic scale with regression data superimposed. From the regression data it is clear that the SNR decreases logarithmically with number of H-PDLC samples in the stack. Though four samples were used in proof of concept experiments, this data shows that more than four H-PDLC samples can be used before reaching the noise threshold of the detector. Using a standard photomultiplier tube (Hamamatsu R2658), with a dark current noise calculated to be at 340 nA, noise threshold is reached using a stack of 26 H-PDLC cells.

In holographic fabrication of H-PDLC cells, there is precision control over the transmission notch center wavelength and repeatability of a 10 nm FWHM transmission bandwidth. Currently transmission notch center wavelengths can be written spanning the entire visible spectrum. Due to a decrease in SNR as more H-PDLC cells are stacked serially in the transmission path, a trade-off between detectable bandwidth and transmitted sensitivity is required. In the sample stacks characterized above, the

notch center wavelengths were spaced 10 nm apart yielding a detectable bandwidth of 40 nm. Detectable bandwidth can be increased by stacking 10 nm FWHM cells spaced 10 nm apart until the noise threshold of the detector is reached. Using a Hamamatsu R2658 PMT as a detector, 26 cells can be stacked before reaching the noise limit equating to a total detectable bandwidth of 260 nm.

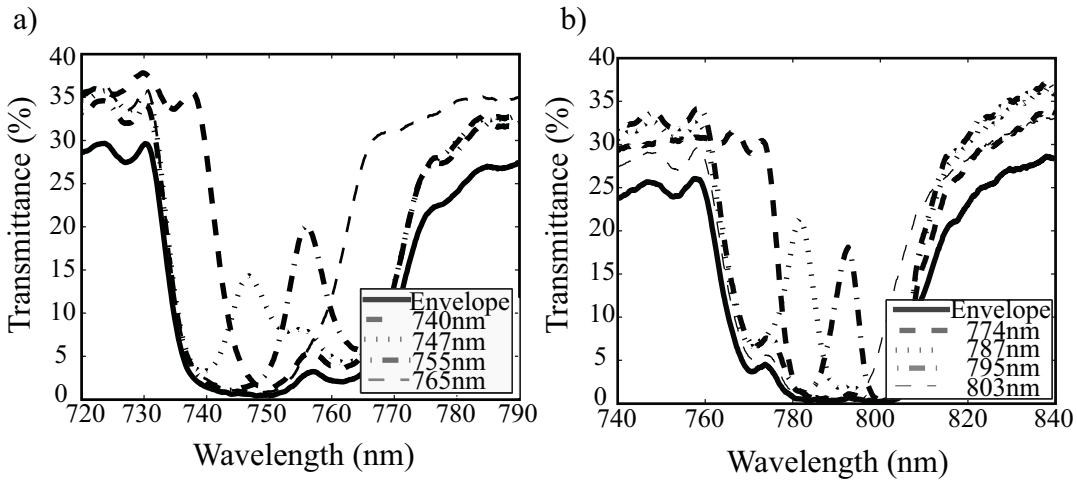

Figure 3.11: a) Spectral response of four H-PDLC cells stacked with NOA65 as an adhesive and index matching fluid. The spectral envelope can be seen as the outline of the four individual transmission notches with intensity loss. Additional superimposed data sets show the spectral response of the envelope as each cell switched. b) Stacked spectral response of four higher wavelength H-PDLC cells stacked with NOA65 as an adhesive and index matching fluid. Superimposed data sets show the envelope response to each constituent cell with applied bias.

Based on the characterization of four H-PDLC cells, it is clear to understand their functionality as the wavelength filtering component of a transmission-mode spectrometer. The signal of undetermined spectrum transmits through the wavelength filtering stack to a detector while the H-PDLC cells are individually modulated. Spectral content of the signal under test can be determined using a software program that equates the wavelength of the modulating cell with a change in detector output. After characterizing the line shape of the notch, wavelength can be extrapolated from the detector

output values in any region where the signal under test is within the transmission notch region of the H-PDLC stack. For each narrow banded input wavelength, there exists a unique transmitted intensity as a function of H-PDLC spectral line shape. This relationship is specific to each set of stacked cells and needs to be characterized for each system based on their exact spectral response.

More specifically, a software algorithm would initiate measurement of an unknown signal first by sequentially switching on each of the stack cells while monitoring the transmitted intensity at the detector to determine within which 10 nm wavelength range the signal exists. Once this is known, the surrounding cells are biased to be transparent to the signal under test. Transmitted intensity of the signal is determined and mapped to a wavelength using the filter's known line shape. Assuming a narrow test signal and known line shape of the H-PDLC transmission band, the wavelength location of the test signal can be determined by equating the transmitted intensity to its location on the filter spectral response curve. This intensity measurement method allows for a resolution that is limited only by SNR of the stack transmission signal and accuracy of the device used as a detector.

To completely characterize the H-PDLC spectrometer device, the wavelength of a test signal was determined using an H-PDLC stack and compared to the output of a commercial spectrometer (Ocean Optics HR4000-UV-IR). Like most commercial spectrometers, the Ocean Optics uses a diffraction grating to spatially disperse the spectral information of the signal under test and a CCD camera to detect intensity of the wavelength components. This commercial spectrometer has a resolution of about 0.25 nm. To compare the two methods, the H-PDLC spectrometer uses the filtering method described above. For proof of concept, we show that both spectrometers can equally detect peak wavelength of a narrow test signal to less than 1 nm. Using the method of mapping percent transmission of the test signal through a filter cell with adjacent cells switched to a fully transparent state, the curve in Figure 3.12b was

Table 3.3: Interpolated wavelength data compared with commercial spectrometer data

Signal Wavelength (nm)	Transmission (%)	Commercial Spectrometer (nm)
700.44	63.786	700.44
700.54	63.395	700.44
700.64	63.004	700.44
700.74	62.613	700.69
700.84	62.222	700.69
700.94	61.831	700.94
701.04	61.440	700.94
701.14	61.049	700.94
701.24	60.658	701.19
701.34	60.267	701.19
701.44	59.876	701.44
701.54	59.732	701.44
701.64	59.588	701.44
701.74	59.444	701.69
701.84	59.300	701.69

obtained. The characterization of the line shape of the spectral response shows the wavelength to photodiode current (shown in percent transmission) relationship that is used for correlating detected intensity to wavelength. This figure shows two adjacent cells characterized for transmitted intensity, each characterized with the other switched to its transparent state. This result shows a unique percent transmission for each 1 nm increment in wavelength indicating that through mapping percent transmitted intensity, 1 nm resolution in peak wavelength detection can be achieved. Using an interpolation between characterized data points, resolution can be further reduced.

For example purposes, using the line shape in Figure 3.12b and a linear interpolation between each 1 nm data point, percent transmission between 700.44 nm and 701.84 nm was calculated for 0.1 nm increments. Table 3.3 compares input signal wavelength, interpolated percent transmission from the H-PDLC stack, and peak

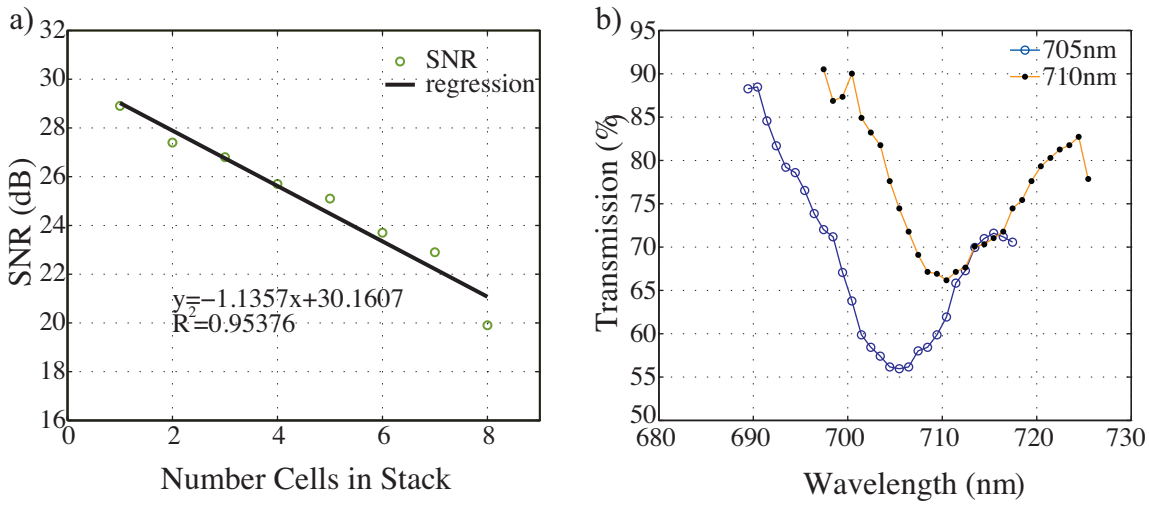

Figure 3.12: a) Signal to noise ratio measured as a function of stack thickness. b) Percent transmission of a test signal through adjacent cells measured using a photodiode. Each cell was switched to its transparent state when the other was measured. Significance is a unique transmission/wavelength relationship shown here for each 1 nm increment. Mapping percent transmission to wavelength is critical for determining peak wavelength.

wavelength measured using the Ocean Optics HR4000-UV-IR spectrometer. This interpolated data shows a unique percent transmission for each 0.1 nm increment corresponding to the peak wavelength of the signal under test. The commercial spectrometer detects a change in peak wavelength at 0.25 nm increments.

Spatially dispersing the signal under test onto a CCD array allows commercial spectrometers to detect intensity of more arbitrarily wide signals with the same resolution, where the H-PDLC spectrometer is limited to narrow banded signals. For the H-PDLC spectrometer to effectively detect wide spectral content, stacks of cells with narrow transmission notches can be used. The trade off exists between detectable

bandwidth and resolution when adapting this system for broader or arbitrarily shaped signals.

Shown in this work is a very important application of H-PDLC, and proof of concept of a wavelength filtering and peak wavelength detecting device constructed of four stacked and adhered H-PDLC thin film cells. Four stacked H-PDLC cells with different transmission notch center wavelengths add spectrally to yield a broadband spectral transmission notch under zero bias conditions. Wavelength filtering capability is demonstrated by an increase in transmission efficiency at specific wavelengths with the application of bias to an individual cell. Though this wavelength filtering device acts serially with application of bias to an individual cell, bias can be applied to any combination of the four cells to variations in the envelope spectral response. Applications for a wavelength filtering device, such as the four H-PDLC voltage controlled stack, include the aforementioned spectrometer with the addition of a CCD camera or intensity sensing device.

This chapter summarizes PDLC and H-PDLC films, two polymer liquid crystal composites that are predominately used in this research. We have discussed the fabrication and characterization technique, along with the material sets and exposure sources used to form these films. Finally, we have discussed many of the important applications that PDLC and H-PDLC have been used for in the recent years, many of which were performed in this group.

Chapter 4. Photolithography Process and Technique

Lithography is the process of transferring an image onto a substrate, a term that is derived from the fields of art and printing. Within the discipline of micro and nanolithography, this term can refer to the process of transferring an image, but on a much smaller scale. Photolithography is a common lithography technique that uses light and masking to optically transfer a master pattern onto a photosensitive substrate, but this technique is far from the only lithographic technique available. Currently lithography extends to serial processes such as electron beam (EBL) and ion beam lithography, parallel processes including photolithography and imprint technique. These pattern transfer techniques on the micro and nanoscale all have unique advantages favoring particular aspects of the process, but usually the trade-off is in time versus resolution. Photolithography is the predominant application used in this research. In this chapter, we review the need and importance of photolithography along with some of the basic principles necessary to understand the main application in this thesis. Since the primary focus is rooted in the optics of photopatterning, we discuss resolution and diffraction effects that occur in contact and proximity printing along with enhancement techniques such as projection systems, diffraction compensating, and multiple exposure techniques.

4.1 Parallel Printing - Cost and Speed

The concept of parallel printing refers to a technique that can pattern many features all at the same time. Photolithography is a technique that accomplishes this by using light to pattern a masked substrate effectively transferring all the light/dark contrast information onto the photosensitive material. The process of photolithog-

raphy consists of several steps including substrate and resist preparation, exposure and development. Photolithography has advantages in its low cost and time efficient processes; parallel processing allows many features to be pattered at once and modern resists have been developed to expose rapidly allowing assembly lines of production to move quickly. Speed and cost efficiency is a trade-off in optical lithography. The disadvantage is that the native resolution of a contact optical printing system is determined by the diffraction limit of light transmitting through the mask. Factors that effect this limit include exposure wavelength and distance from masking surface to substrate surface. Lithography systems have been moving deeper and deeper into UV wavelengths to compensate for diffraction, currently operating at 193 nm [1]. Systems have moved away from contact lithography and have been replaced by projection systems to minimize pattern size, and steppers have become useful in patterning a single substrate in multiple steps. Though technology advances and resolution enhancing systems certainly extend beyond the resolution limit, optical lithography technique does not compete with a serial patterning process for resolution precision.

4.2 Photolithography Importance in Industry

Industry has adopted photolithography as a standard because of its cost and throughput advantages over serial processes such as electron-beam lithography (EBL). Serial processes that achieve the highest resolution, however, are used in the photolithography process to fabricate the master mask. Optical patterning has been used to fabricate printed circuit boards (PCB), micro/nano -electricalmechanical systems (MEMS/NEMS), and integrated electronics (ICs). Feature sizes of ICs limit the amount of processing power and memory storage capacity per unit size that exists within the microelectronics we use today. In 2008, IBM introduced a processor fabricated with 65 nm technology to hold nearly a billion transistors [66], Intel has since

shown 45 nm technology [67]. Moore's Law states that the number of transistors fabricated in a unit volume will double every two years. Though engineers address problems such as heat dissipation of so many components, the fundamental challenge of maintaining this trend is time and cost effective fabrication of IC components at smaller and smaller sizes. This problem is currently being addressed by improving photolithographic technique to reach farther and farther beyond the diffraction limit.

4.3 Photoresist Tones

Photoresist, or the photosensitive polymer used in optical patterning comes in positive and negative tones. A positive photoresist developed structure will yield a positive image of the photomask while a negative toned resist once developed will yield a negative image of the photomask. Photoresist is optically activated to either become soluble or insoluble with the exposure of an appropriate energy and wavelength of light. Positive resist uses a mechanism of chain scission or breaking of the polymer chains to render the resist more soluble for an alkaline solution in the exposed areas. Exposure initiates cross linking in negative resists to render the exposed areas insoluble to a solvent developer. Aside of the tone advantages and disadvantages that can be application specific, positive and negative resists have other benefits and drawbacks for instance the alkaline developer solution used with positive resist is more environmentally safe than the solvent developer used with negative resists. Also, negative resists are known for swelling in developer. Negative resists have advantages in adhesion and wet etch resistance, and can be used as permanent structures [1]. Figure 4.1 illustrates the exposure, development, and final structure stages of positive and negative resist. Right illustrates positive resist patterning, left illustrates negative resist patterning. Application and mask tone may dictate one resist over another.

Resist tone specific patterning may be limited by the polarity of the mask. Masks

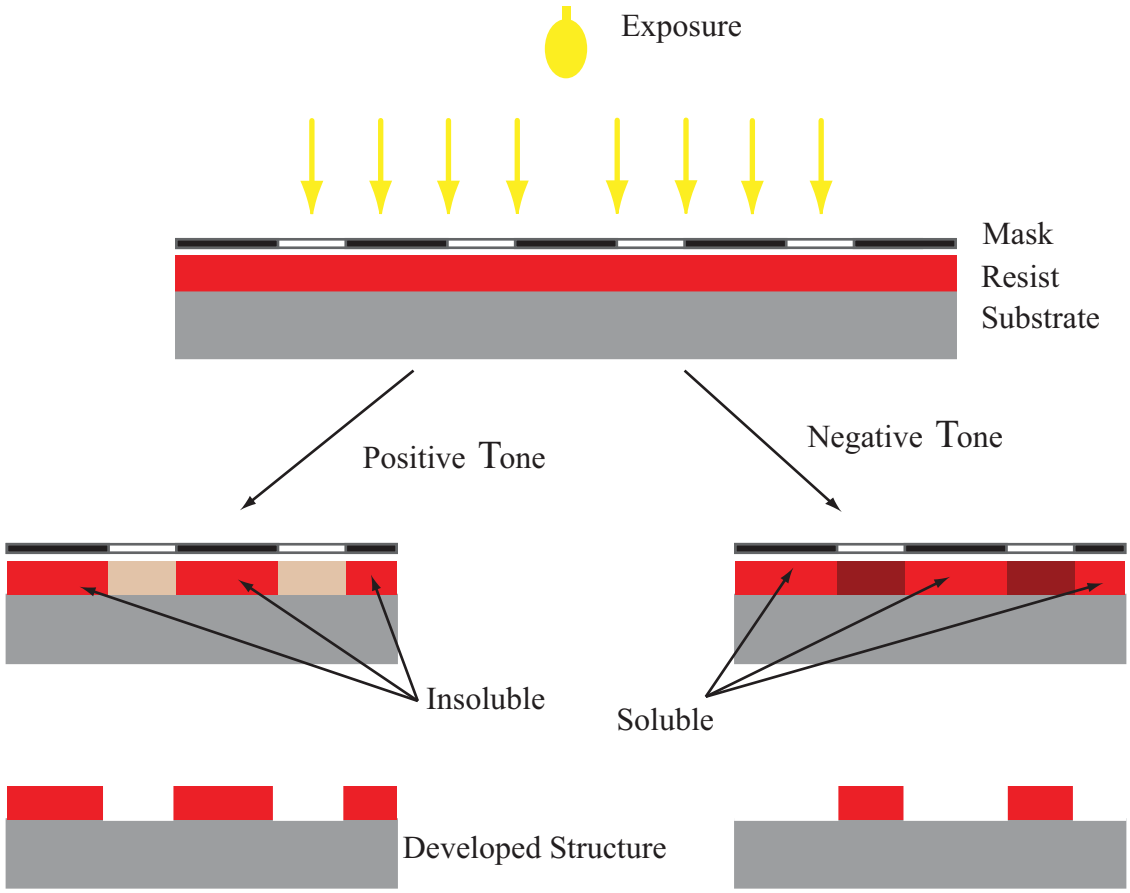

Figure 4.1: This illustration shows the patterning parameters of positive and negative resist tones. On the right, developed positive resist yields a positive image of the mask. On the left, developed negative resist yields a negative image of the mask. Recreated from Madou [CRC Press, 2002, pg. 6]

can be light field or dark field, a parameter designated by the tone of the feature. Clear features with absorbing chrome surrounding are usually referred to as dark field. By combining a choice of resist and mask tone, many options are available.

4.4 Photolithography Steps

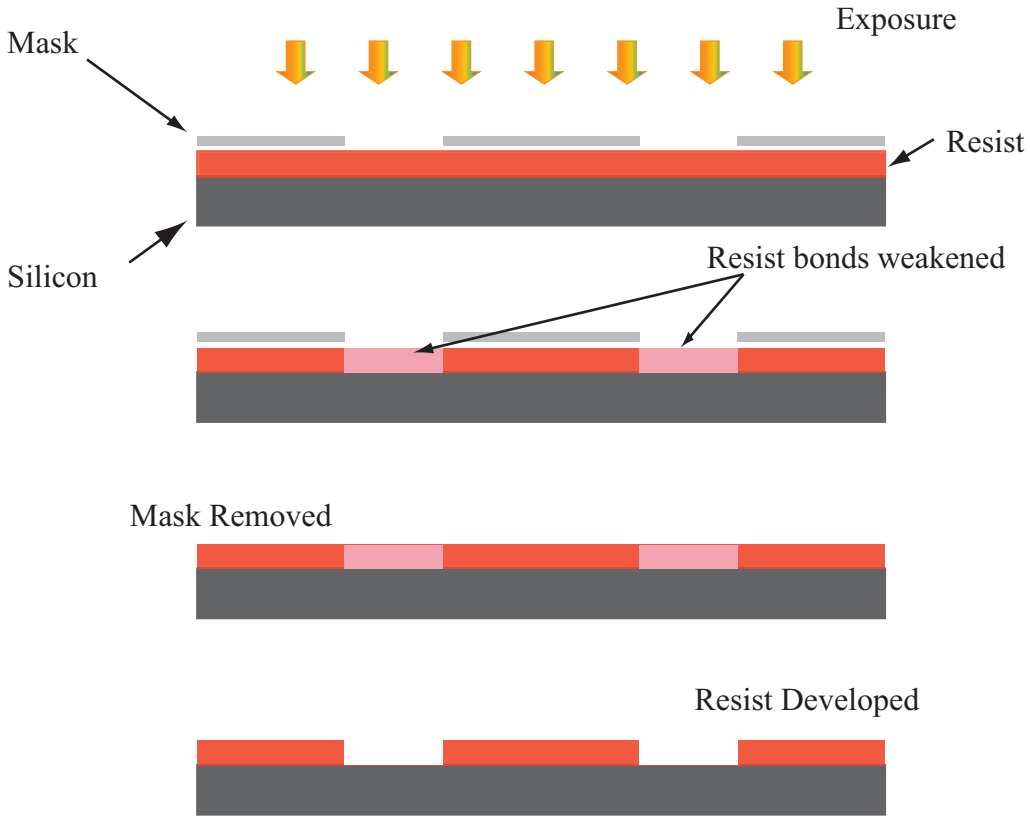

Figure 4.2: This illustration represents the basic steps in patterning positive photoresist. Starting from a cleaned and prepared silicon wafer, photoresist is spun onto the substrate and aligned with a mask. The resist is exposed, mask removed, and developed. Once the final resist structure has formed, an etch or deposition step may be performed before the positive resist is stripped using an organic solvent.

Basic lithography steps are overviewed next. The steps outlined here are important not only in the fabrication of the device developed in this thesis, but in its

operation. Photolithography is used to not only fabricate the device developed in this thesis but also as its main function. These lithography steps are shown in more detail in Figure 4.2 for positive resist systems.

The contact photolithography process starts by preparing the substrate. Glass is cleaned using acetone or methanol to remove grease or other impurities that might interfere with the resist adherence to the substrate. When preparing a silicon wafer, a layer of silicon dioxide may be thermally grown, or intentionally removed from its surface using hydrofluoric acid.

Next resist is spun into the substrate surface. Photosensitive polymer patterned with light, the fundamental step in photolithography, is known as photoresist and is often deposited using a spincoater. The substrate is spun at a controlled high speed for a set amount of time to evenly distribute the polymer over the surface. Material properties of the liquid resist are used to determine the length of spin time and velocity to obtain a particular uniform thickness. The relationship of thickness to polymer concentration and spin speed is

$$T = \frac{KC^{\beta}\eta^{\gamma}}{\omega^{\alpha}} \tag{4.1}$$

where C is the resist concentration, η is the polymer viscosity, and ω is the spin speed. α, β, γ, and K are calibration constants found experimentally and vary with resist type. This information can be found in the resist datasheet. The typical target thickness for this work is between 1.4 and 1.5 μm. Typical spin speed for 1813 series positive resist is 4000 rpm as shown in Figure 4.3. Following resist spinning, a soft bake step is taken to harden the resist and evaporate any solvents remaining in the resist before exposure.

The exposure step is next. Using a mask aligner or a UV light source, the resist is exposed under a mask. Most commercial resists are sensitive to wavelengths in the UV

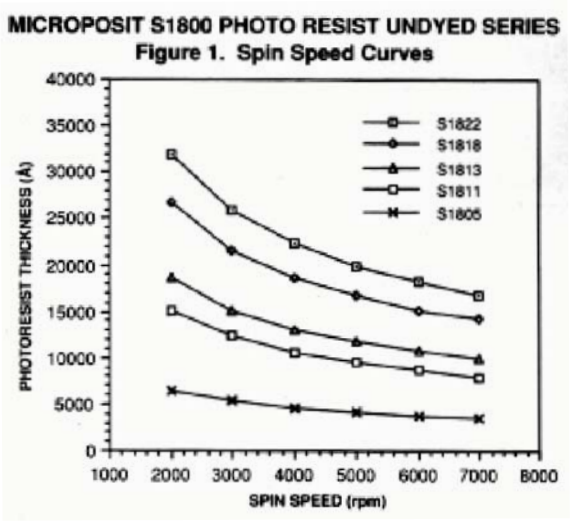

Figure 4.3: Microposit Shipley 1800 series positive photoresist datasheet indicating the spin speed relationship to resist layer thickness. Typically S1813 is used in this thesis.

and correspond to one of the UV lines of a mercury lamp, for example the g-line at 436 nm or the i-line at 365 nm. Since smaller, more resolved features and the diffraction limit of contact lithography are directly related to the wavelength of the exposure light, resists are developed to react to the shortest possible wavelength. Limited commercial resists are available in the visible though many exist throughout the UV. Figure 4.4 shows the 1813 resist material absorbance as a function of wavelength between 300 nm and 500 nm. The material is more sensitive to wavelengths in the UV over near visible wavelengths. For the adaptable photomask fabricated in H-PDLC material, the wavelength used is 436 nm, a wavelength nearly outside of the acceptable range for exposure for UV resists.

Development is the important step that changes the exposed resist into the image (or inverse image) of the mask used during patterning. Depending on resist polarity, wet developers rely on cross-linking or chain scission to produce the desired output. Shipley 1813, a positive resist uses an alkaline solution to dissolve the exposed resist

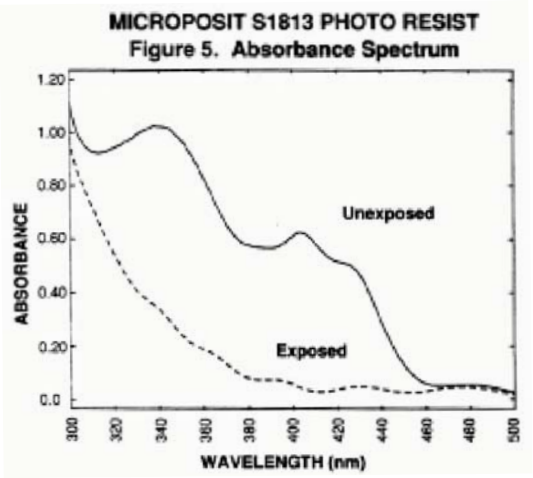

Figure 4.4: Photoresist absorption plotted as a function of wavelength.

areas yielding a positive image of the mask. At this point, the hardened and developed resist becomes a mask for the next process, which can be an etch or a deposition step, depending on the overall plan for the fabrication.

4.5 Lithographic Sensitivity and Contrast

Lithographic sensitivity and contrast are important factors that determine the pattern quality when patterning resist. Variables that effect lithographic sensitivity include resist quantum efficiency, resist type, thickness, wavelength of exposure source, and development conditions. Photochemical quantum efficiency is an intrinsic property of resist and is related to photon absorption and conversion efficiency into resist patterning events. This is heavily effected by the exposure light wavelength and the resist absorbance properties as illustrated by the absorbance curve for Shipley 1813 photoresist shown in Figure 4.4. Resolution is wavelength dependent; shorter wavelengths can pattern smaller features, and sensitivity effects exposure time. The more sensitive the resist at a certain wavelength, the shorter the required exposure dose. Optimizing a resist for brief exposure times at short wavelengths maximizes

throughput and minimizes available feature size.

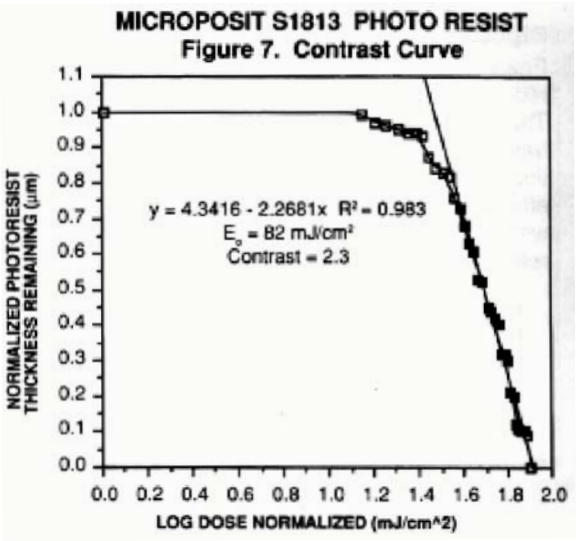

Figure 4.5: Microposit Shipley 1800 series positive photoresist datasheet contrast curve, or the energy dose necessary to remove 0 to 100% of the resist layer.

The dependency of exposure dose to final developed resist thickness can be determined by compiling a resist response curve, like the response curve for Shipley 1813 shown in Figure 4.5. A response curve illustrates normalized resist thickness as a function of log exposure dose where resist contrast is related to the slope and defined as

$$\gamma_p = \frac{1}{(\log D_p - \log D_p^0)} = \left[\log \frac{D_p}{D_p^0}\right]^{-1} \tag{4.2}$$

where D_p is the dose that results in complete solubility and D_p^0 is the dose that begins to develop a resist. Doses less than D_p^0 do not result in resist solubility in developer. Dose values in mJ/cm^2 are extremely important in processing to understand the effect of exposure intensity and time with respect to the profile of the patterned resist. It is also important to note that a mask need not completely eliminate transmitted light, only attenuate it below the threshold for exposure which is defined as D_p^0.

4.6 Resist Profile

Attaining the ideal resist profile requires careful control over both the exposure dose and the development time. When using positive resists, overexposure can cause scattering and reflections which will result in an undercut profile like the profile shown in Figure 4.6a. An ideal pattern transfer can be performed, resulting in the cross section shown in Figure 4.6b, but the more common result when patterning with positive photoresist is the profile shown in Figure 4.6c. The undercut profile is common for positive resist and is usually a result of forced development of underexposed resist. Force developing also typically results in reduction or thinning of the entire layer [1], an effect seen in results of this research.

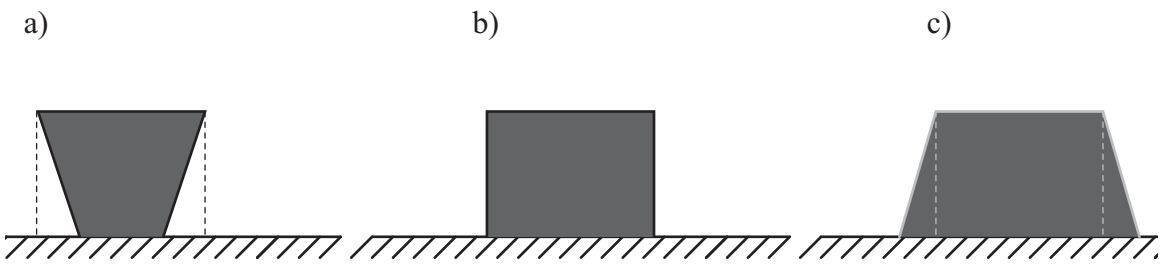

Figure 4.6: Three typical resist profiles typically fabricated when using positive resist. a) The undercut profile is a result of overexposure in positive resist and can be attributed to reflections and scattering. b) The ideal vertical walled profile c) The overcut profile resulting from forced development of underexposed resist. Thinning is also common in this situation. This figure is recreated from M. Madou[CRC Press, 2002, pg. 18].

4.7 Photolithography Limitations: Resolution and Diffraction

In lithography, the minimum patternable feature size that can be achieved consistently across multiple samples is known as the resolution and it depends on several factors. Examples of resolution effecting factors include resist mechanics such as swelling, the

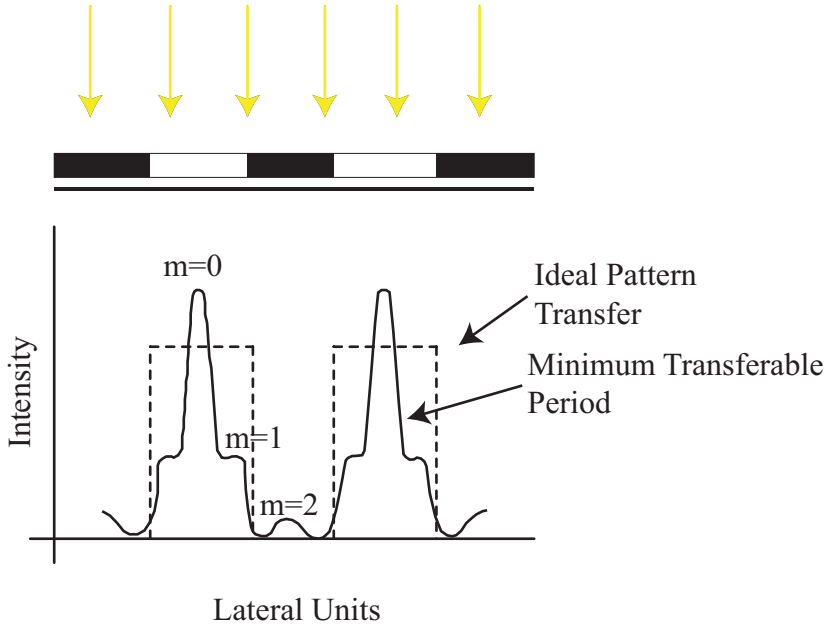

Figure 4.7: Top section is illustrating UV exposure onto a masked substrate. Below the masked substrate is the intensity pattern of light transmitting through the mask with ideal pattern transfer in dotted lines and diffracted pattern transfer in solid. This figure was recreated from D. Widmann [European Solid State Circuits Conference, 1976]

wavelength of exposure light, mask alignment, etc. In contact and proximity printing resolution is heavily dependent on diffraction of exposure light propagating through the photomask. Diffraction describes the nonuniform intensity pattern that occurs when light transmits near the border between a transparent and opaque material, and indicates interference at those sharp edges. Ideal transfer through an aperture would have sharp shadows resembling the pattern of the mask, but because of diffraction, which is a function of the wavelength, aperture size, and distance from mask to image plane, ideal transfer is limited. Figure 4.7, which is adapted from Ref. [68] and reprinted in Ref. [69] and [1], shows a mask with periodic transmissive and opaque regions, with image formation on a plane below. Ideal pattern transfer would resemble an intensity pattern marked with dashed lines, sharp rectangular corners identically

matched to the transmissive and opaque regions of the mask above. Diffracted transmitted light is shown with the solid line.

Using Figure 4.7 the minimum transferable pattern dimensions can be calculated. Diffracted pattern transfer resembles the solid line superimposed intensity pattern showing diffraction maxima and minima. This diagram is designed to show the separation of mask regions defined by the overlap of diffraction maxima and minima as feature size is reduced. This can be visualized in the intensity pattern where it is marked m=2. The relationship between aperture width and diffraction peak orders will enable the calculation of the minimum aperture width condition.

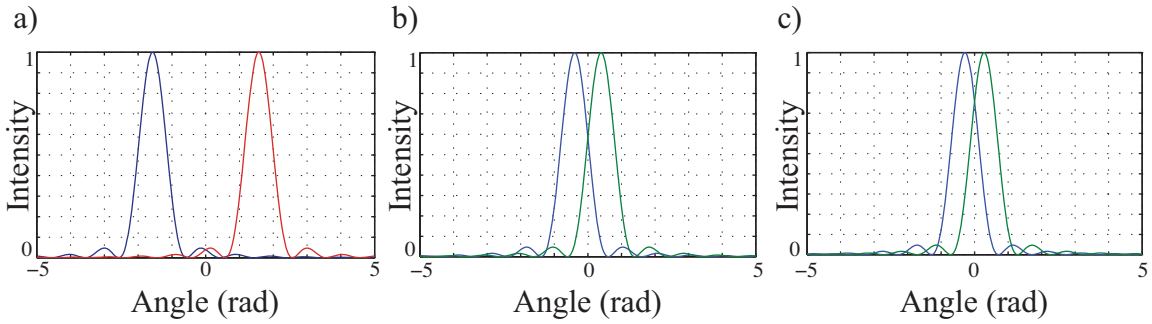

Figure 4.8: This simulation illustrates the definition of the Rayleigh diffraction limit. a) Two sources well resolved on the image plane. b) Sources meeting the Rayleigh diffraction criteria indicating that the first source's primary maximum is equal to the near source's first minimum. c) Two sources that are unresolved on the image plane.

To calculate the minimum width of an aperture that meets the diffraction condition, we first need to define minimum resolution. Lord Rayleigh, when examining distinct stars in a telescope defined the boundary between features clearly resolved and unresolved to be when the central maximum of one star's diffraction pattern overlapped with the first minimum of the second diffraction pattern. This is shown in Figure 4.8 where 4.8a represents two clearly resolved sources, 4.8b shows the limit

with the central maximum of the first source is overlapping with the first minimum of the second source, and finally in 4.8c is displayed an unresolved pair of point sources [70]. The simulations shown in Figure 4.8a-c are intensity lineshapes of a sinc squared function that represents the intensity of a Airy pattern. The y-axis is intensity, the x-axis represents aperture output angle, which is commonly written β. It is convenient to show aperture output angle to illustrate the intensity spatial relationship because it is independent of distance from aperture to image plane. In this case it was simulated to show a general diffraction pattern as a sinc squared function with a second diffracted source in different locations nearby. In order to find an aperture or mask pattern that meets the Rayleigh criteria, assuming spatially coherent light emitted from a collimated mercury arc lamp, it is necessary to visualize the diffraction pattern resulting from transmission through a grating of pitch $2a$, wavelength equal to λ, traveling a distance from mask to image of d.

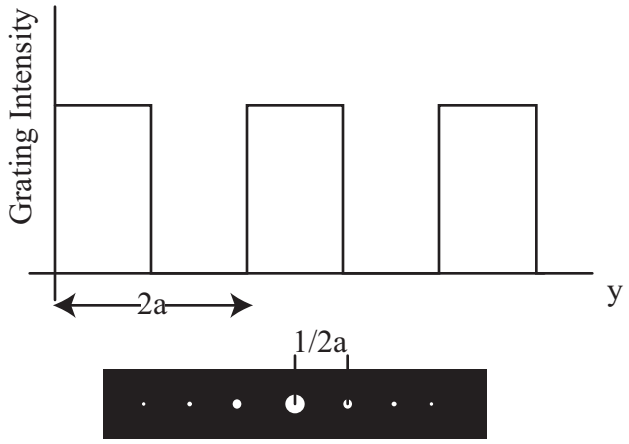

Figure 4.9: As described in Hecht [Addison Wesley, 2002, pg. 609], light transmitting through a grating of period $2a$ will have a diffraction pattern on its Fourier plane with period equal to the reciprocal of the grating period

To derive the resolution equation for contact and shadow printing, we start by assuming a mask with periodic modulation like in Figure 4.7, then we reduce the pitch

of the modulation until the Rayleigh criterium is met. To accomplish this we need to examine the created diffraction pattern on the Fourier plane. Figure 4.9 illustrates the intensity pattern of this mask and its diffraction pattern on the transform plane. The fundamental spatial frequency of this system is $\frac{1}{2a}$ and the distance between diffractive maxima, y, is the fundamental spatial frequency multiplied by distance and wavelength

$$y = \frac{1}{2a}\lambda d \tag{4.3}$$

Overlap of the central maxima and the first minima of two identical gratings occurs at an interval yielding a minimum patterning distance of

$$a_{min} = \frac{3}{2}\sqrt{d\lambda} \tag{4.4}$$

Refs. [1, 69] incorporate resist thickness, z, into the minimum aperture size as

$$a_{min} = \frac{1}{2}\sqrt{\lambda(\frac{z}{2} + d)} \tag{4.5}$$

It can be seen in the equation of minimum patternable feature size that resolution of shadow printing is a function of wavelength, distance of object to image plane, and resist thickness. Perfect contact between mask surface and resist coated substrate will yield the best resolution and the smallest patternable features.

The minimum patternable feature size gives a lower limit to the patterning ability of a system, but indicates less about diffractive effects that occur at apertures slightly larger than the minimum. Depending on the distance from mask to image plane and the wavelength used, diffractive effects can begin to show at much larger aperture sizes.

As summarized in Refs [70,71], diffraction can appear in two major regimes: near-field and far-field, Fresnel and Fraunhofer respectively. The difference in near-field and

far-field is the approximation of impinging wavefront at an opaque object. Far-field diffraction occurs when those impinging waves are approximated as planar rather than spherical as predicted by the Huygens-Fresnel principle. Since this work is dealing with small object-to-image plane distances, we calculate that we are working in the near field with no appropriate way to approximate planar wavefronts. Understanding the differences in resolution regimes will ultimately allow a simulation of diffracted light transmitting through our adaptable mask.

4.8 Resolution Enhancement

Contact lithography has a resolution limit controlled by several factors described in the above section. The best achievable resolution using a contact technique would entail minimizing the exposure wavelength and resist thickness. An approximation of the minimum attainable feature size using a contact technique is 0.8 μm assuming 1.4 μm resist thickness and 436 nm exposure. Current lithography standards in the microelectronics industry are pushing feature size on the order of several tens of nanometers, orders of magnitude smaller than the smallest possible feature size fabricated with contact photolithography. Techniques have been created to push the diffraction limit using optical systems, multiple exposures, and even diffraction compensation in order to fabricate the nanometer sized feature.

4.8.1 Projection

Projection printing is the next natural step towards enhancing feature size limitations. Proximity printing is a method in which mask and substrate are not held in contact, making diffractive effects more significant. While projection printing is also a non-contact method, optics are used to focus and reduce mask image on the substrate. Often a stepper is used in this type of system to expose a small portion of

the substrate then realign and move on to the next exposure automatically. When introducing external optics into the imaging system, certain new parameters begin to effect performance such as numerical aperture, focal length, and aberration of the lens. Positive resist profile or edge slope fabricated using a projection system is the product of a term determined by the exposure system and a term defined by the resist mechanical properties.

$$\frac{dz}{dx} = \left\{ \frac{dz}{dD} \right\} \left\{ \frac{dD}{dx} \right\} \tag{4.6}$$

In this equation, x and z are the lateral and height variables respectively, and D is the exposure dose. The resist mechanical properties can be summarized as

$$\frac{dz}{dD} = -\frac{\gamma_p}{D_p} \tag{4.7}$$

where γ_p is the positive contrast and D_p is the resist sensitivity. The intensity profile term, or the term dominating the optics and exposure component has been defined as

$$\frac{dD}{dx} = \frac{2NA}{\lambda \left[1 - k\left\{ \frac{DOF \cdot NA^2}{\lambda} \right\}\right]^2} \tag{4.8}$$

where NA is the numerical aperture of the exposure, DOF represents depth of focus, λ is the exposure wavelength and k is a multiplication factor representing the coherence of the exposure source. Projection systems relying on the Rayleigh criterium alone have been shown to achieve minimum feature size on the order of the wavelength of exposure [1].

4.8.2 Multiple Exposure Patterning

Multiple exposure patterning techniques currently under development to enhance patterning and reduce diffractive effects can be categorized as double exposure techniques and double patterning techniques. The concept of a multiple exposure technique is

to fabricate two patterns on a single layer of resist, whether the dual patterns are exclusively lithography based or lithography plus other processing. Double exposure technique is performed by exposing a layer of resist, changing masks, exposing the same resist layer with the secondary pattern without moving the substrate from the lithography tool. This technique is beneficial in decomposing series of orthogonal patterns to reduce the undesirable diffractive effects that occur as the resolution limit is neared. The major limitation in this technique is overlay alignment of the individual masks used in the sequential exposures [72].

Double patterning has recently been suggested as the technique that is most viable for reaching 32 nm features in the IC industry [73–77]. Double patterning lithography (DPL) technique differs from double exposure technology in that it usually requires an intermediate processing step between sequential exposures of patterns appearing on the same substrate. Typically double patterning takes on two forms, both requiring an etch or deposition step between patterning of the second mask. A sacrificial layer DPL involves etching of the primary pattern before secondary patterning to create the dual layer patterns. A spacer DPL technique requires deposition of a thin film over the initial pattern prior to secondary patterning.

Not all DPL techniques require an intermediate process step between exposures, as explained in Ref. [73]. Recently a lithography-only technique has emerged as a solution for double patterning indicating that feature sizes pushing the 32 nm limit can be fabricated *without* moving the wafer from the exposure tool. The main idea of the litho-litho-etch (LLE) technique is to couple varying types of resist layers and exposing them sequentially with different masks. Again the primary limitation of this technique is overlay alignment of sequential masks in the lithography tool.

4.8.3 Diffraction Compensating

Diffraction compensation is a method of mask making that solves patterning like an inverse problem. Inverse lithography, as it is known, is the method of solving for optimal mask patterns while using the image plus diffraction as a goal. Historically, inverse lithography was performed using algorithms that randomly switched pixels of a particular pattern and examined the diffractive outcome. Eventually the algorithm would converge on the ideal mask pattern solution though very slowly [78]. More recently, different types of algorithms have been devised to back solve from target to pattern [79–81].

4.9 Grayscaling

In lithography, there exists many techniques to fabricate increasingly small features, as well as interesting 3D features. Parallel or masked photolithography can employ special masks to create a 3D structure in resist without relying on holographic, stereo, or any other direct-write lithography technique. A grayscale or half-tone mask can simulate a partial exposure of the resist while still benefiting from the parallel processing and rapid throughput of a traditional photolithography process.

The key in the grayscale lithography process is encoding 3-dimensional data into a 2-dimenional mask [82]. Varying intensity patterns is the usual method of encoding data to create the blaze or taper pattern, and when using a binary mask, it is attained by modulating chrome and glass with patterns smaller than the resolution limit. Modulating patterns smaller than the resolution limit creates the illusion of a range of intensities on the surface of the resist. Modulation of the chrome and glass pattern can be achieved through either pulse width modulation or pulse density modulation, these patterns differ in the width and density of chrome holes. Pulse width modulation varies the width of the patterned chrome, while pulse density modulation

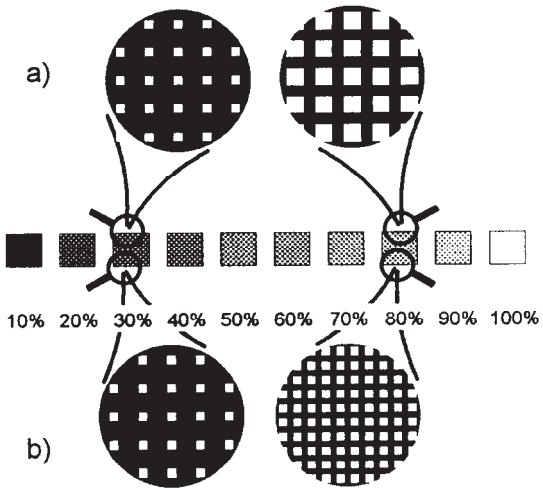

Figure 4.10: From Oppliger [Microelectron. Eng., 1994], micro and macroscopic images of different grayscale mask configurations. a) Upper inset shows pulse width modulation of the cutout pattern. b) Lower inset shows pulse density modulation. Reprinted with permission.

varies the density of the chrome pattern below the diffraction limit [83]. Macroscopically, either pattern appears to have a smooth varying intensity as shown in Figure 4.10. Applications of this technique include micro optics such as blazed gratings and microlens arrays [84, 85], and other interesting 3D shapes such as slopes and cubes [86]. Grayscale can be achieved by using a direct-write method as well as a masked method, as illustrated in Ref. [87] where a MEMS digital micromirror device (TI DMD) was used to pattern the resist.

Grayscale can also be achieved by directly modulating the intensity of exposure through attenuation rather than through a modulation technique. H-PDLC has an analog response to voltage and transmit a wide range of intensities as a function of applied voltage. H-PDLC masking is ideal for grayscale because of the direct control over transmission intensity.

In this chapter, we have reviewed the mechanical and optical concepts of contact and proximity photolithography along with some of the important techniques cur-

rently in use to enhance resolution. Contact and proximity printing have diffraction limitations based on wavelength, resist thickness, and distance from mask to photoresist. Enhancement techniques such as stepping and reduction optics, and very short wavelength exposure light enable a degree of smaller features. Introduction of diffraction compensation and multiple exposure techniques is what will enable the industry to move to the next smallest feature size.

Chapter 5. Review of Adaptable Photolithography Techniques

Lithography as a fabrication tool is an enormous field with many methods and devices. Photolithography is a subset of lithography, but it also contains many variations that all provide benefits one way or another. We are already overviewed holographic lithography as a means for fabricating H-PDLC in Chapter 3, and discussed traditional photolithography methods in Chapter 4. Traditional binary photolithography is a process where many of the steps are repeated in this work, with the difference being in the type of mask used. Binary photolithography masks can be either chrome patterned on glass or ink printed on a transparency, but the key point is that they are static in nature and cannot be pattern reconfigured. In this literature review, we highlight existing and interesting methods of photolithography that use masks with an element of adaptability. This includes masks made using other liquid crystal technology and masks made using microfluidic channels. We will review some recent work in MEMS lithography because it is so prevalent today, but MEMS micromirror and spatial light modulation is considered a maskless lithography technique (similar to the electron beam) and does not offer all of the benefits of a photomask patterning. We will look at a comparison of these different methods and how they differ from an H-PDLC adaptable mask.

5.1 Microfluidic Photomasking

Recently there has been work done in what has been termed "microfluidic photomasking" or μFPM. The main concept of μFPM is fabricating a mask made of polydimethylsiloxane (PDMS) stamped microchannels and filling them with UV absorptive dye. Dye filled microchannels as photomasks stem from work performed by

Whitesides [Sens. Actuators A: Phys., 1999] and specifically by Ref. [88], but in this application they take the place of a binary mask by absorbing light with dye in the photolithography step. Microfluidic photomasks were first shown to have grayscale ability by pumping different concentrations of dye through the channels and that the patterns can change within a few seconds [89]. The result of a μFPM grayscaling experiment is shown in Figure 5.1 which illustrates 5 microchannels with different dye concentrations. Below is the varying height structures patterned using this device as a photomask.

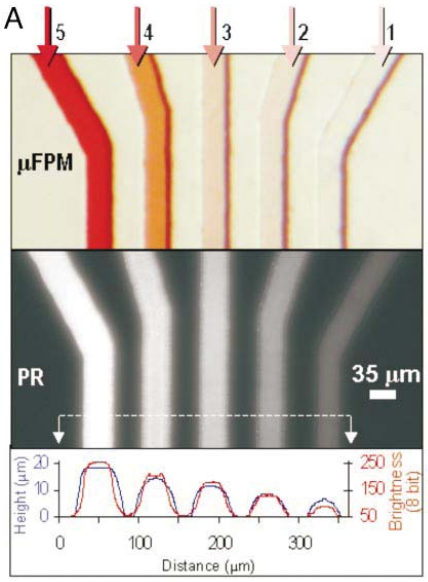

Figure 5.1: From Chen *et. al.* [Proc. Natl. Acad. Sci., 2003] the results of μFPM photomasking of 5 different dye concentrations and the varied height structures they form. Reprinted with permission.

Microfluidic photomasks have also been used for dynamic photomasking by flowing light absorptive dyes though a two layer microfluidic channel matrix [90]. This two layer channel system acts in a sense like a passive addressing scheme for a mobile transparent pixel by flushing and dying layers for different time intervals. The result of this study shows that the adjustable transparent pixel can pattern to a resolution

of about 50 μm and through pumping, can reconfigure on the order of seconds. This method was effective for patterning arrays of 100 μm and 50 μm square pixels in large configurations by flowing alternating streams of dye and clear liquids through the microchannels, this paper illustrates that the clear pixel can be moved around similar to an "Etch-a-Sketch" (as noted in the paper).

To summarize microfluidic photomasking:

- Grayscale has been demonstrated by varying the concentration of light absorbing dyes, but limited by solubility. Features patterned with different heights have been shown.
- Dynamic masking has been demonstrated by pumping a two-layer channel matrix with light absorbing dye. Clear pixel has been shown to have the ability to move around through pumping various dye in the two-layer matrix.
- Pattern change time for grayscale and dynamic on the order of seconds. This is limited by the time it takes to pump or flow dye through microchannels.
- Patterns are limited to channel patterns. In the example of the two-layer matrix, a passively addressed array is available for the motion of the clear pixel. This method is limited to dark field masking with a transparent pixel.
- System requires a large amount of external hardware and likely cannot be miniaturized.

5.2 Ferrofluid Lithography

Ferrofluidic lithography is another interesting type of photolithography involving a dynamic masking technique. The concept of ferrofluid lithography uses ultrafine iron oxide suspended in fluid as a means to block the UV exposure light in the lithographic process. A dynamic aspect can be introduced to this masking process by using electric and magnetic fields to manipulate the positions of ferrofluid aggregates

across a substrate partially prepatterned with cobalt. Once in position, the ferrofluid coated substrate is used as a light field mask exposing where iron aggregates are absent [91, 92]. Results from this work show patterning of positive and negative resist (Shipley 1813, NR-7, and SU-8) circles at diameters on the order of 5 μm and ferrofluid reconfiguration times at less than a second. Optical lithography patterning dosages were highly dependent on ferrofluid concentration. To summarize ferrofluid lithography:

- Dynamic masking has been demonstrated by manipulation of magnetic nanoparticles around a prepatterned substrate using fields
- Patterning dosage dependent on ferrofluid concentration
- Reconfiguration is on the order of less than a second
- Pattern sizes on the order of 5 μm

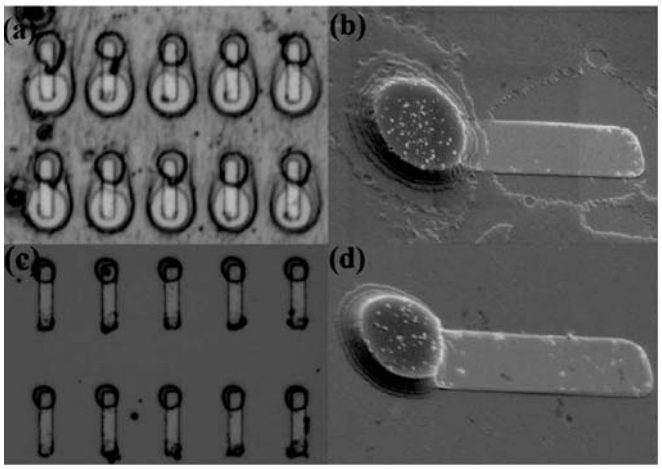

Figure 5.2: From Yellen *et. al.* [IEEE Trans. Magnetics, 2004] SEM results from ferrofluidic photomasking. Reprinted with permission. ©2004 IEEE

5.3 Liquid Crystal Techniques

There have been several methods of reconfigurable photolithography that rely on liquid crystals as a means for electrical control. Liquid crystals, having known light modulation properties, are an ideal medium for behaving as a light valve, and have many uses in other light modulation applications. Liquid crystals and liquid crystal films have, for example, been studied extensively as spatial light modulators and spatial pulse shapers [93–100], and have been examined as light valves for photomasking in a few applications. First, we review the liquid crystal twisted nematic cell, the same cell typically used in a liquid crystal display for its use as a reconfigurable photomask, next we look at other types of liquid crystal polymer films for their use in adaptable photomasking.

5.3.1 Polarization Rotation Lithography

Polarization rotation was one of the first properties that differentiated liquid crystals, nematics, smectics, and chiral smectics for their useful optical properties. Naturally, using the properties of polarization rotation and electric field alignment made this material ideal for applications in light modulation. A very well known and well understood application of liquid crystals is the spatial light modulator that relies on polarization rotation as the means for modulation. Liquid crystal spatial light modulation (SLM) has been investigated in many forms [101]. LC SLMs can be found in a passive form, utilizing passive addressing fabricated on ITO electrodes. Liquid crystal SLMs can also be found in what has been termed "smart" configurations that include VLSI integration of photo detectors, amplifier, and other digital components. LC spatial light modulation devices have been developed using several types of liquid crystal systems including surface stabilized ferroelectric (SSFLC) [102], distorted helix ferroelectric (DHF) [103], electroclinic chiral smectic A (SmA*) [104, 105], and

the most common twisted nematic (TN). SSFLC method was shown in an extremely thin sample that bulk ferroelectric chiral molecules can rotate polarization with very short (∼500 nm) modulation time. Also in extremely thin samples, a distorted helix ferroelectric SLM uses a chiral smectic that relies on a non-surface anchored molecule with free director orientation. Application of bias unwinds the chiral smectic and enables rotation of incident light polarization and phase. SmA* electroclinic SLM modulates light similar to SSFLC, but has the ability to rotate the optic axis linearly with applied bias allowing a wide rotation angle and fast response speeds. Twisted nematic cells are the most common type of LC SLM found today and many applications including the liquid crystal display.

Liquid crystal spatial light modulators made from twisted nematic cells have been used as pixilated photomasks. A diagram of twisted nematic polarization rotation for modulation is shown in Figure 5.3. The twisted nematic cell consists of glass electrodes that have been coated with the polymer polyimide and rubbed to groove the nematic/glass interface. Filling with nematic molecules causes a thin layer of liquid crystal to fall into the grooves and align therein. A second electrode patterned with grooved polyimide is placed orthogonal to the first and because of the long range orientational order in a sample of nematic liquid crystal, the molecular layers near the grooves will align with the previous layer and eventually make a 90 degree "twist" between perpendicular plates. Passing polarized light through a cell such as this will twist the vibrational axis with the twist of the liquid crystal layers. When followed with an analyzer, light rotated in the twisted nematic cell is transmitted. Application of an electric field across the TN cell aligns the bulk of the liquid crystal molecules in the direction of the field, with only the anchoring grooved molecules in orthogonal orientation, there is not enough twist or rotate the light's vibrational axis. In the biased state the unrotated light is not transmitted through the analyzer. This system of TN cell plus polarizer and analyzer makes the functional blocks of a commercial

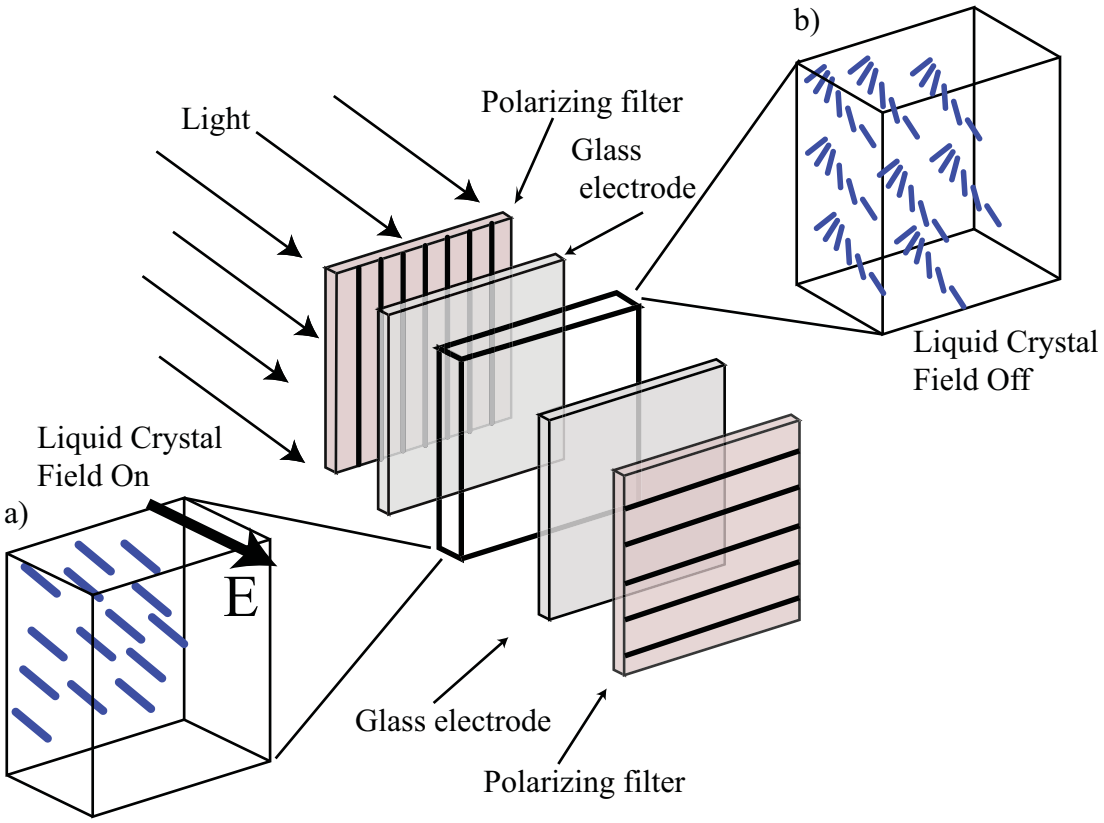

Figure 5.3: Schematic showing the "on" and "off" states of a liquid crystal twisted nematic light value and its surrounding components. a) Twisted nematic molecules in an alignment field do not rotate the polarization of incident light thus light is blocked at the analyzer. b) Twisted nematic molecules rotating the vibrational axis of incident light aligning it for transmission through the analyzer.

liquid crystal display and many other light modulation applications.

The TN cell has been very useful for modulating light in display and SLM technology, it was naturally a good candidate for an addressed electrically controllable photomask [106, 107]. Peng *et. al.* [Opt. Eng., 2003] proposed and simulated a 3D reconfigurable photomask using a commercial LCD panel while Kessels *et. al.* [J. Micro/Nanolithography, MEMS and MOEMS, 2007] showed that an LCD panel can be retrofitted into existing photolithography equipment in place of the reticle of a stepper better than a MEMs spatial light modulator. Examples of this work are

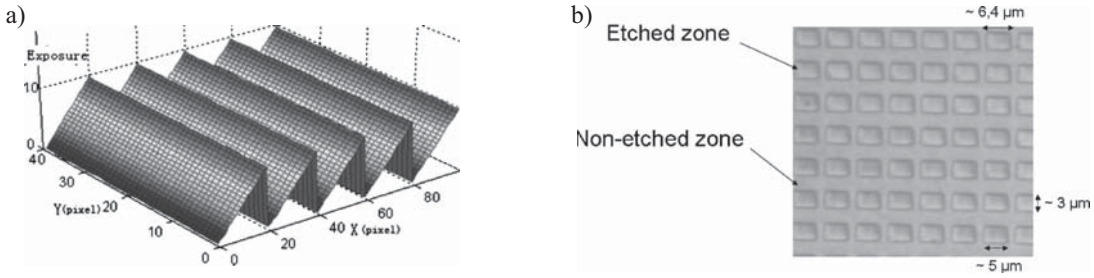

Figure 5.4: a) From Peng *et. al.* [Opt. Eng., 2003] a simulation of a 3D structure patterned using an LCD panel and b) From Kessels *et. al.* [J. Micro/Nanolith, MEMS and MOEMS, 2007] features patterned using an LCD retrofitted into a reduction system. Reprinted with permission.

shown in Figure 5.4a and b. In simulation, the LCD shows the ability for easy fabrication of interesting 3D structures, but runs into some drawbacks experimentally. Peng and coworkers used the LCD panel to modulate 680 nm light patterning silver-halide gelatin because of increasingly poor contrast as the exposure wavelength nears UV. Kessels and coworkers exposed resist using g-line radiation (436 nm) because again, twisted nematic begins to degrade at short wavelengths. Both works found that the resolution was determined by the size of the LCD pixel, while Kessels *et. al.* was using a reduction system, the resolution was cited at about a micron.

Typical photolithography using standard photoresist requires shorter and shorter wavelengths for improvement in resolution. Not only does the twisted nematic cell suffer at short wavelengths, but finding optimal polarizers at those wavelengths becomes difficult. TN cells suffer an increasing amount of absorption, and it will be shown later that LC extinction nears 100 % at wavelengths around 365 nm. Additionally, and as a result of this high absorption, the twisted nematic cells suffer damage from high exposure intensities. Finally, TN cells, due to their directional construction suffer from off-axis light leakage.

Using twisted nematic LCD panels have important benefits in adaptable and 3D

lithography such as an existing and well understood pixilation scheme, plenty of commercially available solutions, and the ability to retrofit into existing reticle systems, but polarization rotation breaks down at short wavelengths and suffers from liquid crystal absorption in the UV.

5.3.2 Polymer Dispersed Liquid Crystal Lithography

The final liquid crystal spatial light modulator method introduced as an adaptable photomask was published by Jeon *et. al.* [Proc. of MEMs, 2006] and uses polymer dispersed liquid crystal films as its modulation element [108]. This group found that forming PDLC over apertures in a photomask enabled them to modulate the anisotropy of their transmission as a function of applied voltage. PDLC does not have an "off" state like H-PDLC rather it has a scattering state. With no applied voltage to the PDLC transmitted UV light was scattered through the aperture resulting in a rounded resist pattern. Increasing voltage on the film gradually aligns liquid crystal droplets and reduces transmissive scatter, which in turn reduces the anisotropy of the resist pattern. Complete alignment of the liquid crystal droplets results in minimized scatter and therefore the most isotropic resist pattern. These states can be seen in the results from Jeon and coworkers paper shown in Figure 5.5 where at low voltage shallow rounded patterns start to appear as a result of high scattering, with increasing voltage and decreased scatter the etch shows more vertical walls. It is interesting to note in the SEM micrographs in Figure 5.5, specifically the high voltage image that the walls are not perfectly vertical as would be the case in a transparent mask. These 50 μm cutouts suffer from a small amount of edge slope likely from resolution limiting due to electrode thickness. As shown in the paper, PDLC can modulate the i-line of a UV source with effectiveness.

To summarize liquid crystal adaptable photomasking techniques:

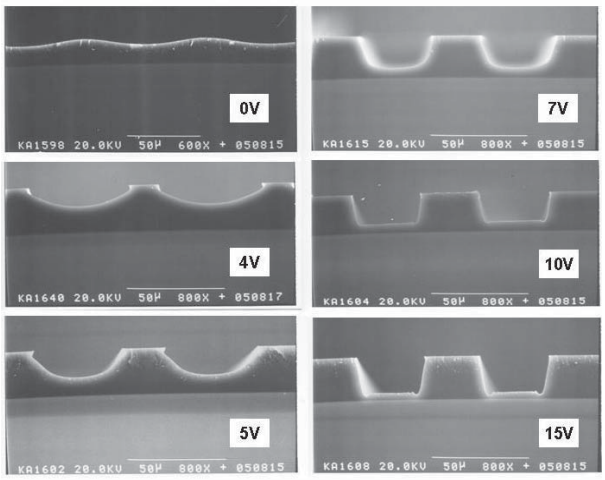

Figure 5.5: From Jeon *et. al* [Proc. MEMS, 2006] PDLC patterned photoresist. Low voltages equate to high scatter in PDLC resulting in shallow rounded resist patterns. With increasing voltage to the PDLC film, transmissive scatter is reduced and resist walls appear more vertical.

- Techniques that currently exist include spatial light modulation using a twisted nematic cell and a PDLC film.
- Benefits of using TN cells include well understood and commercially available solutions with electronics for control. Benefits also include the ability to retrofit into existing reduction and stepper reticle systems.
- Drawbacks of TN panels used in photolithography is an inability to reach short wavelengths due to breakdown of the liquid crystal molecules and high absorption near 365 nm. Peng and coworkers illustrate the ability of the LCD as a reconfigurable photolithography tool, but only with visible wavelengths. Kessels shows patterning using the g-line.
- PDLC films can modulate the shape of a resist pattern, but cannot truly modulate patterning intensity. Varying scatter enables controllable anisotropy of the resist-captured image, but does not really have an "off" state. This technology also suffers from electrode thickness diffraction limiting.

5.4 Maskless MicroElectroMechanical Systems

The current state-of-the-art in adaptable lithography cannot be summarized without examining a maskless patterning technique that uses MEMS spatial light modulators. Though the device designed in this work is a photomasking technique rather than a projection or a maskless technique, MEMS modulators need to be discussed in comparison for compete investigation of real-time reconfigurable imaging. This concept is also a state-of-the-art adaptable or reconfigurable lithography tool that has many of the same benefits of as the H-PDLC mask.

Recently there has been many reports of using MEMS spatial light modulators as maskless lithography patterning tools [109–118]. The concept of the MEMS SLM patterning devices requires exposure light be reflected or diffracted from a tilting or a piston-type micromirror array. Both micromirror styles can rotate the direction of incident light by reflective surface position adjustments thus illuminating or diffusing the exposure aperture. Some groups have worked specifically with Texas Instruments Digital MultiMirror Device (DMD), which functions as a tilt-type micromirror array [87, 119, 120]. Commercial MEMS exposure systems have been well developed to achieve all of the same patterning properties as a binary reticle system including optical proximity correction and other enhancement techniques, making the transition to MEMS a realistic choice for low-volume production with potential of 65 nm features [121]. Figure 5.6 from Martinsson *et. al.* [J. Microlithogr. Microfabr. Microsyst., 2005] is on the left a schematic of a MEMS patterning system showing the 193 nm pulsed excimer source sent through a beamsplitter up into the SLM and reflected back towards the aperture through a series of reduction and spatial filtering lenses. The stepper system is shown with an xy axis and interferometer for alignment below [121]. To the right, Martinsson *et. al.* shows a photograph of a micromirror array and an SEM of the tilt type array.

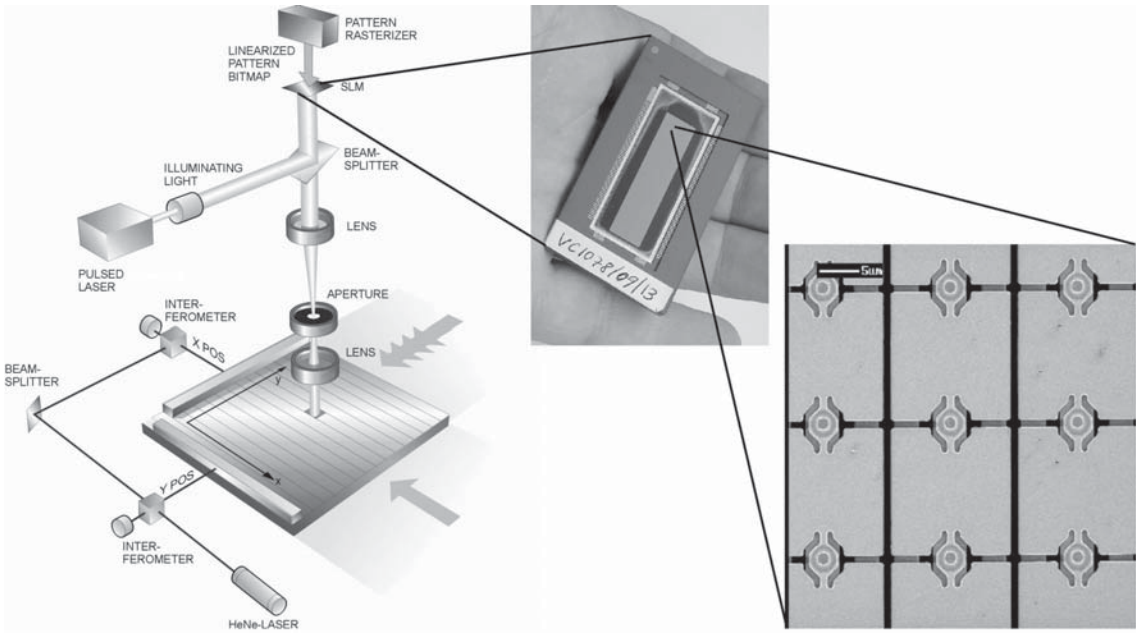

Figure 5.6: From Martinsson *et. al* [J. Microlithogr. Microfabr. Microsyst., 2005] schematic configuration of a MEMS SLM used in maskless lithography configuration. Next is a photo of a MEMS micromirror array with an SEM of a tilt-style micromirror.

MEMS SLM patterning has been proven market desirable and cost-effective for semiconductor manufacturing runs in which mask design and fabrication costs exceed several million dollars, especially if it is a "low volume" run. Martinsson points out that the cost per layer of a commercial semiconductor at 90 nm is significantly less using maskless lithography for wafer runs smaller than 600 wafers/mask. This is mainly due to elimination of the mask fabrication costs, and it is also shown that patterning quality is on par with traditional masked systems. This research shows that maskless patterning devices may be are compelling to the semiconductor industry dealing in 65 - 90 nm features and millions of dollars of cost per run [121].

MEMS maskless lithography has been reported for prototyping and research, and on smaller scales as well by using an array of grating light valves modulating exposure and focused using Fresnel zone plates [122]. The grating light valve has similar

dynamics as a piston-type micromirror array, but was chosen by the author of this work because of a faster response time. Results showed that this system could modulate pattern size from 1 μm to 150 nm with the arbitrary pattern generation of a micromirror array and diffractive focusing provided by the zone plates. An important contribution pointed out in this work was the versatility of using diffractive modes over reflective modes and its ability to be adapted to virtually any exposure wavelength including 193 nm.

To compare MEMS SLM projection lithography as a state-of-the-art adaptable lithography tool with the H-PDLC mask, we must consider the advantages and drawbacks of each technique. Both devices have the potential for arbitrary patterning, this concept is more refined in MEMS systems currently, but fabrication of H-PDLC onto an LCD TFT backplane can provide this function. Both devices are capable of grayscale, SLM uses pulse-width modulation rather than analog attenuation as in the H-PDLC, but this allows for arbitrary levels of grayscaling. Using projection and reduction, MEMS SLM is capable of reaching 150 nm feature size. Currently, in its proof-of-concept form the H-PDLC mask can pattern to its theoretical resolution limit of 25 μm. As will be discussed in Chapter 9 this is form-factor limited by proximity effects due to a thick electrode, but can be solved by eliminating the electrode. This enables contact resolution limit of less than 1 μm. Introducing a 10x reduction system can bring patternable size down to 100 nm. H-PDLC mask can be retrofitted into existing photolithography equipment, SLM projection mask requires new equipment. H-PDLC mask has the potential for phase masking control. Phase control is discussed in Chapter 9, and due to H-PDLC adjusting light delay through index modulation inside the film, interference and diffraction effects can be potentially cancelled through phase analysis.

To summarize MEMS maskless lithography:

- Considered a lithography technique more similar to electron beam lithography than photolithography
- Has been shown to provide the same quality patterning as a commercial reticle system at lower cost for smaller runs in semiconductor fabrication
- This technique has also been shown for prototyping and research
- Requires a laser source for illumination rather than a mercury arc lamp
- Requires development or purchase of a different piece of equipment, in other words, MEMS SLM is not compatible with existing reticle systems. Purchasing a device may not be cost effective for small scale operations such as research or prototyping.

5.5 Comparison Summary and Objectives

The major application of this work, a study of spatially coherent propagation effects inside a patterned nanostructure, is the ability to modulate and pattern photoresist in an adaptable, masked fashion. We will show that modulating through H-PDLC has advantages over μfluidic photomasking because of its scalability and rapid real-time reconfiguration. H-PDLC differs from LCD masking in that it does not rely on polarization rotation of light, therefore no polarizers are required. Additionally, H-PDLC functions on what is termed coherent scattering, or the Bragg effect which is not limited to visible wavelengths. Liquid crystal material sets have limiting resonant absorption in the deep UV and have the potential for extrapolation below 365 nm. H-PDLC does not suffer off-axis light leakage though blue shifted attenuation can be slightly less. Finally, H-PDLC has an analog transmission intensity as a function of applied bias, LCD methods need pulse width modulation for grayscaling.

H-PDLC, LCD, PDLC, and μFPM are not really comparable technologies to MEMS patterning. MEMS pattering is a maskless technique more like e-beam than

photolithography, though it is an important technology to consider in this study. MEMS patterning requires new devices or the development of new optical systems for functionality, while liquid crystal SLMs are retrofittable into existing stepper or mask aligners. Although MEMS patterning has been shown to be very high quality offering the same performance as a commercial semiconductor industry reticle system, cost effectiveness is reached for fabrication runs that reach into the millions of dollars. These maskless devices may not be attainable for prototyping or research purposes with the design of complicated optical tabletop systems and laser sources.

Summarized in this chapter are several unique lithography methods that have an element of adaptability in the mask pattern. H-PDLC masking is not the first liquid crystal type adaptable mask, but has several advantages over existing reconfigurable mask technology. Ferrofluidic and microfluidic masking are unique and interesting as well, but are slightly less applicable as they are not liquid crystal techniques. Finally, MEMS projection lithography has been shown to be a technique competitive with standard reticle systems currently used in industry, but may be cost prohibitive for small scale operations.

Several other adaptable photomask and maskless techniques exist, as illustrated above and can be summarized in Table 5.1 and the advantages and disadvantages of these techniques are summarized in Table 5.2.

Table 5.1: Comparison of adaptable lithography techniques

	H-PDLC	LCD	PDLC	μFPM	MEMS
Resolution Limitation	Depends on pixel and reduction	Depends on pixel and reduction	Depends on pixel and reduction	Depends on microchannel size	Depends on micromirror array
Adaptability Time	μs time frame	μs time frame	μs time frame	seconds	μs time frame
Grayscale	analog with applied bias	Pulse width modulation	analog with applied bias	Depends on pumped dye concentration	Pulse width modulation
Retrofit	Retrofits into existing stepper or mask aligner	Retrofits into existing stepper or mask aligner	Retrofits into existing stepper or mask aligner	Does not retrofit	Requires new system
Scalable	Yes	Yes	Yes	Not scalable due to pumps	Not scalable due to optical path
Source	Mercury arc lamp	Mercury arc lamp	Mercury arc lamp	Mercury arc lamp	Laser
Wavelength	>365 nm	>365 nm	>365 nm though PDLC can scatter a broad range	Limited to dye absorption bands	Versatile when used in diffraction mode
Usage	Research	Research	Research	Research	Semiconductor industry

Table 5.2: Advantages and disadvantages of adaptable techniques

	Advantages	Disadvantages
H-PDLC	Fast adaptability, grayscale as a function of applied bias, retrofit existing systems, can be extrapolated into deeper UV, cost effective	Currently not as refined as MEMS systems
LCD	Fast adaptability, retrofit into existing stepper systems, LCD panels are well refined	PWM for grayscale, little UV range, susceptible to UV damage, off-axis light leakage
PDLC	Fast modulation, retrofit into existing systems, cost effective, can modulate broad wavelength range, good for modulating an isotropic to anisotropic etch	Does not have an "off" state, only a scatter state
μFPM	Unique method for adaptability and grayscale	Slow response time, Dye concentration limited grayscale, non-scalable, wavelength range limited by dye absorption, not truly arbitrary pattern limited by microchannels
MEMS	Well refined and shown to perform as well as standard reticle systems	Not cost effective for research, requires the purchase or the development of a new optical system to use

Chapter 6. Stratified Periodic Media and H-PDLC Simulations

As a first step in understanding the patterning quality or the image formation ability of the H-PDLC nanostructure, it is necessary to mathematically understand propagation through the periodically index modulated structure. It is important to visualize spatially coherent single wavelength light interacting with individual layers of the H-PDLC and summing for an overall response. The mathematical relationship between the transmission stop-band, layer thicknesses, and indices in a Bragg reflector are examined to model the H-PDLC first as an ideal grating and then using a model that incorporates the experimental liquid crystal material properties. Using a matrix method for modeling periodic multilayer structures, experimental grating measurements are compared with the simulation results to show very good agreement between the model and the measured spectrum. In this chapter, we first show ideal Bragg grating simulation results based on a model for periodic stratified media, then we incorporate experimental H-PDLC material properties measured from SEM images such as layer thickness and droplet fill factor to complete a model of H-PDLC.

6.1 Ideal Grating Simulations

When using white light to reconstruct the reflection hologram, there exists a propagation stop-band with center wavelength and FWHM determined by layer thickness and layer index. The light prohibited from transmitting within the structure is reflected from internal layers and is subject to constructive and destructive interference upon recombination. A first order approximation for diffraction and reflection efficiency incorporates an effective medium approach in which each layer is treated as a uniform isotropic monolayer [123, 124]. The reasoning for using a monolayer approximation

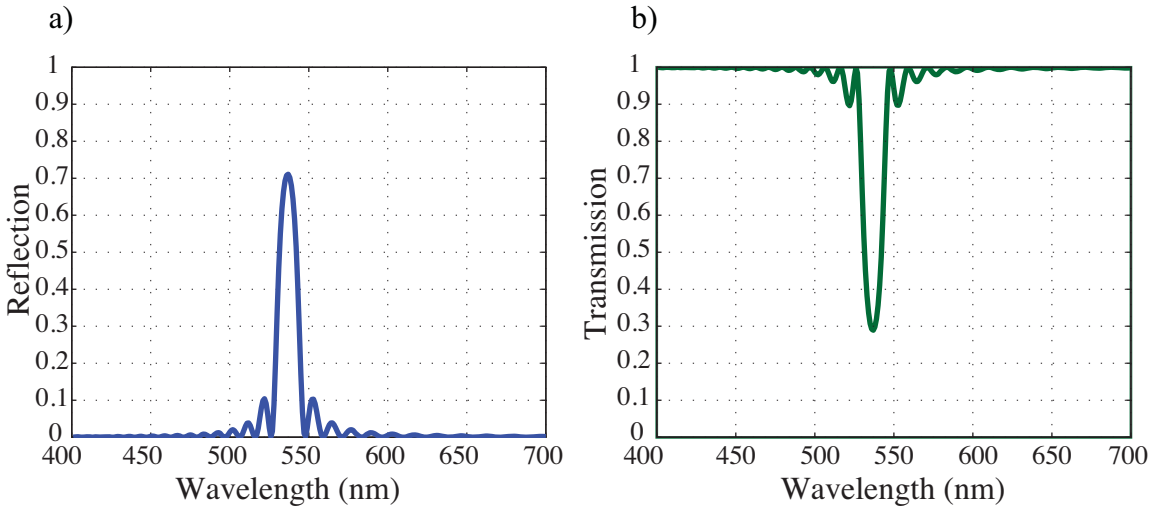

Figure 6.1: Simulated reflection and transmission bands for an ideal Bragg grating with indices and layer thicknesses appropriate for H-PDLC material modeled in Matlab.

is a result of H-PDLC studies that show that the polymer layer is well stratified and uniform, and the liquid crystal rich domains are distinct. The liquid crystal density in LC rich domains has been shown to be high, up to 60% in thiolene gratings presenting a material with a defined 2-layer system. Additionally, the droplets are small with respect to incident wavelengths and well dispersed. A simulation was performed using an ideal grating monolayer model to show reflection and transmission through uniform stratified media. Simulated reflection and transmission bands are shown for an ideal Bragg reflector using indices and layer thicknesses appropriate for H-PDLC in Figure 6.1 with parameters listed in Table 6.1.

There exist several methods of calculating the interference patterns of reflected and transmitted light in a distributed Bragg reflector, examples being an iterative solution that determines the interaction at each interface and carries it through the entire structure [125]. Coupled wave theory provides an analytical expression for the diffraction efficiency of the grating and all its harmonics through expansion and

operation on a Fourier series, but treats index variation throughout the grating layer with a sinusoidal dependence [126–128]. Using a translation matrix based on coupled wave theory is a straightforward method for simulating waves in stratified media [71, 129], which is the method was used to simulate the reflection and transmission curves in Figure 6.1. The code written to generate these transmission and reflection curves is shown in Appendix A and was written in Matlab.

A comparison of the ideal grating model and an experimental grating transmission curve is shown in Figure 6.2. When comparing these two curves, it is clear that the ideal grating is matched in center wavelength and diffraction efficiency, factors that are controlled in simulation with layer thickness and total number of layers. The values used for this comparison were typical of a real grating. The full-width half-maximum is remarkably similar between ideal and actual curves indicating that the translation matrix method is an accurate method of modeling multilayer interference. The baseline, or the out-of-band transmission of the ideal grating is nearly 100% except in the center and side modes, a factor inconsistent with the real grating curve. Modifications of the translation matrix simulation need to be made for a more realistic model.

6.2 Matrix Method for Ideal Bragg Reflectors

Using Yeh *et al.* [J. Opt. Soc. Am., 1977] as a starting point for developing a transfer matrix solution for a distributed Bragg reflector, we define uniform layers of isotropic material with index

$$n(x) = \begin{cases} n_2, & 0 < x < b \\ n_1, & b < x < \Lambda \end{cases}$$

where n_1 and n_2 are indices of layer materials and Λ is grating pitch as shown in Figure 6.3. The sum of a and b is Λ. We can define the incident normal field to be

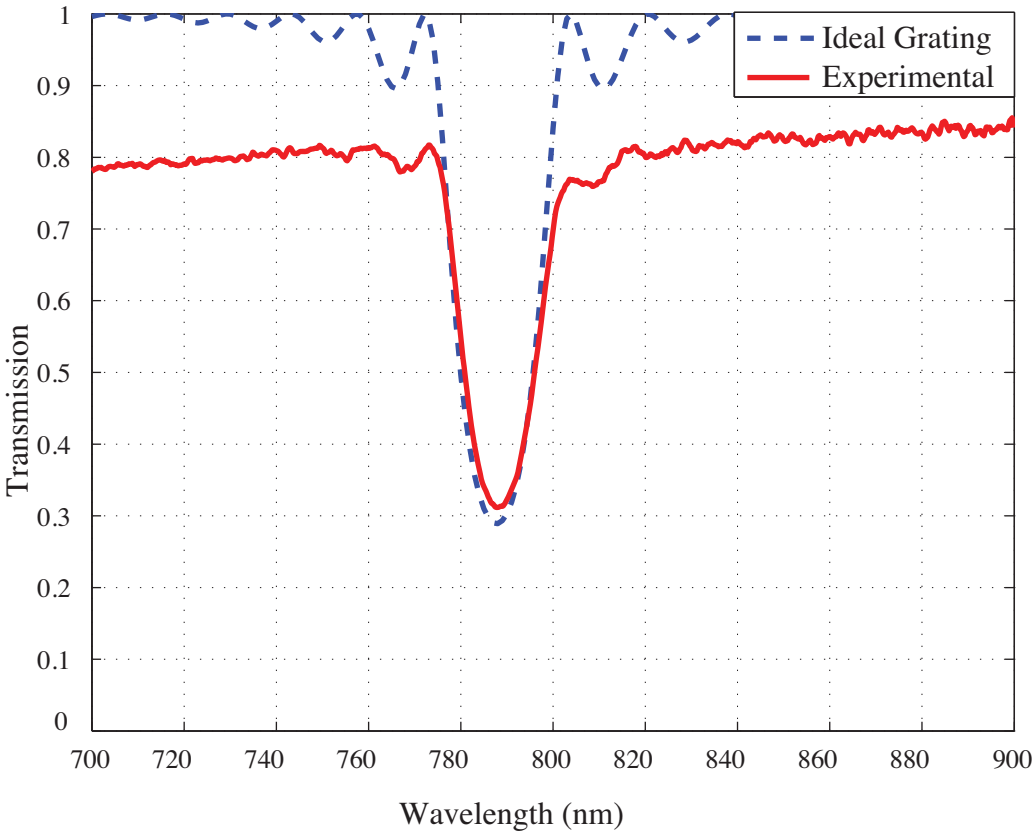

Figure 6.2: Comparison of the lineshape of an ideal grating with the lineshape of an H-PDLC transmission curve. Major differences exist in the transmission outside of the stop-band notch. Ideal curve modeled in Matlab, experimental curve measured using Ocean Optics fiber-based spectrometer.

$$E(x,z) = E(x)e^{i\beta z} \tag{6.1}$$

where x is perpendicular to the layers and β is related to wavelength and incident angle. Since the electric field can be written as the sum of incident and reflected waves within a particular layer, the electric field in the α layer of the n^{th} unit cell can be represented as

$$E(x,z) = (a_n^{(\alpha)} e^{ik}\alpha x^{(x-n\Lambda)} + b_n^{(\alpha)} e^{-ik}\alpha x^{(x-n\Lambda)})e^{i\beta z} \tag{6.2}$$

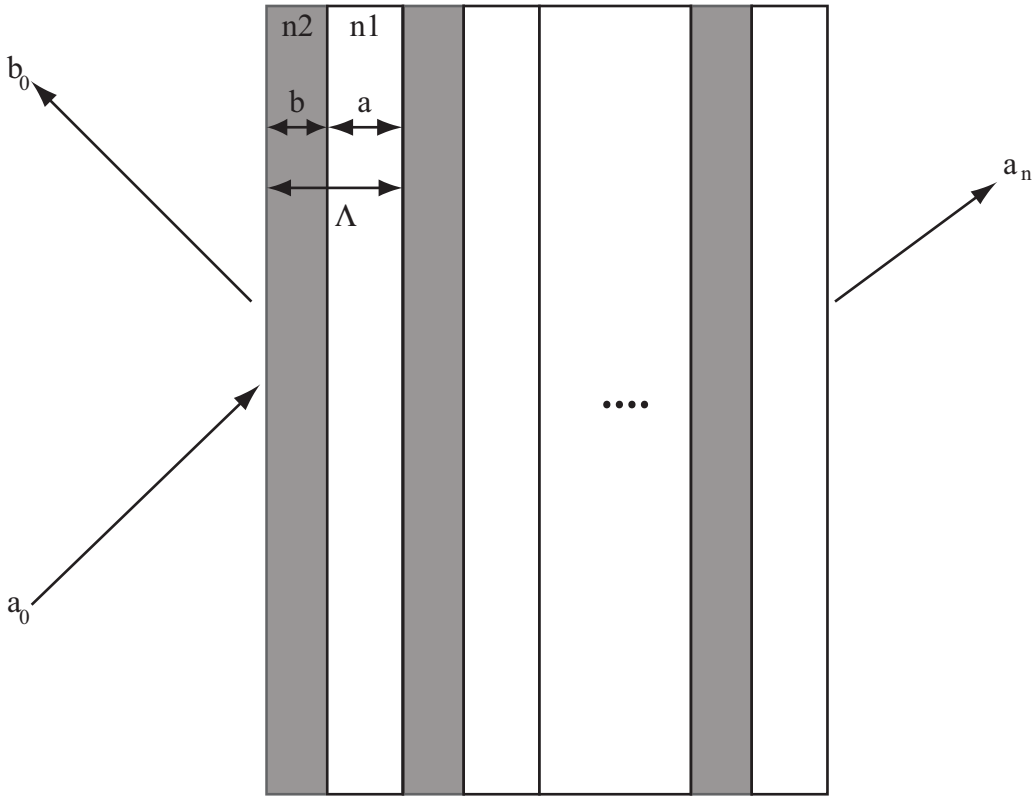

Figure 6.3: Model for stratified periodic media redrawn from Yeh *et al.* [J. Opt. Soc. Am., 1977]. Layers have thicknesses a and b summing for a pitch of Λ with indices n_1 and n_2. Incident field is defined as a_0 with initial reflection of b_0. Transmissive output summed across all layers is defined as a_n. Reprinted with permission.

with

$$k_{\alpha x} = \{[(\omega/c)n_\alpha]^2 - \beta^2\}^{1/2} \tag{6.3}$$

for $\alpha = 1, 2$. For normal incidence β is equal to 0. The constituent vectors of this equation are related through layer continuity and boundary conditions. Assuming continuity of E at layer interfaces yields

$$a_{n-1} + b_{n-1} = e^{-ik_{2x}\Lambda}c_n + e^{ik_{2x}\Lambda}d_n \tag{6.4}$$

$$ik_{1x}(a_{n-1} - b_{n-1}) = ik_{2x}(e^{-ik_{2x}\Lambda}c_n - e^{ik_{2x}\Lambda}d_n) \tag{6.5}$$

$$e^{-ik_{2x}a}c_n + e^{ik_{2x}a}d_n = e^{-ik_{1x}a}a_n + e^{ik_{1x}a}b_n \tag{6.6}$$

$$ik_{2x}(e^{-ik_{2x}a}c_n - e^{ik_{2x}a}d_n) = ik_{1x}(e^{-ik_{1x}a}a_n - e^{ik_{1x}a}b_n) \tag{6.7}$$

By writing these equations in matrix form and defining

$$a_n \equiv a_n^{(1)} \qquad b_n \equiv b_n^{(1)} \tag{6.8}$$

$$c_n \equiv a_n^{(2)} \qquad d_n \equiv b_n^{(2)} \tag{6.9}$$

a transfer matrix is obtained.

$$\begin{pmatrix} a_{n-1} \\ b_{n-1} \end{pmatrix} = \begin{pmatrix} A & B \\ C & D \end{pmatrix} \begin{pmatrix} a_n \\ b_n \end{pmatrix} \tag{6.10}$$

Matrix elements are

$$A = e^{-ik_{1x}a}\left[\cos k_{2x}b - \frac{1}{2}i(\frac{k_{2x}}{k_{1x}} + \frac{k_{1x}}{k_{2x}})\sin k_{2x}b\right] \tag{6.11}$$

$$B = e^{ik_{1x}a}\left[-\frac{1}{2}i(\frac{k_{2x}}{k_{1x}} + \frac{k_{1x}}{k_{2x}})\sin k_{2x}b\right] \tag{6.12}$$

$$C = e^{-ik_{1x}a}\left[-\frac{1}{2}i(\frac{k_{2x}}{k_{1x}} + \frac{k_{1x}}{k_{2x}})\sin k_{2x}b\right] \tag{6.13}$$

$$D = e^{ik_{1x}a}\left[\cos k_{2x}b - \frac{1}{2}i(\frac{k_{2x}}{k_{1x}} + \frac{k_{1x}}{k_{2x}})\sin k_{2x}b\right] \tag{6.14}$$

We find the dispersion relation between angular frequency and β by applying the eigenvector solution for Bloch waves in periodic media [129].

$$K(\beta, \omega) = \frac{1}{\Lambda}\cos^{-1}\left[\frac{1}{2}(A + D)\right] \tag{6.15}$$

The translation matrix for N unit cells of periodic stratified media of thicknesses a and b, indices n_1 and n_2, and period Λ is written

$$\begin{pmatrix} a_0 \\ b_0 \end{pmatrix} = \begin{pmatrix} A & B \\ C & D \end{pmatrix}^N \begin{pmatrix} a_N \\ b_N \end{pmatrix} \tag{6.16}$$

with

$$r_N = (b_0/a_0)_{b_N=0} \tag{6.17}$$

representing the coefficient of reflection. A schematic of this model is shown in Figure 6.3. With expansion and substitution we can write an expression for the magnitude of reflection coefficient

$$|r_N|^2 = \frac{|C|^2}{|C|^2 + (\sin K\Lambda / \sin NK\Lambda)^2} \tag{6.18}$$

C is a result of reflection from a single unit cell.

$$|C|^2 = \frac{|r_1|^2}{(1 - |r_1|^2)} \tag{6.19}$$

where r_1 is defined by Fresnel's equations for the initial pair of layers.

Simulating the translation matrix solution for stratified media yields the transmission spectrum for an ideal grating as shown in Figure 6.2. Superimposed in this figure is an experimental grating transmission curve for comparison. The diffraction efficiency of an ideal grating is related to the number of layers and the transmission notch center wavelength is defined by the thickness of layers a and b. The diffraction efficiency, FWHM, and notch center wavelength agree with real data for approximate thicknesses and number of layers. The parameters used in this simulation are defined in Appendix A and are summarized in Table 6.1.

Table 6.1: Ideal Grating Simulation Parameters

Parameter	Symbol	Value
Layer 1 Index	n1	1.524
Layer 2 Index	n2	1.6227
Layer 1 Thickness (nm)	a	200
Layer 2 Thickness (nm)	b	210
Number Layers	N	50
Pitch (nm)	Γ	410

6.3 Simulation Incorporating Material Properties

Treating the H-PDLC as a distributed Bragg reflector implies that it is composed of uniform monolayers, which is a simplified or first order approach to determining its optical properties. Sutherland *et al.* [J. Appl. Phys., 2006] developed a model for H-PDLC taking into account many factors that are not ideal including anisotropy, interfacial roughness, and index variations within layers [33]. Using TEM and SEM, many of the experimental parameters were determined and incorporated into an ideal grating model to produce very accurate simulation of experimental grating stop-band transmission curves. We perform a similar analysis using parameters of experimental gratings fabricated and imaged in-house to produce simulation of experimental H-PDLC.

An experimental H-PDLC consists of layers of polymer encapsulating liquid crystal droplets, which has a different morphology than isotropic stratified media. Gratings made with a thiolene chemistry are known to have highly spherical droplets with high packing density of up to 60% droplets in the liquid crystal rich regions. As a result of this high packing, the interdroplet spacing is small, on the order of $\lambda/3$. Though an effective media approach provides a very good estimation of grating behavior, factors such as absorption, scattering, layer index variation, droplet anisotropy, and

surface roughness affect optical properties and need to be considered in the model. Following Sutherland *et al.*[J. Appl. Phys., 2006], we begin with an analysis of the material that phase separates into different layers and how layer index is affected. Defining layers of polymer and liquid crystal as a and b like before, but rather than using a uniform index for each layer, we derive n_h and n_l to represent the high and low index regions. The low index region consists mainly of polymer matrix however in holographic writing a small volume of liquid crystal remains intertwined within the polymer. The high index regions consists predominately of liquid crystal phase separated into droplets, but again, a volume fraction of liquid crystal remains in solution in the interdroplet areas. We can define the total volume fraction f_0 as

$$f_0 = f_{HS} + f_{LS} + f_d \tag{6.20}$$

where f_{HS} represents the volume of liquid crystal in solution in the high index region. f_{LS} represents the volume of liquid crystal in solution intertwined in the polymer matrix and f_d is the volume of liquid crystals that has formed droplets. The volume fractions between layers are related through layer thickness and grating pitch

$$\alpha = \frac{\langle D \rangle}{\Lambda} \tag{6.21}$$

where $\langle D \rangle$ is the average droplet size and Λ is grating pitch. Total liquid crystal volume fraction can be related as

$$f_0 = \alpha(f_{HS} + f_d) + (1 - \alpha) f_{LS} \tag{6.22}$$

Understanding that each layer is comprised of volume fractions of liquid crystal in solution and in droplet form allows writing of an expression for layer indices. Bulk nematic liquid crystal index is known to be an average of its ordinary and extraordi-

nary axes, where the ordinary and extraordinary axes are wavelength dependent like shown in Figure 6.4.

$$n_i = \sqrt{\frac{1}{3}(2n_o^2 + n_e^2)} \tag{6.23}$$

The index of the polymer matrix region can be written as the sum of indices of liquid crystal in solution and the polymer

$$n_l = \sqrt{f_{LS}n_i^2 + (1 - f_{LS})n_p^2} \tag{6.24}$$

Index of the matrix can be written

$$n_m = \sqrt{\frac{f_{HS}n_i^2 + (1 - f_{HS} - f_d)n_p^2}{1 - f_d}} \tag{6.25}$$

Incorporating a better expression for layer index and volume fraction allows development of a model with a more exact estimation of the layer's affect on incident light.

The previous analysis provides good approximations for index and volume fraction of polymer rich regions and liquid crystal in solution, but does not take into account anisotropic index of the liquid crystal droplets. Index distribution of molecules within a droplet can be modeled by assuming an effective pair of anisotropic indices that are an average over the entire droplet. With this assumption, an average order parameter can be written to account for alignment variation averaged over the droplet. Sutherland *et al.* examine three cases, one of which yields a model with anisotropic orientation and the index of the droplet rich region can be written

$$n_d = \sqrt{n_i^2 + S(\beta_e n_e^2 - \beta_o n_o^2)} \tag{6.26}$$

where order parameter, S, for spherical droplets is 1/3, with β_e =2/3 and β_o =-

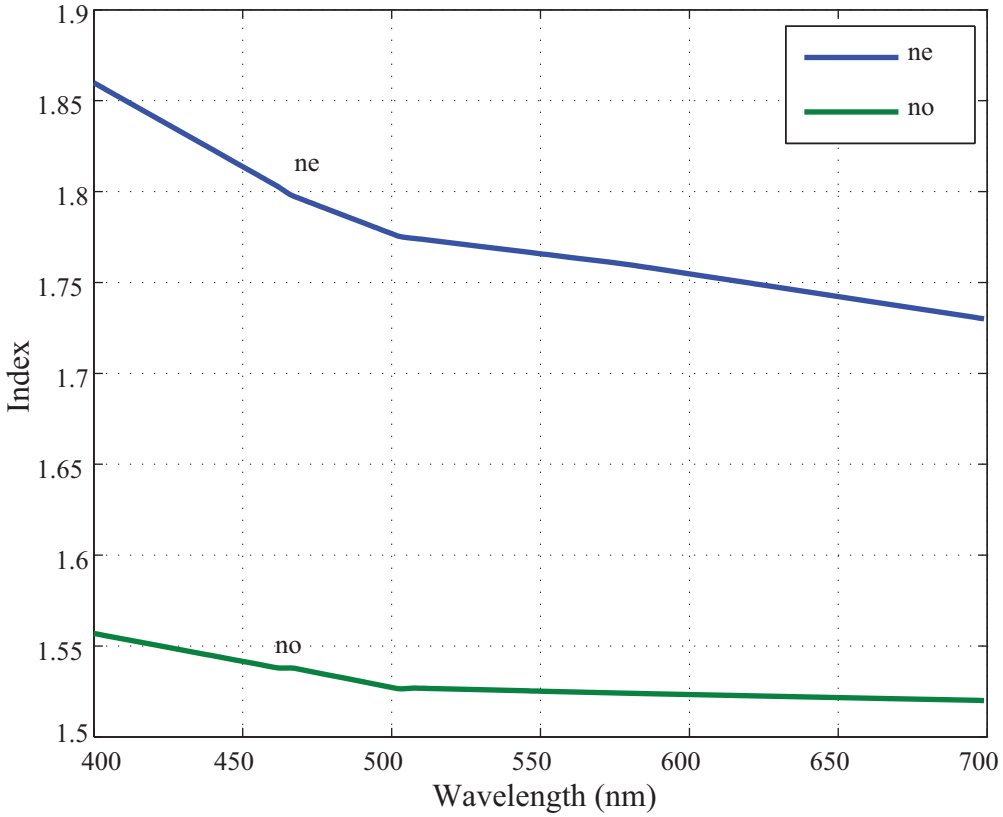

Figure 6.4: Ordinary and extraordinary E7 liquid crystal indices plotted as a function of wavelength.

1/3 [130]. Using this estimation for droplet index (shown as a function of wavelength in Figure 6.4), index of the liquid crystal rich region can be expressed as

$$n_h = \sqrt{f_d n_d^2 + (1 - f_d) n_m^2}. \tag{6.27}$$

To ensure that all optical interactions are accounted for, the simulation incorporated Sutherland's analysis of layer index and volume fraction, and wavelength dependent bulk liquid crystal index and absorption and scattering. The ordinary and extraordinary indices have well documented wavelength dependence, and these values were added to the simulation to be calculated in each index expression (Figure 6.4).

Thorough analysis by Wu *et al.* [Appl. Opt., 1987] shows that in bulk liquid crystals the absorption coefficient in nonresonant regions varies with λ^{-2} while scattering coefficient varies with λ^{-4} [18]. Absorption and scattering coefficient are also functions of cell thickness, a factor also calculated into the transmission and reflection model expressions.

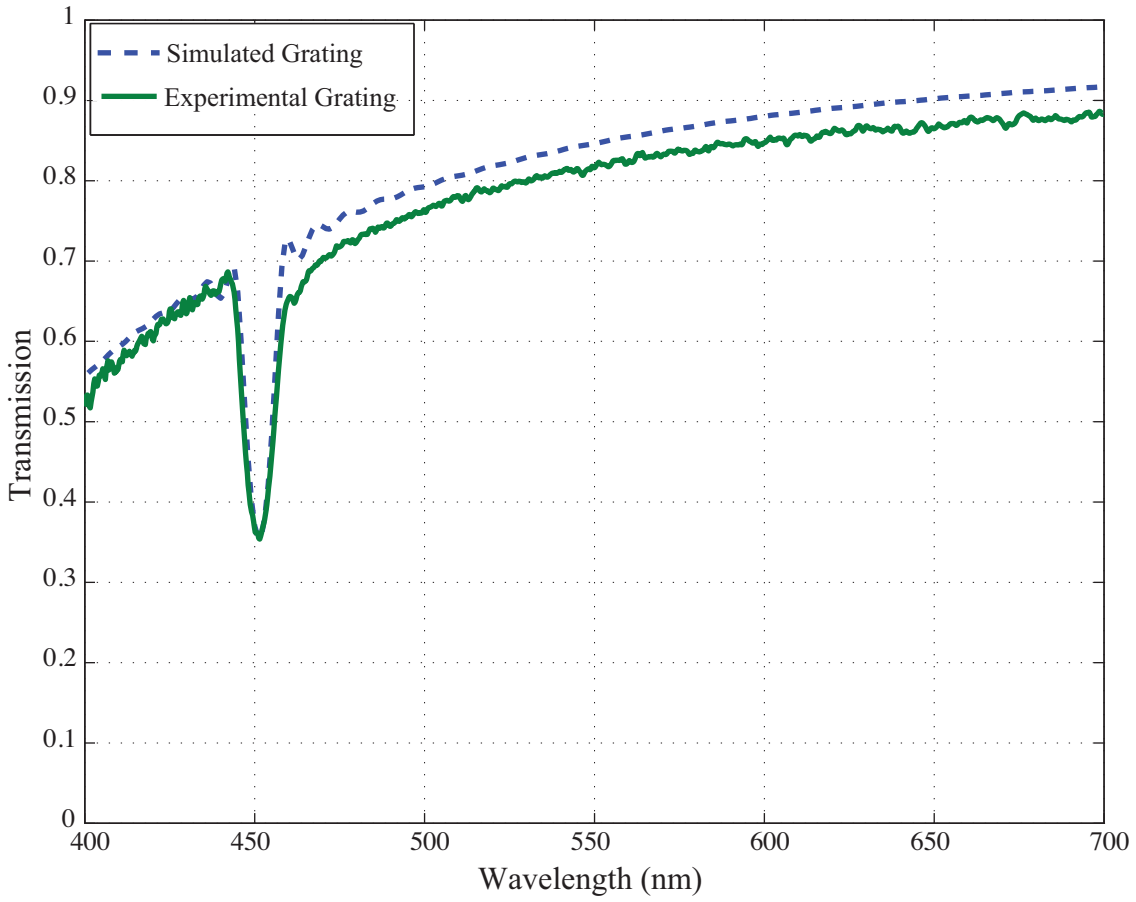

Figure 6.5: Comparison of H-PDLC transmission model with a real grating transmission spectrum. Experimental parameters are incorporated including an absorption (λ^{-2} dependence) and a droplet scattering (λ^{-4} dependence). Simulated curve obtained using Matlab, experimental curve measured using Ocean Optics fiber-based spectrometer.

Observing the volume fraction of bulk liquid crystal remaining in solution in an

H-PDLC, it is clear that the contribution resulting from this effect is minimal. This is readily seen in simulation and has the appearance of an ideal grating. Small volume fractions and thin cells indicate that absorption and scattering from bulk liquid crystal molecules are negligible. However realistic H-PDLC gratings have a pronounced wavelength dependent baseline even far from the resonant region. Since absorption is an isotropic effect, baseline interaction can be attributed to droplet scattering. Sutherland cites several reasons for droplet scattering including interfacial roughness and index variations, and further states that interfacial roughness results from droplet size and centerline variation. Droplet scattering analysis is performed by incorporating statistical information gathered from real samples into the model and expanding into a Taylor series with terms that vary with λ^{-2} and λ^{-4}; higher order terms are excluded. Using a λ^{-4} dependence for scattering is an expected result considering the size and composition of the droplets, which place them in the Rayleigh regime. This dependence was integrated into the simulation to account for wavelength dependent droplet scattering and enables a close match to actual grating spectrum.

Figure 6.5 compares the results of this model for thiolene H-PDLC with a real grating transmission spectrum. Simulation code written in Matlab can be found in Appendix B and parameters listed in Table 6.2. The actual indices used were calculated using the Sutherland approximation for different regions, cell thickness was set to be approximately 15 μm and periodic layers were designed to be realistic to gratings made in-house. It is clear to see that by matching realistic values for pitch and number of layers, the diffraction efficiency and FWHM of the transmission notch are similar. It is also interesting to note that the actual grating exhibits secondary lobes at wavelengths similar to the simulated grating. The baseline at wavelengths greater than the notch appears lower in transmission than the simulation, but the λ^{-4} trend is consistent. This is likely a result of less than optimal interfacial roughness and

Table 6.2: H-PDLC Grating Simulation Parameters

Parameter	Symbol	Value
LC Ordinary Index	n_o	See Figure 6.4
LC Extraordinary Index	n_e	See Figure 6.4
Polymer Index	n_p	1.524
Bulk Absorption	abscoef	$\sim \lambda^{-}2$
Bulk Scattering	scattcoef	$\sim \lambda^{-}4$
Layer 1 Thickness (nm)	a	100
Layer 2 Thickness (nm)	b	169
Number Layers	N	60
Pitch (nm)	Γ	269
Order Parameter	S	1/3
Volume Fraction	F0	0.35

liquid crystal centerline offset, both factors that can impact out-of-band transmission.

Observing both the measured spectrum and the simulated spectrum it is obvious that transmission decreases with shorter wavelengths. This is both a result of droplet scattering yielding a λ^{-4} relationship and movement towards resonant absorption. Expanded into the 200-400 nm range, transmission is entirely attenuated as a result of these factors.

6.4 Simulation of Blueshift as a Function of Incident Angle

Simulating and measuring blueshift is an important characterization for photomasking applications. Off axis light leakage is a problem for other liquid crystal modulation techniques including LCD modulation. Although it is usually assumed that collimated light reaches a photomask when using traditional masking equipment, there may exist scenarios that include off axis exposure. Blueshift incorporates two effects: the stop-band center wavelength shifts with off axis illumination and the diffraction efficiency of the stop-band notch decreases.

The transmission spectrum of a distributed Bragg reflector has an explicit de-

pendence on the angle of incident light, as does any reflecting surface governed by Fresnel's laws. As the incident angle changes, so does the intensity of light penetrating into the layers of Bragg grating. Off normal, not all variations of transverse light propagates similarly: light with different directions can propagate in uneven amounts. Since the stop-band center wavelength is determined by the thickness of the layer, introducing off-axis light essentially increases the length of layer that light propagates through before passing into a subsequent layer. All of these factors contribute to blueshift.

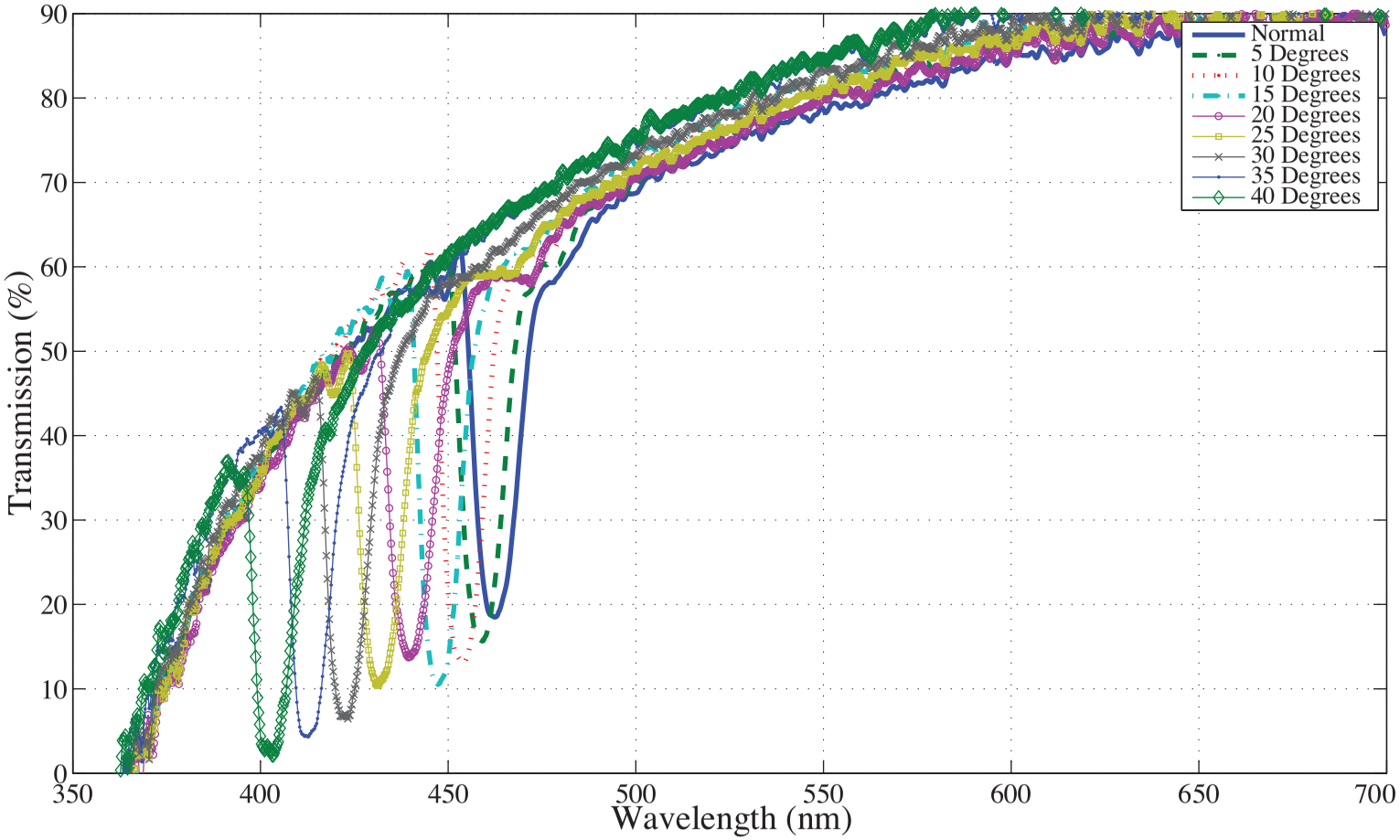

Figure 6.6: H-PDLC transmission curves plotted as a function of wavelength. Superimposed curves represent blue shift as the incident white light is shifted in 5 degree increments collected using an Ocean Optics fiber-based spectrometer.

Center wavelength of the reflection peak is known to blueshift as the angle of incident light increases. Including Fresnel's laws into the model enables simulation of this blueshift by specifying a particular angle of impinging white light. Measured with an Ocean Optics white light source and fiber-based spectrometer, the curves in Figure 6.6 shows several measured spectra blueshifting with increased angle of incidence. In this figure, clearly the center stop-band is moving towards shorter wavelengths as the incident light angle is rotated in 5 degree increments. Diffraction efficiency shifts with an increase in illumination angle, their baseline becomes less transparent as well. The baseline trend that these curves are following, as shown above in the simulation, is a λ^{-4} scattering shape, which is an expected occurrence as curves move more into the UV. Diffraction efficiency is reduced accordingly. Though diffraction efficiency is reduced, this grating maintains the ability to modulate off axis light unlike other types of liquid crystal modulators.

Figure 6.7 is a comparison of the simulated center wavelength shift with measured center wavelength shift of an actual grating. In order to simulate the center wavelength shift, we needed to add Fresnel's laws to the matrix method code previously written. The simulation starts with initial conditions related to reflection and transmission from the first pair of layers, application of Fresnel's laws was added here. There is also a propagation term introduced in the electric field vector representing light in the medium, β, from equation 6.3. This term was assumed to be zero for normal incidence, but to show off-normal incidence, this term was replaced with an angular term. Data collected for the curves in Figure 6.7 was obtained by plotting the full transmission curve and subtracting the center wavelength difference from normal as incident angle was increased. This was done in measurement and in simulation. We would like to show in this result that there is good agreement between simulated and measured blueshift, but also that there is less than 10 nm blueshift for up to 10 degrees of angular rotation. If off axis illumination is a problem in masking sys-

tems such as the LCD, we can show that light modulation is possible when using an H-PDLC mask.

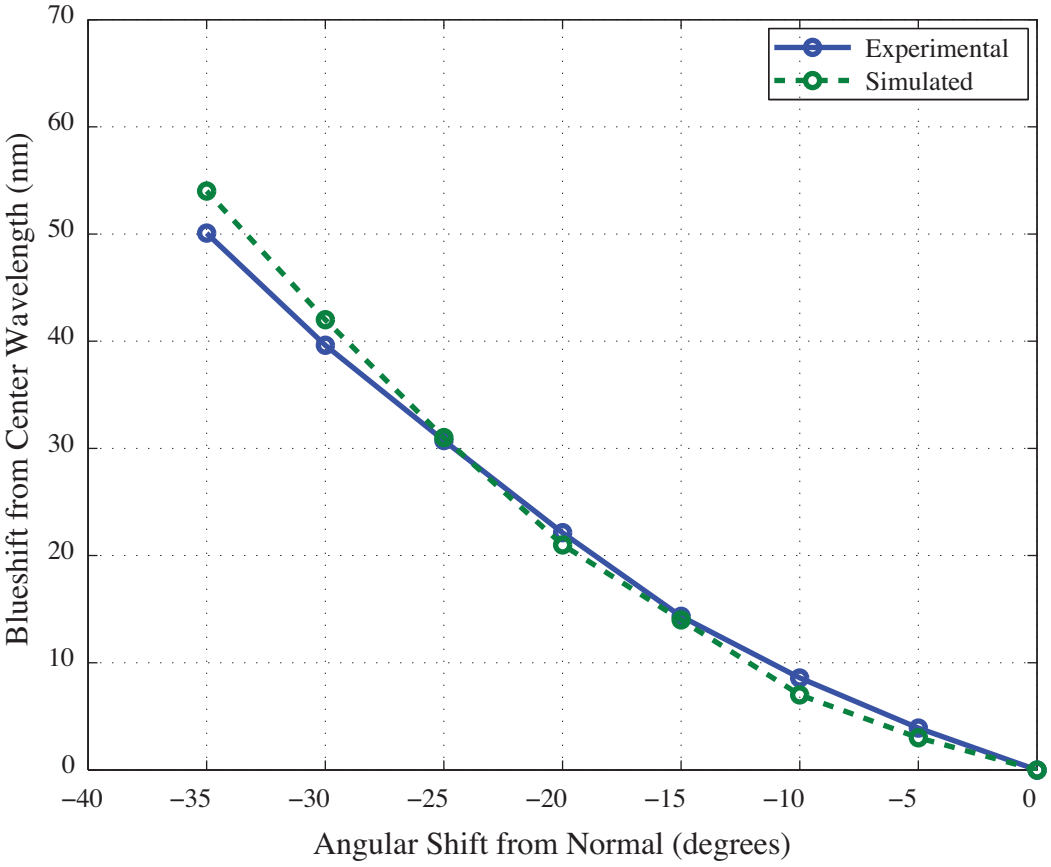

Figure 6.7: Simulated center wavelength shift as a function of incident angle for a simulated H-PDLC reflector compared to experimental offset. Simulated data modeled in Matlab, experimental data collected using Ocean Optics fiber-based spectrometer.

Chapter 7. Device Application Concept, Fabrication Methods, and Initial Patterning

In this chapter, we present the application concept of H-PDLC developed in this thesis, the thin film adaptable photomask. We start by describing the device and the parameters for 2D photopatterning followed with several initial examples of patterning and morphology. To ensure that this device patterns resist sufficiently, we next performed deposition, lift-off, wet etch, and dry etch procedures and compared to binary patterned structures.

7.1 Device Concept Description

The application developed in this thesis uses a holographically formed polymer dispersed liquid crystal film light valve as a digitally reconfigurable photomask. The science of H-PDLC and photomasking has been explained in Chapters 3 and 4, now the application concept that combines the two is presented. Digitally controlled photomasking is a novel concept only partially attained in previous work by other groups working in microfluidic and liquid crystal technology. Though direct write lithography methods using real-time controllable MEMS devices exist, no prior work has yielded a true adaptable masking system to replace a traditional binary photomask. This new technique will replace binary masks for 2D patterning and offers many advancements in lithographic technology because of its real time pattern reconfigurability.

A photomask with software controlled pattern reconfiguration eliminates the need for multiple masks, which can make lithography more cost effective for the educational environment. In the industrial setting, a digitally controlled mask can eliminate alignment error brought about by using several masks for a single structure. This device will enable rapid prototyping of structures and rapid mask design debugging, it also

introduces a method of testing inverse lithography masks before the final mask pattern is set. Inverse lithography is a method of tailoring a mask pattern to the desired sub-diffraction limit structure when the mask and the structure are not visibly the same pattern. Until recently, inverse lithography depended on complicated simulations to predict what mask pattern resulted in the desired subdiffraction limit structure, with a real time adaptable mask, multiple patterns can be tested to optimize the structure prior to fabricating a binary mask. Finally, the H-PDLC mask offers software controlled grayscaling. The analog nature of the H-PDLC transmission properties yields a light valve that can transmit intermediate intensities of exposure light resulting in a real-time reconfigurable grayscale device. Introducing grayscale to this application enables not only 2-dimensional patterning but also 3-dimensional patterning with a single mask element.

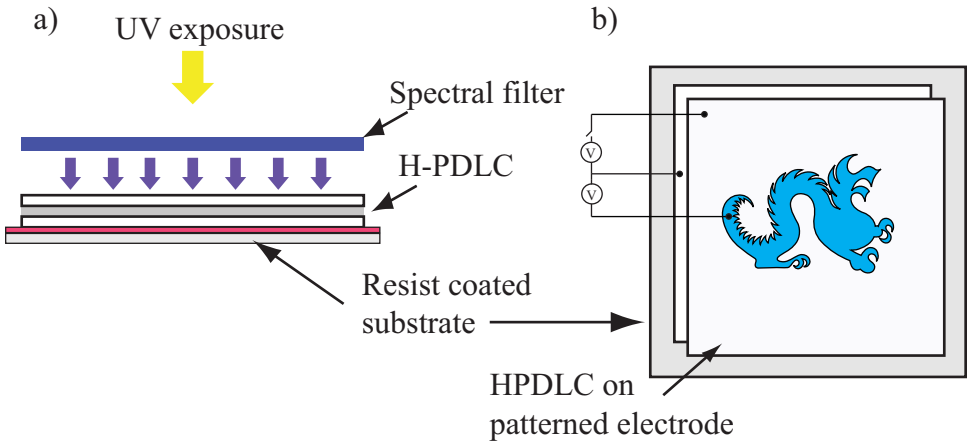

Figure 7.1: Schematic drawing of the adaptable photomask device. (a) The device set up for lithographic exposure showing UV light first being filtered to 436 nm, then transmitted through layers of ITO glass, selectively reflected at the H-PDLC grating, and finally exposing the resist surface. (b) The device from above (spectral filter is not shown). The two regions of patterned electrode can be biased either way.

The proposed device replaces a binary photomask used in the lithographic process with an H-PDLC film fabricated between thin ITO electrodes. Since H-PDLC

responds to local applied electric field, the ITO can be etched into electrically isolated regions that can be independently controlled to modulate separate regions of film. A method such as this one is known as patterned electrode control, and it is the primary method of modulating H-PDLC regions in this research. An advantage of this modulation scheme is proof-of-concept that this device can pattern multiple structures using a single mask, disadvantages include the limitation of available structures.

A step beyond patterned electrode control that enables a slightly higher level of arbitrary pattern control is a method known as electrode passive addressing. Using electrically isolated rows and columns on the upper and lower electrode surface, application of bias to a particular row and column will modulate the intersecting cell. Passive addressing further indicates that addressed biasing can yield an arbitrary structure, but the available patterns are still limited. For instance, passive addressing cannot form a ring or any type of enclosed structure.

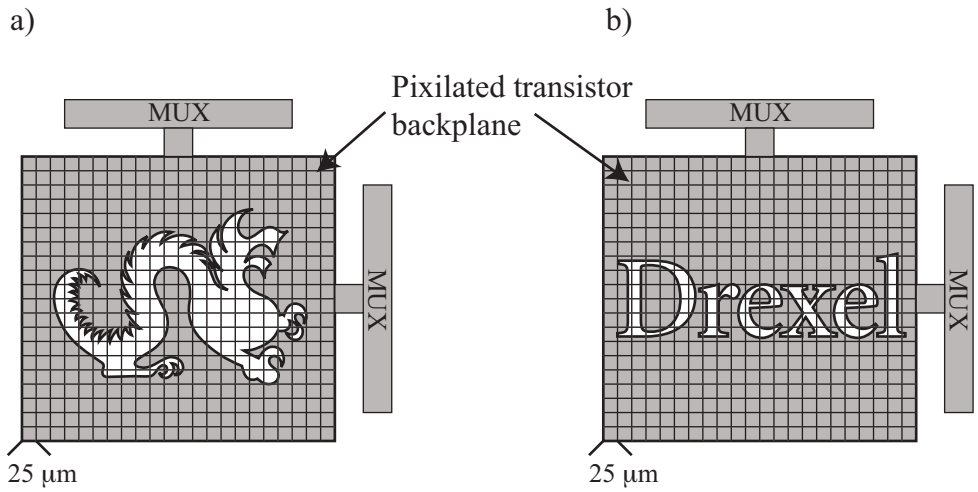

Figure 7.2: Figure of the device being used with a pixilated backplane. The mesh drawn across the mask represents the pixilation currently, for this system form factor limited at 25 μm. a and b represent arbitrary patterns being made clear or opaque through MUX and computer control.

The ultimate solution to this problem is fabrication of H-PDLC on a backplane

similar to that of an LCD device. Using sophisticated computer control and multiplexed addressing, LCD devices can operate on single pixels at small resolutions. Patterned electrodes and passive addressing are proof-of-concept steps that indicate H-PDLC films can operate in a separated environment and fabricate resist structures in an arbitrary fashion, but application of an LCD backplane has the potential to offer true arbitrary pattern generation. Using these methods we can measure the H-PDLC performance on patterns of similar size and shape, and we can characterize effects that are determined by the proximity of closely spaced structures. Figure 7.2 shows the feature constructed now using 25 μm pixels rather than sets of patterned electrodes. Figures 7.2a and b are drawn to show that by using a pixilated LCD backplane, a truly arbitrary pattern can be formed. Implementing an actual LCD backplane is outside the scope of this thesis and left for future work.

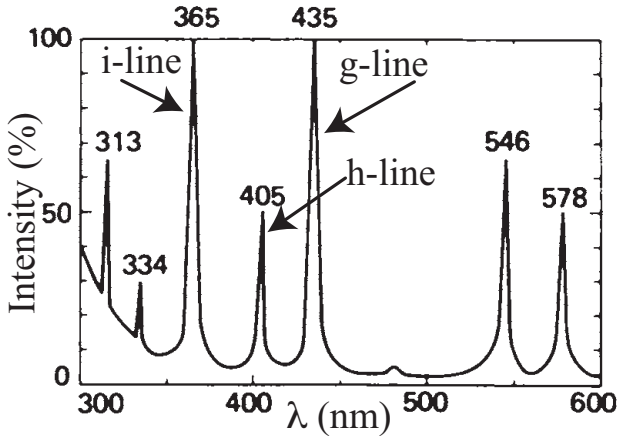

Figure 7.3: Emission spectrum of a mercury arc lamp, a common source for exposing photoresist. i-line at 365 nm, h-line at 405 nm, and g-line at 436 nm are labeled.

H-PDLC film fabricated on patterned electrodes acts both as the attenuation and the transmission material analogous to the chrome and glass sections of a traditional binary mask. All areas of the film can be configured to be either the transmission or the attenuation portion, and each section can be reconfigured an arbitrary number of

times. H-PDLC transmission stop-band center wavelength and diffraction efficiency, we have previous shown in Chapter 3, is a function of layer index, thickness, and quantity. The FWHM of the stop-band is determined by the interference that results from layer reflections and is typically approximately 10 nm FWHM. Figure 7.3 displays the emission spectrum of a mercury arc lamp, the typical exposure source used in photolithography [131,132]. Shipley 1800 series photoresist, the positive resist used in this research can be exposed with light sources emitting between 350 nm and 450 nm, but is optimized for g-line or 436 nm light. Within the sensitivity range of this resist, it can be seen from the figure that there are two additional strong emission lines, h-line and i-line corresponding to 405 nm and 365 nm respectively. For proof of concept purposes the exposure light was spectrally filtered to isolate the g-line with a 10 nm FWHM band pass centered at 436 nm. Fabricating an H-PDLC with a stop-band centered at the g-line combined with a spectral filter enables modulation of the light Shipley 1800 series photoresist is most sensitive to, 436 nm.

Potential implementations of an all H-PDLC system has been proposed to replace the spectral filter for a more dynamic mask that can be used with resist sensitized to the h-line or the i-line (common in negative resists) including the development of an H-PDLC with a broadened transmission stop-band and stacking multiple cells centered at the strong UV lines [45, 133].

Figure 7.1 is a schematic representation of the H-PDLC real-time adaptable photomask. Figure 7.1a is a cross sectional view showing the mercury lamp illumination filtered with a 436 nm spectral filter to eliminate wavelengths outside of the modulation range of the H-PDLC. Below the filter is the H-PDLC attenuating or transmitting light selectively based on bias in different regions across the film. Finally below the H-PDLC is the resist coated substrate. Figure 7.1b illustrates a top-down schematic of the device. Note that the spectral filter is not shown in this illustration. The H-PDLC mask composes the top layer and is shown to have two electrically isolated

areas with voltage supplies attached. The mask as it is shown in this schematic can be configured into two shapes that are inverse of one another. Below the H-PDLC is the resist coated substrate.

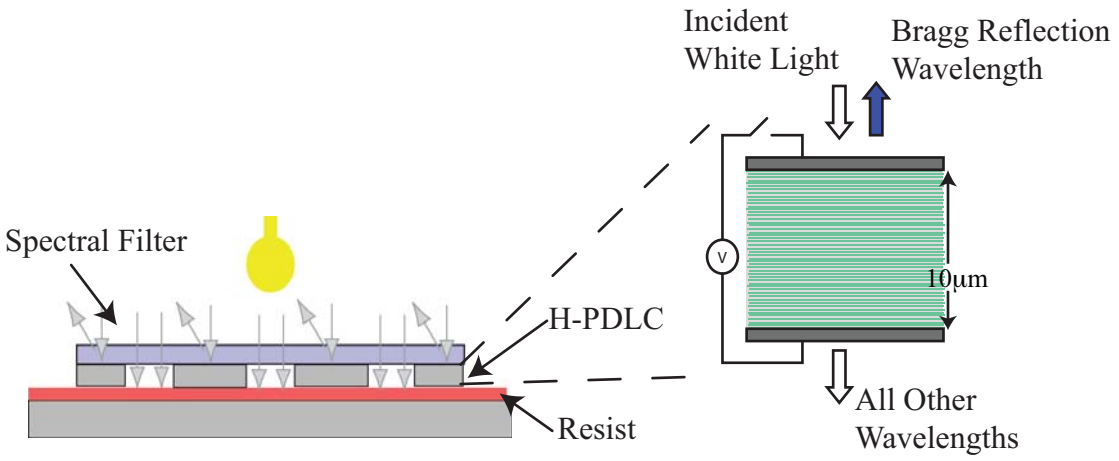

Figure 7.4: On the left is a schematic of the device concept. The H-PDLC layer is shown with more detail on the right indicating where it fits into the schematic of the device concept, which is below the spectral filter sitting above the photosensitive resist.

Figure 7.4 shows a representation of the device fitting into the photolithography scheme, sitting below the spectral filter but above the resist-coated surface. The inset to the right is designed to illustrate the individual components of the H-PDLC device namely the glass electrodes positioned top and bottom of the sample. The electrodes currently used range from 600 μm to 1 mm, which is governed by the thickness of the bottom piece of glass.

Figure 7.5 is a measured spectrum of an H-PDLC used as a photomask device. Shown are curves of unbiased transmission, or the transmission with intact stop-band and a curve showing biased transmission. From unbiased to biased states it can be seen from this curve that the H-PDLC can modulate approximately 70% of g-line emission, which is the difference between the notch minimum transmission value of

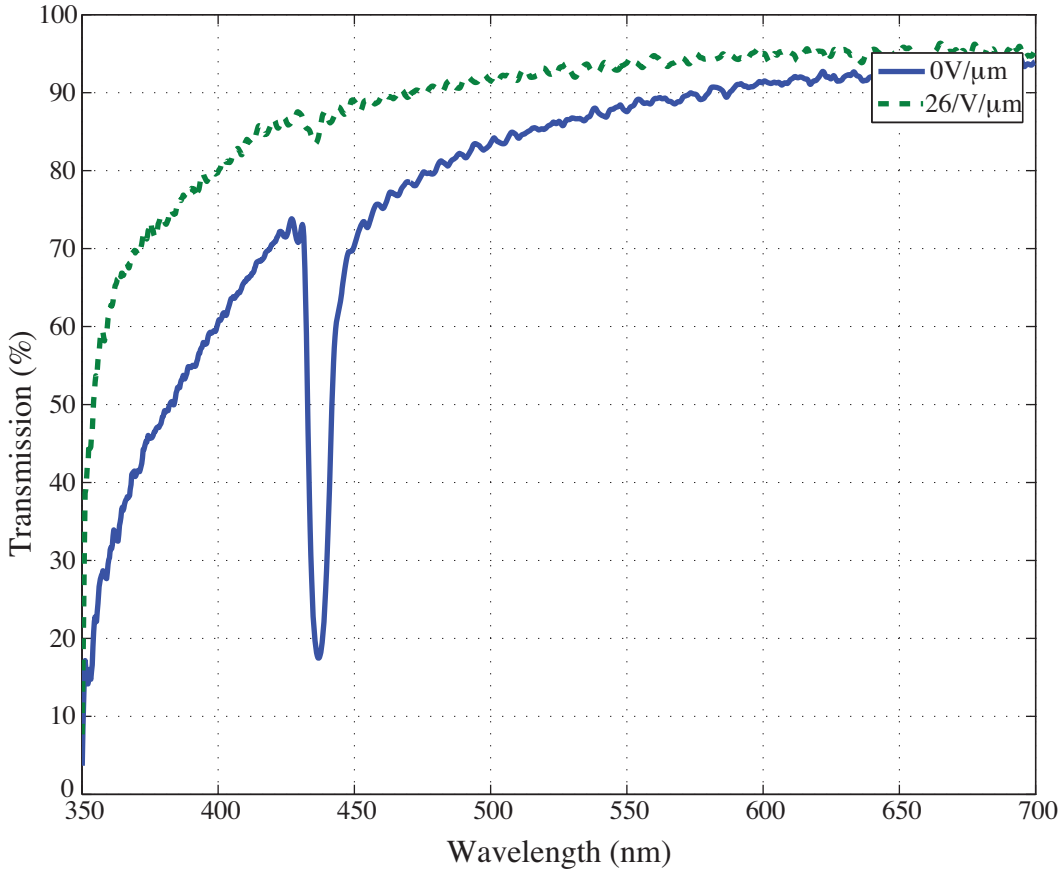

Figure 7.5: Measured spectrum of an H-PDLC used in masking showing the transmission stop-band and the biased H-PDLC reversing the stop-band. The stop-band notch wavelength is centered at 436 nm and the diffraction efficiency of this grating is approximately 50%, the modulation is about 70%. Bias values are indicated in the legend and experimental data collected using an Ocean Optics fiber-based spectrometer.

15% to the biased transmission at 436 nm of 85%. Finally it is important to note that although Shipley 1813 is optimized for g-line exposure, it rapidly approaches negligible absorption as nears 450 nm.

H-PDLC can modulate up to about 70% of 436 nm light, as illustrated in Figure 7.5. Figure 7.6a shows the Shipley 1813 contrast curve with the minimum and maximum patterning dose values indicated. Based on the datasheet defined equation and E_0 energy, the minimum dose for patterning is 82 mJ/cm^2 and the maximum dose for full development is 227.4 mJ/cm^2, a difference of about 36%. In order for H-PDLC to reach both dose extremes, it needs to be able to modulate at least 36% to be effective, which is easily attainable at center wavelengths of 436 nm using the thiolene chemistry predominately used in this research.

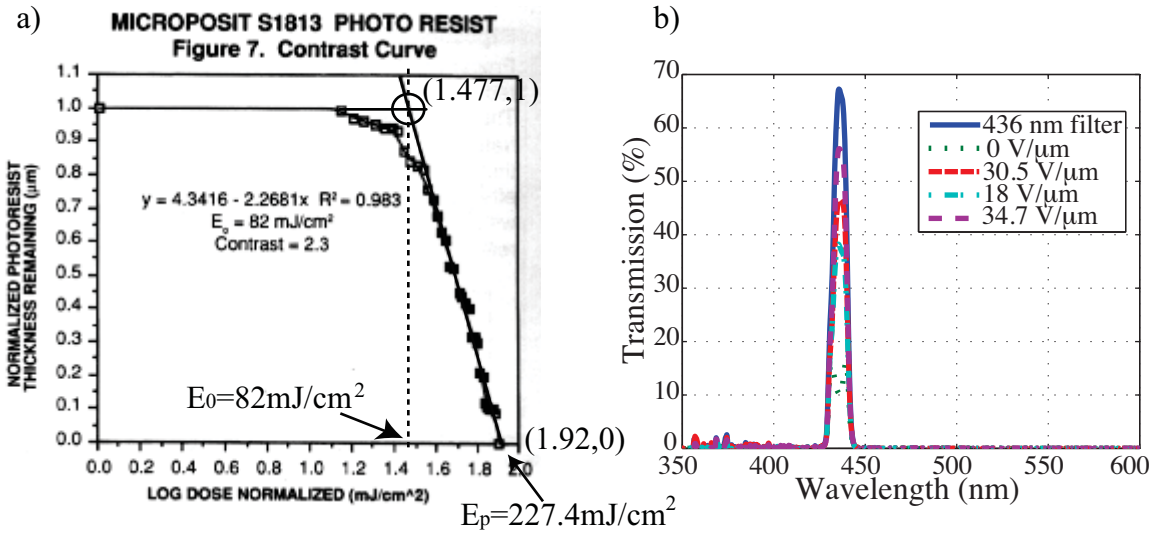

Figure 7.6: a) The contrast curve from the Shipley 1813 datasheet showing on it the calculated dosages for no exposure and complete exposure. b) Different amounts of light modulated through the H-PDLC and a g-line filter experimentally collected using an Ocean Optics fiber-based spectrometer.

In Figure 7.6b, we show white light transmission through first the 436 nm spectral filter then through an H-PDLC under different biasing conditions. In the unbiased or

"off" state, the resulting transmission is the most attenuated curve. In the "on" state, we show the highest transmission. This figure is intended to show the light differential as it is seen by the photosensitive resist under the different voltage conditions. It is also useful in visualizing the grayscale ability with a number of intermediate transmission values between the maximum and minimum points.

7.2 Initial Patterning Characterization

This first proof of concept section details the adaptable photomask concept and analyzes the first resist patterns formed with the device. This is also a manuscript published by the author in *Applied Physics Letters* [134]. Here we elaborate on an application in which H-PDLC reflection gratings are used as a real-time reconfigurable photomask to replace traditional contact photomasks in the lithographic process.

7.2.1 H-PDLC Material Selection and Fabrication Method

H-PDLC films used in this study were formed using a thiolene based syrup consisting of 65% Norland Optical Adhesive 65 (Norland Optical Products, Inc.), 30% BL038 liquid crystal (EM Industries), and 5% Darocure 4265 UV initiator (Aldrich, Inc.) as outlined in the section describing H-PDLC material sets and summarized Table 7.1. The ordinary refractive index of BL038 is n_o=1.527, and its birefringence is Δn=0.272. The index of cured NOA65 polymer is n=1.524. Index matching of BL038 and cured NOA65 in the biased state is within 0.2%. The laser used to form the gratings was a Coherent 308C Ar:Ion tuned to 351nm courtesy of the Display Laboratory at Brown University . The intensity used was approximately 80mW/cm^2. The method of fabricating the gratings was the prism method, developed by Natarajan [Chem Mat., 2003] and coworkers [29], which uses total internal reflection inside a prism as the source of the optical interference used to form the H-PDLC grating. This procedure

is also summarized in Chapter 3.

H-PDLC films were formed on ITO coated Corning 1737 glass prefabricated with electrically isolated rows. ITO rows were etched 5 mm wide with 264.6 μm isolation gaps. These structures were fabricated using a photolithography pattern transfer technique with positive resist and an HCl etch.

7.2.2 H-PDLC Patterned Resist Fabrication Method

To use the H-PDLC film formed on etched ITO glass as a reconfigurable photomask, the mask was placed in contact with a resist coated substrate. A filter was placed above the H-PDLC mask device. Bias was applied to regions intended to be transparent. Regions with no bias acted as light valves for the 436 nm light reaching the mask, attenuating it below the threshold for curing. Exposure dose measured in transparent "on" regions was 120 mJ/cm^2; attenuated dose in the reflecting "off" regions was measured to be 93 mJ/cm^2. Resist used was Shipley 1813 positive photoresist spin-coated to a thickness of 1.4 μm. Post exposure, samples were developed in Microposit 351 for 2 minutes. The exposure tool used in this study was not a mask aligner, but a UV curing lamp. Although these two devices house the same mercury bulb, a mask aligner filters the exposure using a pinhole ensuring some level of spatial coherence. The mask aligner also collimates the beam. A UV curing tool does not alter the exposure, so the exposures were incoherent and not collimated. Using the H-PDLC to modulate the light will be possible regardless of coherency, but the quality of the image formed in resist may be lower than what would be formed using a mask aligner. To show proof of concept that H-PDLC can sufficiently modulate resist curing UV light, structures with intentionally large feature size were fabricated. The smallest reproducible feature fabricated was a 264.5 μm line. This feature was fabricated both using the H-PDLC photomask device and a static mask under similar

Table 7.1: Thiolene H-PDLC pre-polymer syrup as percent weight

Component	Percent
Darocure 4265 (Aldrich, Inc.)	5.00%
BL038 (EMD Industries)	30.00%
NOA65 (Norland Inc.)	65.00%

exposure and development conditions for comparison.

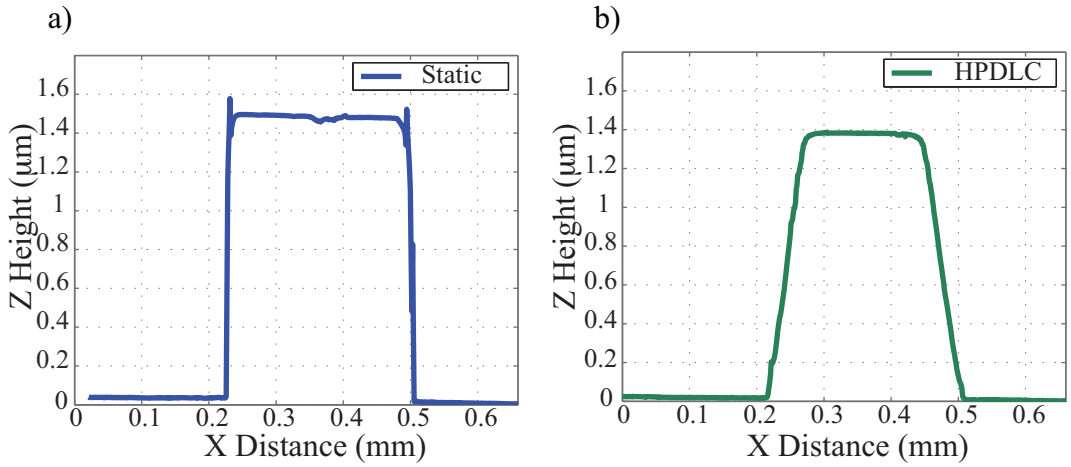

Figure 7.7: Initial patterning of a 265 μm feature patterned using a binary mask and an H-PDLC mask imaged using an optical profilometer. a) Feature patterned using a binary mask. b) Feature patterned using an H-PDLC mask.

7.2.3 Patterned Resist Characterization Technique

Figure 7.7 is an example of the line shape of the smallest reproducible structure using an H-PDLC mask superimposed with a similar sized feature fabricated with a static mask. This data was collected using a Zygo NewView 6200 white light interferometic profilometer. The ideal line width of this structure is 264.5 μm, the mean line width (measured at the base of the microstructure) of several samples fabricated using the static mask was 320.7 μm while the mean line width of the same structure fabricated

Table 7.2: Characterization data of microstructure samples

	Static Mask	HPDLC Mask
Edge Slope	25.2μm/mm	19.0μm/mm
Mean Linewidth	320.7μm	321.4μm
STD Linewidth	37.2μm	53.4μm
Linewidth Error from ideal	21.2%	21.5%

under the same exposure and development conditions using the H-PDLC photomask device was 321.4 μm. As summarized in Table 7.2, it can be seen that the line width profiles between structures fabricated using the H-PDLC mask and the static mask are on average within a percent of one another. The calculated standard deviation between samples shows that the static mask produces a more repeatable line width than the H-PDLC mask.

Structure edge slope in positive resist is governed by several factors. It can be seen in Figure 7.7 that both resist structures have different amounts of overcut in their profile though line width measured from the base is approximately the same. The expression for edge slope or dz/dx can be separated into the product of a derivative term entirely dependent on resist and developer properties, dz/dD, and a derivative term entirely dependent on the exposure wavelength, intensity, and imaging system, dD/dx. In these derivative terms, z is defined as the feature height, x is defined as the lateral distance across the substrate, and D is the exposure dose. dz/dD is referred to as the developer elution term, and it defines the final structure profile as a function of resist and developer properties. dD/dx is known as the intensity profile term which characterizes the final structure's dependence on the exposure optical properties [1]. Rewriting the developer elution term as the quotient of resist contrast

and resist sensitivity, and simplifying the expression

$$\frac{dz}{dD} = -\frac{1}{D_p\left\{log\frac{D_p}{D_p^0}\right\}} \tag{7.1}$$

it can be seen that this term is a function of D_p and D_p^0. D_p^0 is a threshold term defining the minimum exposure dose required to develop resist while D_p is defined as the dose required to fully develop a layer of resist. These terms are dependent on resist thickness and absorbance, which are properties of the positive resist used for the lithography process. This term is independent of imaging system and should stay constant between sample structures fabricated using the static and H-PDLC mask.

Examining the intensity profile term, the derivative can be written

$$\frac{dD}{dx} = \frac{2NA}{\lambda\left[1 - k\left\{\frac{\delta NA^2}{\lambda}\right\}\right]^2} \tag{7.2}$$

where λ is the wavelength of the exposure, δ is the depth of focus of the exposure optical system, NA is the numerical aperture of the imaging optics, and k is a constant quantifying the coherence of the exposure light. It is clear that this term is defined only by the exposure wavelength and optical imaging system, and is independent of resist properties [1].

In order to quantify the discrepancy in edge slope between the structures made using the different mask systems, it is necessary to examine the intensity profile term. This term is highly dependent on exposure wavelength, but that variable was held constant in comparisons between the two masking systems. Depth of focus is a term that itself is related to numerical aperture of the imaging system, the variable that was not controlled in the comparison experiments. Since we are performing a strict comparison of resist shape between two masks regardless of source coherency, we can consider the k factor to be constant between the two samples. Of course this image

could be better formed using a mask aligner with a more coherent source, this test is performed later. Numerical aperture of the imaging system used to pattern resist structures is dependent on the angle of the light spreading out from the mask reaching the resist. Diffraction from the mask edges accounts for an increase in numerical aperture for both the static and the H-PDLC mask. There is, on average, a 24.6% difference in edge slope between samples fabricated using the two masking methods; it is expected that there is approximately that much discrepancy in the numerical aperture of the two imaging systems introduced by propagation in the nanostructure.

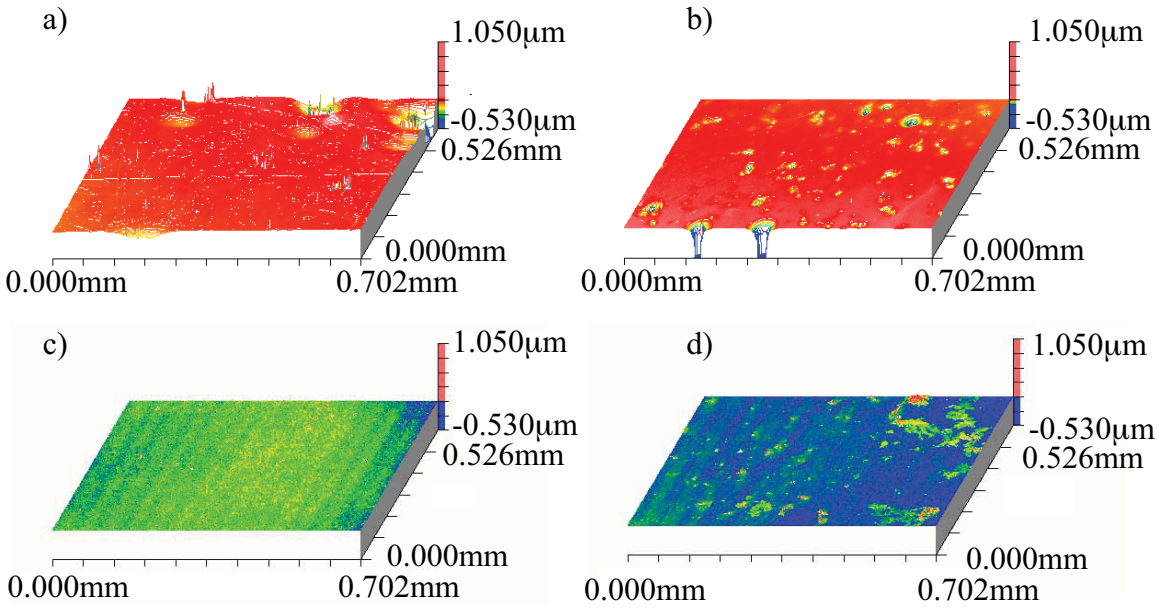

Figure 7.8: Contour maps of developed surfaces formed with an H-PDLC mask and its static mask counterpart imaged using an optical profilometer. (a) Developed resist surface fabricated with an H-PDLC mask in its reflective state. (b) Developed resist under static mask. (c) Developed glass substrate formed with the H-PDLC mask in its transparent state. (d) Developed glass substrate formed under a light field static mask showing a small amount of resist residue after development.

In order to ensure that the H-PDLC photomask device was attenuating the UV exposure light below the threshold for curing resist, profilometry was performed to

determine the quality of the developed resist and glass areas. Resist samples for this comparison were fabricated using the H-PDLC mask in both the biased and unbiased state to show that the grating can fully modulate the exposure dose to cure or protect from curing the resist substrate. To fabricate the sample shown in Figure 7.8a, the H-PDLC mask is unbiased, therefore, preventing UV exposure. The resulting bulk region formed under the grating shows some indentation and dimpling, but these defects are comparable to a typical region of developed resist formed with the static mask shown in Figure 7.8b. No grating line defects are apparent or other evidence that it was cured under a film grating. The inverse sample was subsequently formed by biasing the H-PDLC mask into its transparent state. The exposure penetrates the mask curing the resist. The resist is developed leaving little resist residue, as shown in Figure 7.8c, compared to the sampled formed with the static mask (Figure 7.8d) which indicates a small amount of resist residue is left on the glass substrate.

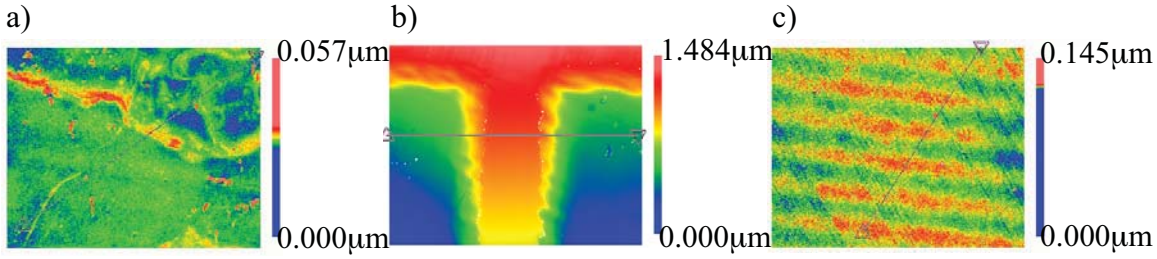

Figure 7.9: An example of a structure fabricated with the H-PDLC mask imaged using an optical profilometer. Progression shows no pattern (developed resist), t-shaped pattern, and finally transparent mask (exposed glass).

Finally, an example of a structure patterned using an H-PDLC mask is shown in Figure 7.9. Two samples were fabricated, first with the H-PDLC mask in an unbiased reflective state resulting in a flat developed resist area. The second sample was fabricated with the H-PDLC mask in a transmissive state. Regions of conducting ITO switch the mask and allow resist exposure (Figure 7.9b).

This first set of results shows proof of concept of an adaptable and computer controllable photomask using H-PDLC reflection gratings as a method for selecting UV exposure regions. We should that though edge slope exists between the binary and the adaptable mask, repeatable features can be formed with this electro optic material. We also show the the morphologies of developed substrates, both glass and resist, for bulk regions exposed using a binary mask and an H-PDLC mask. We see that the regions are unaltered as a result of H-PDLC transmission. Finally, a sequence of preliminary dynamic patterns are detailed. The mask in this example could transmit, make a t-shape, and attenuate the exposure. We show all three variations.

In this initial patterning work, we show that H-PDLC can modulate 436 nm light to selectively pattern or prevent patterning of Shipley 1813. We see that there is a slight overcut discrepancy between patterns formed when light is transmitted through the nanostructure in comparison to structures formed with no nanostructure, but morphologically the resist surface and glass surfaces pattern cleanly. The edge slope discrepancy is a result of optical effects in propagation and is discussed in Chapter 9.

7.3 Edge Slope Characterization

This work was published by the author in *Journal of Micro/Nanolithography, MEMS, and MOEMS* and in *Proc. SPIE: Symposium on Photomask Technology* [135, 136].

In this next work we compare feature edges fabricated using the thin film mask and the ink-jet transparency printed mask, and lines of different widths fabricated using both methods. Under optimal exposure and development conditions, vertical walls would be expected. In the scenario that optimal conditions cannot be reached, resist edge slope affects feature resolution. We show that, in holding the development and resist mechanical characteristics constant, the thin film mask can modulate the

exposure dose and provide an appropriate contrast to form features nearly as precise as a commonly used ink-jet transparency mask. Finally, we present a surface morphology study demonstrating that the H-PDLC mask can cure or prevent curing of the resist in bulk areas.

7.3.1 H-PDLC and Patterned Electrode Fabrication Procedure

Liquid crystal polymer composite film photomasks are fabricated by holographically forming H-PDLC on indium-tin-oxide (ITO) patterned glass. In order to pattern the ITO, a static mask is created using a drawing tool or CAD program and the pattern is ink-jet printed onto a transparency. 1"x1" pieces of Corning 1737 glass coated with conductive ITO are cleaned and prebaked to remove solvents before lithographic patterning. Microposit 1813 (Shipley Corp.) positive photoresist is spun onto the glass forming a 1.4 μm layer. The resist coated glass is baked again for 3 minutes at 120°C to ensure moisture is removed from the polymer. The transparency pattern is transfered to the resist with a UV exposure dose of approximately 110 mJ/cm^2. The glass is post baked for 3 minutes at 120°C and the pattern is developed for 30 seconds in 5:1 solution of deionized water to Microposit 351 developer. ITO is etched in a 50:50 9M HCl to deionized water solution for 60 minutes. Remaining resist is dissolved with acetone.

H-PDLC films are formed on ITO patterned glass using a thiolene based syrup consisting of 65% Norland Optical Adhesive 65 (Norland Optical Products, Inc.), 30% BL038 liquid crystal (EM Industries), and 5% Darocure 4265 UV initiator (Aldrich, Inc.) as summarized in Table 3.1. The laser used to form the gratings is a Coherent 308C Ar:Ion tuned to 365 nm with output intensity of approximately 120 mW/cm^2, courtesy of the Drexel University Material Science Department. The method of fabricating the gratings was the prism method [29] which uses total internal reflection

inside a prism as the source of the optical interference used to form the H-PDLC grating. Rotating the prism causes a shift in the grating pitch allowing precision control over the reflected wavelength.

Glass substrates are cleaned and prebaked, then spincoated with a 1.4 μm layer of Microposit 1813 positive photoresist. The substrates are softbaked and exposed using a broadband UV flood lamp. The substrate is positioned under the H-PDLC mask with bias voltages applied, and a 10 nm FWHM spectral filter centered at 436 nm is placed in contact with the mask. Optimal exposure dose for a 1.4 μm layer of 1813 photoresist is 120 mJ/cm^2. Measured exposure dose of 436 nm light reaching the resist substrate using the H-PDLC mask is 140 mJ/cm^2 in the transmissive state and 93 mJ/cm^2 in the reflecting state. Once exposed, the substrates are hard baked and developed in 5:1 deionized water to Microposit 351 solution.

Structures fabricated using the static mask are exposed and processed in an identical manner. The static mask itself consists of an ink jet transparency printed with the desired static pattern adhered between the same ITO glass used for the H-PDLC substrate.

7.3.2 Resist Structure Analysis

The first set of structures analyzed, shown in Figures 7.10a and 7.10b, are edge profiles of developed resist structures fabricated using the H-PDLC mask and a static (ink-jet transparency) mask. Under ideal exposure and development conditions, vertical walls would be expected. Figure 7.10a illustrates the edge profile of a feature patterned using the thin film mask. This particular example has an edge width of approximately 60 μm while its binary masked counterpart in Figure 7.10b displays a more narrow edge width of less than 40 μm. These examples illustrate the general shape of a patterned edge and fall near the average of all the samples measured. Both structures

Table 7.3: Edge characterization of fabricated microstructures

	Static Mask	HPDLC Mask
Average Edge Width(μm)	54.37	56.67
Edge Width Std(μm)	13.32	9.11
Edge Width Error		4.23%

have smooth, even resist regions at the predicted height of 1.4 μm determined by the spin speed of the resist onto the substrate before exposure. Summarized in Table 7.3 are average edge widths of features fabricated using the static mask compared to features patterned with the thin film mask. The method of determining edge width was the difference from 10% to 90% of the maximum height of the feature. It can be seen in the table that on average over 20 samples, the edge width differs by 4.23%.

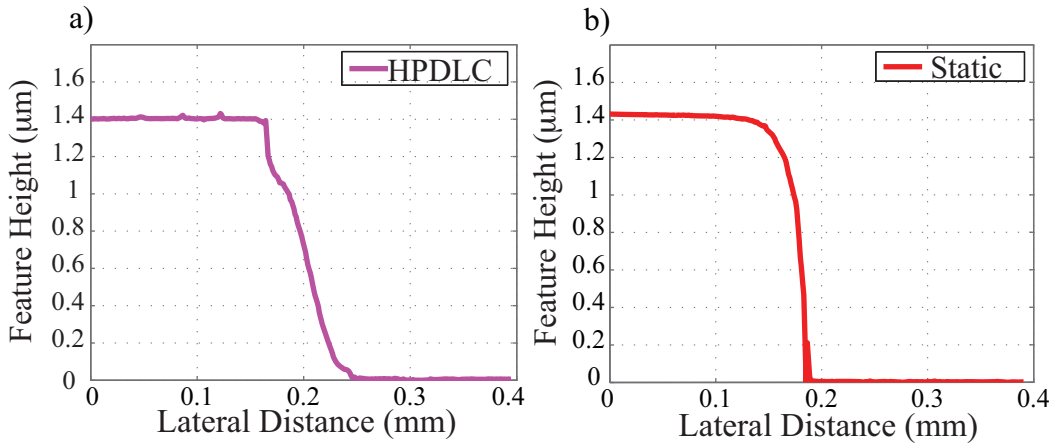

Figure 7.10: Structures in resist formed with (a) H-PDLC mask and (b) static mask imaged using an optical profilometer.

The next set of structures fabricated was a pattern of lines with decreasing width. The thickest line fabricated was 121 μm and the thinnest was 84 μm. The purpose of fabricating structures with this pattern was to determine if the H-PDLC mask has a minimum feature size limit. The master mask was printed from an ink jet printer onto

a transparency, which had a limiting feature size of 84 μm. This master mask was used to pattern the ITO electrodes on which the H-PDLC mask was formed. Again using the optical profilometer, these structures of decreasing width were compared by measuring their base-to-base width. This minimum width of about 84 μm was measured on the ITO glass substrate after etching, but before the H-PDLC was formed. Comparing structures fabricated with the static mask using this pattern and the H-PDLC mask formed on the ITO etched in this pattern as shown in Table 7.4, the H-PDLC mask formed a structure within 5% of the ideal pattern transfer. The static mask formed a wider structure, over 25% larger than the ideal pattern transfer. With increasing structure width, the H-PDLC and static masks both produce features with near ideal pattern transfer. In Table 7.4, 121 μm ideal line width is compared with the results using the two experimental masks. The static mask produced a line width within 1.6% of ideal while the H-PDLC mask produced a line width within 7.4% of ideal pattern transfer. It can be seen from Table 7.4 that using this system, the H-PDLC mask fabricated a comparable, if not more resolved structure than its static counterpart at narrow line widths when used in this configuration.

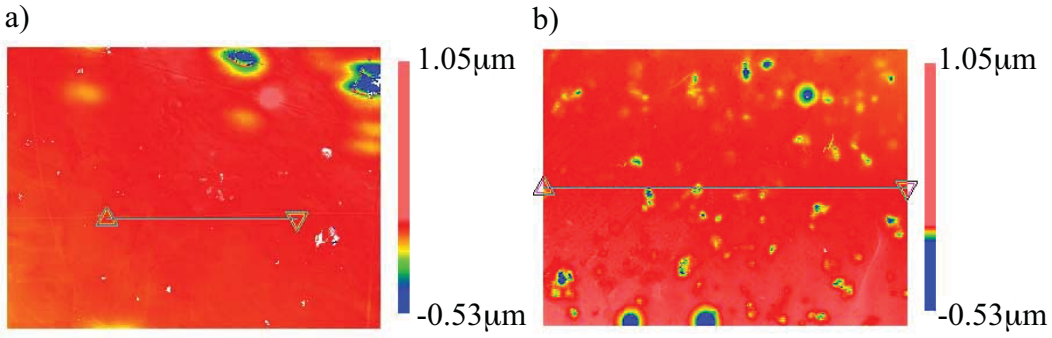

Figure 7.11: Surface morphology of bulk developed resist areas (a) resist developed under H-PDLC mask (b) resist developed under static mask imaged using an optical profilometer.

The optical profilometer was also used to analyze the morphology of developed bulk glass and resist areas to ensure that all the resist was removed in the glass regions, and that there were no structural defects such as puckering or indentations in the resist regions due to being formed under a grating. Figure 7.11a is the contour map of a developed bulk resist region formed under the H-PDLC mask. Figure 7.11b is the contour map of a bulk region formed using the static mask. Both regions have some indentations, but clearly the resist developed using the H-PDLC mask has a smoother, more uniform surface. It is known that even in the reflecting state, H-PDLC allows a small amount of scattered light to transmit through the film. Forward scattered light was measured to be on the order of 0.5 mJ/cm^2. This exposure dose is well below the threshold to cure resist confirming that no scattered light from the H-PDLC forms an anisotropic etch as in the case of PDLC reported by Jeon [Proc. MEMS, 2006] [108].

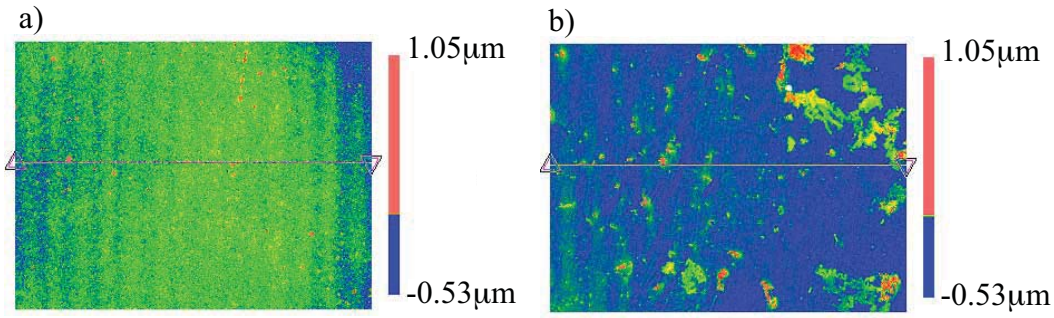

Figure 7.12: Surface morphology of bulk developed glass areas (a) glass developed under H-PDLC mask (b) glass developed under static mask imaged using an optical profilometer.

The contour maps in Figure 7.12 are regions of substrate in which the resist was developed and removed. In Figure 7.12a, the glass developed under the H-PDLC mask, the resist is entirely removed leaving a flat piece of substrate. In Figure 7.12b, the developed region using a static mask, a small amount of resist residue remains on

Table 7.4: Linewidth characterization of fabricated microstructures

	Ideal	Static Mask	HPDLC Mask
Line Width(μm)	84	107	88
Line Width Error	0	27.4%	4.7%
Line Width (μm)	121	123	130
Line Width Error	0	1.6%	7.4%

the glass.

Finally, a static mask and a patterned electrode H-PDLC mask were used to pattern the same image in resist, the samples were evaporated with chromium and a lift-off technique was performed to remove the remaining resist. Results of this are shown in Figure 7.13a and b. Figure 7.13a is the pattern formed with the static mask on a 1" piece of glass substrate. Figure 7.13b, also on a 1" substrate, is the same image formed using the H-PDLC mask.

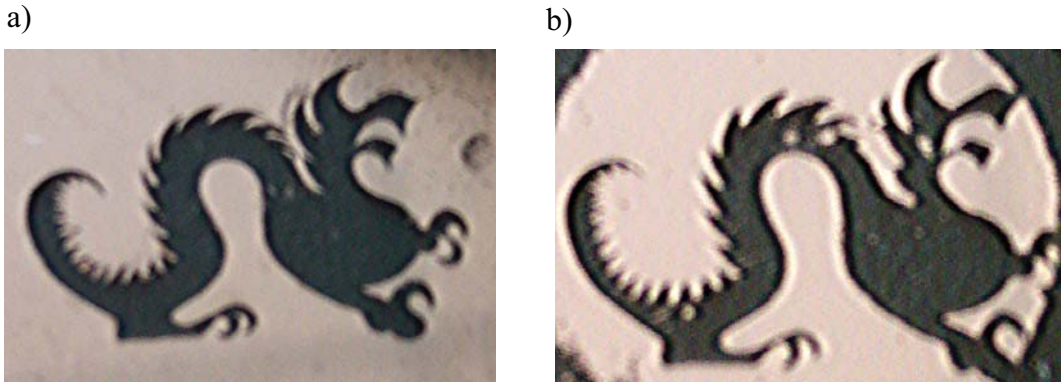

Figure 7.13: Example of image patterned using (a) static mask and (b) H-PDLC mask. Image is chrome evaporated onto glass substrate, then developed in acetone to remove the resist. Image captured via photograph. Both samples are 1"x1".

We have shown a prototype of an adaptable, computer controllable photomask device made from liquid crystal polymer composite films. Using known methods for fabricating patterned electrodes and H-PDLC films, we show that this material is

ideal for use as a reconfigurable photomask that can selectively block or transmit the UV exposure wavelengths. The edge profiles of structures formed with adaptable H-PDLC masks and static mask equivalents differ in edge width by less than 5%. The H-PDLC mask can fabricate structures as narrow as 88 μm with better resolution than the static mask when used in this configuration. Currently minimum line width is limited to what can be printed on an ink jet printer, rather than being limited by the masks. We have also shown that bulk developed resist formed under the H-PDLC mask does not experience dimpling or indentation due to being formed under the grating, nor does it exhibit defects as a result of forward scattered light from the grating when in its reflective state. Resist developed for removal under the H-PDLC mask rinsed completely, better than its static mask counterpart in this configuration. Finally, an example of a pattern processed with a chromium evaporation and lift-off technique is presented.

7.4 Etching H-PDLC Patterned Substrates

This next proof of concept study illustrates that H-PDLC patterned resist can withstand a subsequent etch step. We examine two types of etch methods on silicon, and compare to resist patterned using a set of chrome on glass and ink-jet transparency masks. Judging by the appearance, thickness and morphology, there is no reason to think that H-PDLC patterned resist would not withstand an etch, but verification was necessary for completeness. This work has been published by the author in *Proc. SPIE:Symposium on Integrated Optoelectronic Devices, Practical Holography XXII: Materials and Applications* and has been submitted to *Journal of Micro/Nanolithography, MEMS, and MOEMS* [137] [138].

In this work, we expand on the proof of concept work by using the H-PDLC reconfigurable photomask in more advanced lithographic processes. Previously, we

have focused on resist profile and patterning. To further this work, we demonstrate the next step by determining the H-PDLC patterned resist's ability to withstand different substrate etching mechanisms including reactive ion etching and chemical wet etching. We compare etched features patterned using a chrome on quartz glass mask, a ink jet printed transparency mask, and the H-PDLC mask.

7.4.1 H-PDLC Photomask Fabrication Technique

In order to fabricate this device, the conductively coated glass in which the H-PDLC is formed on is etched, then the H-PDLC is holographically formed. Once the photomask device is complete, the test samples are fabricated, developed, and etched using standard photolithographic technique.

Electrical control over selected sections of the H-PDLC film is achieved by etching the optically clear yet conductive layer of indium-tin-oxide (ITO) from a glass substrate that confines the thin film. Previously, these masks were made with two isolated regions enabling a set pattern to be exposed, or by reversing the bias, the inverse pattern. The masks used currently have the ability to form many different structures, enhancing the concept of arbitrary pattern generation. Specifically, a seven-segment numeral and a 16-pixel square pattern have been fabricated. To etch the ITO, a binary mask is drawn and printed on a transparency. That pattern is transfered to Shipley 1813 positive photoresist spin coated to a thickness of 1.0 μm on a Corning 1737 and ITO substrate. Spin speed is 4000 RPM for 30 seconds. The substrate is softbaked at 120C for 3 minutes and patterned 120 J/cm^2. The substrate is developed in a 1:3 ratio of Microposit 351 to deionized water solution for 45 seconds and hardbaked for 5 minutes at 120C. The ITO is etched using 1:1 ratio of 38% HCl to deionized water solution for 2 minutes and 45 seconds each.

H-PDLC films are fabricated using a homogeneous mixture of monomer, photoini-

tiator, and liquid crystal exposed to an optical interference pattern that forces phase separation and the formation of stratified liquid crystal and polymer planes. The components of the prepolymer syrup are NOA65 thiolene based monomer (Norland Optical Products, Inc.), Darocure 4265 UV initiator (Aldrich, Inc.), and nematic liquid crystal BL038 (EM Industries) in weight percents described in Table 3.1.

The homogeneous mixture is pressed in 20 μm spaced cells of Corning 1737 glass coated with patterned electrode ITO for electrical control over the finished sample. The pressed cells are exposed using a Coherent 308C Ar:ion laser tuned to 351 nm at approximately 65 mW/cm^2. The interference pattern used to induce the periodic layers of polymer and liquid crystal droplets is generated using total internal reflection inside a prism [29].

7.4.2 Patterning Resist using Comparison Masks

Photolithography was performed to fabricate features using three different types of masks for comparison purposes. The first mask used was a chrome patterned quartz glass mask formed using electron beam lithography. This type of lithography yields the highest resolution, but is slow and expensive to perform. The next mask was made from a pattern generated using AutoCad and printed onto an ink jet transparency. Here, the resolution is limited by the ink jet printer and is estimated to be about 50 μm. Finally, patterns were fabricated using the H-PDLC mask. Structures were fabricated using the three masking solutions on [100] silicon and silicon dioxide wafers.

Using the H-PDLC reconfigurable photomask, several structures were patterned onto [100] silicon substrates for RIE etching and [100] silicon substrate with 800 nm of SiO_2 for wet etch purposes. Silicon wafers were washed in a hydrofluoric acid bath to remove any thin oxide on the substrate and cleaned in acetone, SiO_2 wafers were cleaned only with acetone. The wafers were spin-coated with 1.0 μm Shipley

1813 positive photoresist and soft baked at 120^{o}C for 3 minutes. The substrate was masked with the H-PDLC biased to create a pattern and stacked with a 436 nm filter to remove UV wavelengths outside of the H-PDLC modulation range. The resist was exposed at 120 mJ/cm^2 and developed for 30 seconds in a 1:3 Microposit 351 to deionized water solution and hard baked for 10 minutes before etching.

The first process performed was a silicon dry etch. The silicon substrates were etched using a deep reactive ion etcher to create vertically walled trenches. Since the selectivity of silicon to 1813 is approximately 5, the target trench depth was 5 μm. The chemistry used was a C_4F_8, SF_6 and O_2 cycle at 25 mTorr. To accomplish a 5 μm etch, this system was run for 11 cycles or approximately three minutes. Upon completion, remaining positive resist was removed from the wafer using acetone and the etch depths were characterized.

Next, a wet etch was performed. Wet etching of silicon first requires patterning and etching of the SiO_2 layer, then etching of the underlying silicon. The positive resist coated silicon dioxide layer was etched in buffered HF for 12 minutes exposing the silicon below. The positive resist was removed with acetone and the silicon was etched using 45% potassium hydroxide for 8 hours. The wafers were characterized and replaced in the etching solution again for a total of 22 hours.

7.4.3 Reactive Ion Etching (RIE) of Patterned Silicon Substrate

Upon completion of the reactive ion etch process, the photoresist was stripped from the silicon substrates and the substrates were characterized using optical profilometry. Etch depth and edge thickness were among the parameters measured for each RIE sample for the three different mask types. Their mean values are tabulated in Table 7.5. Using a slightly shorter etch cycle of 1.5 minutes, a more shallow etch occurred in the first RIE sample. Mean etch depth of the H-PDLC patterned features using

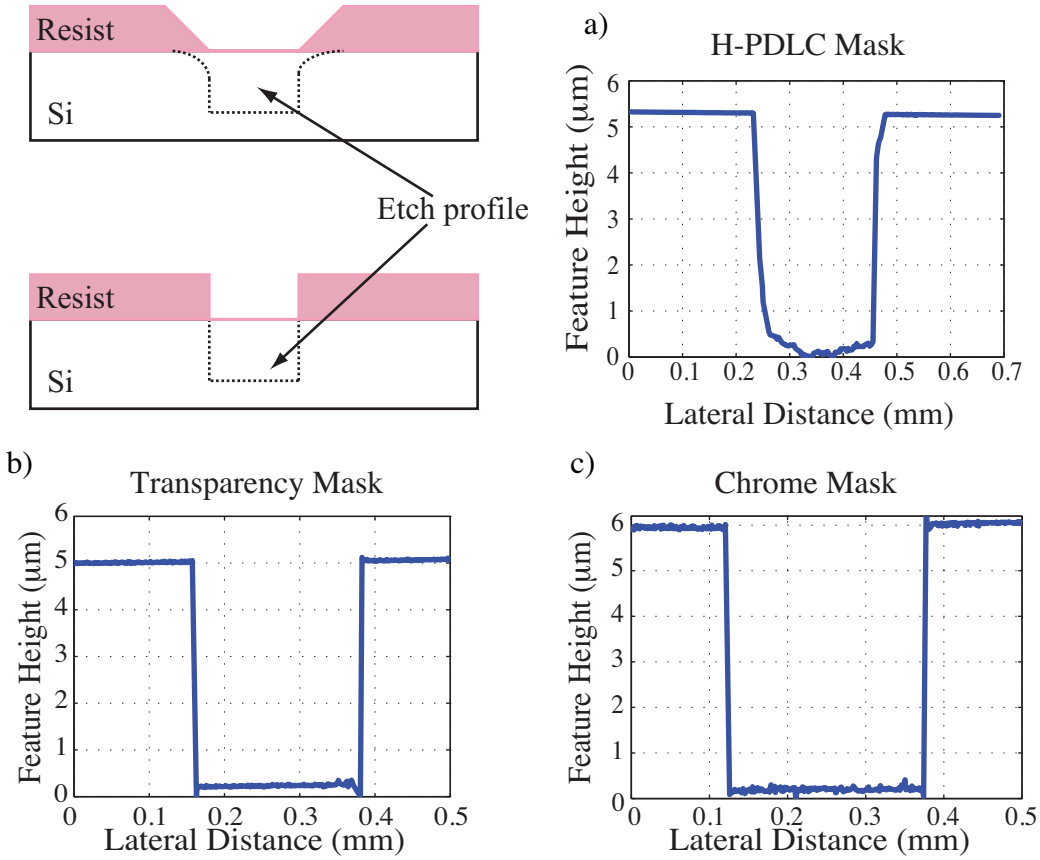

Figure 7.14: Reactive ion etch trench of features patterned using different types of masks imaged using an optical profilometer. a) Feature patterned using an H-PDLC mask. This structure was patterned using a long RIE cycle of approximately 3 minutes. The notable characteristics are the rough silicon floor and the sloping edges at the top of the structure. b) Feature patterned using an ink jet printed transparency. Note sharp and vertical walls. c) Feature patterned using a chrome on glass mask. Again, note the sharp and vertical walls.

Table 7.5: RIE Etch Results for 2 H-PDLC etch depths plus binary mask results

Sample	H-PDLC 1	H-PDLC 2	Transparency	Chrome
Mean Etch Depth (μm)	2.117	4.849	4.657	5.823
Depth Standard Deviation	0.197	0.599	0.178	0.062
Mean Edge Width (μm)	11.558	18.980	6.877	5.140
Width Standard Deviation	3.140	5.739	5.706	2.129
Mean Edge Slope	0.183	0.255	0.677	1.133
Slope Standard Deviation	0.0532	0.0930	0.706	0.4155

the 1.5 minute cycle was 2.117 μm with standard deviation of 0.197. Subsequent H-PDLC patterned features were etched for 3 minutes yielding a mean etch depth of 4.849 μm confirming a silicon etch rate of approximately 1.6 μm/minute and a selectivity of about 5:1 with 1813 positive photoresist. Additional samples patterned using an ink jet transparency mask and a chrome on quartz glass mask yielded similar etch depths for 3 minutes cycles of 4.657 μm and 5.823 μm respectively.

Edge width was measured for each trench to quantify the etch profile. When masked properly and using an appropriate chemistry, edges etched using RIE technology should be near vertical. Mean widths measured for the short cycle H-PDLC patterned features was 11.558 μm and the long cycle H-PDLC patterned features yielded a width of 18.980 μm. Transparency and chrome masks yielded more narrow edge widths of 6.877 μm and 5.140 μm respectively. Edge slope (μm/μm) was calculated from these two characterizations and yielded a similar result: chrome mask and transparency mask show more vertical walls than the short and long cycle H-PDLC patterned features.

Figure 7.14 are line shape characterizations of etch trenches measured using a long cycle H-PDLC mask, ink jet printed transparency mask, and chrome on quartz glass mask. In Figure 7.14a, the etch profile of the H-PDLC patterned feature displays a mildly sloped wall and less refined silicon etch at the bottom of the well. More

Table 7.6: KOH Wet Etch Results- 8 hour etch

Sample	H-PDLC	Transparency	Chrome
Mean Etch Depth (μm)	30.787	30.328	32.288
Depth Standard Deviation	0.786	0.502	0.314
Mean Edge Width (μm)	28.75	30.35	28.48
Width Standard Deviation	7.548	4.237	2.472
Mean Edge Slope	1.130	1.017	1.141
Slope Standard Deviation	0.256	0.154	0.104
Exposed {111} Plane Angle (Degrees)	46.96	44.98	48.58
Error from ideal {111} Plane Angle	14.29%	17.91%	11.33%

Table 7.7: KOH Wet Etch Results- 22 hour etch

Sample	H-PDLC	Transparency	Chrome
Mean Etch Depth (μm)	107.405	106.511	112.952
Mean Edge Width (μm)	85.3	84.23	76.08
Exposed {111} Plane Angle (Degrees)	51.54	51.66	56.04
Error from ideal {111} Plane Angle	5.93%	5.71%	2.28%

pronounced are the rounded edges between the etched and un-etched regions at the top of the feature. In Figure 7.14b and c, the ink jet printed transparency mask patterned feature and the metal mask patterned feature display vertical walls and sharp contrast between the etched and un-etched silicon regions.

We have previously shown that scattering from the liquid crystal droplets in the H-PDLC mask can account for a 25% discrepancy in patterned photoresist edge profile as a result of a difference in numerical aperture of the exposure system when patterned in an identical fashion. Non-uniform positive resist masking an RIE process will yield a sloped etch as thin regions of resist are etched away faster than the thick regions exposing the substrate to additional etching in the thinly patterned areas.

7.4.4 Potassium Hydroxide (KOH) Wet Etching of Patterned Silicon Substrate

Upon completion of an 8 hour silicon wet etch, the samples were characterized using optical profilometry. In a similar characterization to features dry etched, the wet etch wafers were measured for etch trench depth and edge width. As in the previous RIE experiment, etched features were patterned with a chrome mask, a transparency mask, and an H-PDLC mask for comparison. Unlike reactive ion etch processes, silicon wet etch technique does not yield a trench with vertical walls. Rather, this process yields sloped walls as a result of the KOH selectivity between the {100} surface plane and the much more densely packed {111} plane of the substrate. The exposed {111} plane etches more slowly than the surface plane leaving an angle of 54.79^o at the interface.

Results for the H-PDLC patterned features show mean trench depth to be 30.787 μm with an edge width of 28.75 μm as tabulated in Table 7.6. The calculated {100} plane to {111} plane angle for these features is 46.96^o, which differs from the ideal angle by about 14.3%. Similar analysis shows that the features patterned using the transparency mask and the metal mask display etch angles of about 45^o and 48.6^o respectively. Difference from ideal etch angle for these features is about 18% and 11.3%. It can be seen from these results that the chrome on glass mask yields the most ideal etch angle, but the features patterned using the H-PDLC mask are very close to that of the metal mask only differing by another 3%.

Summarized in Table 7.7 is the mean trench depth and edge width of the same patterns after a 22 hour etch. The {111} to {100} plane angle for the features patterned using the H-PDLC mask is 51.5^o differing from ideal by about 5.9% while the transparency masked features and the metal masked features display angles of about 51.5^o and 56^o respectively. Following the same trend as in the 8 hour etch, the metal masked features have an angle closest to idea followed by the H-PDLC masked

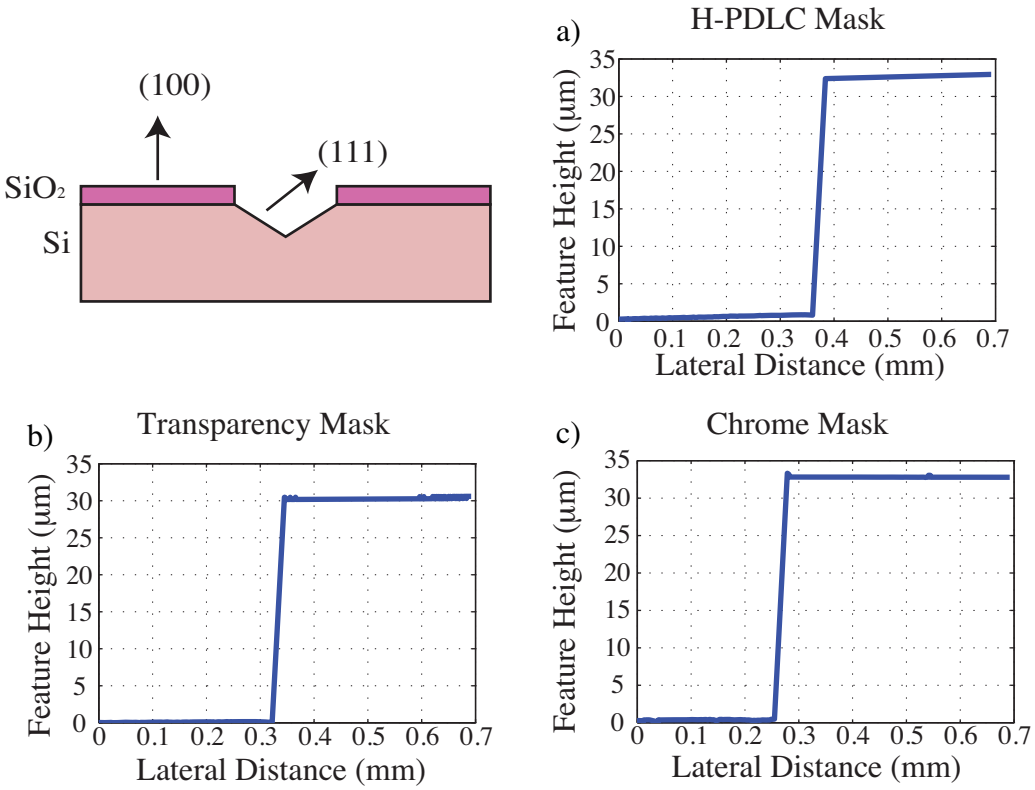

Figure 7.15: Line shape results for silicon substrate KOH wet etched for 8 hours. Lineshapes captured using an optical profilometer. a) These results show the features masked using an H-PDLC. b) This result shows features masked using an ink jet printed transparency. c) This line shape is that of a feature masked using chrome on quartz glass.

features and the transparency masked features with similar errors.

Figure 7.15 are the line shapes of the KOH 8 hour wet etches for the features patterned using the three different types of masks. Figure 7.15a is the feature masked using H-PDLC, Figure 7.15b is the structure masked with an ink jet printed transparency, and the third are the results for a structure patterned using a chrome mask. All three line shapes show an expected slope along their etch wall indicating the interface between the {111} and {100} plane.

We have shown a comparison of silicon etches for features patterned using an

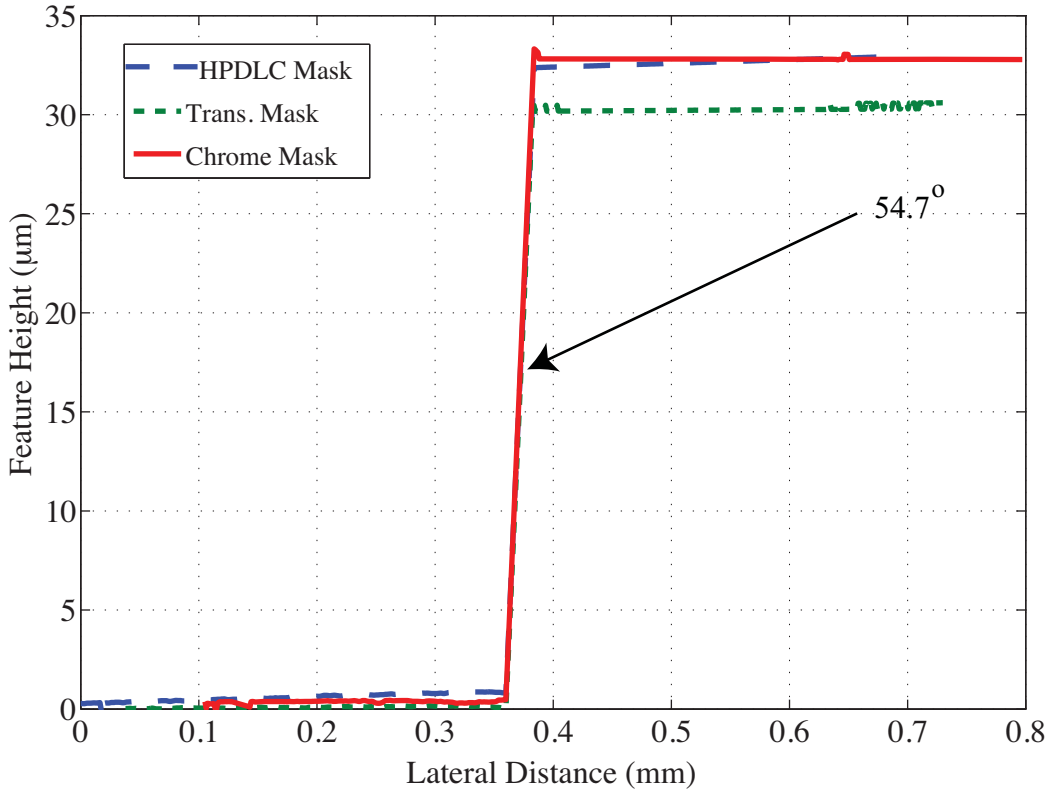

Figure 7.16: Overlay of H-PDLC, transparency, and chrome masked featured after a KOH wet etch. Lineshapes captured using an optical profilometer. The exposed {111} plane of the silicon is the predicted 54.7 degrees

H-PDLC mask, an ink jet printed transparency mask, and a chrome on glass mask using two different etch techniques. Results indicate that in dry etching the small edge slope created by the H-PDLC mask causes a slightly sloped etch well rather than the expected vertical walls. In wet etching, the H-PDLC mask performs as well as the ink jet transparency mask and only differs in etch angle by about 3% from that of the chrome mask.

To summarize, the parameters used in the fabrication of H-PDLC optimized for use as an adaptable mask are tabulated in Table 7.8. Fabrication parameters for patterning using an H-PDLC adaptable mask are summarized in Table 7.9.

Table 7.8: Fabrication parameters for optimal H-PDLC mask

Parameter	Amount
Darocure 4265 (Aldrich, Inc.)	5.00%
BL038 (EMD Industries)	30.00%
NOA65 (Norland Inc.)	65.00%
Exposure	80mW/cm^2
Technique	Prism Method (total internal reflection)
Laser	Ar:Ion 365 nm
Prism Angle	-1 degree of normal
Notch Center Wavelength	436 nm
Thickness	20 μm

Table 7.9: Fabrication parameters for patterning with H-PDLC mask

Parameter	Amount
Resist	Shipley 1813
Resist Thickness	1.4 μm
Exposure Wavelength	g-line (436 nm)
Dose Modulation	93 - 120 mJ/cm^2
Development	5:1 351:Deionized for 30 seconds

In this chapter we have shown multiple proof of device concept studies and results indicating that H-PDLC can modulate 436 nm light well enough to transmit or attenuate patterning of resist. Resist edges have slight differences when compared to a binary mask, but bulk morphology appears normal. We have also shown etch and liftoff steps using H-PDLC patterned resist. Next we examine the microscopic and propagation properties of light inside the nanostructure and its affect on patterning.

Chapter 8. Scale Pattern Structures Presentation

The next step in exploring the capabilities of this patterning device is to examine features patterned under a variety of different circumstances. To perform this next step, test patterns were etched into ITO electrodes allowing patterning of features with different sizes, on different scales, and representing light and dark field applications. We examine the approach to the calculated diffraction limit of this system, we see multiple features of differing patterns formed using the same adaptable mask, and we study structures patterned using a passive addressing scheme. Finally, we examine the effect of varying exposure dose through the thin film mask.

8.1 Materials and Methods for Scalability Study

As described in Chapter 7, part of the functionality of this device relies on patterning of indium-tin-oxide electrodes around which the H-PDLC can act as a reflecting or a transmitting element. In order to test the scalability of the adaptable photomask, a test mask was designed using AutoCad to serve as a master for patterning the ITO. Previous to this study, master masks for ITO etching were created using AutoCad or Adobe Illustrator and printed on a transparency using an ink jet printer. Although this method of creating the master works well at large, $\sim$300 μm features, scaling down quickly exceeds the resolution of the printers we have in-house for this type of activity. Commercial mask making devices such as an electron beam lithography tool can easily fabricate a chrome mask well below the resolution needed for this study, so the clear solution was to send the design out for commercial fabrication.

The design of the test mask, shown in Appendix C incorporates size scales ranging from $\sim$200 μm down below the expected resolution limit of the system, which was

calculated to be ∼25 μm. A secondary consideration of resolution went to the Karl Suss MA6 contact mask aligner that is limited to about 2 μm of patterning size. The test mask was designed to create ITO patterns behaving like light field and dark field areas meaning that in certain areas the film is primarily transparent, patterning scaled cutouts. Other regions were designed for the film to be primarily reflecting with scaled transparent cutouts. The dark field regions of test mask were also designed to have individual control over "pixels" for the purpose of demonstrating the H-PDLC mask's dynamic capability. Finally, the mask was designed to have 100 and 50 μm grating lines for passive addressing. For closer inspection, the test mask design is recreated in Appendix C.

Using the commercially fabricated test mask, 3x3" sheets of ITO were coated with positive resist and patterned according to a standard procedure detailed in Appendix D. Prior to etching the ITO, the patterned positive resist was examined using a Zygo NewView 1800 optical profilometer and several resist images are displayed in Figure 8.1. These patterns in positive resist had an expected height profile of approximately 1.4 μm, it can be seen from the displayed profiles that the average height is about 1.44 μm. The four patterns shown represent light field regions of ITO on the adaptable mask, in other words the areas protected with resist will not be etched and therefore switch to create a predominately transparent H-PDLC mask with square cutouts. Figure 8.1a,b, and c show 200 μm squares spaced 200, 100, and 50 μm apart. The fourth contour map, Figure 8.1d shows grating lines 50 μm by 50 μm. HCl etch and resist strip of indium-tin-oxide was performed using a standard procedure. Etched ITO examined in the optical profilometer yielded well defined vertical edges of approximately 20 nm like the profile shown in Figure 8.2a and b.

Using the patterned ITO glass, 20 μm thick H-PDLCs were made using a thiolene monomer, BL038 liquid crystal, and UV initiator as outlined in 3.1. Gratings were patterned holographically using an Ar:Ion laser tuned to 365 nm. Power ranged

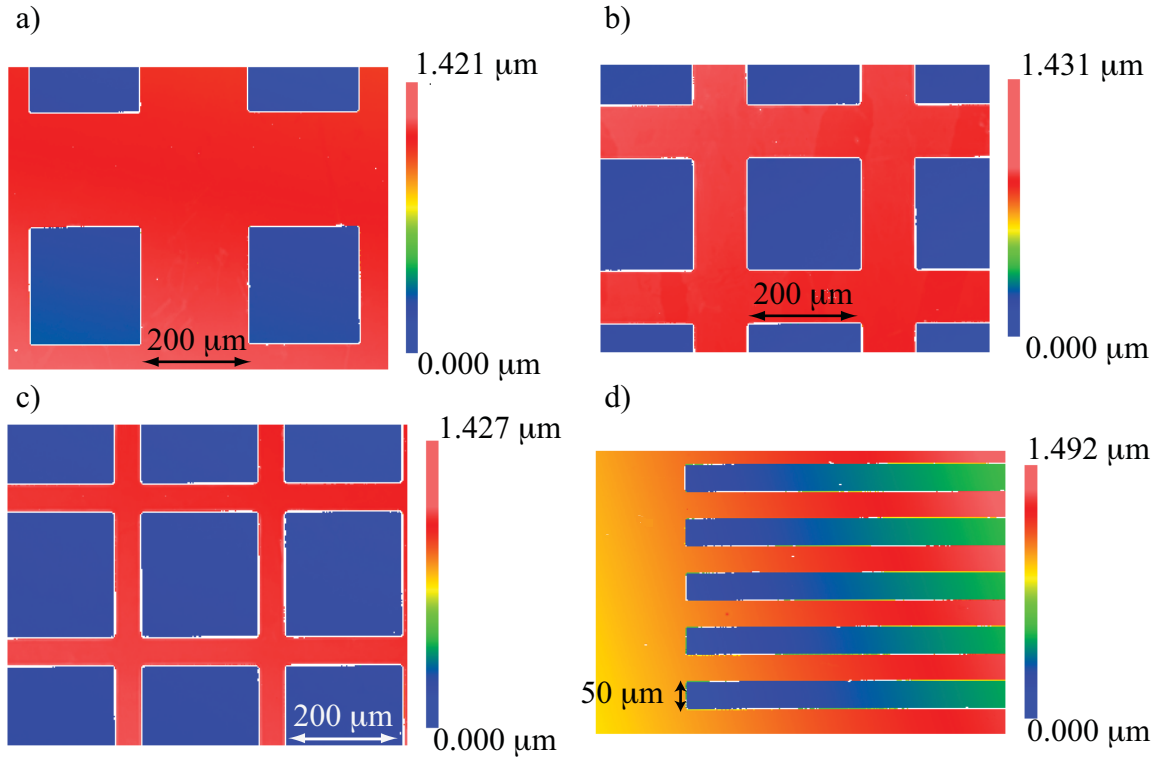

Figure 8.1: Contour maps of resist patterned using the master test mask captured using an optical profilometer. a) 200 μm squares spaced 200 μm. b) 200 μm squares spaced 100 μm. c) 200 μm squares spaced 50 μm. d) Grating lines spaced 50 μm x 50 μm.

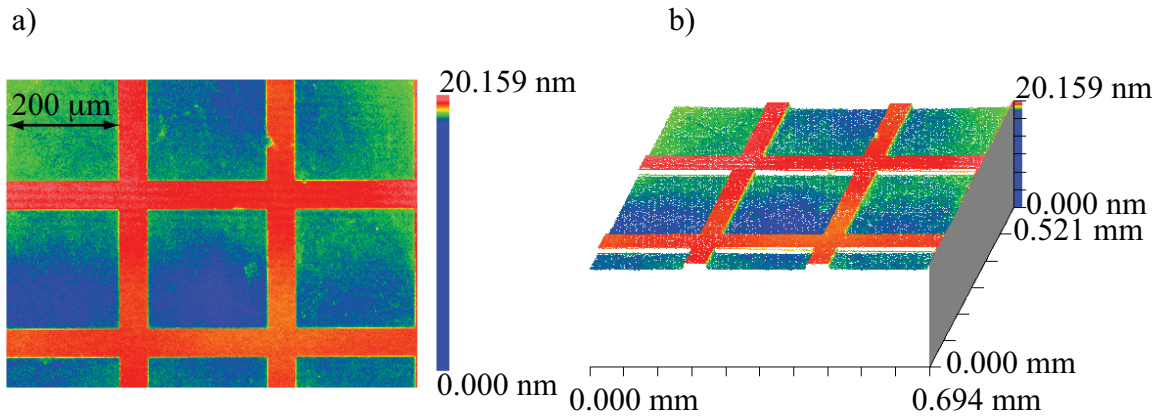

Figure 8.2: Profilometer image of etched ITO on Corning 1737 substrate. a) Contour map. b) 3D profile.

between 45 and 60 mW/cm^2 with exposure time of 45 seconds. The fabrication method most efficient for writing of gratings with a stop-band equal to 436 nm is total internal reflection or the "prism method". Using this tool, grating center stop-band wavelength could be tuned to 436 nm $\pm$1 nm with a typical diffraction efficiency ranging from 35 to 65%. Finalizing the H-PDLC masks included soldering leads to the conductive regions or securing an edge connector to access the individual solder pads for multi-pixel control.

Using the H-PDLC masks in patterning applications is very similar to the standard process used to pattern the master mask. Shipley 1813 positive photoresist was used on a microscope slide glass substrate. Expected resist thickness was 1.4 μm. The glass and resist substrate, the adaptable mask, and a spectral filter were stacked in the MA6 mask aligner. Voltage was applied to the mask areas desired to be transparent using approximately 10V/μm to complete a switch. Due to excess light loss through the film, exposure dose was increased to 30 seconds at 10 mW/cm^2. Samples were developed in a solution of 5:1 deionized water to Microposit 351 developer and observed in the profilometer.

8.2 Initial Patterning of Scale Study Structures

Initial patterning resulted in the next set of lineshapes and contour maps. Using the light field region of mask, or the region predominately coated with ITO for a maximum area of transparency, several features were captured. Figure 8.3 is the first and largest of features captured using the test mask system. This contour map shows 200 μm squares spaced 200 μm apart; the squares are designed to be cutout or stand alone pillars. It is important to note in this contour map that the glass area is clean of resist and the tops of the pillars are flat and relatively uniform, though rough compared to the chrome masked feature due to force development. Some defects are

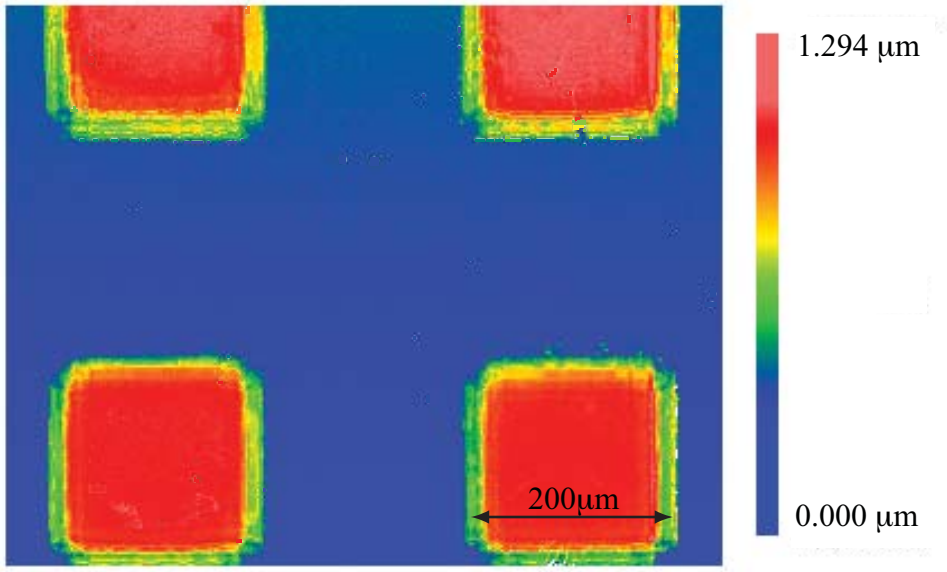

Figure 8.3: Contour of 200 μm features spaced 200 μm apart patterned using the adaptable mask imaged using an optical profilometer.

seen around the edges of the squares.

Figure 8.4a displays the lineshapes of features patterned using a chrome mask as compared to Figure 8.4b which displays features patterned using the H-PDLC mask. Here is a better opportunity to see the defects beginning to occur at the edge of the pillar, but the shape appears to be otherwise sound with clean glass area. Note that the height is slightly reduced from the expected 1.4 μm, resist thinning is common in positive resists. The morphology of the top of resist appears slightly thinned and rough due to the force development necessary to completely develop the resist being removed.

Proceeding to a smaller feature, next examined was the 200 μm squares separated by 100 μm. Figure 8.5 shows a contour map of these pillars. Similar to the larger spaced pillars, the glass area in between is clean showing a slight defect in the center square. The feature tops are flat, uniform, and not significantly thinned from devel-

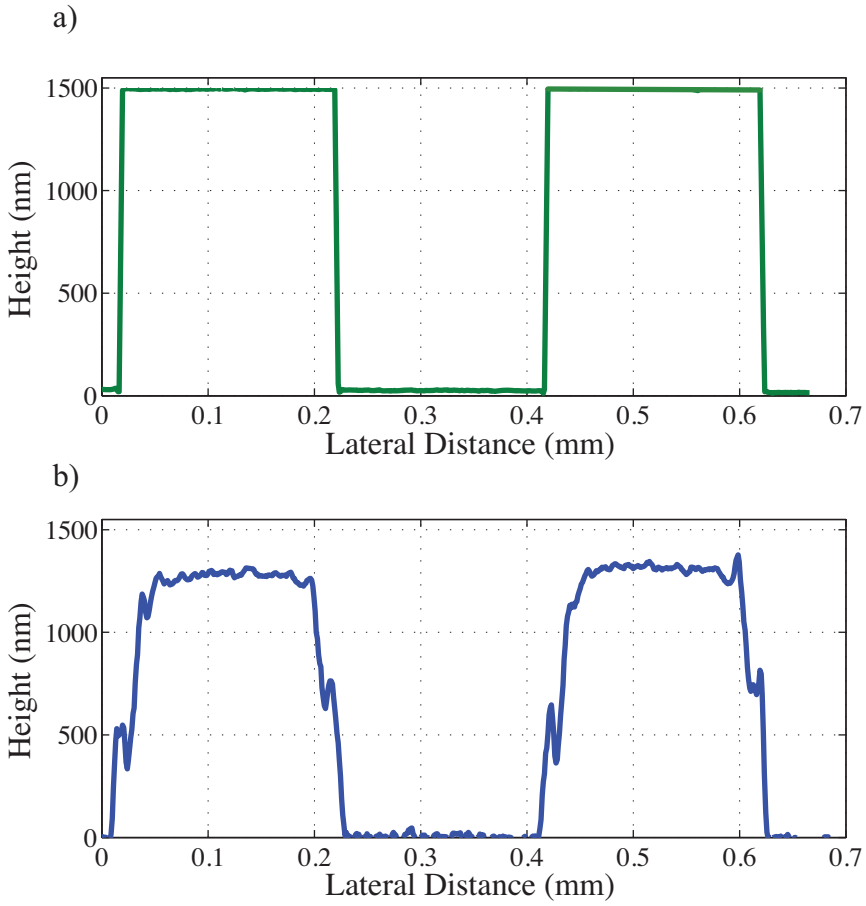

Figure 8.4: Comparison of lineshapes of 200 μm features fabricated using a chrome mask and the H-PDLC mask lineshape captured using an optical profilometer. a) Chrome patterned resist. b) H-PDLC patterned resist.

opment. Again, also seen in the larger spaced features, defects starting to occur near the edges of the squares. An important feature to note in this contour appears on the partially cut off squares at the bottom of the figure. Each pillar seems to have a line of resist parallel to its edge, the first sighting of an important artifact discussed in depth later.

Figure 8.6 compares the lineshapes of the 200 μm squares spaced 100 μm. The cross section lineshape shows the side lobe defect near the edge of the patterned

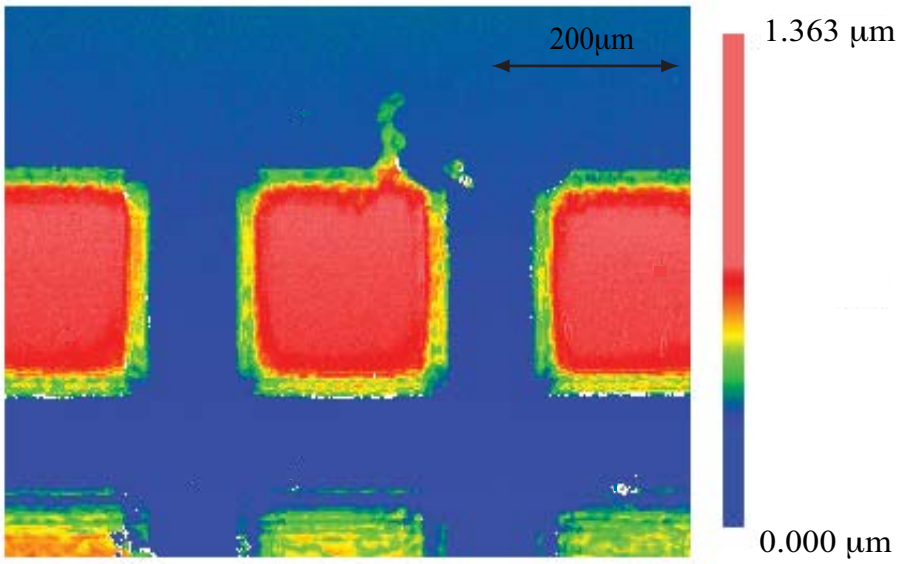

Figure 8.5: Contour of 200 μm features spaced 100 μm apart patterned using the adaptable mask imaged using an optical profilometer.

feature. There appears to be edge slope, but the glass areas are clean and the feature tops are flat and not significantly thinned from the expected 1.4 μm.

Next 200 μm features spaced 50 μm apart were fabricated and compared with an ideal replication of the master mask. Figure 8.7 shows the contour map captured by the optical profilometer. This contour map has many of the same qualities as the previous, larger features, but the thin resist line bordering the pillar is more apparent as the separation width decreases. Although this effect appears in the large 200 μm pillars, it becomes very apparent in smaller features.

Figure 8.8 is a lineshape comparison of the ideal transfer versus the H-PDLC mask transfer. As the separation decreases, it is clear to see the features begin to reach the resolution limit. Figure 8.9 is the lineshape of the same 200 μm square with only 25 μm separation. The sloping lineshapes indicate the nearing of the resolution

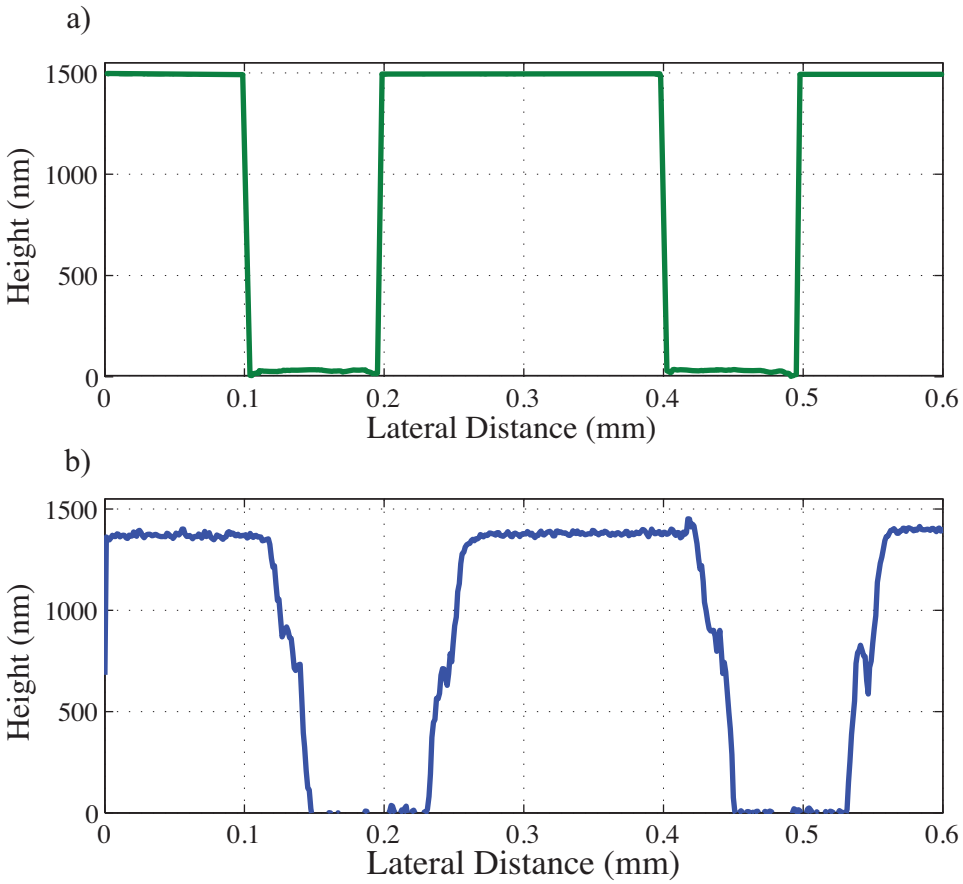

Figure 8.6: Comparison of lineshapes of 200 μm features spaced 100 μm fabricated using a chrome mask and the H-PDLC mask captured using an optical profilometer. a) Chrome patterned resist. b) H-PDLC patterned resist.

limit. Within the narrow channel, the two side lobes between features become very noticeable, these lobe correspond to the thin line of resist seen earlier in the contour maps.

Figure 8.9 is the result of patterning 200 μm squares spaced by 25 μm. Clearly the separation between features has reached its resolution limit, which was estimated at 25 μm considering the thickness of the bottom electrode and wavelength of exposure light. More importantly are the clear side lobes that seem to be dominating the channel between features. The resist is not significantly thinned, and the channel

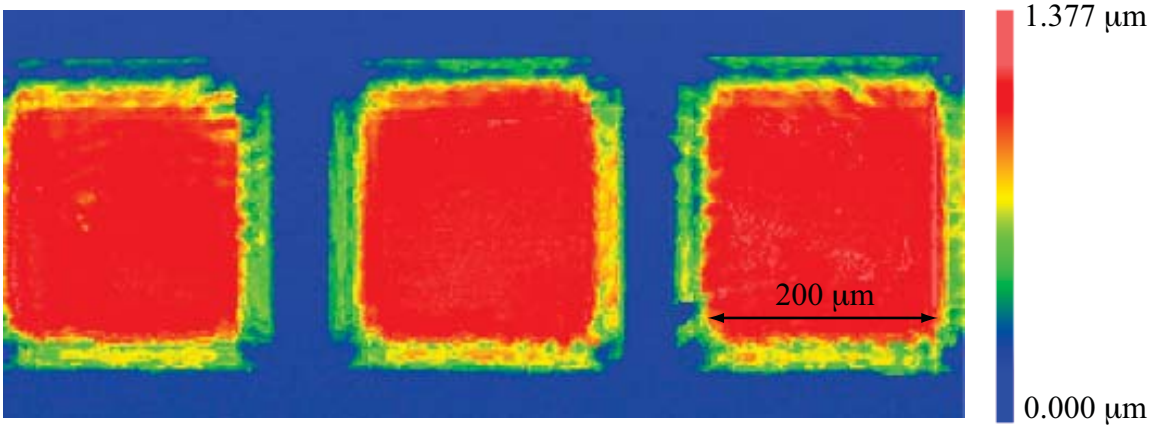

Figure 8.7: Contour of 200 μm features spaced 50 μm apart patterned using the adaptable mask imaged using an optical profilometer.

does reach the substrate in the center.

In initial patterning of 200 μm pillars with varying spaced cutouts, there is clear reduction in feature resolution as a function of channel spacing. This is consistent with the nearing of the diffraction limit of patternable features estimated at approximately 25 μm when exposure wavelength, distance of mask to resist surface, and resist thickness are taken into account. Diffraction limiting can cause the sloping of the edges seen in the four decreasing channel examples, but does not explain the existence of the side lobes visible in all four lineshapes.

8.3 Dynamic Patterning

The next test performed was a dynamic capability characterization of the thin film photomask. The layout of the ITO in the previous characterization allowed large portions of film to be switched with cutouts or regions in which the ITO was etched (light field). In order to dynamically pattern, different regions must have individual electrical control. The layout of the ITO in this characterization looks more like small

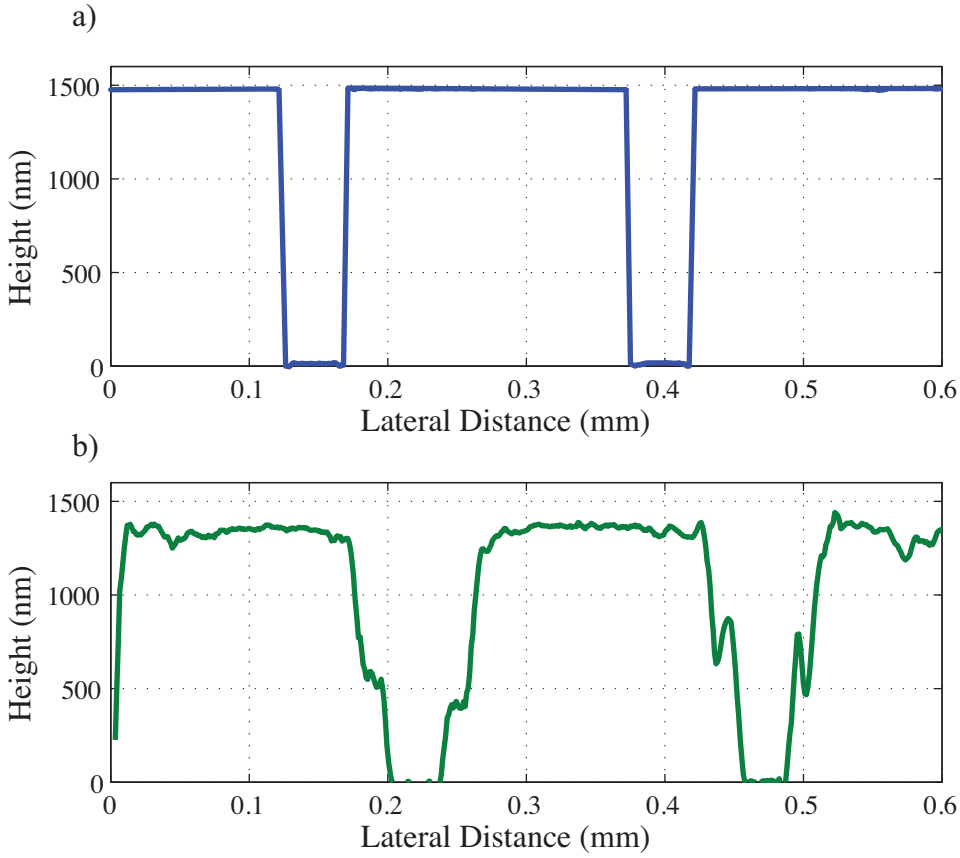

Figure 8.8: Comparison of lineshapes of 200 μm features spaced 50 μm fabricated using a chrome mask and the H-PDLC mask. a) Chrome patterned resist. b) H-PDLC patterned resist.

ITO features connected to solder pads with etched glass surrounding. It forms a dark field mask when made using H-PDLC. By activating different electrical connections, different combinations were configured.

Figure 8.10 illustrates three combinations of a set of three 100 μm grating lines. Each line is connected to its own voltage source and is therefore controllable by switching on and off the supply. All three examples were made in sequence using the same H-PDLC mask. There is some minor thinning in the resist layer in all three examples with respect to the expected thickness of 1.4 μm, also apparent is some

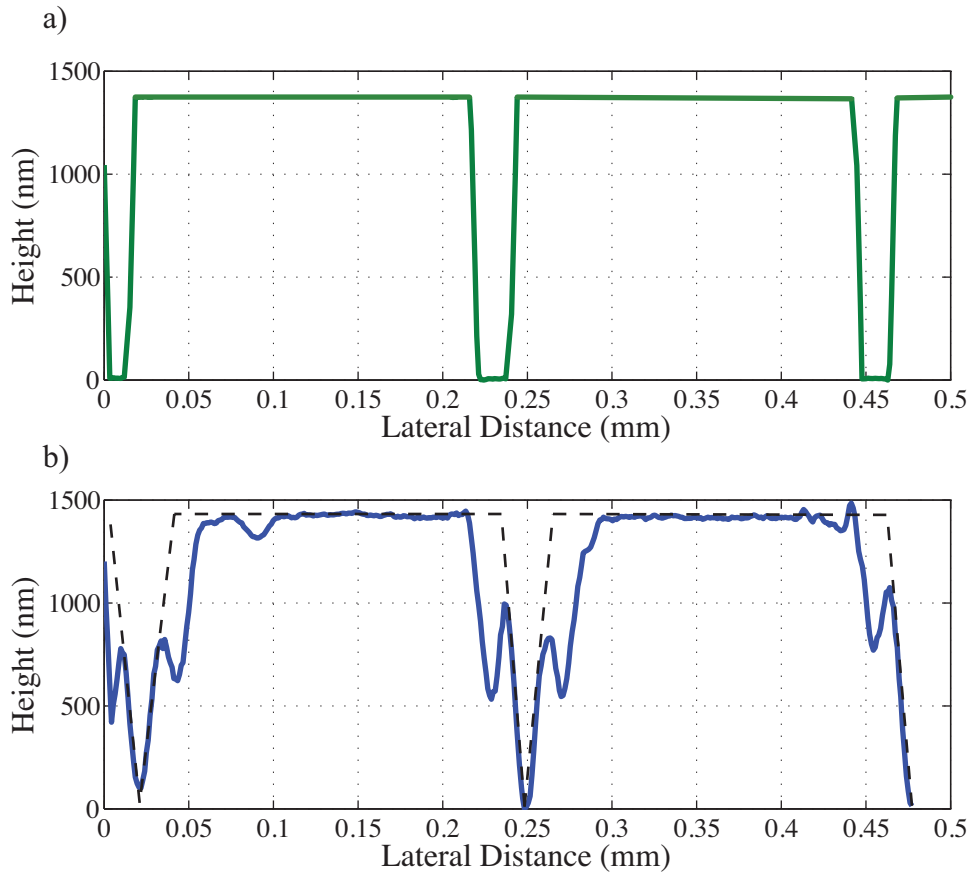

Figure 8.9: Comparison of lineshapes of 200 μm features spaced 25 μm fabricated using a chrome mask and the H-PDLC mask imaged using an optical profilometer. a) Chrome patterned resist. b) H-PDLC patterned resist with diffraction limit showing in a dashed line.

edge sloping consistent with what was previously seen. This can be visualized best in Figure 8.10d.

The next example of multiple patterns with a single mask is displayed in Figure 8.11. These individually controlled 200 μm squares can be turned on and off for many unique combinations, again these four samples were patterned sequentially using the same mask. It is interesting to see that in Figure 8.11b,c, and d there is a small amount of light leakage due to partial switching of the surrounding squares. In d, the

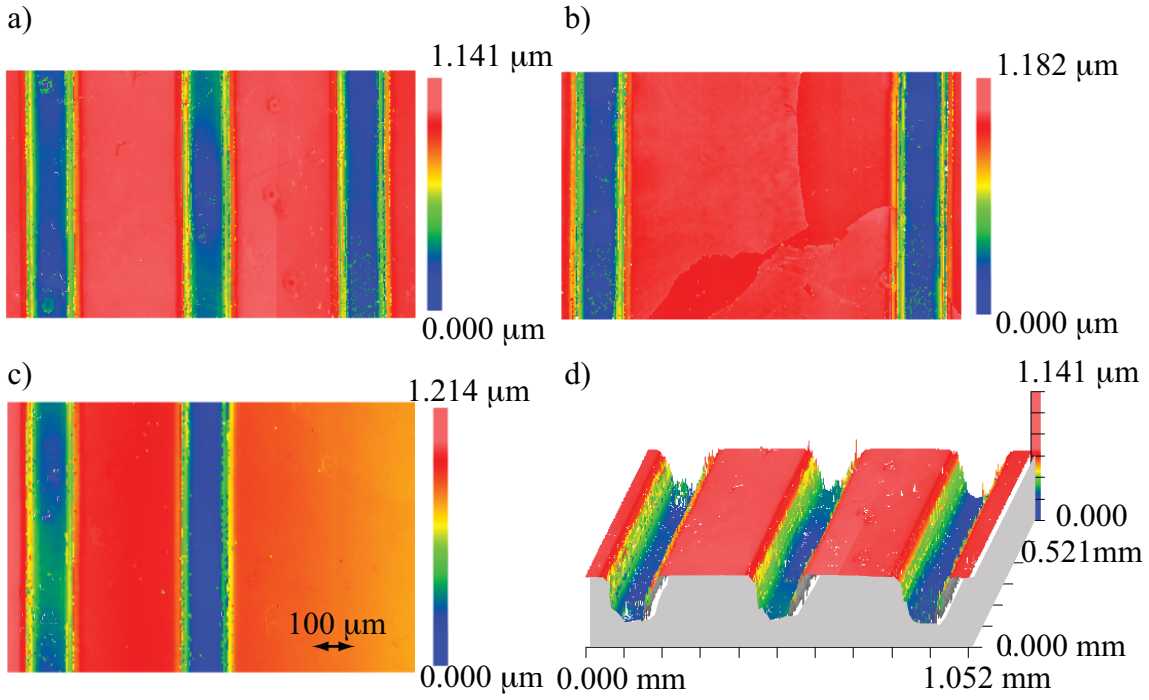

Figure 8.10: Patterning of several different features using the same mask imaged using an optical profilometer. a,b,c) Three combinations of 100 μm grating lines. d) 3D profile of grating lines.

bottom left square is maximally biased while the right two are completely unbiased. There is no evidence of any activity on the right of this sample. The top left square however, is biased at 50%, enough to allow a partial patterning. This is an example of grayscaling capability or partial patterning with partial bias.

When patterning with partial bias, the resist image is more sensitive to diffractive maxima and minima because the overall intensity within the transparent region is not enough to completely expose the resist. Maxima and minima will appear as peaks and valleys in resist. In Figure 8.11d, the top left partially patterned square clearly shows an expected diffractive pattern near the edge of the structure and the faint halo of a side lobe outside the feature.

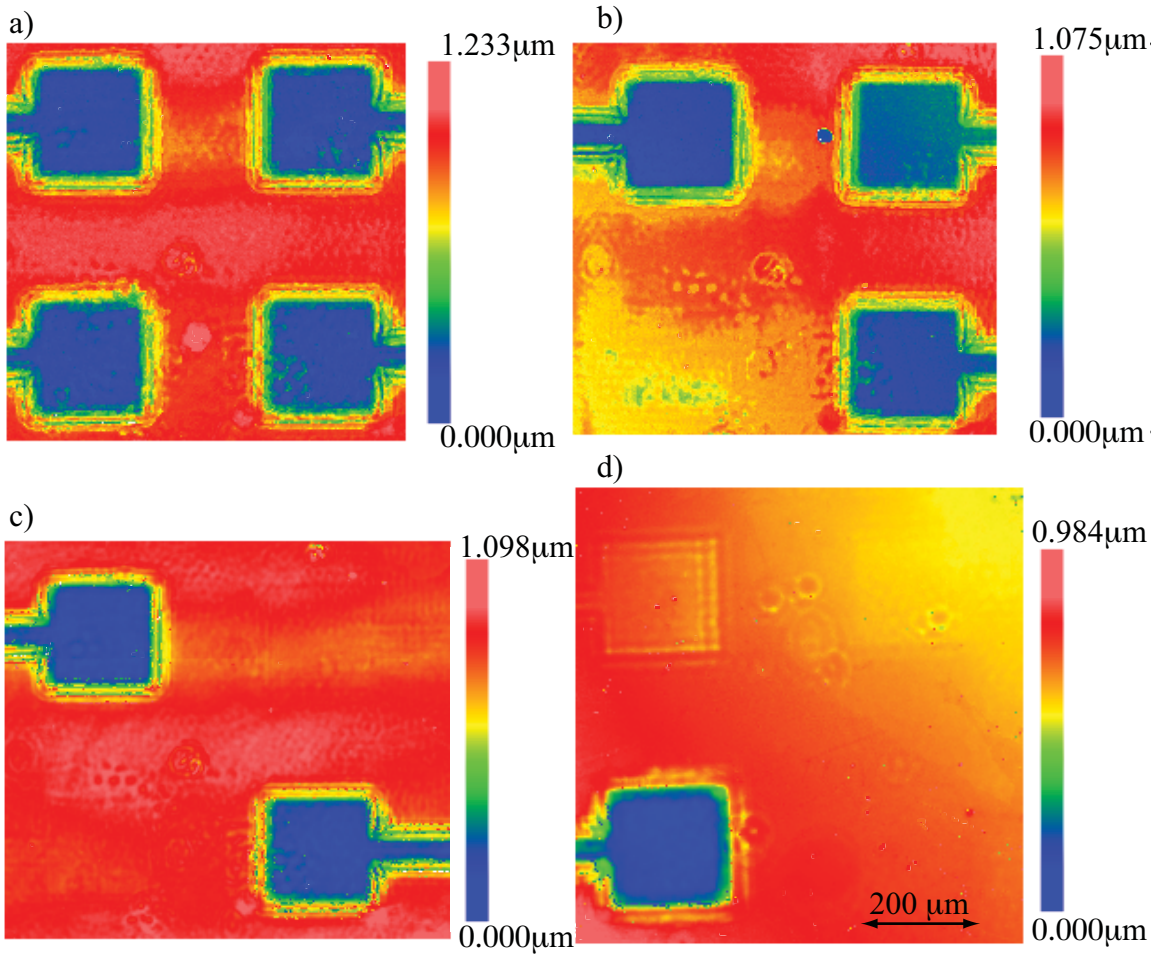

Figure 8.11: 200 μm squares. All four examples patterned using the same thin film mask. Contour maps captured using optical profilometry.

8.4 Passively Addressed Arrays

Passive addressing is a convenient method of addressing a large array of pixels when using a top to bottom electrode system. This particular method works through orthogonal rows and columns of individually electrically controlled electrodes located on the top and bottom of the switchable sample. By activating a row on the top and a column on the bottom only in the intersection of the row and column is there a large enough voltage drop to create a complete switch. There can be a partial switch in non-intersecting regions of activated rows and columns, but optimal transparency occurs only at the intersection. This system works really well for large arrays where running a trace to each pixel is space prohibitive. Passive addressing has some limitations such as the inability to create a ring structure, or a structure with a cutout in the center. Also depending on the potential of the activated rows and columns, there may be partial switching elsewhere in the array. Figure 8.12 is a schematic of this system. Figure 8.12a and b show the etched ITO forming rows and columns for the top and bottom electrodes. The gray represents ITO and white is nonconductive glass. These rows and columns can be the same pattern as long as the patterns are orthogonal to one another. The H-PDLC is fabricated on this set of top and bottom electrodes to have positions seen in Figure 8.12c. Applying bias to a row and column will cause a voltage difference great enough for a switch at the intersection of the activated row and column as shown in schematic Figure 8.12d.

Passive arrays developed using the test mask were 10x10 arrays of 100 μm squares and 10x10 arrays of 50 μm squares. Figure 8.13 is an example of a 100 μm array with all 10 rows activated. By activating a single column, the result is shown in Figure 8.13a. A second sample was patterned using the same mask but featuring a different activated column. Some partial switching occurred in columns left and right of the activated one.

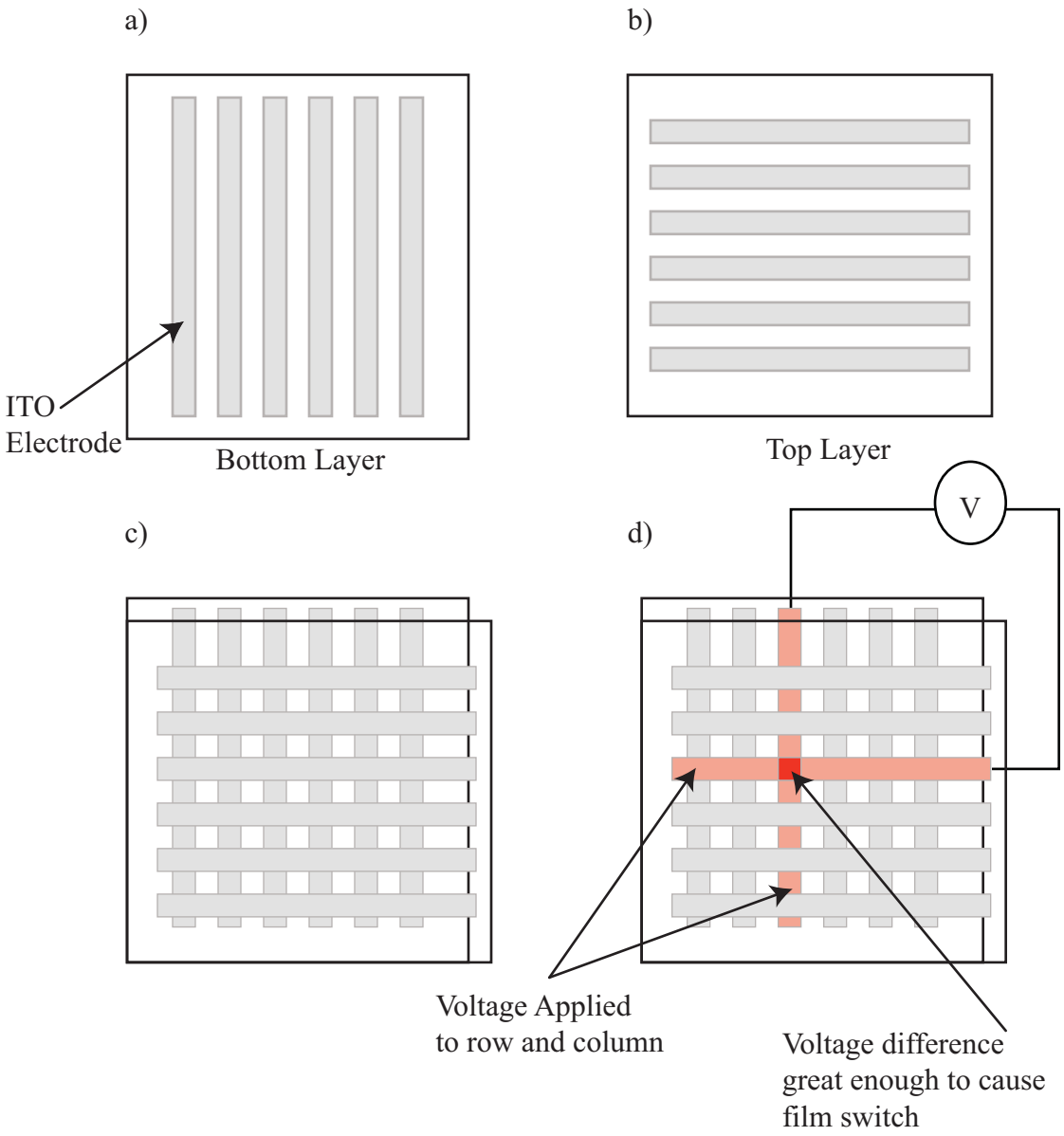

Figure 8.12: Schematic of passively addressed arrays. a) Etched ITO electrode forming columns on the bottom layer. b) Etched ITO electrode forming rows for the top layer. c) The position of the rows and columns surrounding the fabricated film. d) Applying bias to a row and column creates partial switch along the row and column, the potential difference is great enough for a full switch only at the intersection of the biased row and column.

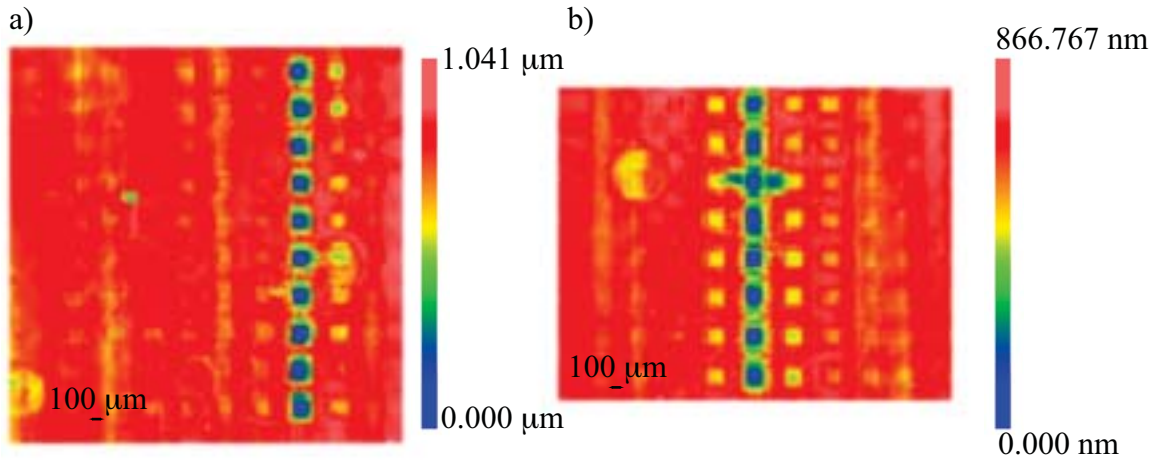

Figure 8.13: Two examples of a passively addressed array showing different rows turned on imaged using an optical profilometer.

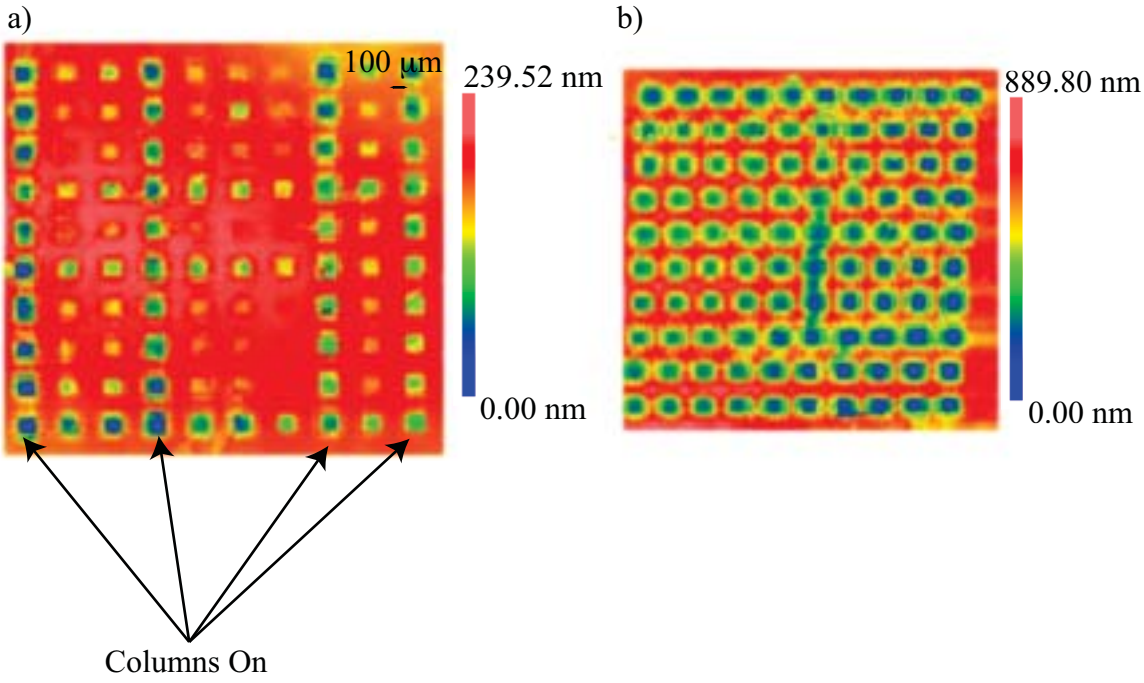

Figure 8.14: 100 μm arrays designed to show more than a single transparent column imaged using an optical profilometer. a) 10 rows and four columns activated. b) 10 rows and 10 columns activated

In the next patterned array example, Figure 8.14a, the pattern was intended to show all rows and four columns turned on but partial switching through out the sample causes many other pixels to switch or partially transmit enough light to mark the resist. Note also that there was significant thinning of the resist during this process due to force development. Figure 8.14b shows all 10 rows and columns activated to transmit. In this figure, again the appearance of side lobe marking outside of the patternable area are noticeable around all four edges of each square, as evidenced in a closer look at the pattern.

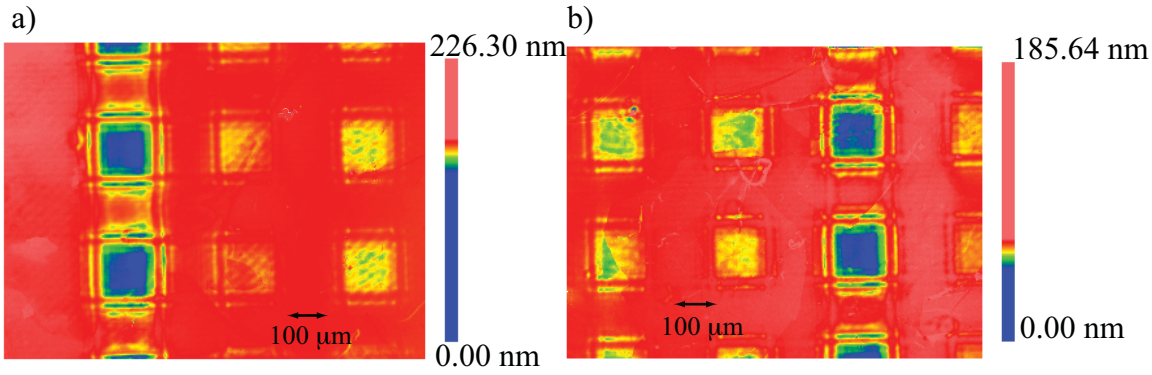

Figure 8.15: A closer look at a 100 μm array showing side lobes around the structure imaged using an optical profilometer. a and b are fabricated from a single mask with different columns activated.

A closer look at the 100 μm array elements is displayed in Figure 8.15a and b. Faint diffraction defects can be seen inside the square structure and two orders of side lobes can be clearly seen outside the square structure in these examples.

Next patterned were 50 μm passively addressed arrays. In a similar experiment to the 100 μm arrays, columns were turned on and patterned. Figure 8.16 displays contour maps of well patterned 50 μm squares. The contour map in a shows an amount of partial transmission of surrounding cells near the center; Figure 8.16b is a good example with little partial transmission. As the separation distance decreases

between features, the side lobes become very obvious, in the case of the 50 μm squares, two orders of side lobes are visible around each feature.

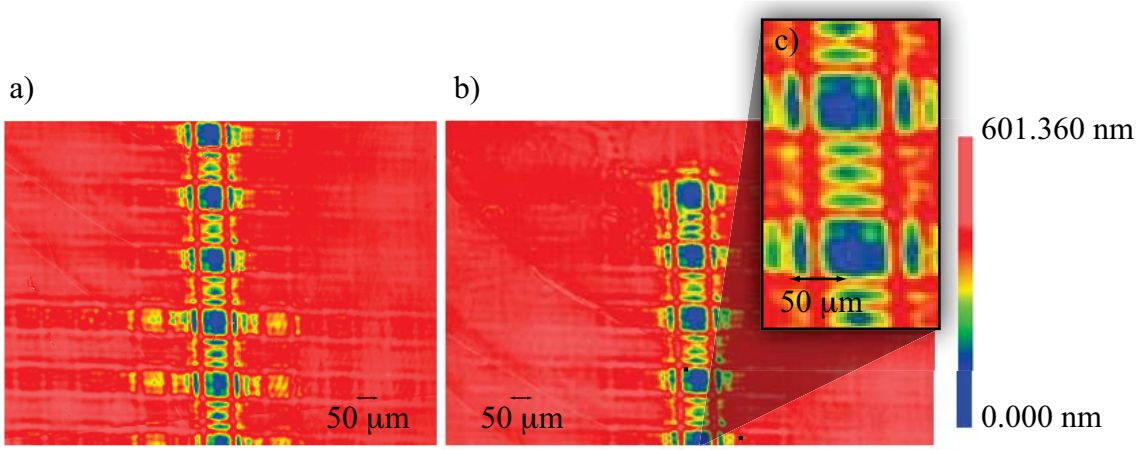

Figure 8.16: 50 μm passively addressed array imaged using an optical profilometer. a) and b) are examples of two different patterned samples. c) is a closer view of sample in b)

8.5 Exposure Dose Variance

The next experiment entailed varying exposure dose to determine the effect of dosage on patterning through the adaptable mask. Varying exposure dose can be done in a few different ways, since a mask aligner was used for these experiments, the most straight forward method of dose variance was naturally to modulate the exposure time. What is understood about dosages in positive resist relates back to the contrast curve equating exposure to resist development. To summarize, the curve indicates that after a certain energy level or threshold point the resist development is more or less linear (except for at just post-threshold exposures) until all the resist is developed away. This assumes constant developer solution concentration and development time. To measure this mapping, multiple exposures were patterned in increments of 1 second. Since the source used was calibrated to be 10 mW/cm^2, the dose variance per

second was 10 mJ/cm^2 and the samples were uniformly developed in a 5:1 solution of DI:Microposit 351 for 30 seconds.

Though many dose study samples were examined, data from two of the studies at selected dosages are presented in Figures 8.17, 8.18, and 8.19. The first pair of studies shows a 200 μm square feature exposed for 20 seconds up to 40 seconds, clearly the 20 second exposure was barely enough to develop any of the positive resist while 40 seconds shows overexposure and resist thinning. In all cases of reasonable exposure the side lobe effect is clearly visible. The next pair of dose study curves and contours details exposure of a 100 μm grating lines. The side lobes that appear in these data sets are prominent regardless of exposure, even more so than in the 200 μm features. This is an effect that we have seen before: 200 μm features show slightly less prominent side lobes than smaller sized patterns, but they are clearly present in both cases more or less regardless of exposure dose.

One of the important attributes we were interested in tracking through dose studies is the existence of the side-lobes and their relative locations or positions as a function of dose. Understanding the dose relationship to these side lobes may help in determining their origin. Tabulated in Table 8.1 and 8.2 are the locations of the first side mode with respect to the theoretical pattern boundary for 200 and 100 μm features. It is interesting to see that regardless of dose the location of the primary side lobe is essentially constant with respect to the boundary, but moves vertically in the resist. The trend seems to indicate that the higher the exposure, the deeper into the resist the side lobe presents itself. This can be seen dramatically in the 35 second exposure for the 100 μm feature where the modes are vertically much lower than the preceding exposure. According to data presented here, the side modes are positionally invariant to dose on the width axis but sensitive in height. We will see in Chapter 9 that the side lobes are a result of index mismatch at the interface which results in exposure light self interference. By varying the dose and noting that the

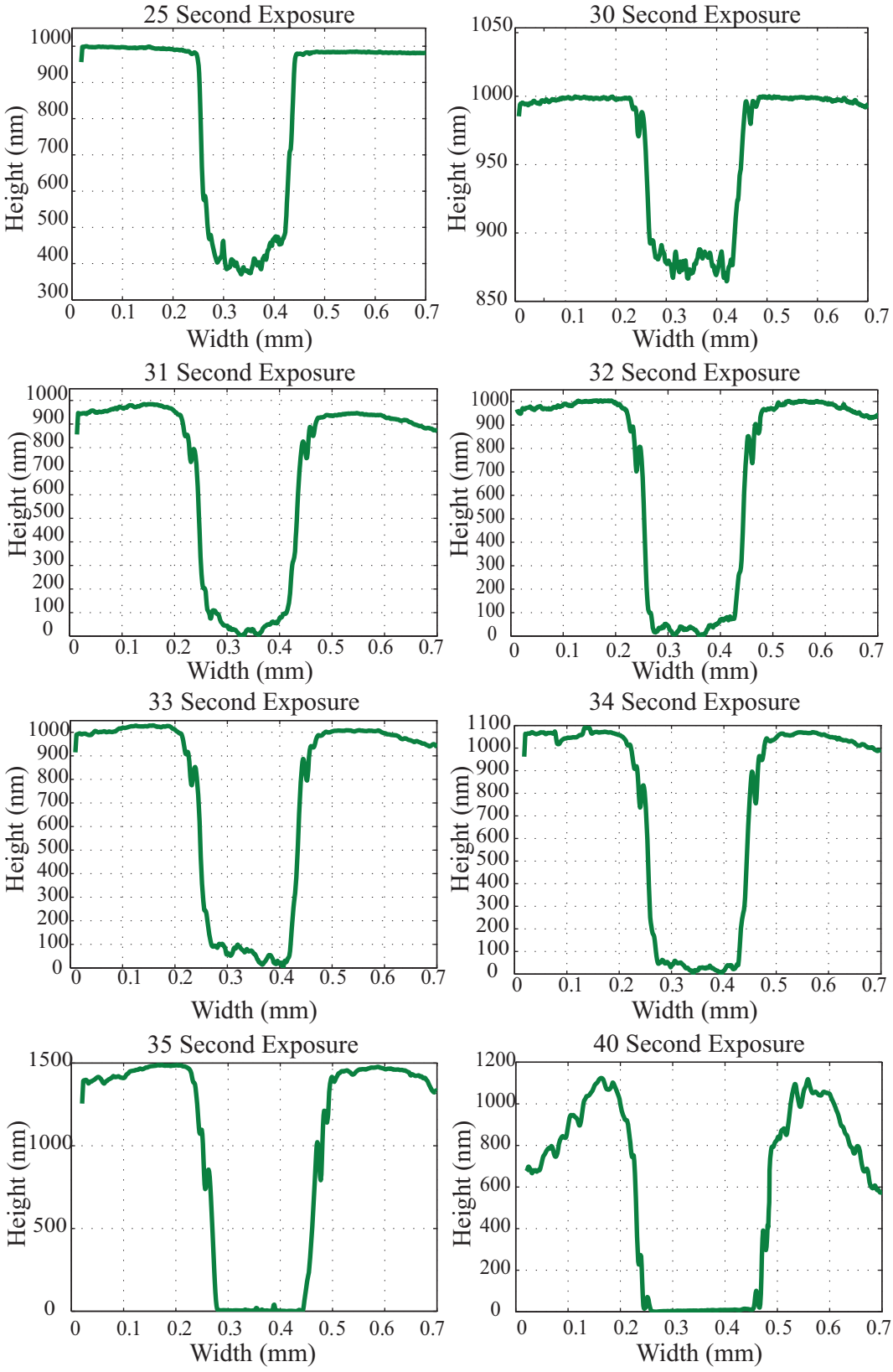

Figure 8.17: Resist lineshape as a function of exposure time of a 200 μm feature. Lineshapes captured using optical profilometry.

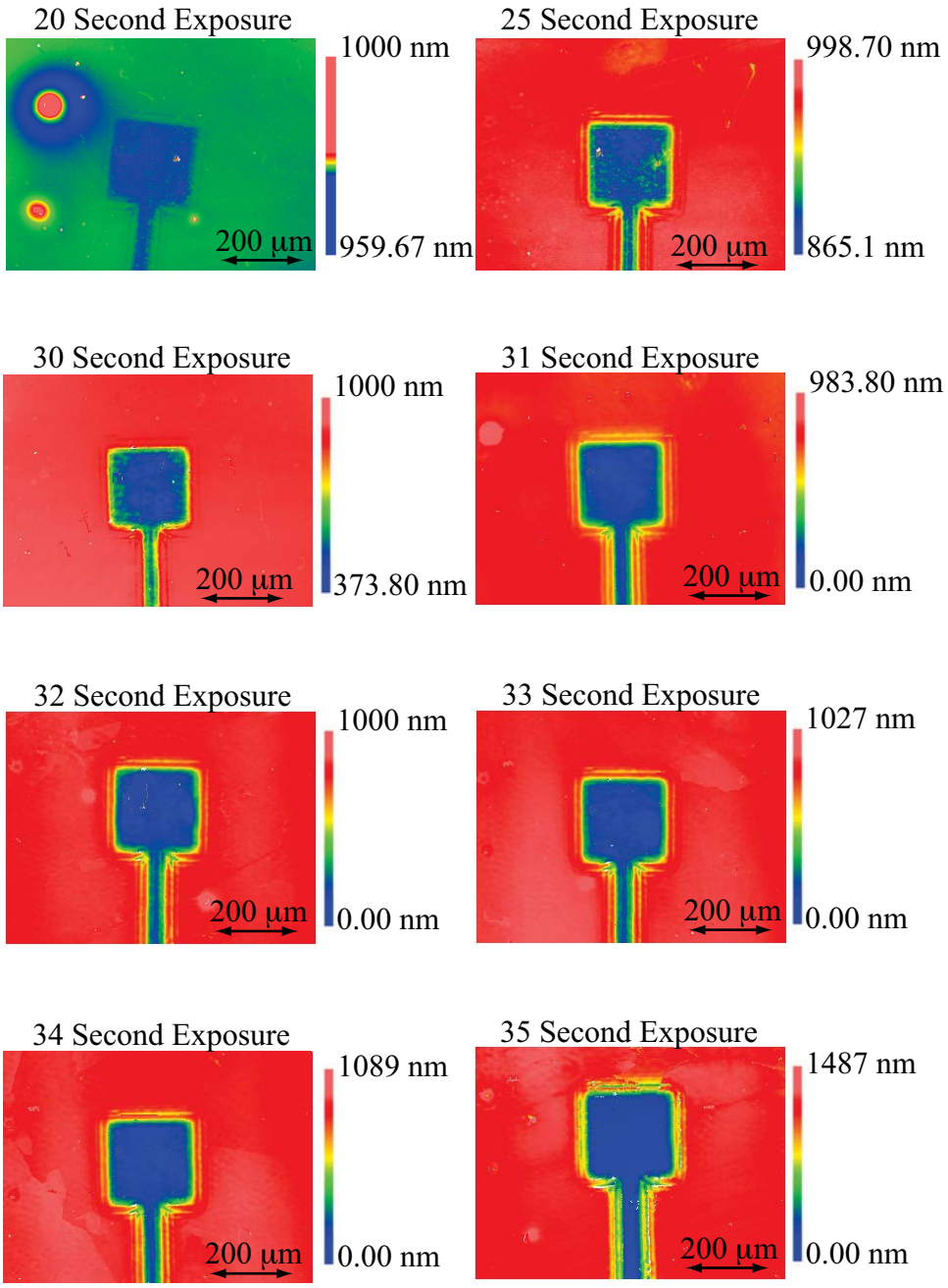

Figure 8.18: Resist contours as a function of exposure time for a 200 μm feature imaged using an optical profilometer.

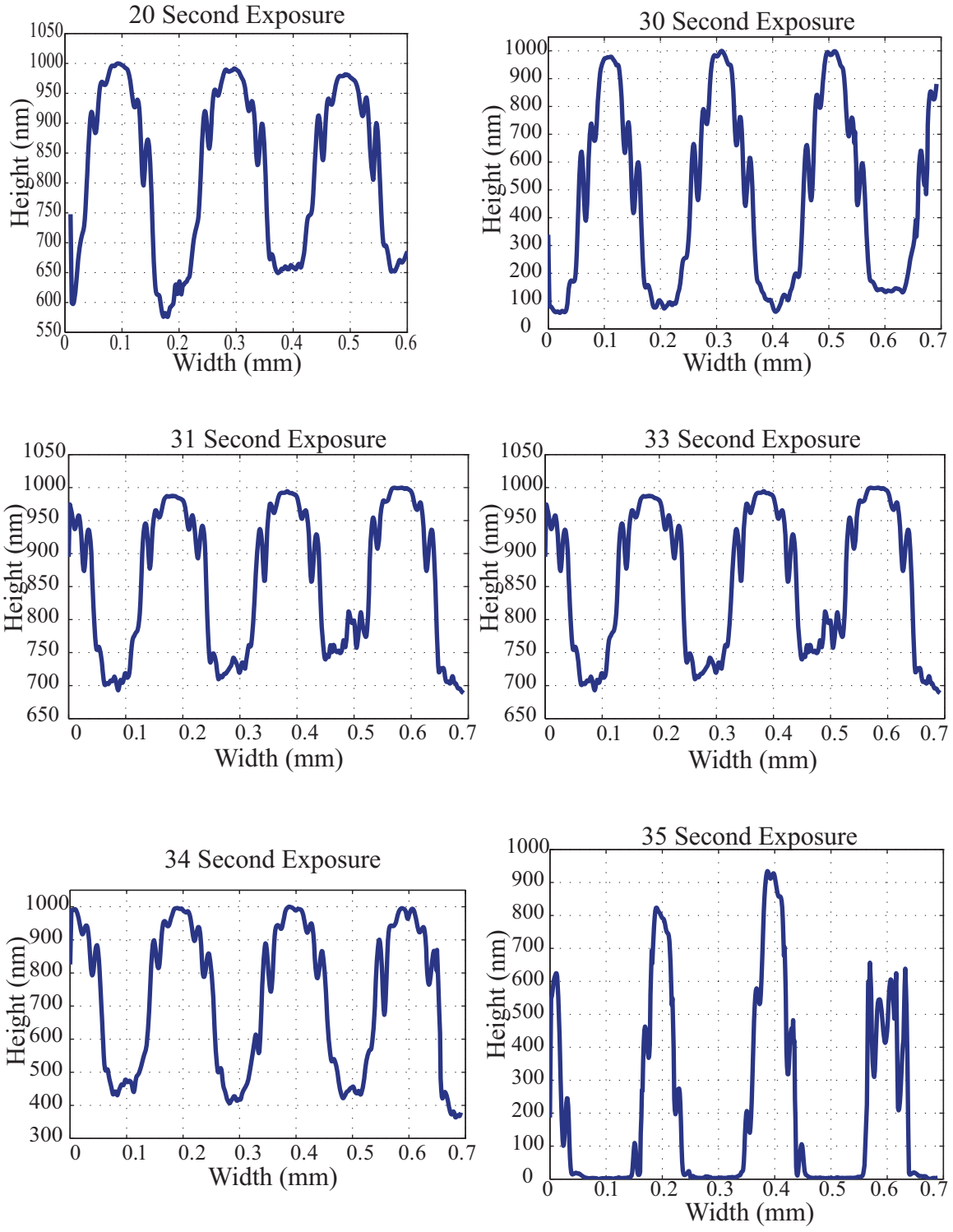

Figure 8.19: Resist lineshape as a function of exposure time of a 100 μm feature imaged using an optical profilometer.

Table 8.1: Side lobe location and resist thickness as a function of dose 200 μm

	Sidelobe Left (μm)	SidelobeRight (μm)	Thickness (nm)
25 seconds	0	0	134.9
30 seconds	2.4	8.7	629.4
31 seconds	5.4	6.5	983.7
32 seconds	6.5	7.6	1003
33 seconds	7.6	6.5	1029
34 seconds	5.4	7.5	1089
35 seconds	6.5	6.5	1486
40 seconds	7.6	6.5	1123

side lobe locations do not change, we can infer that the modes do not occur as a result of the mechanics of the patterning, but as a result of optical interaction within the film.

Height of the patterned resist is also tabulated in Tables 8.1 and 8.2. We would expect that in the underexposed situation the resist etch would be shallow, at near optimal exposure the resist would be roughly 1.4 μm, then post optimal exposure would result in resist thinning on the top surface. The series of 200 μm features follows this trend better than the 100 μm series and illustrates 33-34 seconds as the ideal dose for this particular mask. Examining the second series, it is harder to judge where the optimal dose is for this mask, which leads us to discuss the variability in grating masks.

Each grating has a slightly different attenuation band, and it makes sense to examine attenuation bands in percentage. The typical H-PDLC made for this work can modulate anywhere between 35% and 70% of total g-line light, as we have already shown. This modulation percent should be enough to selectively pattern or prevent patterning, but the dose needs to be intensity "centered" in that range such that there is excessive dose on the high side, which will not be problematic for the "on" state, but will not be modulated on the "off" side. Of course the same applies in the

Table 8.2: Side lobe location and resist thickness as a function of dose 100 μm

	Sidelobe Left (μm)	SidelobeRight (μm)	Thickness (nm)
20 seconds	7.9	6.8	424.20
30 seconds	7.2	8.3	938.32
31 seconds	7.9	7.1	937.28
33 seconds	7.9	8.6	311.50
34 seconds	8.7	7.9	633.40
35 seconds	5.4	7.6	934.60

other direction: Too little exposure will be find for the "off" state, but not enough to transmit through in the "on" state. Modulation dose study is a good way to get a sense of the typical behavior of the gratings uses here. It was found that an appropriate dose for most 20 μm thick gratings proved to be about 30 seconds or 300 mJ/cm^2.

8.6 Data Presentation Summary

In this chapter, we have presented many examples of features patterned using the adaptable H-PDLC mask. We show feature cut outs approaching the expected diffraction limit of approximately 25 μm in the first section. Valleys wider than 25 μm appear to have edge slope, but can be differentiated as illustrated above. Side lobes appear prominently in narrow cutouts. Next we show several patterns formed demonstrating the adaptability of this mask, that is, we shows multiple features patterned using the same mask with different biasing conditions. After that is a summary of 100 μm and 50 μm passively addressed arrays. Finally, two examples of exposure dose studies that detail the nanostructures response to varying transmitted light. In the next chapter, we will more closely examine and simulate the causes of defects in these patterns including the existence of side lobes. Table 8.3 summarizes the parameters studied for patterning in this thesis.

Table 8.3: Configuration Parameters Summarized

Parameter	Configuration
H-PDLC Details	
Film Thickness (μm)	20
Glass Thickness (μm)	600
ITO Thickness (nm)	20
H-PDLC Chemistry	Thiol
Liquid Crystal	BL038
Exposure (nm)	365
Formation Dose (mW/cm^2)	50
Formation Time (s)	45
Method	Total Internal Reflection
Center Stop-Band (nm)	436 nm
Formation Angle from Normal (degrees)	-1
Lithography Details	
Resist	Shipley 1813 Positive
Resist Thickness (μm)	1.4
Exposure Time (s)	30
Exposure Power (mW/cm^2)	10
Exposure Dose (mJ/cm^2)	300
Developer	5:1 DI: Microposit 351
Developer Time (s)	30

Chapter 9. Optical Transmission Analysis: Simulation and Experimental

When developing an emerging lithography technique such as the device in design here, factors that effect the minimum patternable feature size must be thoroughly examined. We have previously illustrated in Chapter 7 that edge slope of a patterned feature is dependent on the product of a term related to the mechanical properties of the resist and a term consisting of optical properties of the exposure system. When examining features identically patterned only substituting an H-PDLC mask for a traditional mask, we found an increase in edge slope. The process of eliminating resist and developer mechanical factors leads us to conclude that light propagating through the H-PDLC device yields a deviation in patterning dynamics. Here we will discuss several simulations and experiments that pertain to light transmission in the H-PDLC nanostructure and patterning limitations resulting from diffraction and interference. First we examine Fresnel Diffraction, an effect that is predicted to be a limiting factor in this system. After that we examine coherency, nanostructure scatter, wavefront, and interference as they pertain to patterning in a transmissive manner.

9.1 Diffractive Effects

The design of the H-PDLC mask in its most standard state, a configuration that consists of top and bottom electrodes encapsulating the masking film incorporates an amount of diffraction. It was discussed previously that in proximity printing, minimizing the distance from mask to substrate surface yields the highest patterning resolution. Separation between the two decreases patternable feature size with the square root of that distance value when keeping all other parameter such as wave-

length constant. The thin film adaptable mask sits approximately 600 μm, or the thickness of the encapsulating glass substrate from the masking surface introducing an amount of Fresnel diffraction into the pattern. Minimum patternable feature size or critical dimension defines a lower limit corresponding to the Rayleigh criterium of indistinguishability, but diffractive effects appear regardless of feature size as a function of the mask/substrate separation. Of course as long as the features are larger than the patterning resolution, the diffractive effects will not limit the critical dimension.

9.1.1 Fresnel Diffraction Simulations

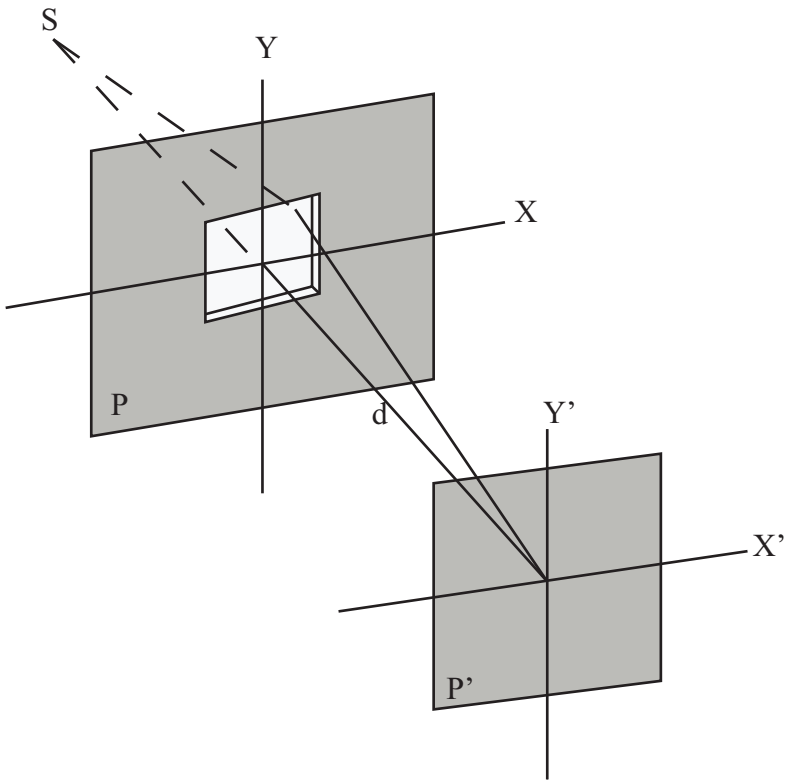

Figure 9.1: Mask plane P and image plane P' are separated by distance d. Point source S is spatially coherent. Configuration recreated from Abedin [Opt. and Laser Tech., 2005]

The H-PDLC adaptable mask device, as it is typically formed for this proof of concept work, consists of light modulating polymer film bound with glass electrodes. The thickness of the glass electrode can range from 600 μm to 1 mm. Since this work targets g-line modulation, the exposure wavelength is 436 nm. Assuming the typical 1.4 μm thick positive resist coating, the calculated minimum feature size ranges from 25 μm to 31 μm depending on electrode thickness. Rather than falsely assuming that diffractive effects do not appear at feature sizes larger than the minimum, it is prudent to build and simulate a model to visualize diffraction at different aperture sizes.

Fresnel diffraction can be calculated by employing a setup presented in Figure 9.1 similar to Ref. [70, 71, 139] where light of wavelength λ is emitted from a point source S and passes through aperture P. Transmitted light travels a distance d to the image screen. Since we cannot assume planar wavefront, we must integrate the individual Huygens -Fresnel spherical wavelet contribution of energy over the aperture area. The resulting energy over the aperture area can be written

$$E_P = \frac{E_0}{2}\left[C(u) + iS(u)\right]\left[C(v) + iS(v)\right] \tag{9.1}$$

where $S(u)$ and $C(u)$ are the Fresnel sine and cosine integrals which are defined

$$S(x) = \int_0^x \sin(t^2)dt = \sum_{n=0}^{\infty}(-1)^n \frac{x^{4n+3}}{(4n+3)(2n+1)!} \tag{9.2}$$

$$C(x) = \int_0^x \cos(t^2)dt = \sum_{n=0}^{\infty}(-1)^n \frac{x^{4n+1}}{(4n+1)(2n)!}. \tag{9.3}$$

Assuming collimated illumination a distance from point source S, u and v are defined as

$$u = x\sqrt{\frac{2}{\lambda d}} \tag{9.4}$$

$$v = y\sqrt{\frac{2}{\lambda d}} \tag{9.5}$$

where x and y are the aperture length and width variables. Intensity of this system can be plotted by solving

$$I_P = \frac{I_0}{4}\{[C(u_2) - C(u_1)]^2 + [S(u_2) - S(u_1)]^2\} * \{[C(v_2) - C(v_1)]^2 + [S(v_2) - S(v_1)]^2\} \tag{9.6}$$

Simulation code, written in Matlab, can be found in Appendix E. The result of this simulation shows the intensity lineshape and the contour image of light transmitting through varying sized square apertures at user defined distances from the image plane. The assumed wavelength is 436 nm. Intensity lineshapes appear similar in graphical style to patterned resist profiles however they are not illustrating the same concept though they can be though of as approximate inverses when used with positive resist.

It has been mentioned numerous times that the thickness of the bottom glass electrode is ultimately the limiting factor in this patterning system as it is currently configured. The original work done with the masking system used Corning 1737 glass of a slightly thicker variety. 1000 μm glass was first used to prove this concept when the sloping sidewalls were originally detected in the preliminary experiments. Understanding that diffraction effects patterning, but also that flimsy glass effects H-PDLC formation, a compromise of glass thickness was reached at 600 μm thick. H-PDLC needs to have firm bounds during its holographic formation to maintain a seal, maintain a constant sample thickness, and to prevent flowing keeping in mind that prepolymer syrup is low viscosity. An experiment in thin glass was performed using 100 μm coverslips as substrates yielded no H-PDLC formation.

To compare diffraction between two different glass thicknesses used, a simulation was performed with different thicknesses as parameters. Figure 9.2a and b are simulated intensity lineshapes for diffraction through a 200 μm aperture with 600 μm and

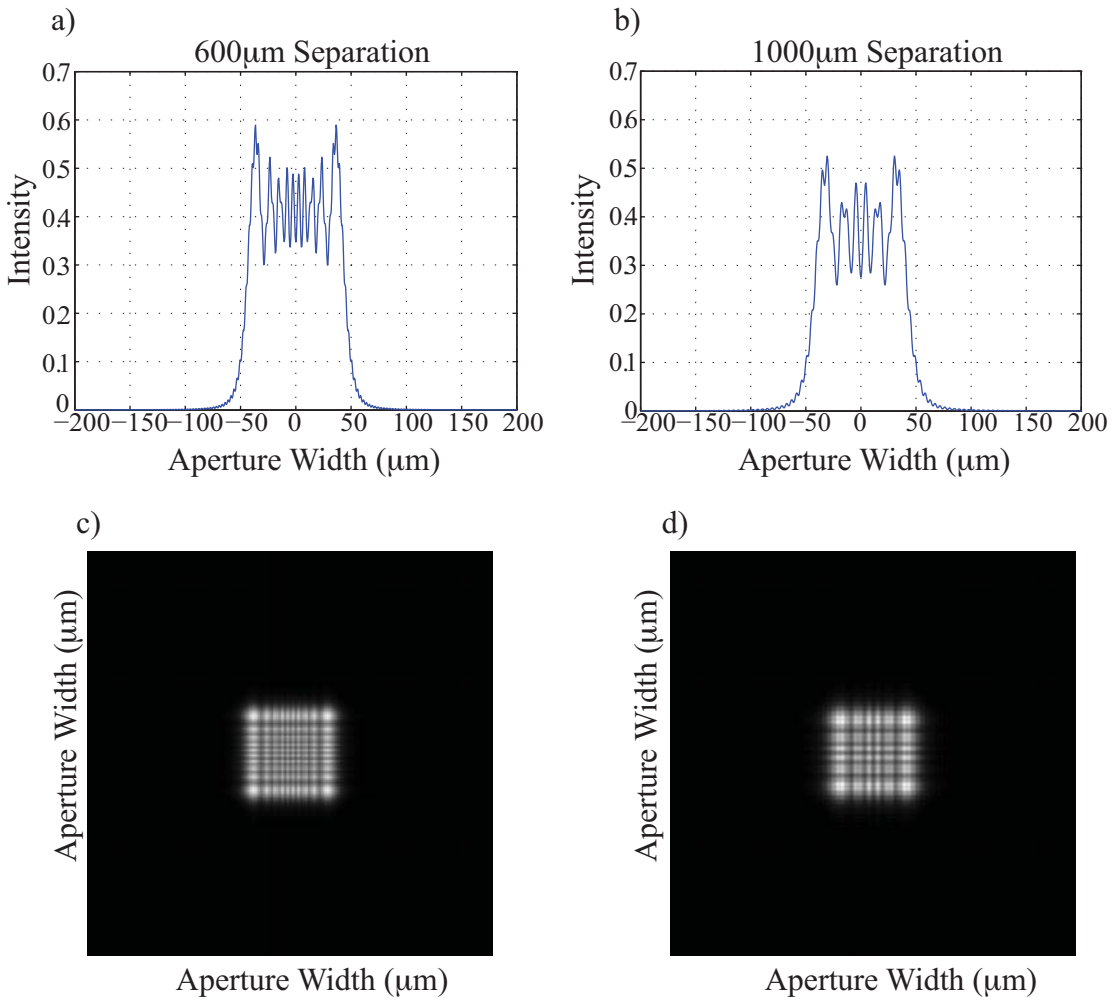

Figure 9.2: Comparison of different glass thicknesses (1 mm and 600 μm) for a 200 μm aperture

1 mm separation. Figure 9.2c and d are the intensity images of the same structure. Comparing the diffractive lineshapes to one another, it is clear to see the increase in diffraction with separation distance: the maxima and minima are more defined and the overall intensity is less. In the contour images its clear that maxima and minima exist in both cases, but the lines are thicker and more internal to the square in the 1 mm map.

Understanding the diffraction differences between the two glass thicknesses used, and assuming that samples from here are made using 600 μm thick Corning 1737, the next step was to look at the expected diffraction as a function of aperture size. Diffraction increases with a decrease in aperture size, so simulations were performed for some of the common apertures patterned in this work: 200 μm, 100 μm, and 50 μm. These simulations were performed assuming 436 nm monochromatic light at a distance of mask to image plane of 600 μm. These apertures, wavelengths, and distances meet the criterium for Fresnel diffraction. In the simulation results figures, each diffractive map and lineshape is compared with its ideal transmission counterpart. Ideal transmission was simulated using the same program calculating Fresnel diffraction, the difference being the distance from mask to image plane which was reduced to 1 nm.

We have considered and eliminated any contribution of diffraction from the top piece of glass due to its uniform index and flatness. Etching of the ITO on the top glass contributes a marginal delay difference, but it will be shown later that the primary source of delay or index mismatch is introduced in the H-PDLC.

Expected diffractive image maps are shown in Figure 9.3 for several apertures used repeatedly in this work. Naturally, ideal transmission would result in the image maps shown in a,c,e for the several apertures but the 600 μm separation between mask and image plane cause significant interference within in the area of the aperture. It is important to note, and something discussed in depth later, that outside the area of

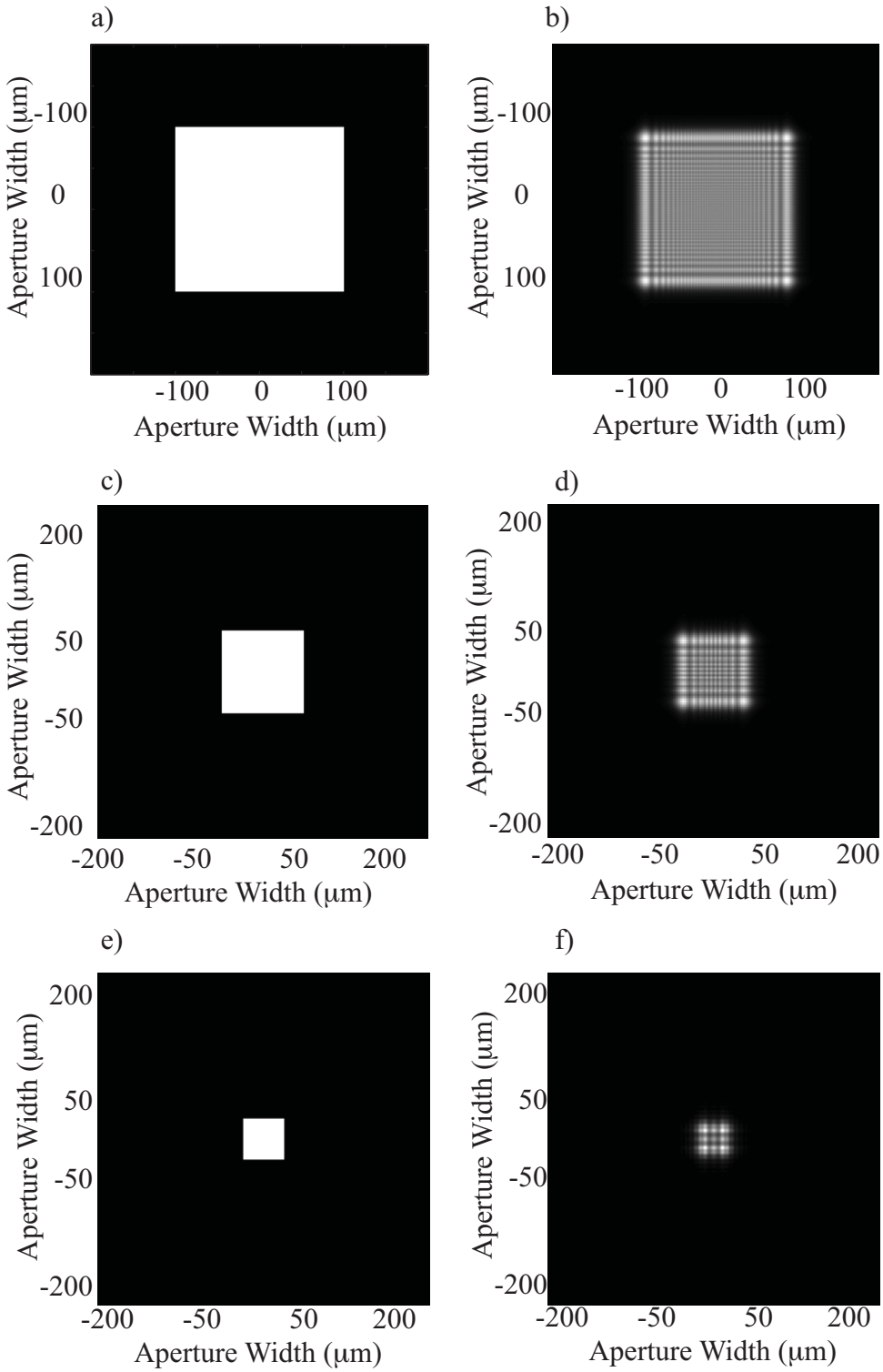

Figure 9.3: Image maps of ideal versus separated diffraction patterns for 200 μm apertures, 100 μm apertures, and 50 μm apertures. Ideal simulations were created by reducing the mask/image plane distance to 1 nm while the diffractive images are representative of the actual distance in the adaptive mask samples.

the aperture, there is no intensity profile in the simulated diffractive situations.

Simulated diffractive intensity lineshape was plotted in cross section for the same common apertures in Figure 9.4. Rather than displaying the ideal and separated lineshapes on individual graphs, the two are superimposed for comparison. Note that the ideal intensity profile extends to unity intensity for exactly the width of the aperture while the diffractive intensity profile reaches only a fraction of that and varies with aperture width. Also note that in cross section the edge of the diffractive intensity profile is sloped inward with respect to the ideal and only a small amount of light reaches outside the bounds of the aperture width even in the smallest aperture. It was originally believed that diffraction may be the cause of the tremendous side lobes appearing in H-PDLC patterned features, but the simulation shows that very little light escapes the width of the aperture as a result of diffraction.

Diffraction is the limiting size factor in photolithography, and it has been calculated and shown in Section 8.2 that the resolution of this patterning system approaches its limit as it nears 25 μm feature size. Figure 9.5 and Figure 9.6 are Fresnel diffraction simulations for apertures of 25 μm and 20 μm. The purpose of this simulation is to compare an aperture at the resolution limit size and below the resolution limit size. At apertures smaller than the resolution limit size, as seen in Figure 9.6a, there appears to be no second maximum within the aperture minimum width (20 μm) unlike the lineshape in Figure 9.5a in which the second maximum is just disappearing at $\pm$12.5 μm.

Finally, a simulation was performed to show a 10 μm aperture in this system. This aperture width is significantly below the resolution limit dominated by the 600 μm glass gap between masking surface and resist substrate. Figure 9.7 shows the intensity lineshape in a and the contour map in b, clearly from the lineshape there is no second maximum within the $\pm$5 μm aperture width, light is so diffracted by this aperture that it does not reach its first minima until $\pm$ 25 μm, much greater than the

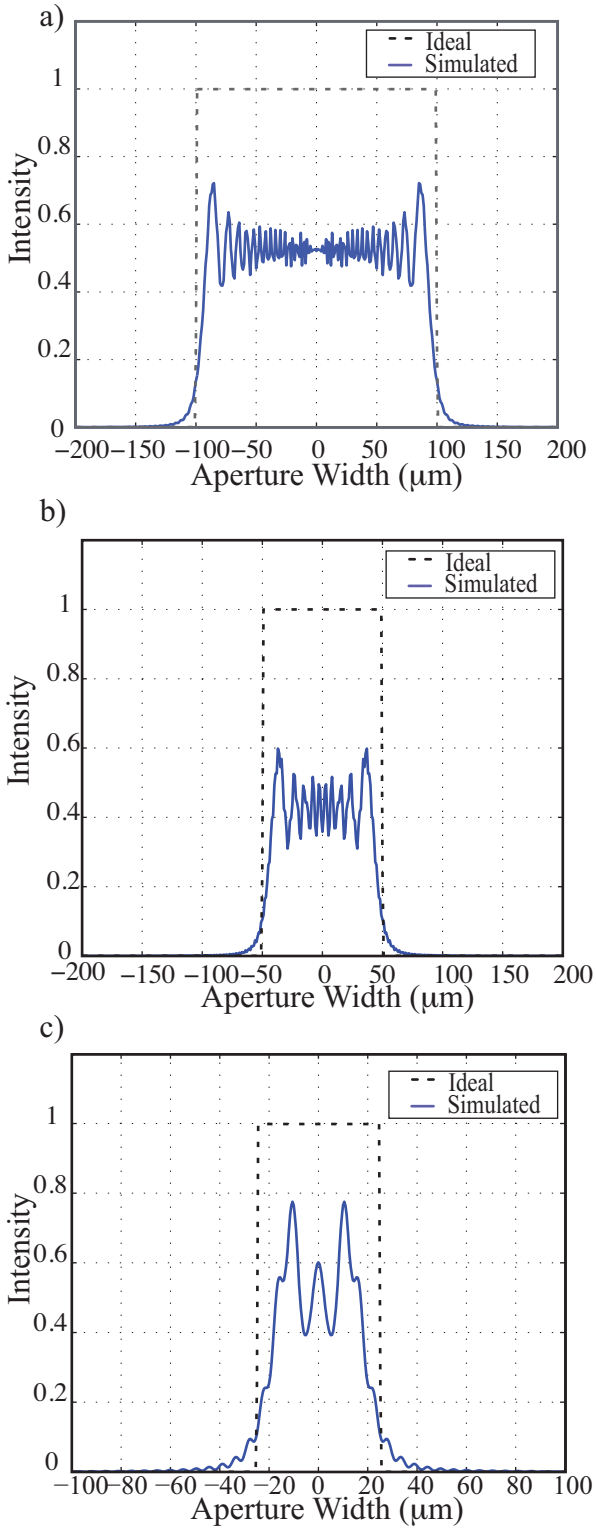

Figure 9.4: Simulated lineshapes of ideal and diffracted intensity as a function of aperture size for 200 μm, 100 μm, and 50 μm apertures. Ideal intensity lineshape is superimposed on diffracted lineshape for comparison.

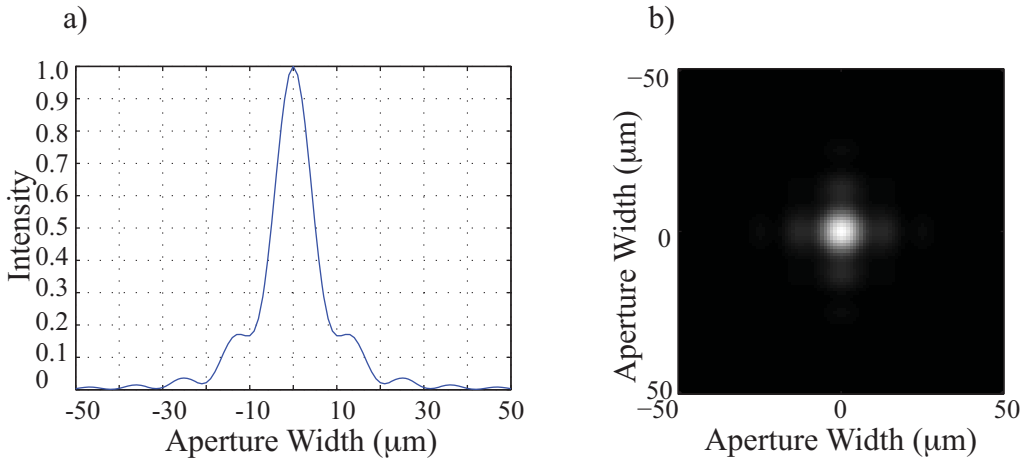

Figure 9.5: a) Diffraction intensity lineshape and b) contour map of a 25 μm aperture.

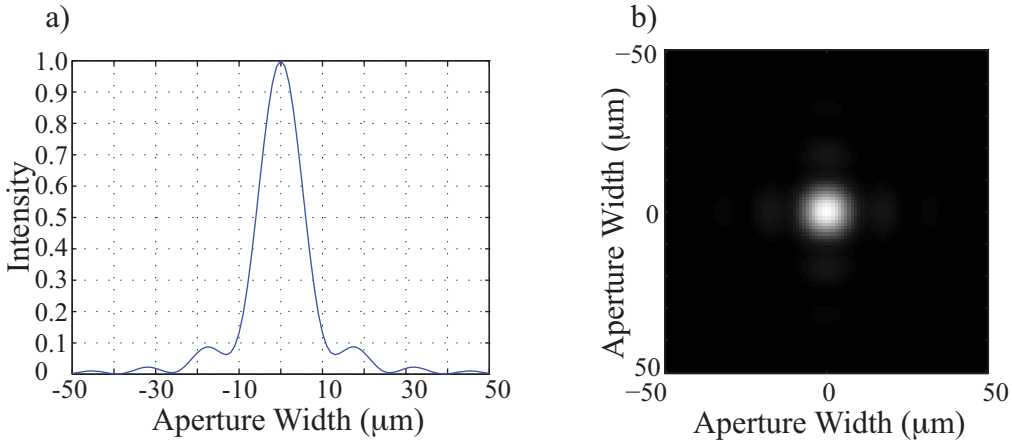

Figure 9.6: a) Diffraction intensity lineshape and b) contour map of a 20 μm aperture.

aperture width of 1 μm.

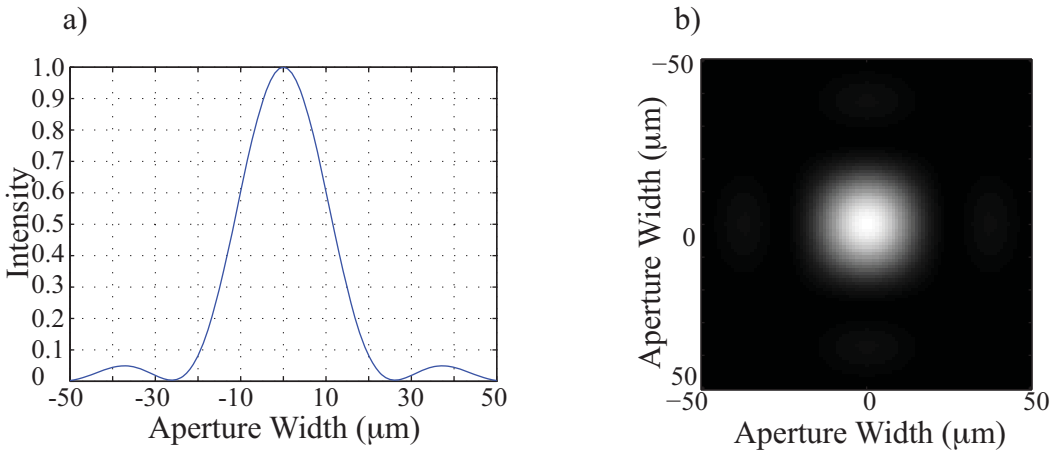

Figure 9.7: a) Diffraction intensity lineshape and b) contour map of a 10 μm aperture.

9.1.2 Chrome Deposited with Optical Adhesive Form Factor Experiments

To determine if diffraction effects were a result of nanostructure transmission or a result of the 600 μm glass thickness, an experiment was designed to replace the H-PDLC with a clear sample of similar form factor. This experiment, designed to characterize the limitations of this device brought about through structural conditions, was developed using chrome plated Corning 1737 imitation H-PDLC to have identical dimensions as an adaptable thin film mask. Using the same master test mask used to pattern ITO on Corning 1737 substrates, glass was prepared but rather than etching the ITO to form H-PDLC light blocking regions, these samples were deposited with a optical opaque layer of chrome. Lift off process was performed to create chrome patterned substrates. Masks were fabricated using 20 μm spacers and NOA65 thiolene adhesive. Using this monomer in its intended form as an optical adhesive provided not only a way to space and appropriately dimension the sample; using the very same thiolene monomer as in the H-PDLC recipe enables imaging comparison between a

layer of monomer with and without the liquid crystal droplets. The layout of this test mask device is illustrated in Figure 9.8.

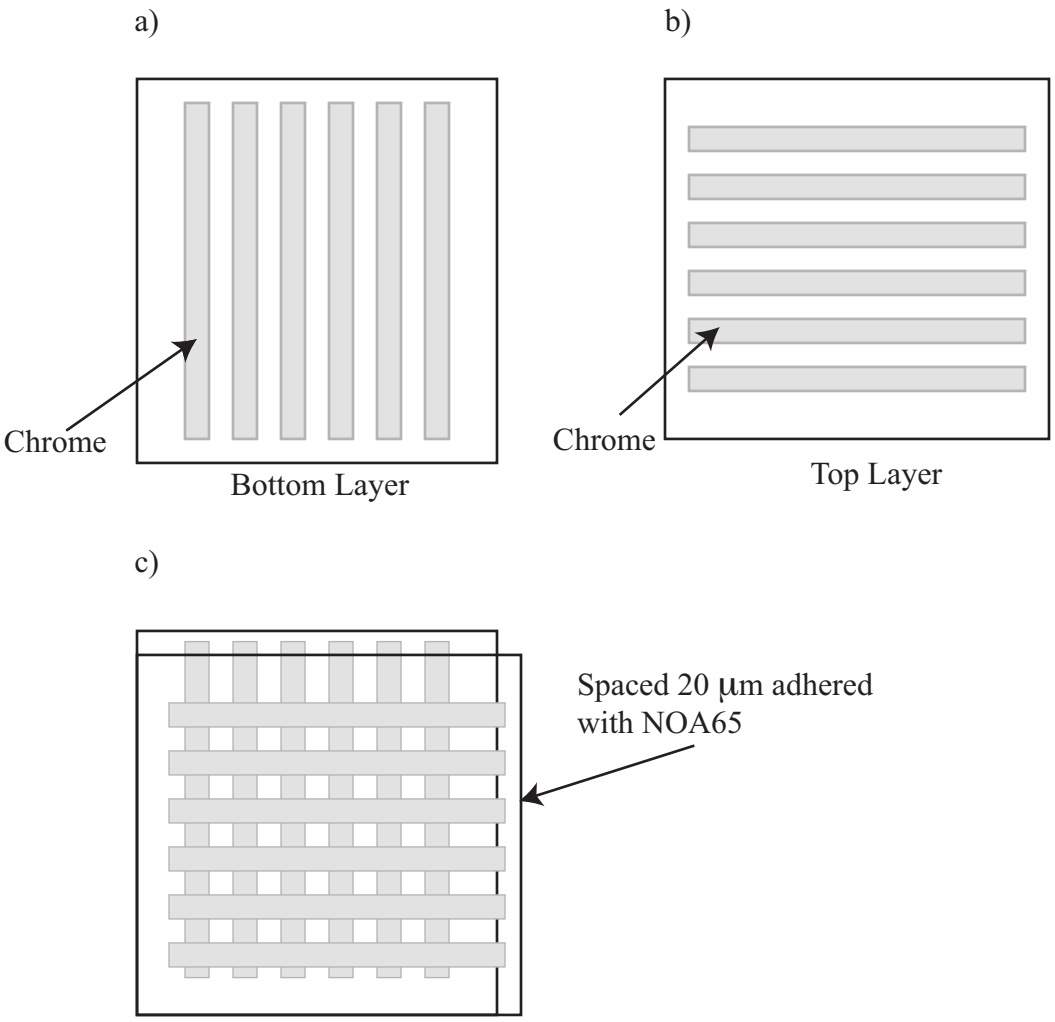

Figure 9.8: Layout of the chrome form-factor mask. a) Top electrode patterned with chrome. b) Bottom electrode patterned with chrome. c) The glass/chrome electrodes are spaced at 20 μm and adhered using NOA65 optical adhesive.

Resist samples were patterned using the chrome/thiol adhesive masks samples to verify the diffractive lineshapes appearing in the H-PDLC samples. Simulation shows diffractive effects in the Fresnel regime impact the pattern with jagged maxima and minima entirely *within* the bounds of the aperture size. Figure 9.9a shows the

simulated image of diffracted light intensity as it passes through a 200 μm aperture with a distance of 600 μm. In Figure 9.9b, the image displays resist patterned using a 200 μm aperture. It is important to note that in order to capture diffraction in resist, a complete exposure may lead to development of the diffraction lines therefore a slight underexposure is necessary to produce a slightly higher contrast. The resist image in Figure 9.9b is highly underexposed yet maintains a clear diffraction pattern.

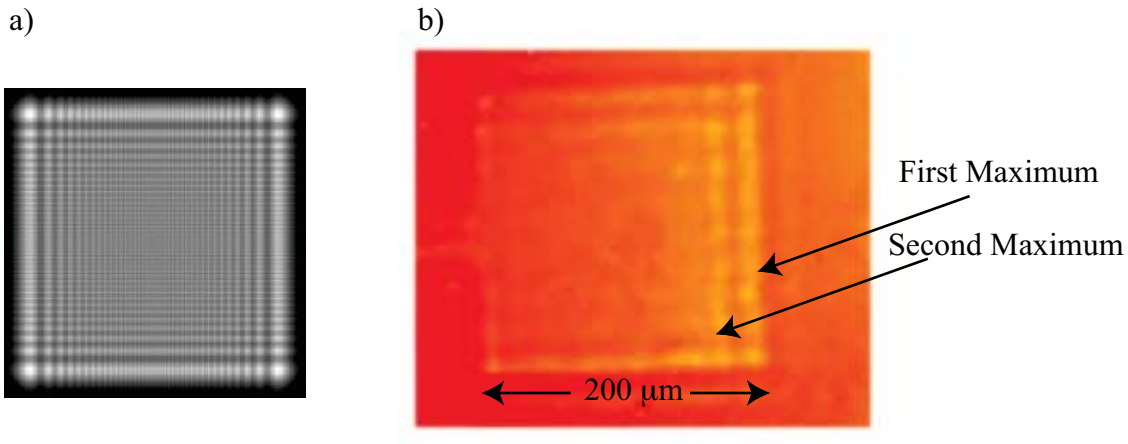

Figure 9.9: Image of simulated diffraction pattern along side of an H-PDLC patterned feature of the same aperture size. A diffraction pattern is clearly visible in the structure collected using an optical profilometer.

The need for high contrast when capturing diffraction lines is shown well in Figure 9.10. This lineshape, fabricated using 50 μm grating lines features on a chrome/glue form-factor mask created very clear and resolved 50 μm lines. The diffraction maxima and minima within the 50 μm aperture are not visible because complete exposure developed the resist all the way to the glass. Diffraction is still apparent in the sloping of the edges, but not captured between features.

A compromise in exposure dose was reached to produce the features in 9.11. Enough energy was transmitted through the chrome/adhesive mask aperture to pattern the transparent regions, but not enough to cause complete exposure. Diffraction

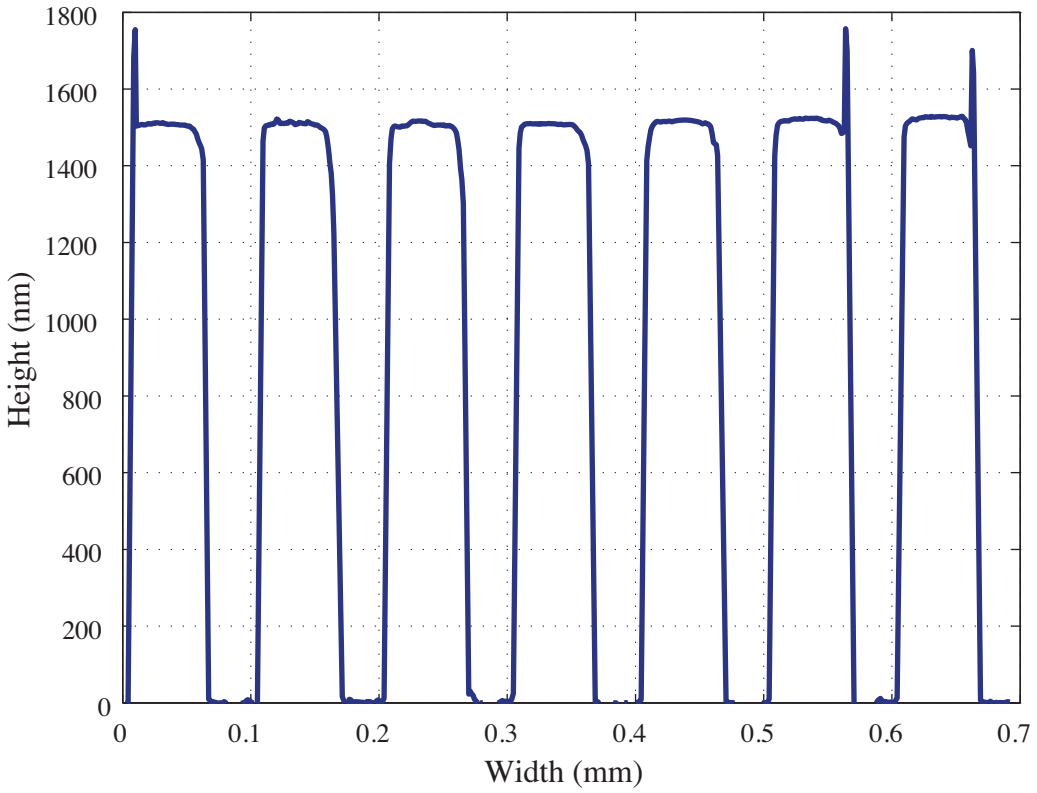

Figure 9.10: Lineshape of resist pattern of 50 μm grating lines made with a chrome mask collected using optical profilometry.

lines are clearly visible around the edges of the squares and in the traces.

Finally, a table was compiled of the peak widths of several of the maxima and minima for features patterned with the chrome/thiol mask, H-PDLC mask, and H-PDLC formed on a chrome substrate in order to quantitatively see the locations of the peaks. All features patterned using an aperture spaced a distance from the substrate should result in similar diffraction maxima and minima regardless of transmission through nanostructure or polymer. Tables 9.1 and 9.2 compare these locations and finds agreement for multiple peaks within 100 μm features and 50 μm features.

Regarding an expected amount of Fresnel diffraction caused by the electrode sep-

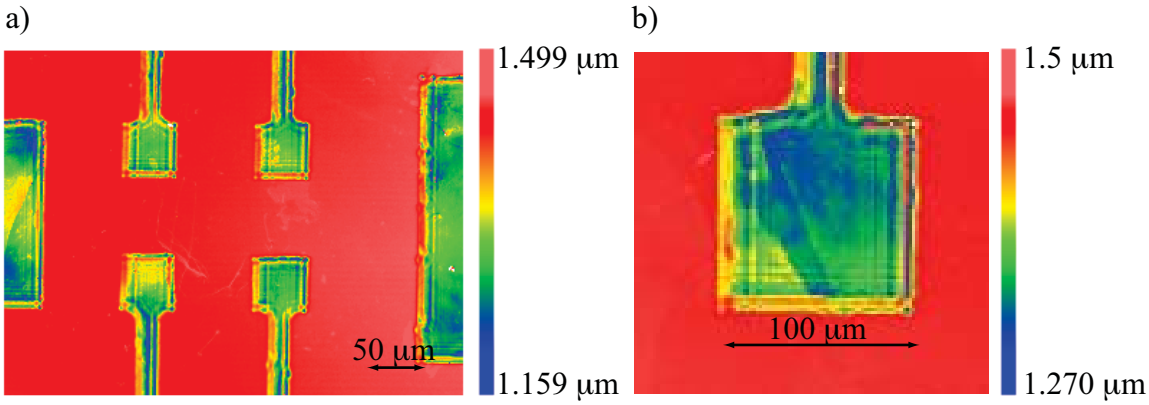

Figure 9.11: Images of features patterned using the chrome and adhesive mask. Diffraction is clearly visible in the features collected using optical profilometry.

Table 9.1: Peak widths of 100 μm diffraction maxima and minima compared with simulation

100 μm Features	Width of 1st Max	Width of 1st Min
Simulated Value (μm)	73.00	67.00
H-PDLC Mask (μm)	74.30	64.55
Error %	1.78%	3.65%
Chrome H-PDLC Mask (μm)	75.08	64.88
Error %	2.84%	3.16%
Chrome Mask (μm)	73.70	66.20
Error %	0.96%	1.19%

Table 9.2: 50 μm feature first maximum peak width comparison between simulated and measured

50 μm Features	Simulated	H-PDLC Mask	Chrome H-PDLC	Chrome Mask
Value (μm)	21.00	22.80	22.50	24.94
Error (%)	0%	8.57%	7.14%	18.76%

arating the mask from the substrate, we have shown that H-PDLC masks, as well as imitation form-factor masks of the same thickness cause nearly identical diffraction lines. These lines have been compared with a simulation of Fresnel diffraction and their maximum and minimum intensities align to within a few percent. No diffractive defects are patterned with widths greater than the original aperture, so it is reasonable to conclude that the sidelobes seen in the H-PDLC patterns are **not** as result of Fresnel diffraction due to mask/substrate separation. Though Fresnel diffraction does account for patterning defects within the bounds of the aperture. We have shown in this section that Fresnel diffraction occurs as a result of the 600 μm glass electrode regardless of whether the sample consists of H-PDLC nanostructure. The maxima and minima agree with simulated results to within a few percent. We also determine that Fresnel diffraction is *not* the cause of the side lobes found when fabricating through an H-PDLC nanostructure.

9.2 Interference Effects

It has been previously shown that Fresnel diffraction effects occur as predicted due to the distance of the mask to the substrate. These effects appear as maximum and minimum modes existing within the bounds of the aperture structure. For instance, in the Fresnel regime a 50 μm aperture will have very little transmission outside of a 50 μm width and its major maxima and minima occur at widths less than 50 μm. As the features patterned with the adaptable mask shrink in size, the appearance of large sidelobes become more and more visible and a larger percentage of the total feature size. Shown in Figure 9.12 are contours of 100 μm and 50 μm features patterned using the adaptable mask. The square patterned in the center of each figure shows the expected feature with a corresponding width while the arrows point out the sidelobe modes apparent as the features get smaller. In Figure 9.12a, the 100 μm feature, one

mode is clearly visible with the second mode partially visible. Figure 9.12b clearly shows two orders of sidelobe patterned around a 50 μm feature. Interesting to note that in Figure 9.12a the Fresnel diffraction is also visible within the center square.

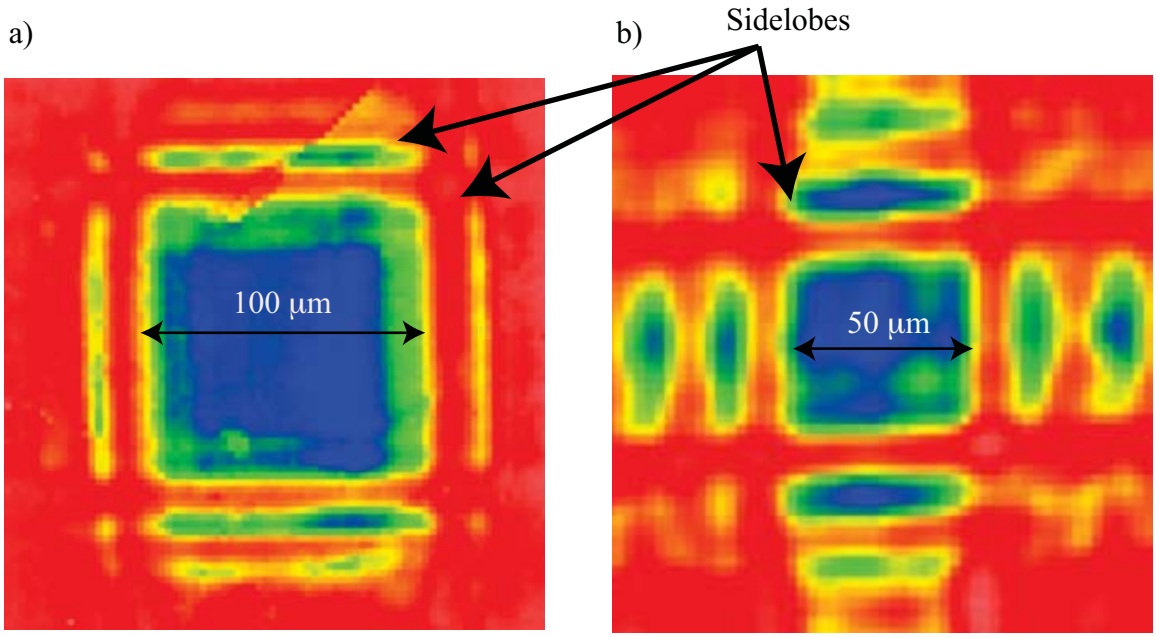

Figure 9.12: 100 μm and 50 μm features patterned using the adaptable mask. Several orders of sidelobes are clearly visible as captured using an optical profilometer. a) 100 μm feature. b) 50 μm feature.

9.2.1 Near Field and Far Field Diffraction Theory

In order to isolate the source of this effect, we discuss several potential causes. Though the diffraction simulation does not show effects larger than the aperture, it was necessary to eliminate diffraction as the cause of these patterning defects. Fresnel diffraction theory states that diffractive effects cannot occur at intervals larger than the original aperture size, the side lobes captures are outside of that bound. The rule of

thumb for determining diffraction regime is

$$\frac{a^2}{\lambda d} > 1 \tag{9.7}$$

indicates Fresnel diffraction. Assuming aperture size a as 50 μm, exposure wavelength λ equal to 436 nm, and distance d 600 μm the left side of this inequality is equal to about 9.5 which is greater than 1. So we can say that we are in the Fresnel regime, but to examine limits, we will vary first aperture size, then distance to see where this inequality begins to break down. To solve

$$\frac{a^2}{\lambda d} = 1 \tag{9.8}$$

we find that either aperture size a must be reduced to 16 μm or distance must be increased to 5.7 mm. We can conclude that light transmitting through this aperture is not experiencing far field diffraction even though the side lobe patterns in Figure 9.12 appear like a textbook far field diffraction pattern.

To experimentally verify this, using the chrome and thiol form factor test mask discussed earlier made of Corning 1737 chromed and spaced with 20 μm of thiol optical adhesive, patterned resist was fabricated and examined for sidelobe interference. This experiment showed the limitation of diffraction within the aperture width agreeing with the simulation, but did not show sidelobe interference.

9.2.2 Scattering and Chrome Plated H-PDLC Experiments

Eliminating diffraction due to the separation between mask and substrate as the cause of this effect leads us to examine the nanostructure for potential scattering or other H-PDLC related optical effects. Scattering modes occur in H-PDLC, but the angle of scattering mode maxima and minima was calculated to be much greater than the

Table 9.3: Average side mode locations for 100 μm and 50 μm features with respect to theoretical aperture edge.

100 μm Features	Peak Width (μm)
m=0	9.53
m=1/2	19.90
m=1	27.46
50 μm Features	Peak Width (μm)
m=0	8.28
m=1/2	16.67
m=1	25.10

location of these sidelobe patterns. Analysis of thiolene H-PDLC as shown in Figure 3.7 exhibits a scattering mode minimum at approximately 75 degrees from normal which would equate to a patterning minimum at approximately 2.24 mm assuming 600 μm of separation between mask and substrate. Tabulated in Table 9.3 are average mode distances for 50 and 100 μm features showing maxima and minima much closer to the interface that possibly caused by scattering modes.

Though scattering from H-PDLC nanostructure can be theoretically eliminated knowing the scattering mode angles of 20 μm thiolene gratings, it was necessary to examine this experimentally. Another set of chrome form-factor masks was made to help understand this effect. The original chrome/adhesive mask fabricated to examine separation effects did not have a nanostructure, it consisted of spaced thiol polymer to be the specific thickness of the adaptable grating mask. The second version of the chrome imitation mask was made to not only have the same form factor as the adaptable mask, but it also consisted of holographically patterned nanostructure. They layout of this test mask is illustrated in Figure 9.13.

Corning 1737 glass coated with ITO, the same glass used in the adaptable mask was patterned using the test pattern and chromed rather than etched. The first form factor mask was chromed glass spaced and adhered with thiol glue, for this second

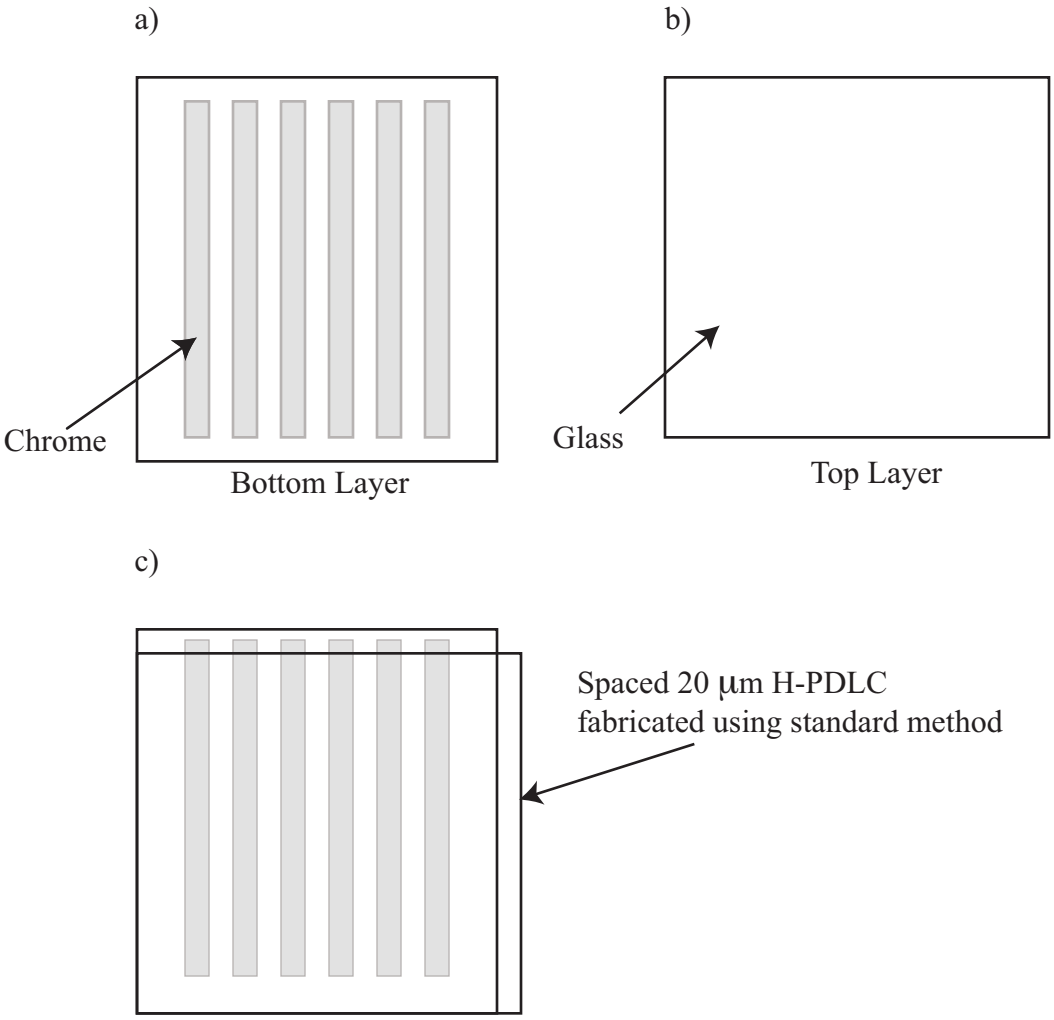

Figure 9.13: Layout of the chrome/H-PDLC test mask. a) Top electrode patterned with chrome. b) Bottom electrode transparent ITO glass. c) H-PDLC spaced at 20 μm is patterned in between.

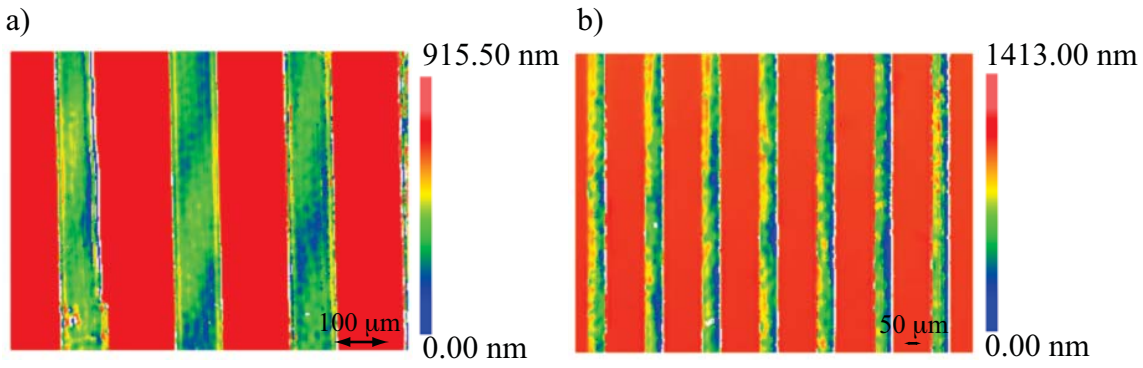

Figure 9.14: Results of patterning using a chrome and H-PDLC mask for 100 μm and 50 μm features captured using an optical profilometer. No side modes are present in either.

experimental mask the chromed glass was holographically patterned with H-PDLC mixture similar other H-PDLC films. The purpose of this mask was to have a switchable nanostructure in the clear regions of the mask, but rather than relying on the H-PDLC to attenuate the dark mask regions, the chrome blocked that light. Blocking the light with chrome in the "off" regions eliminates any potential interference that may be caused between light transmitting in the adjacent regions. Diffraction due to separation should still be apparent in fabricated features, but the appearance of sidelobes isolates the cause to something related to the nanostructure. Figure 9.14a and b show the results of patterning with the chrome and H-PDLC mask. No side lobes are present due to light propagating in the nanostructure. This indicates that side lobes are not caused by scattering or an other effect related to the spherical liquid crystal nanodomains in H-PDLC.

The result of this patterning experiment does indicate that the side lobes are related to adjacent region interference. What appears to be occurring is H-PDLC, in the "off" state allows a small amount of light be to transmitted through. H-PDLC functionality is reliant on index difference between its transparent and its opaque states therefore light transmitting through adjacent H-PDLC regions will

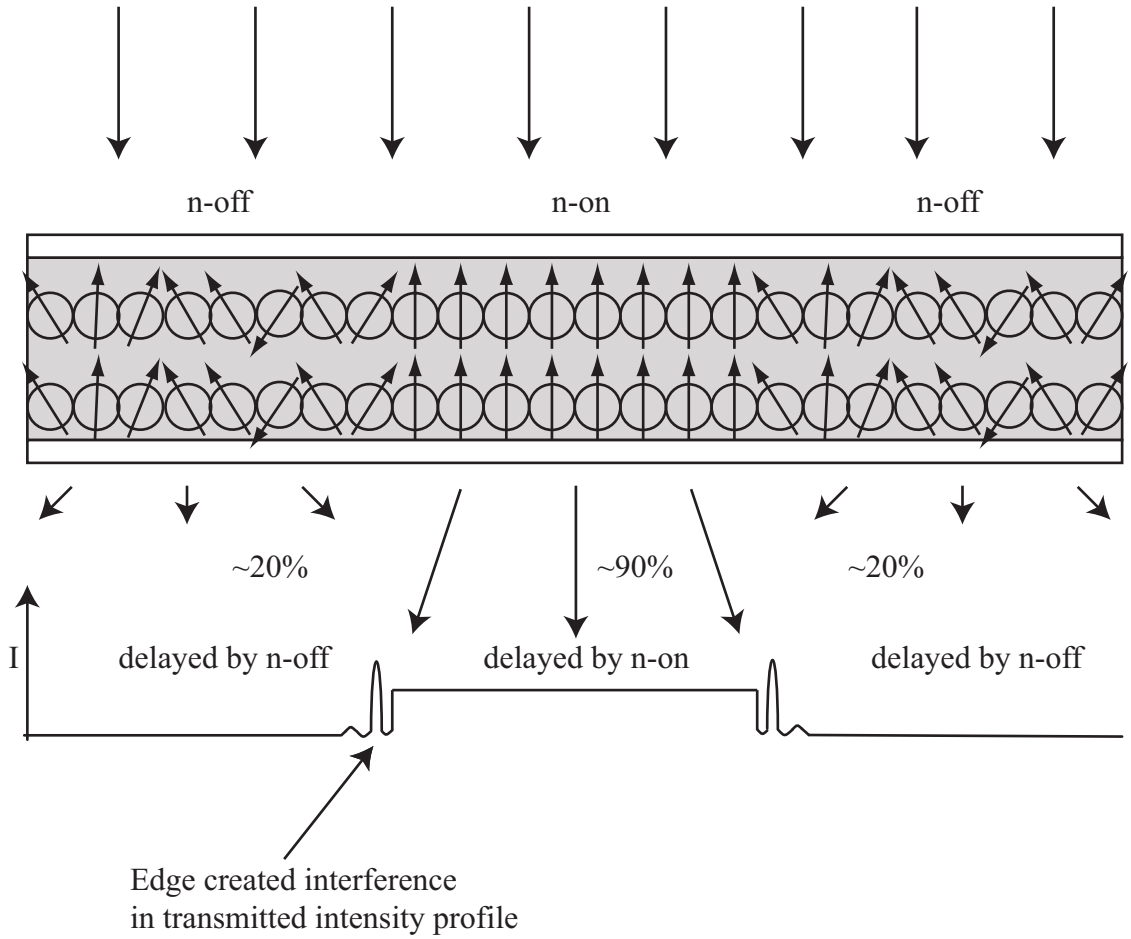

Figure 9.15: Schematic showing adjacent regions of H-PDLC with transmission through differing index. The result self interference of the exposure light at the interface between differing index regions.

have different phase delay. Exposure light self interferes with a phase-shifted version of itself near aperture edges due to the difference in bias and therefore the difference in film index. Figure 9.15 is a schematic of light transmitting through adjacent regions with differing index. Light transmitting through the regions with index "n-off" will have a different phase then light propagating through index "n-on". Interference will occur near the edges of the adjacent interfaces, which is shown in Figure 9.15 in the intensity profile of transmitted light, I.

What we have shown in this section is that light transmitting through H-PDLC, even in small apertures, does not exhibit side mode patterning without the presence of H-PDLC attenuated "off" section counterparts. Chrome attenuated neighboring regions causes elimination of side lobes, but Fresnel diffraction still exists. This leads us to further examine adjacent regions interference as the cause of side lobe interaction.

9.2.3 Sidelobe Maxima and Minima Locations Compared to Fresnel Diffraction

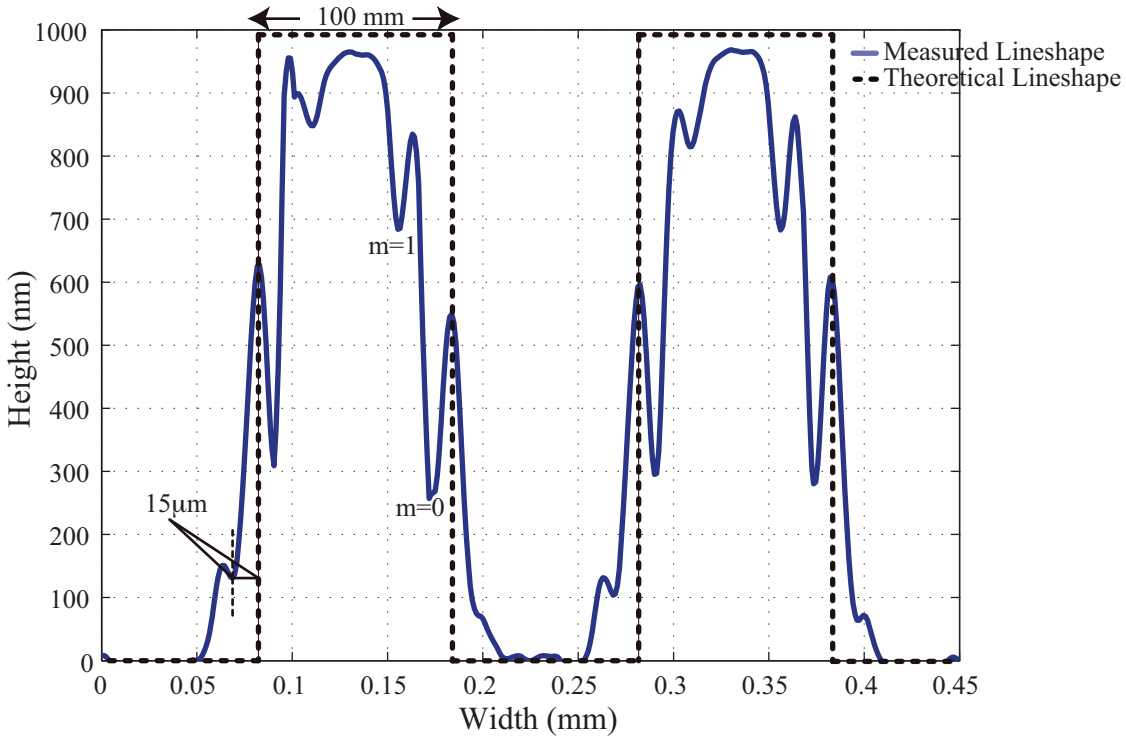

Figure 9.16: Lineshape of 100 μm feature patterned using the thin film mask with the ideal pattern superimposed. Lineshape captured using an optical profilometer. Interference intensity modes are labeled m=0 and m=1.

Figure 9.16 is the lineshape of a 100 μm feature patterned using the adaptable mask. In lineshapes previous to this figure, side lobes have been clear and noted in the

analysis of thin film mask features, here the lobe widths and spacings are examined. This figure is showing the cross section of two 100 μm adjacent squares patterned from a passively addressed array. It should be pointed out that all scale features patterned with the adaptable mask show sidelobes, not exclusively passively addressed arrays exhibit this behavior. Superimposed in this figure is the ideal lineshape, or the mask pattern for this shape. Looking first to the center, mask "transparent" regions of this pattern (appearing between 0.2 and 0.25 mm, less than 0.1 mm and greater than 0.4 mm in this figure), we see the resist fall to a minimum but with a certain slope and with some apparent modes. Marked in the figure is the distance of the left hand first intensity maximum (appears as a resist minimum) at about 15 μm from the ideal aperture boundary which agrees with the simulated location of the first maximum. Those intensity maxima are apparent in both the right and left hand features. Diffraction is the source of modes where the aperture should be clear. The same effect is shown for a 50 μm feature in Figure 9.17 also with ideal lineshape superimposed and intensity modes 0 and 1 identified.

Aperture diffraction on the other hand does not explain modes captured in resist where the aperture should be preventing the development of resist. Marked in Figure 9.16 are intensity maxima modes m=0 and m=1 corresponding to a repetitive pattern of interference modes in resist where no modes should exist, and do not exist for features patterned with imitation form-factor masks. Table 9.3 tabulates the average location of these maxima and minima modes for 100 μm and 50 μm features as locational offset from the ideal mask boundary i.e. m=0 appears on average 9.53 μm from the vertical line indicating the ideal aperture. These locations represented in offset from the region boundary is significant because these interference modes are caused by adjacent region interference centered at the edge of each boundary.

Knowing that a small amount of light transmits through the "off" region of the H-PDLC begs the question whether Fresnel diffraction is the cause of these sidelobes.

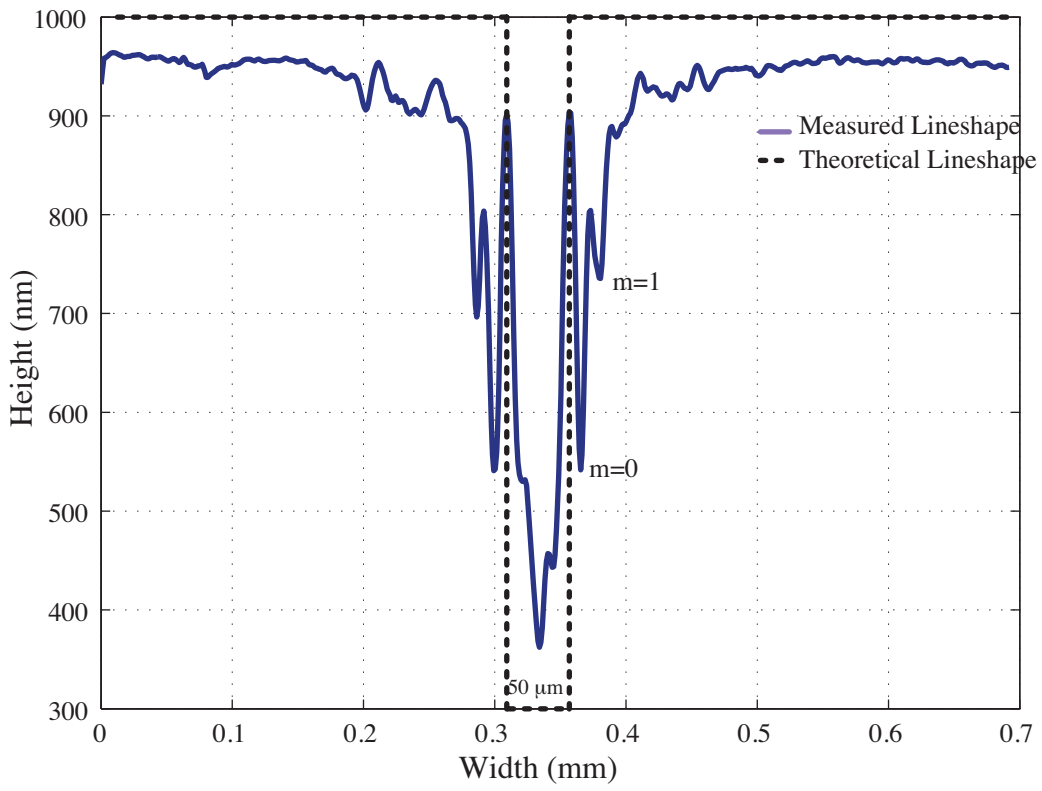

Figure 9.17: Lineshape of 50 μm feature patterned using the thin film mask with the ideal pattern superimposed. Lineshape captured using an optical profilometer. Interference intensity modes are labeled m=0 and m=1.

The simulation of aperture diffraction was extended to three 100 μm adjacent regions with about 20 % transmission in the "off" regions and full transmission in the transparent region. The intensity lineshape result is displayed in Figure 9.18 and the locations of the maxima and minima do not match the resist patterned lineshapes. The first diffracted maximum is located 15 μm from the boundary while the corresponding resist minima (m=0) appears only 9 μm from the boundary for the 100 μm feature.

Shown in Tables 9.4 and 9.5 are the offset locations between maxima and minima created by light leakage diffraction as compared to the experimental intensity maxima and minima captured in resist. Clearly large errors indicate that the captured maxima

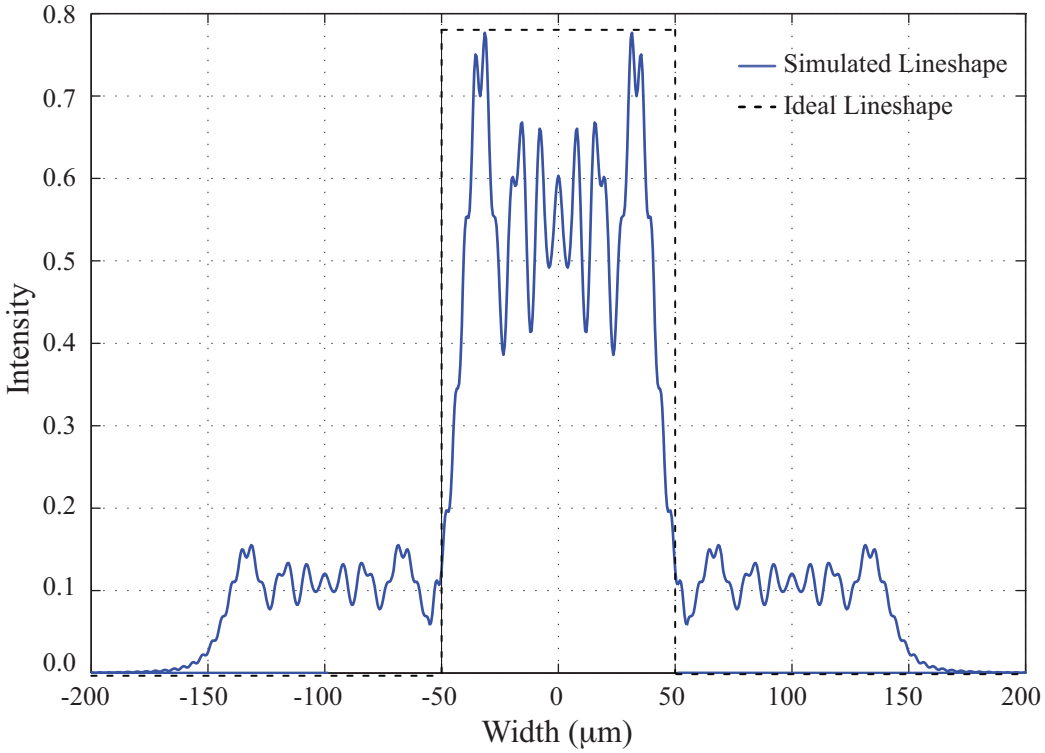

Figure 9.18: Fresnel diffraction simulated through 3 100 μm regions with varying transmission simulated using Matlab.

Table 9.4: Maxima and minima locations captured in resist compared to Fresnel diffraction modes due to light leakage for 100 μm feature.

	Experimental Peak Location (μm)	Simulated Location (μm)	Error (%)
m=0	9.53	15.50	38.52%
m=1/2	19.90	27.00	26.30%
m=1	27.46	34.50	20.41%

Table 9.5: Maxima and minima locations captured in resist compared to Fresnel diffraction modes due to light leakage for 50 μm feature.

	Experimental Peak Location (μm)	Simulated Location (μm)	Error (%)
m=0	8.28	17.50	52.69%
m=1/2	16.67	25.00	33.32%
m=1	25.09	33.00	23.97%

and minima do not correspond with light leakage aperture diffraction.

We have shown in this section that light leakage from "off" sections will not have corresponding Fresnel modes with the measured side lobe locations. This was determined through simulation of Fresnel maxima and minima in adjacent regions.

9.2.4 Coherency Analysis

In order to see that the the sidelobes forming in this system are caused by interference, it is necessary to examine the coherency of the exposure light. Mercury arc lamps are common for UV exposure, and the source used in the Suss mask aligner used for these experiments. Mask aligner optics are set up such that there is an amount of spatial coherence in the exposing beam though perfect spatial coherency (and temporal coherency) is unnecessary for photolithography [69]. A degree of spatial coherence (σ=0.7) in the exposing light phase also indicates that the interference terms of the summation of these exposing waves does not cancel to zero as would be the case of incoherent exposure. Partial spatial coherence can be introduced in a mask aligner using a pinhole or narrow aperture near the bulb to create a "point" source and then is followed with collimating optics.

An experiment was performed to verify resist interference dependence on spatial coherence. Resist was patterned using a typical H-PDLC mask, a mask used pre-

viously to exposure cutouts that resulted in clear sidelobes near edges, but rather than patterning in the mask aligner, this resist was patterned using a UV lamp. A UV lamp has the same exposure source tool, a mercury arc lamp, but it is not equipped with a point source aperture or collimating optics. The degree of coherency of this source is much less than that of the mask aligner and should result is not only a poorly transfered pattern, but no interference fringes should appear around the aperture edge.

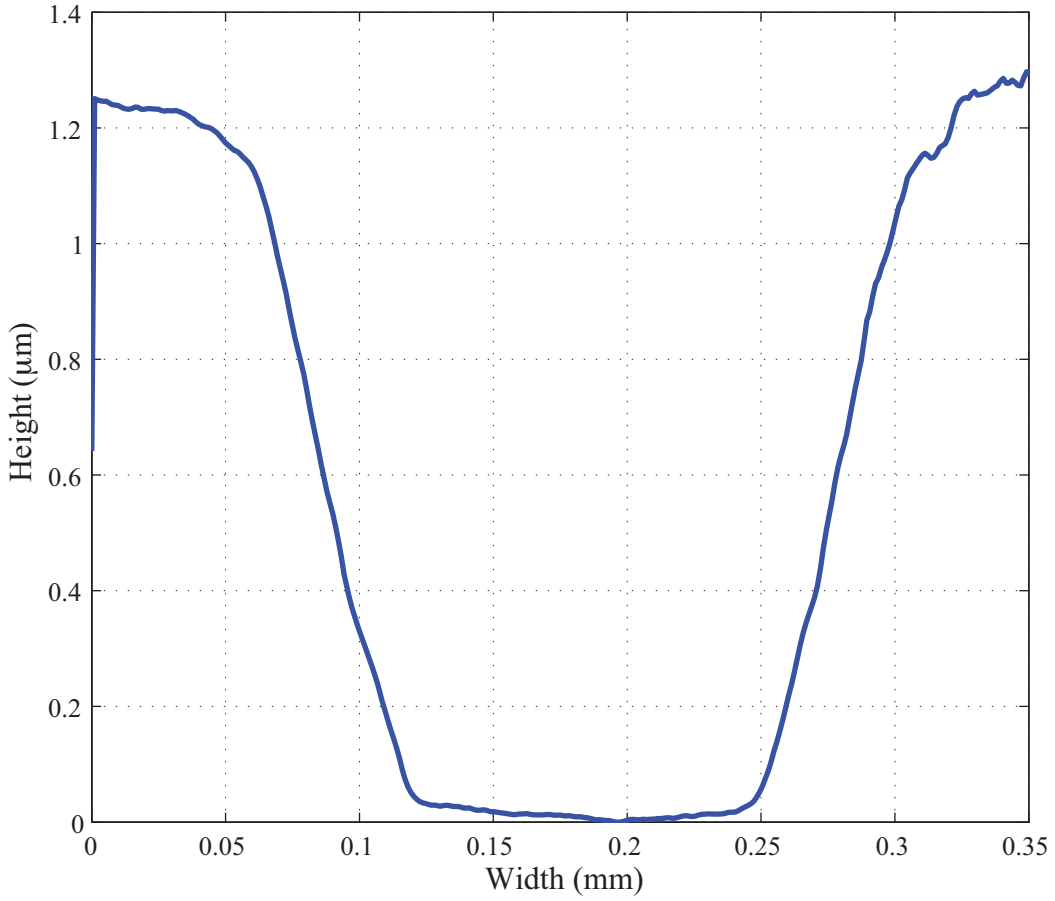

Figure 9.19: 200 μm cutout patterned using the thin film mask with a source of low spatial coherency. No interference fringes result in this pattern. Lineshape captured using an optical profilometer.

Figure 9.19 is the lineshape of a 200 μm cutout patterned using an identical

method to other resist patterned discussed here, the difference being the source. Lack of an degree of spatial coherence yields sloped sidewalls and no interference fringes outside the aperture width. A higher degree of spatial coherence is necessary to obtain interference fringes, this is also the reason no side modes were observed in initial large aperture patterning using this device. Until small scale patterning was investigated, a UV exposure source was used in place of a mask aligner.

9.2.5 Interference Simulation

Now that we understand that the sidelobe effect is not caused by Fresnel diffraction, only occur at index variation edges of H-PDLC where there is partial transmission, and do not occur with in coherent light, we can proceed to model the source of this effect. The light sourced from the mask aligner impinging on H-PDLC can be looked as a series of spatially coherent point sources radiating as modeled in Huygens-Fresnel theory. Using Matlab, we model the index differing regions of biased and unbiased H-PDLC will introduce extra delay terms depending on the defined location of the radiating point source. We can sum the electric field around the N radiating sources as (outlined in Ref. [70])

$$E = E_0(r)e^{-j\omega t}e^{jkr_1} * \left[1 + (e^{j\delta}) + (e^{j\delta})^2 + .. + (e^{j\delta})^{N-1}\right] \tag{9.9}$$

where δ represents the phase difference between point sources, k is the wave vector and ω is the frequency of the source. This can be rearranged as

$$E = E_0(r)e^{-j\omega t}e^{jkr_1} * \frac{e^{jN\delta/2}\left[e^{jN\delta/2} - e^{-jN\delta/2}\right]}{e^{j\delta/2}\left[e^{j\delta/2} - e^{-j\delta/2}\right]}. \tag{9.10}$$

Intensity of the interference pattern created by this radiating system can be found as the magnitude of E

$$I = I_0 \frac{sin^2\left[N(kd/2)sin\theta\right]}{sin^2\left[(kd/2)sin\theta\right]} \tag{9.11}$$

where $\delta = kd\sin\theta + \epsilon$ and θ represents emission angle observed on the image plane and ϵ is additional phase shift introduced by index modulation. Integrated over the area of the aperture edge results in an interference pattern as a function of emission angle. Converting to unit on the observation (or resist) plane we can compute the locations of maxima and minima.

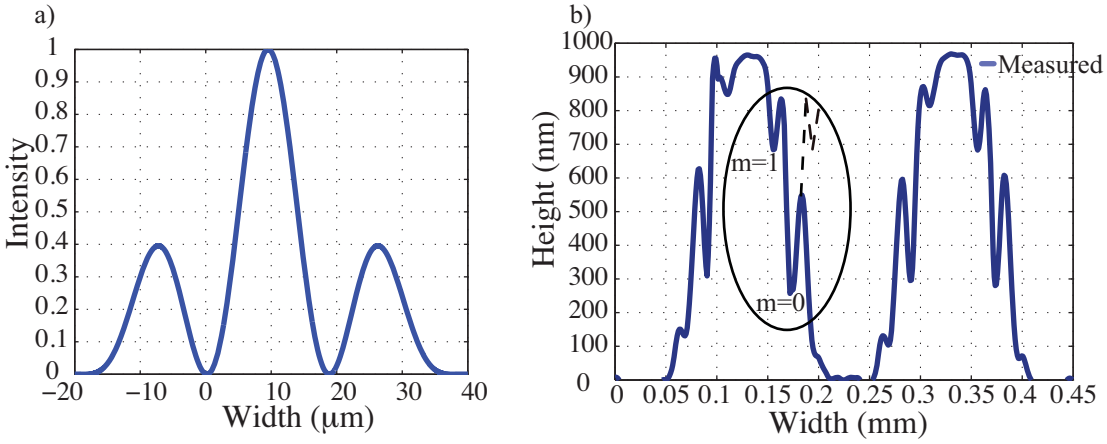

Figure 9.20: Simulated interference pattern around an edge for phase difference between on and off regions of H-PDLC. a) Simulated intensity lineshape modeled in Matlab. b) Image captured using an optical profilometer in resist with an inverted version of the interference pattern slightly offset into the "dark" mask area.

The simulated interference lineshape is shown in Figure 9.20a. Figure 9.20b is the measure resist lineshape for a 100 μm feature. The circled region in the figure represents the area near the aperture edge. The intensity lineshape will result in an inverted version of itself when captured in positive resist, but in this case only half of the interference pattern is captured. The phase difference between regions shifts the primary maximum into the "dark" region of H-PDLC, but only by about 10 μm.

Table 9.6: Side mode location compared to interference fringe offset location for 100 μm and 50 μm features.

100 μm	Experimental Peak Location (μm)	Simulated Location (μm)	Error (%)
m=0	9.53	9.94	4.13%
m=1/2	19.90	19.29	3.16%
m=1	27.46	28.63	4.08%
50 μm	Experimental Peak Location (μm)	Simulated Location (μm)	Error (%)
m=0	8.28	8.37	1.10%
m=1/2	16.67	16.90	1.37%
m=1	25.09	25.43	1.34%

The first minimum and second maximum to the "clear" side of the H-PDLC are not captured because the overall intensity of transmitted light washes out such a fine detail.

Table 9.6 shows a comparison of maxima and minima offset between the measured interference peaks and the simulated interference peaks. Simulated for both 100 μm and 50 μm features, the error between the simulated and measured maxima and minima locations is just a few percent. This low error leads us to believe that the side lobes are truly occurring as a result of interference between adjacent H-PDLC regions. To summarize, a small amount of light leaks in the "off" regions, and due to index difference in the biased and unbiased H-PDLC regions, incident exposure light self interferes causing side modes that are captured in the less illuminated side of the pattern. The interference pattern is symmetrical, but is washed out due to intensity difference in the bright or more transmissive side. Coherency plays an important role here. A necessary condition for discernible interference is a degree of spatial coherence, which is found high enough in a mask aligner, but not in a UV hood source. Patterning with a non-optically aligned UV source results in a lack of interference modes.

9.3 Transmissive Wavefront Analysis

Selected data from this transmission and wavefront study was published by the author in *Molecular Crystals and Liquid Crystals*, Ref [140].

Applications such as imaging through and patterning resist using a thin film mask rely on maximum transmission with minimum wavefront distortion through the layers of H-PDLC for functionality. An important enhancement we are interested in investigating includes elimination of the spectral filter in the patterning stack and replacing it with an entirely H-PDLC system. Maximizing transmission in multi H-PDLC stacks will enable our patterning technique to work without the spectral filter limiting the UV source to the g-line and improve possibilities for electrical control over all UV wavelength lines. Recently there has been work devoted to looking at multi wavelength attenuation of H-PDLC and broadening of H-PDLC peaks [45, 133] and an example of how a multi wavelength H-PDLC can attenuate the g-line and the h-line simultaneously is demonstrated. Eventually we would like to be able to completely control the mercury emission using H-PDLC therefore measuring multi H-PDLC transmission and wavefront characteristics is necessary to completely understand the optics of the proposed system.

In order to make advancements in this system to include an all-H-PDLC control system, one that has electrical modulation control over multiple UV lines, we needed to fabricate H-PDLC with either multiple stop-bands or a very broad stop-band. Recently there has been work in stacking H-PDLC [46, 133, 140] by methods including adhering individual cell together to reduce transmission losses and fabricating films back-to-back on a single piece of double-sided ITO glass. There has also been work in spatially multiplexing gratings, microscopic layers of different grating pitch resulting in the macroscopic appearance of a broadened stop-band [45]. Achieving these parameters using either of these methods will result in an all H-PDLC attenuation

system for imaging and patterning resist. Figure 9.21 is an example of a back-to-back grating fabricated with stop-bands centered at 436 nm and 405 nm. The intention is to naturally attenuate both the g-line and the h-line of the UV source and to maintain electrical control over both lines.

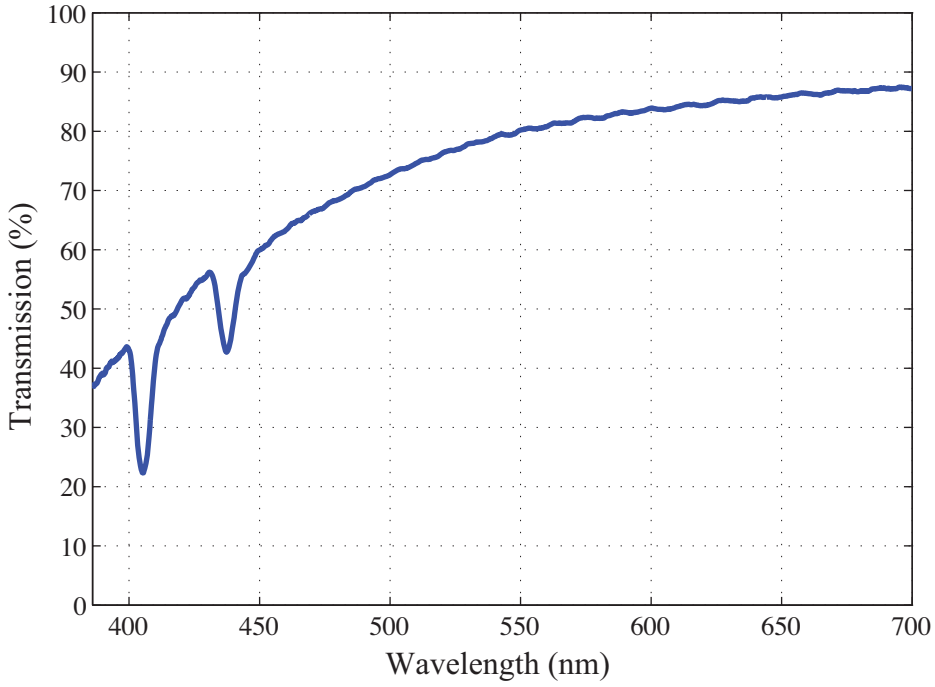

Figure 9.21: Figure illustrating a concept for modulating multiple UV lines experimentally measured using Ocean Optics fiber based spectrometer. This in particular modulates g-line and h-line.

It is difficult to form H-PDLC with a stop-band centered at the mercury i-line, or 365 nm. The proposed method of controlling the g-line and the h-line can use the natural absorption region of the material to its advantage to attenuate the i-line. Examining the transmission curve in Figure 9.22, liquid crystal transmission shows a steep decline around the wavelength of the i-line. Transmission in the UV was examined first for all of the separate components of the H-PDLC system. Based on the resonant absorption characteristics known about the individual components of

the system, we expect the liquid crystal molecules to be the limiting factor in UV transmission. When measured individually, it was found that uncoated Corning 1737 reached its absorption maximum (transmission minimum) near 200 nm, while index-matched glass and thiol polymer absorbed maximally at about 300 nm. The liquid crystal had the expected longest wavelength absorption maximum at about 365 nm. H-PDLC is limited by the liquid crystal molecules aromatic ring resonances in the near UV as illustrated in Figure 9.22. This important absorption property of the

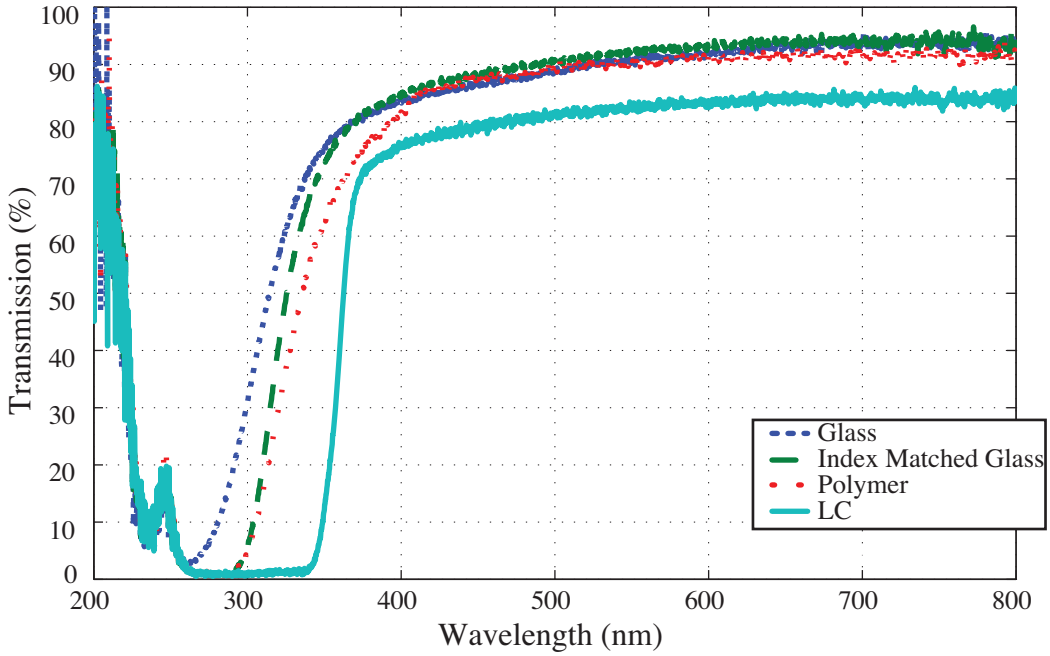

Figure 9.22: This figure shows transmission as a function of wavelength measured using Ocean Optics fiber based spectrometer for the components of the reconfigurable photomask

liquid crystal molecules used for these H-PDLCs is a property that enables a future enhancement of the imaging device to electrically control g-line and h-line radiation with the use of a spectral filter.

As light propagates through or reflects from any surface, distortions in that surface will disturb the light's wavefront. Wavefront distortion is quantified in multiple

ways, but usually measured using a Shack-Hartmann wavefront analyzer. A Shack-Hartmann style wavefront analyzer measures the displacement of a series of focal spots produced when the incident beam passes through a 2-dimensional lens array. The derivative of the optical path difference determined from the focal spot displacement is the wavefront slope [141]. Using this information, software analysis derives wavefront fringe pattern, Strehl ratio, and Zernike polynomial fits for the wavefront. It would be expected that transmission through ITO glass with etched regions would cause very small amounts of delay due to the differing indices and thicknesses the light experiences. Additionally, transmission through H-PDLC causes delay related to the different index regions. Here we address the question whether this phase delay in the transmitted beam effects the quality of the wavefront, so we examine transmissive wavefront of etched Corning 1737 ITO glass and thiolene H-PDLC fabricated on this type of etched glass.

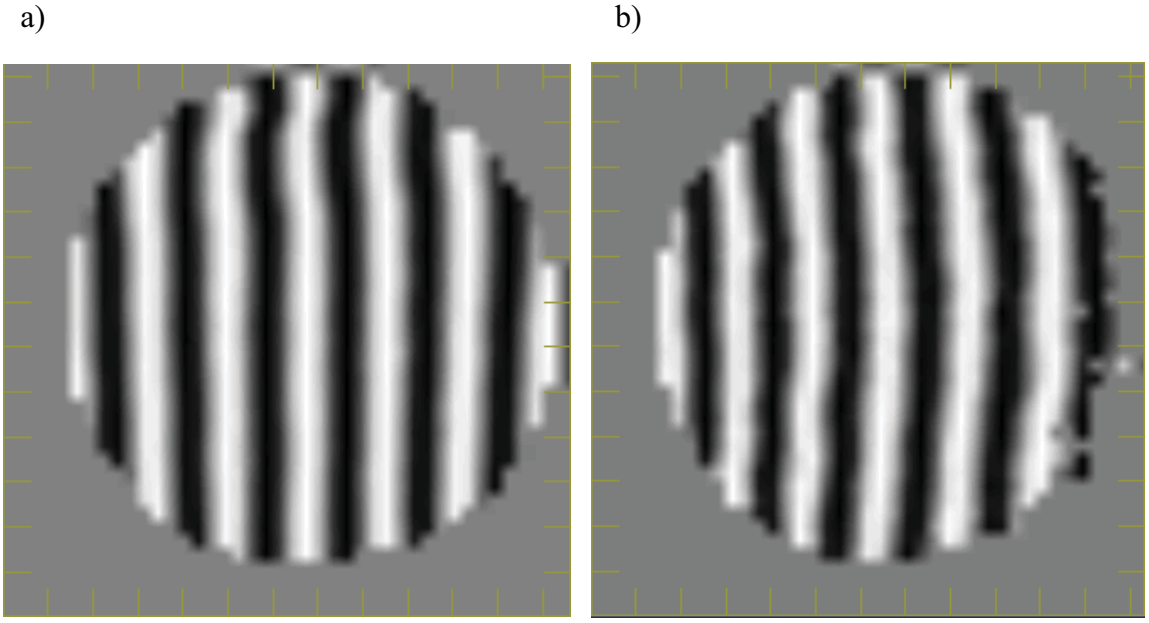

Figure 9.23: Wavefront interferograms of etched ITO coated Corning 1737 glass and thiolene H-PDLC on that glass measured using Adaptive Optics wavefront analyzer.

The Shack-Hartmann wavefront analyzer can produce a fringe pattern, known as an interferogram, which is a qualitative measure of wavefront error [142]. A perfectly unaberrated interferogram has parallel and evenly spaced fringes as this is a representation of the source and test light interfering with one another. The method that the wavefront analyzer obtains this interferogram is by comparing the source illumination to light transmitted through (or reflected from) a sample. The interference pattern will show different patterns that can be correlated to different types of aberration. Parallel evenly spaced fringes indicate a very small amount of introduced aberration. Figure 9.23a and b show interferograms for (a) etched Corning 1737 glass and (b) thiolene H-PDLC formed on the same glass. The lenslet array used was spaced at 300 μm with a circular aperture of 11 mm. There was speculation that the delay introduced by the etching of the ITO may show up in a wavefront image, and result in aberration showing in the interference pattern, but the small (20 nm) thick index matched ITO does not provide enough delay for this instrument to detect. There is a slight degradation of the fringe pattern noticeable between Figure 9.23a and b, this is to be expected as the interferogram in b is propagation through 20 μm of nanostructure after transmission through the etched glass. This difference is more readily noted in a Strehl ratio measurement.

Strehl ratio is the ratio of the peak intensity of an optical system's point spread function for an aberrated system compared with that of an unaberrated system [143]. Strehl ratio can be equivocated to wavefront quality using the Rayleigh quarter-wave rule suggesting a Strehl ratio of 0.80 has a peak-to-valley (PV) wavefront error of $\lambda/4$ [71] or by the Maréchal criterion that states a Strehl ratio greater than 0.8 yields an RMS wavefront error better than $\lambda/14$ [144]. A Strehl ratio of 1 indicates no aberration between reference and test sources.

Strehl ratio is related to RMS wavefront error for a point on the image plane P

Table 9.7: Strehl ratio and Wavefront Errors

Etched Glass		
	Strehl Ratio	0.9356
	RMS Wavefront Error (μm)	0.0168
	Peak-Valley Wavefront Error (μm)	0.1111
Thiolene H-PDLC		
	Strehl Ratio	0.7307
	RMS Wavefront Error (μm)	0.0474
	Peak-Valley Wavefront Error (μm)	0.2366

by

$$I(P) = 1 - (\frac{2\pi}{\lambda})^2(\Delta\Phi_P)^2 \tag{9.12}$$

where $I(P)$ represents Strehl ratio and $\Delta\Phi_p$ is the RMS wavefront error measured in waves [71]. Table 9.7 displays calculated RMS wavefront error from the Strehl ratios for each of the measured samples. RMS wavefront error represents the difference in wavefront quality with the addition of an H-PDLC sample with respect to a calibrated source.

What is shown in Table 9.7 indicates that the etched glass, with a Strehl ratio of greater than 0.9 has PV wavefront error of much less than a quarter of a wave. This indicates a small amount of introduced aberration in transmission through etched glass. Strehl ratio of less than 0.8 indicates more aberration introduced in transmission through the H-PDLC, this is an expected result as this value will also increase with thickness.

The Zernike numbers obtained for this wavefront are a polynomial fit for the coefficients that describe the wavefront. Displayed in Table 9.8 are the primary aberration coefficients. Clearly, all primary aberrations have a contribution to the distortion of the wavefront except defocus. By tabulating these polynomial coefficients, the individual aberration contribution can be isolated. There are 35 Zernike coefficients in

Table 9.8: Primary aberration Zernike numbers

Primary Aberration	Etched Glass	Thiolene H-PDLC
X Tilt	-0.006167	0.017277
Y Tilt	-0.004791	0.005584
Focus	0.00000	0.00000
0^0 Astigmatism	0.017037	0.121414
45^0 Astigmatism	0.018699	-0.001487
X Coma	0.001249	-0.008963
Y Coma	0.004714	-0.003268
Spherical	0.009799	0.004780

total, Table 9.8 tabulates the 8 first order aberration coefficients.

To recreate the wavefront expression using the Zernike coefficients, a polynomial expansion can be used. The equation relating wavefront as a function of position $W(x, y)$ with the sources of primary aberration

$$W(x,y) = A(x^2+y^2)^2 + By(x^2+y^2) + C(x^2+3y^2) + D(x^2+y^2) + Ey + Fx + G \quad (9.13)$$

where A is the coefficient representing spherical aberration, B is the coefficient for coma, C represents astigmatism, D represents defocus, E and F represent tilt in the x and y directions, and G represents piston [142].

Understanding and characterizing transmissive wavefront aberration that is introduced in this system allows us to make some future generalizations about this device. Although the device is currently limited to proximity printing, and can be improved to contact with elimination about the bottom electrode, retrofitting this device into a reticle or reduction system is not out of the question. Once resolution limits near very small sizes, an optical element's ability to maintain unaberrated wavefront becomes key in the projection system. Minimal aberration is introduced in transmission through etched ITO and the H-PDLC itself making it possible for retrofitting into a

reduction system.

9.4 Field Fringing

To completely understand the light propagation though an electro-optic film configured in this system, it is necessary to examine the electric field and interactions in and around the electrodes controlling the index of the film. We usually assume that the electric field is constant between the electrodes and that edge fringing is negligible, but with the decreasing dimensions of the etched electrodes compared to the constant width of the film, electric field can play an important and potentially limiting role.

Patterned electrodes in this configuration can be viewed as parallel plate capacitors with plate length and width equal to the electrode pad area and plate separation equal to the film thickness. It is understood that there are index (or dielectric constant) variations periodically within the film, but for the this calculation, we will assume an average dielectric constant for the value of the material within the plates. Inside the area of the plates the electric field is constant in amplitude and direction. This can be shown as simply the solution to Laplace's equation for dielectric in the absence of free charge

$$\nabla^2 V = 0. \tag{9.14}$$

Considering Cartesian coordinates for this system and that the electric field will extend in the y direction over the thickness of the dielectric (d), from 0 to a in the x direction, and 0 to b in the z direction. Therefore the differential equation governing this simple problem is

$$\frac{d^2V}{dy^2} = 0 \tag{9.15}$$

since there is only electric field variation in the y direction. Integrating and applying boundary conditions of $y = 0, V = 0$ and $y = d, V = V_0$, the linear relationship of

potential in the y direction is found.

$$V = \frac{V_0}{d} y \tag{9.16}$$

The electric field relationship to potential is defined as

$$E = -\nabla V = -\hat{y}\frac{dV}{dy} \tag{9.17}$$

which is linear and constant over the area $0 < x < a$ and $0 < z < b$ [145]. This common derivation of electric field across a dielectric easily shows us that the field is constant, linear, and perpendicular to equipotential lines, but disregards fringing around the exterior edge of the system. In the limit that the area of the electrode is much greater than the separation of electrodes, field fringing can be calculated as a boundary value problem [146, 147]. In the adaptable film mask configuration, pixel sizes rapidly approach the thickness of the film and therefore fringing fields need to be calculated using a finite element modeling method.

Using Comsol Femlab, a finite difference time domain simulation software, the total electric field and potential around patterned electrodes were found for 100 μm and 50 μm pixels. This software is a 3-dimensional differential equation solver that operates using a graphical interface of the object. The user needs only choose the differential equation, and set material properties and boundary conditions. The geometry was drawn to represent 100 μm and 50 μm pads at 100 V alternating with regions of charge-less dielectric representing the glass substrate and polymer film. Dielectric values were given to be an average across the film and thicknesses were set to be consistent with the actual system. Figure 9.24 and 9.25 are results of the 2D FDTD simulation of the system for 100 μm and 50 μm electrodes. Appendix F shows a full page image of these results in landscape for better resolution. The

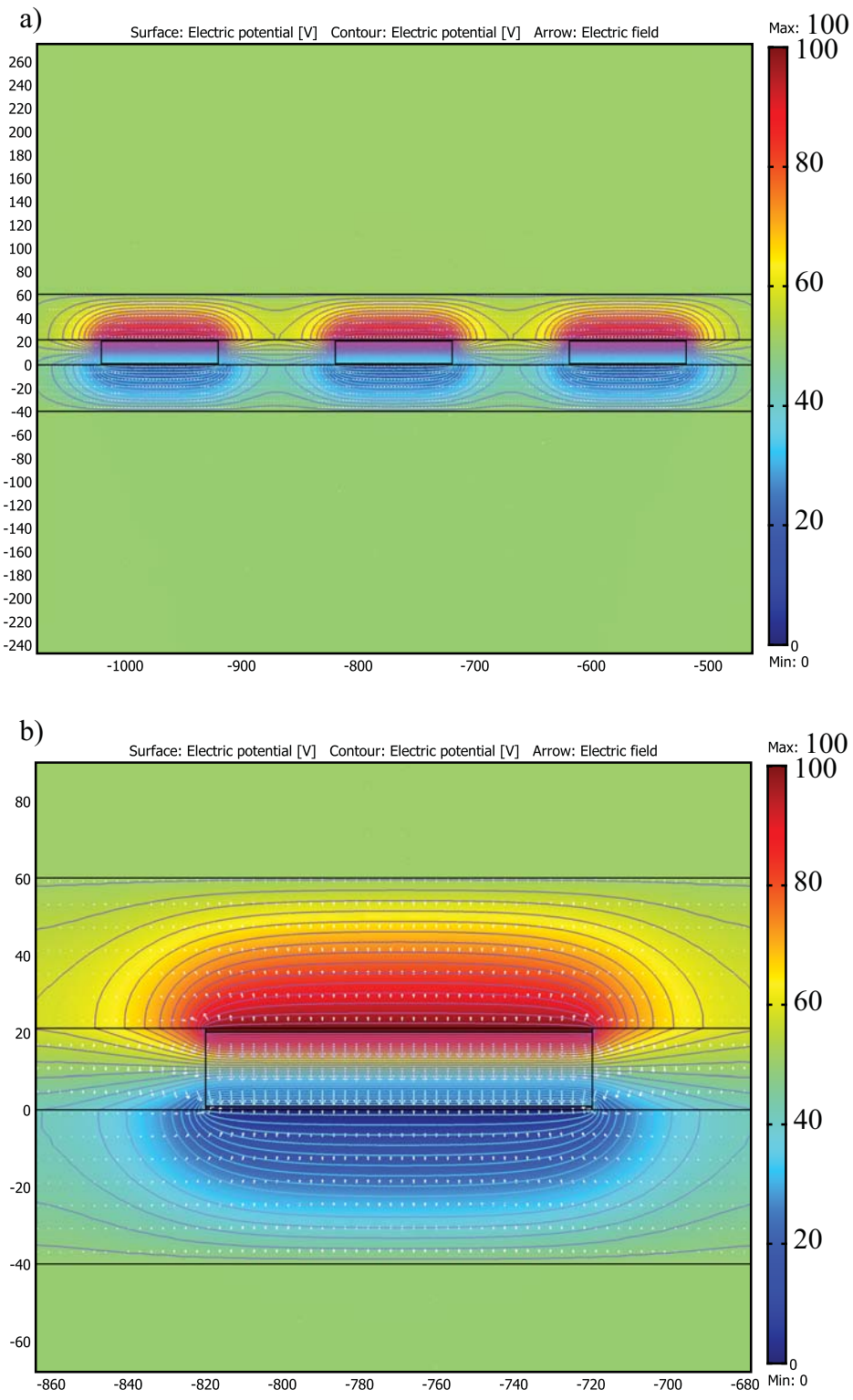

Figure 9.24: Comsol simulation of potential and electric field around 100 μm electrodes. Lines of equipotential are shown. a) Three adjacent electrodes. b) Zoom into a single electrode.

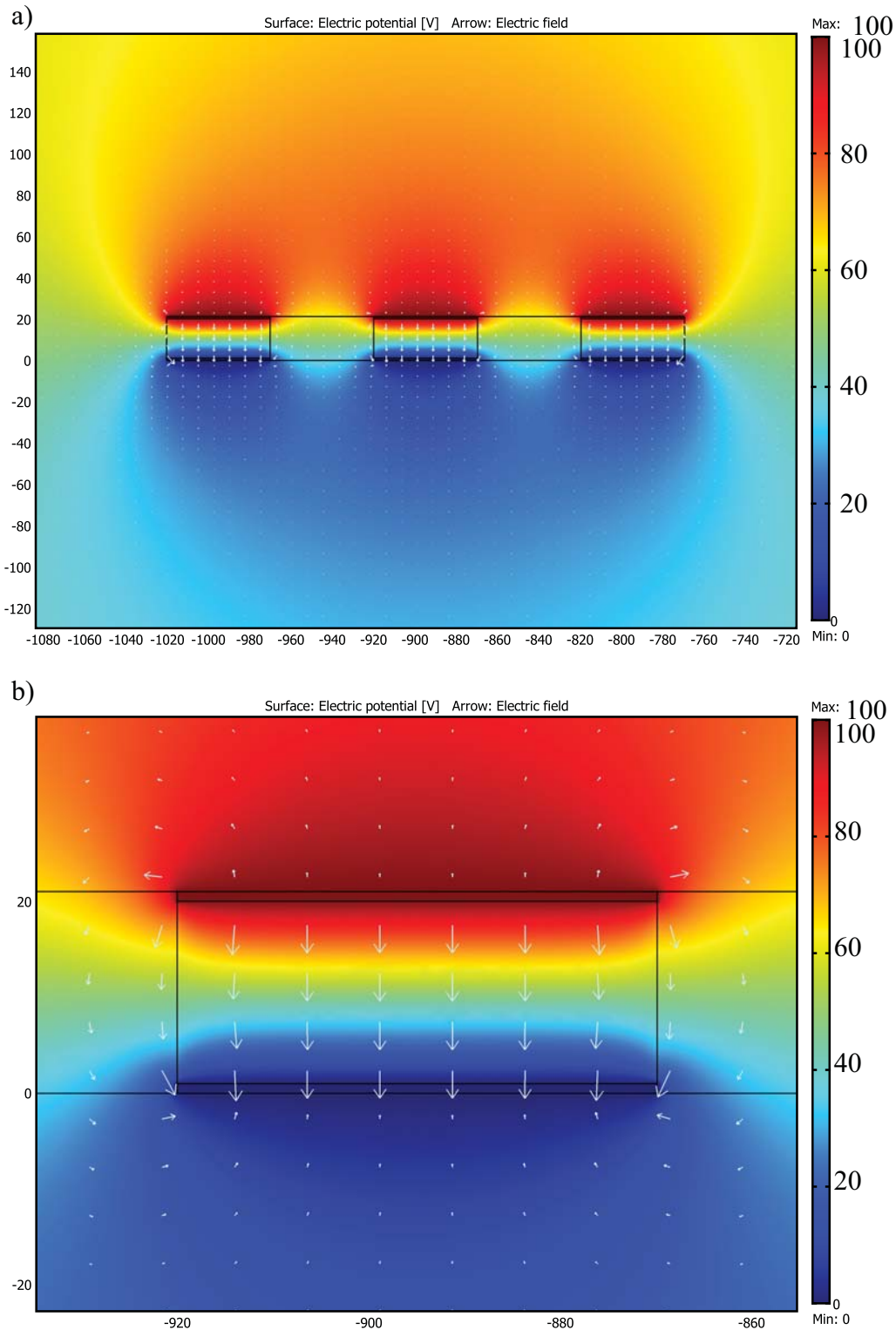

Figure 9.25: Comsol simulation of potential and electric field around 50 μm electrodes. Lines of equipotential are not shown, but indicated in the color map. a) Three adjacent electrodes. b) Zoom into a single electrode.

Table 9.9: Simulated percent potential differences as a function of distance from an electrode compared with % H-PDLC switch.

Distance from Edge	Potential Difference	% Reflection	H-PDLC State
10 μm	20%	>90 %	Reflecting
5 μm	40%	88%	Near reflecting
2.5 μm	75%	25%	In transition
1 μm	85%	15%	In transition
0 μm	100%	0%	Transmitting

colormap in each of these simulation results represent areas of equipotential with the top electrode set to 100 V and the bottom electrode set to 0 V. The linear nature of the potential is seen between the electrodes, and in Figure 9.24 the contour lines corresponding to the colormap are evenly spaced reinforcing the linearity of the potential between electrodes. By definition, the electric field vector is orthogonal to the lines of equipotential because it is the gradient of the voltage surface, this can be visualized clearly in between the electrodes where the electric field arrows are perpendicular to the potential lines. Outside of the electrodes, the electric field vector arrows continue to be perpendicular to the equipotential lines, but are no longer orthogonal to the electrode structure. What is seen instead is the field fringing around the edges of the electrode boundary, the direction of the electric field is bowing outward with decreasing amplitude as a function of distance from the edge. Vector field amplitude is usually shown as a relative arrow length while the direction is obviously pointing in the direction of the symbol arrow.

Using the colormaps to indicate the potential values in between electrode regions, the potential difference as a function of distance was calculated from the simulation results. A curve tabulating percent reflection of the film as a function of applied voltage will assist understand the state of the H-PDLC as the applied voltage changes. In Figure 9.26 the 10% and 90% points are marking to indicate when the film is defined

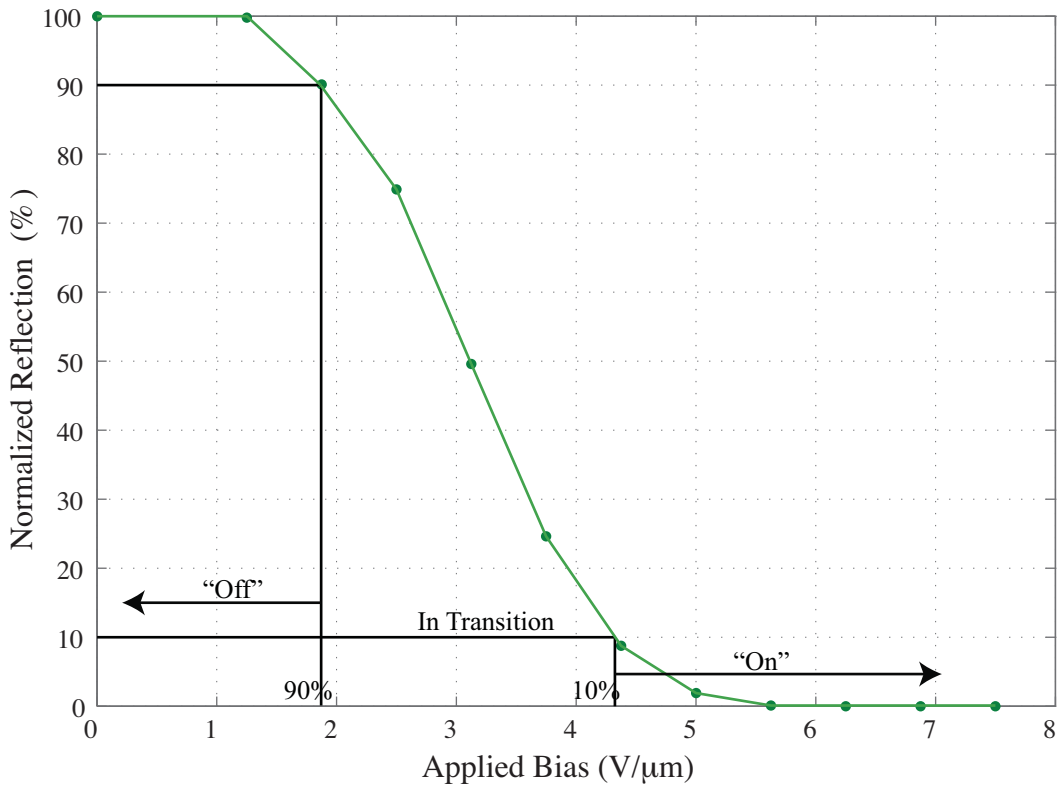

Figure 9.26: A plot of reflection percentage as a function of applied voltage in V/μm. The definition of reflection and transmissive percentages are marked, as well as the state of the film under these biasing conditions.

as reflecting (>90%) and transparent (<10%). The x-axis of this curve was converted from V/μm to volts assuming a 20 μm film for this comparison.

As expected the maximum potential difference was calculated from top electrode to bottom electrode. Also predicted is the rapid decrease in potential difference with distance from the electrode which is seen near the edge of the electrode. As tabulated in Table 9.9, at a distance of 1 μm from the electrode the percent potential difference was calculated to be about 85%. Using a curve that tabulates switching voltage, the H-PDLC at that distance will have about 15% reflection and can be considered in transition, but near transmissive. Near 5 μm from the edge the percent potential difference has decreased to 40 % and can be equated to 88% reflection, nearly the

definition of the "off" state. Finally, at 10 μm the simulated potential difference is less than 20% yielding greater than 90% reflection, or a completely reflecting film.

To summarize, field fringing does occur in this system at edge distances less than 5 μm, but at an attenuated level due to the analog nature of the H-PDLC switch. Full transmission outside the electrode occurs at distances less than 1 μm. This effect occurs well below the threshold for impacting patterning as the diffraction limit of the system is nearly 25 μm.

In this chapter, we examine the optical properties of light as it transmits through the H-PDLC system and patterns the resist. Fresnel diffraction, a factor that was predicted to be the limiting one in patterning resist, can be simulated and correlated to maxima and minima occurring in the patterned resist to within a few percent. The occurrence of side modes is not predicted or simulated to be a result of Fresnel diffraction. Two form factor type masks were made to isolate to the reasons for the formation of side modes. First, a chrome/glass mask was made spaced with 20 μm spacers and adhered with thiol adhesive in order to have identical form factor to H-PDLC, but not have liquid crystal droplets. Patterning with this form factor mask enables the capture of Fresnel diffraction to compare with that captured in simulation and with an experimental H-PDLC. The maxima and minima aligned to within a few percent. No side lobes resulted. Next, a form factor mask was made using chrome patterned on glass, and H-PDLC was formed within the patterned electrodes. Patterning using this mask allowed for us to examine light transmitting through biased H-PDLC, but without the effects of "off" regions H-PDLC (that was attenuated with the chrome). Fresnel diffraction occurred, but no side lobes. Scattering occurs in modes, as measured in Chapter 3, but the angles of the scattering modes translated across 600 μm of glass do not correspond with the locations of the measured side modes. Additionally, if scattering was to be a source of these side lobes, they would be apparent using this chrome/glass/H-PDLC mask.

Table 9.10: Optical Configuration Parameters Summarized

Parameter	Configuration
Optical Details	
Modulation	g-line
Resolution (μm)	25
Scattering Modes (degrees)	$\pm$75
Scattering Modes Pattern	2.24 mm
Coherency	Maintained with Mask Aligner
Strehl Ratio Diff (glass to H-PDLC)	0.2049
Field Fringe Parameter (μm)	$<$2.5
Interference	Phase delay adjustable at interface

Neighboring region interference with index related delay was attributed to cause the side modes. This was further confirmed when no side modes occurred when illuminated using an incoherent source. Finally, simulation of delay related interference occurring at the junction between "on" and "off" regions confirmed edge interference causing side modes to form.

Transmission and wavefront analysis provides a solution to using a spatial filter, and replaces it with an all H-PDLC electrically controllable system. Wavefront analysis indicates that transmission through etched glass does not provide enough delay offset to be measurable, and transmission through H-PDLC decreases Strehl ratio, but not significantly.

Finally, examination of electric field fringing around patterned electrodes has intensities strong enough to switch H-PDLC, but only within about a 1 μm radius from the biased edge. Our calculation of resolution is 25 times greater than that factor.

Optical parameters are summarized in Table 9.10.

Chapter 10. Conclusions and Applications

10.1 Conclusions

This thesis describes a study of light propagation properties through a nanostructured thin film and its imaging and patterning applications in photolithography. The idea of using H-PDLC as an adaptable photomask opens the door for many interesting and unique possibilities, but before it can be fully developed, understanding the imaging science and examining proof of the concept is necessary.

To summarize the important milestones of this proof of concept work, we determined that H-PDLC can modulate the g-line of a mercury source at efficiencies greater that 35 % with zero to full bias. According to the contrast curve, this is enough modulation to pattern or prevent patterning of Shipley 1813 photoresist. The analog transmission nature of H-PDLC with incremental bias is shown with its potential for grayscale applications. Initial patterning using a traditional binary and a thin film mask are compared to see that there exists a small difference in the edge slope of features patterned using the adaptable mask. Using this device naturally introduces a small amount of near field diffraction that can account for the difference. Resist and developed substrate quality are examined to ensure that masking using the thin film does not effect bulk regions, the developed resist is mainly examined to ensure no dimpling due to light leakage or large scale variation in the patterning H-PDLC. No adverse marking in the developed resist are found as a result of the thin film.

Next, H-PDLC patterned resist was used for etching and deposition treatment. It was expected that resist patterned using the adaptable mask would hold up to these next step lithography methods because it was normal in thickness and morphology, but we needed to verify. We found a minor difference in a DRIE etch of a silicon

substrate due to the sloping resist profile that results in H-PDLC patterning, and we found virtually no difference when wet etching silicon with respect to features patterned using the binary mask counterpart.

This proof of concept work tells us that using a thin film adaptable mask passes the first tests of being a useful device, but to truly characterize and understand its functionality, the science behind the patterning needed to be thoroughly examined. To find the limitations of an optical imaging system such as this one, it is logical to scale into the micron regime. We did this through a test ITO mask designed to push the patternable size limit below the expected diffraction limit. Using elements of the test mask, we show features approaching the calculated resolution limit of the device, $\sim$25 μm due to the thickness of the bottom electrode. Clearly resolved cut outs are patterned at sizes above 25 μm, the feature presented has a cut out of exactly 25 μm, and the slope of the sidewalls converges nearly at the point, but maintains the full height of the resist. We can conclude from this that should another method of switching be introduced, such as in-plane switching that eliminates the thick bottom electrode, the resolution limit governed by near field diffraction can be improved. Note that this only applies to the converging edge slopes at 25 μm, not the side mode interference pattern appearing near edges.

Part of the innovation of this device is its proposed ability to mask different patterns using the same mask, or dynamically pattern resist. This interesting aspect is shown with two sets of data. Both sets contain several (3 or 4) distinct patterns formed on different samples using the same mask. We show that changing the mask pattern is simply as easy as changing the bias on the film regions.

A second approach to dynamic patterning was taken in the use of a passively addressed array. Patterning using passive addressing is the first step toward an arbitrary system, we show 50 μm and 100 μm rows and columns being activated and used for patterning.

Before starting an analysis of patterning, it was necessary to mathematically understand and model propagation through an index modulated dielectric structure. Matrix solutions were determined first for an ideal grating structure to show the frequency stop-band as a function of index variation, layer thickness, and total film thickness. Next properties of H-PDLC made in-house were applied to this model using information such as droplet diameter, fill factor, and shape from SEM micrographs. Experimental scattering and absorption extinction coefficients were incorporated, and the scattering factor was added. When compared to real H-PDLC transmission, a close likeness resulted and it can be concluded that index modulation, thickness, stop-band, and experimental H-PDLC droplet, shape, and extinction properties are correctly assumed. Next, using this model, blueshift was modeled and compared to measured data. We conclude from this that although film properties change with off axis illumination, the shift is not significant until angles greater than 10 degrees.

An analysis of the patterned features shows some interesting deviation from the expected lineshapes. Of all of the optical properties examined, there was a solid expectation that Fresnel diffraction would show some effects. This was calculated, and assumed because of the electrode thickness, to be the cause of edge sloping exhibited in the initial patterning tests. A simulation was written to calculate spatial Fresnel diffraction and center lineshape as a function of aperture width, mask/image distance, and wavelength. We show that the maxima and minima captured in resist samples correspond with simulated maxima and minima for diffraction occurring within the bounds of the aperture.

The next interesting and somewhat unexpected patterning result is the interference sidelobes seen with increasing predominance with decreasing aperture size. To confirm that they were not an artifact of Fresnel diffraction, chrome/thiol masks were made of the same form factor as the thin film mask. The difference was that rather than blocking light with H-PDLC, light was attenuated using a chrome layer. These

chromed glass pieces were spaced at 20 μm and secured with thiolene adhesive. Resist patterned using these imitation form-factor masks showed perfectly predictable diffraction patterns within their aperture openings, but no sidelobes appeared.

Scattering is a known cause of transmissive losses in H-PDLC. The spherical liquid crystal droplets in the nanostructure cause a λ^{-4} attenuation response which would be expected for scattering centers of their size. Additionally, scattering modes occur as a function of rotation around the scattering cell. This was considered as a potential cause for the sidelobes appearing in patterning, but after calculating where a scattering mode would cause a deviation in patterning light, it was eliminated as a possibility due to the distance not corresponding with the measured modes.

Next, to rule out nanostructure interaction such as scatter from the "on" section outside its bounds a second form-factor mask was developed. This mask was exactly like the first chrome/thiol adhesive except rather than thiolene glue, H-PDLC was formed on chromed glass. The resulting patterns again showed the expected diffraction pattern inside the aperture opening, but also lacked sidelobes leading us to the conclusion that scatter or redirection due to the nanostructure was not the cause of these lobes.

After examining the periodicity of the side modes around an aperture, the conclusion was reached that interference is the cause of these modes. A small amount of light leaks through the H-PDLC in its "off" state, not enough to necessarily pattern resist but enough to cause interference when brought near a transmissive region. Phase delay of propagating light adds another interesting aspect: H-PDLC light modulation functions on bias-induced index difference. Regions of H-PDLC that is reflecting light has different index than H-PDLC transmitting light, and that index is analog for any bias placed in between. Propagating through different index regions is equivalent to introducing different phase delay. Illuminating dielectric with spatially coherent light near an interface of two slightly different index regions (and assuming at least

a small amount of light transmits through both regions) causes interference modes. Those modes are shifted from the axis of the interface by a factor of λ times Δn. We found that the location of the modes remained virtually constant with respect to the distance from the aperture edge, which would support this finding. A simulation was performed modeling edge interference from phase delayed spatially coherent sources yielding mode locations within a few percent of the captured interference modes.

Coherency in patterning is important, we show that the thin film mask can maintain spatial coherence of the patterning light by comparing to features patterned using an incoherent source. Features patterned using the mask aligner, a device designed to deliver spatially coherent and collimated light to the aperture, exhibited diffraction and interference consistent with what would be expected of a single wavelength coherent source. Features patterned using a blanket UV curing lamp (same mercury arc lamp, no spatial filtering or collimating optics) resulted in poor undefined patterns with no observable diffraction or interference. The lack of coherence eliminates any recordable interference pattern. Coherency was also a contributing factor in edge slope deviations found in initial large aperture patterning because these initial structures were not fabricated using the mask aligner. The conclusion regarding coherency is that it is maintained within the nanostructure.

As the application requires deeper UV wavelengths for better resolution patterning, absorption in liquid crystals becomes a limiting factor. It is known that resonances occur for these molecules in the deep UV ($\sim$200 nm) yet off resonance absorption limits H-PDLC transmission around 365 nm and scatter causes attenuation at wavelengths just above. Until a material set is developed that overcomes this, g-line and h-line radiation can be modulated either individually or using a stack of multiple H-PDLCs. We characterize transmissive wavefront of propagating light through etched ITO glass and H-PDLC to ensure that patterning is not corrupted by aberration introduced into to system.

10.2 Optimized Technology

Using the optical study results, we can draw conclusions regarding an optimized device design. The diffraction limit that indicates that patterning resolution is approximately 25 μm is governed entirely by the thickness of the device bottom electrode. Diffraction that occurs agrees with simulated diffraction peaks and could be eliminated by removing that electrode. A device enhancement that improves the resolution is the elimination of the bottom electrode allowing contact between mask and resist.

Interference effects found as a result of phase delay in H-PDLC may appear as a challenge limiting the resolution of the patterning system. Having the ability to control phase through bias and film thickness is a factor that can potentially lead to great advancements. Using phase control and phase masking, subdiffraction limit patterning is possible by utilizing the side lobes as patterning features. Additionally, control over phase can possibly enable diffraction and interference effect cancellation.

H-PDLC layer morphology has been shown to be imperfect. This information was used in the grating simulation, and can be seen in SEMs of H-PDLC layers. This interfacial roughness and centerline misalignment is a cause of transmission attenuation and wavefront aberration. Introduction of a more morphologically perfect grating may solve these problems. A liquid crystal polymer structure exists that is fabricated similarly but rather than using nematic liquid crystal in the prepolymer syrup, the grating is formed at an isotropic temperature and cooled back to the liquid crystal phase. This POLICRYPS grating forms well defined liquid crystal and polymer slices with high baseline and good diffraction efficiency [148], and has the potential to eliminate the wavefront and transmission attenuation found in H-PDLC.

From this information, we can examine this device integrating into state-of-the-art lithography systems. Currently, device limitations are functions of form factor, inability to truly pixilate the electrode, and lack of more advanced lithography equip-

ment. As mentioned and simulated earlier, the bottom electrode of the H-PDLC film causes diffraction and limits resolution to 25 μm. This value has been calculated and measured using the parameters of the current application form factor. Eliminating the bottom electrode and allowing the masking surface to sit in contact with the resist will improve the resolution to less than 1 μm. Retrofitting this device into a projection system has the potential to improve the patterning resolution to less than 100 nm. When using projection systems, wavefront aberrations introduced may impact patterning. Typically lithography projection systems use optics that introduce little or no aberration; a small decrease in Strehl ratio in transmission through the film may decrease patterning ability with respect to the capability of a chrome and glass mask. The wavefront of transmission through glass is 20% better than H-PDLC film. Beyond introducing aberration free optics and a projection/ stepper system, to attain state-of-the-art resolution diffraction compensation methods such as double patterning and inverse lithography are employed, methods that can be used and enhanced using an adaptable H-PDLC photomask.

Solutions to elimination of the diffraction source is removing the bottom electrode of the device. Using a display technique known as in-plane switching (IPS), LCDs can be single plane electrode controlled. IPS uses dual electrodes, but rather than arranging them like parallel plates, the electrodes are interwoven on a single plane and the field lines arc across. Fabricating H-PDLC in this environment can be accomplished by spin-coating the prepolymer syrup and exposing using the prism method, a work still being perfected.

A second enhancement is fabrication of H-PDLC on an LCD backplane. Whether the backplane in IPS mode or otherwise, addition of multiplexed control and individual transistors for each pixel would greatly improve the arbitrary nature of this device. Using IPS mode, resolution of LCD backplane that could be achieved in contact mode would be less than 1 μm.

10.3 Contributions of this Thesis

The contributions of this thesis are:

- Development of proof of concept of an adaptable thin film photomask device based on H-PDLC technology. Patterning of features down to the diffraction limit has been shown. In addition, patterning multiple features using a single mask by changing bias and passively addressed arrays are illustrated. Morphology of developed resist and substrate has been characterized to show it compares with features patterned using a binary mask. Next step lithography has been performed including DRIE etching of silicon patterned using the thin film mask and KOH wet etching of silicon patterned using the adaptable mask.
- Simulation of propagation through H-PDLC with experimental parameters determined from SEM micrographs obtained in-house. Simulations of propagation in stratified media are not new, and simulations of H-PDLC in general is something that has been published, but using parameters taken from TEM and SEM images pertaining to those gratings. Incorporating microscopic parameters such as layer thickness, droplet shape, droplet isotropy, droplet layer fill factor, total number of layers, for H-PDLC formed in-house using images collected in-house yields simulations best suiting films that are made and used here. Simulating and comparing blueshift using the model built with in-house collected parameters is something that has never been performed before this work.
- Application of Fresnel diffraction theory to imaging through H-PDLC nanostructure is work that is currently brand new. Using photoresist to capture images of light propagating in H-PDLC is a new concept, and we found that near field diffraction occurs as predicted by theory when bound in a thin film aperture.
- Edge interference is simulated and characterized as it pertains to image formation on the resist plane. We show that phase delay near the aperture edge combined

with small amounts of light leakage cause interference modes shifted slightly with respect to the edge axis. We show that in a resist image patterned using the thin film mask, diffraction modes can be identified and isolated from interference modes by their spacing and their location inside or outside of the ideal aperture shape.

- We have shown that coherency is maintained within an H-PDLC nanostructure as it pertains to image formation on the resist plane. When spatial coherence is introduced to the system, defined interference and diffraction modes appear in resist images, whereas when illuminated with a lack of coherence, no modes are observed.
- The measurement of field fringing pertaining to H-PDLC pattern edges is a new calculation. Understanding at what length scale fringing occurs inside H-PDLC and how it effects droplet rotation at its maximum intensities is shown.
- Measuring of scattering and wavefront in H-PDLC as it pertains to transmissive imaging in photoresist is a concept reported here. We have for the first time shown that scattering modes and wavefront do not effect photoresist patterning when illuminated through adjacent regions of different index.

The optimal configurations for the H-PDLC device, the lithography patterning, and the optical parameters are summarized in Table 10.1.

10.4 Enabled Technology

Throughout this thesis, photolithography has been discussed as the primary application of this device. Based on what we have shown, we can be specific about some of the potential improvements to the field this technology can offer. Several techniques have been reviewed or briefly discussed previously, but here their use will be explained based on the results presented in earlier chapters. Using this type of photomask may

Table 10.1: Optimal Configuration of the H-PDLC Adaptable Photomask Device

Parameter	Configuration
H-PDLC Details	
Film Thickness (μm)	20
Glass Thickness (μm)	600
ITO Thickness (nm)	20
H-PDLC Chemistry	Thiol (Norland Optical Adhesive, Inc.)
Liquid Crystal	BL038 (EMD Industries)
Exposure (nm)	365 (Coherent Inc. Ar:Ion)
Formation Dose (mW/cm^2)	50
Formation Time (s)	45
Method	Total Internal Reflection
Center Stop-Band (nm)	436 nm
Formation Angle from Normal (degrees)	-1
Lithography Details	
Resist	Shipley 1813 Positive (Microposit)
Resist Thickness (μm)	1.4
Exposure Time (s)	30
Exposure Power (mW/cm^2)	10
Developer	5:1 DI: Microposit 351 (Microposit)
Developer Time (s)	30
Optical Details	
Modulation	g-line
Resolution (μm)	25
Scattering Modes (degrees)	$\pm$75
Coherency	Maintained with Mask Aligner
Strehl Ratio Diff (glass to H-PDLC)	0.2049
Field Fringe Parameter (μm)	$<$2.5
Interference	Phase delay adjustable at interface

be obvious for applications such as printed circuit board (PCB) or MEMS devices, integrating this thin film into a stepper or a reduction system would enable features smaller than what we have discussed, which have been limited by proximity printing, for smaller feature fabrication.

Double patterning or multiple exposure patterning has been discussed as an important idea in the semiconductor industry to achieve the next generation of small feature sizes. As mentioned in the background chapter, this technology relies on multiple mask exposure prior to a development step, usually used to decompose "complicated" features into horizontal and vertical components that fabricate with less diffractive effects. This is not a diffraction compensating method, rather it works around some diffraction through this decomposition. The limiting factor in this technology is mask alignment error. The patterned features can only be as resolved to within the error introduced in swapping masks and realignment of the next mask. Figure 10.1 is a simplified illustration of a final pattern that would have diffraction effects, likely edge rounding inside of the horseshoe, at small scale. Decomposing the vertical and horizontal can relieve some of that rounding. By using an adaptable thin film mask for this application, there is no need to move and replace mask layers eliminating physical realignment error. Though the mask does not need to be physically moved and replaced, it does need to be reprogrammed for the second pattern. Error introduced in reprogramming can be significantly reduced by designing multiple patterns together to be perfectly layered in software, and overlay error can be reduced to the size of the digital pixilation.

Inverse lithography was also discussed as part of the solution for reaching the next generation of small scale semiconductors. This method essentially works backward from the desired small scale pattern, taking diffraction into account, a mask is developed to form that desired feature. This technique is used with double patterning for very small sized features. At such small sizes, where diffraction plays an important

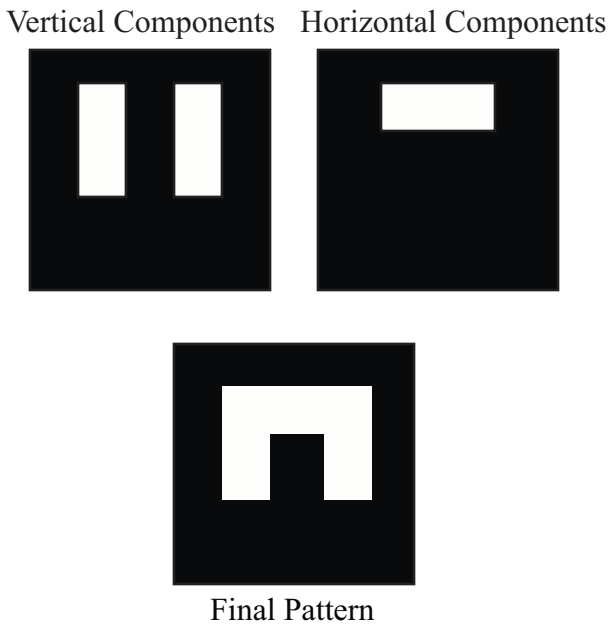

Figure 10.1: Vertical and horizontal components of a "complicated" pattern.

role, there is a good chance that the mask may not resemble the pattern, and complicated algorithms are used to calculate these relationships. Using a programmable mask enables real-time pattern formation and testing of these diffraction compensation masks. To within the resolution of the pixel array, diffraction compensation masks can be tested and adjusted prior to fabricating an expensive chrome on quartz mask.

Grayscale lithography discussed was as a method for achieving 3D structures without using a maskless technique such as e-beam or MEMS projection. Though we have seen multiple possibilities for dynamic grayscaling, besides μfluidic photomasking, all other devices require some sort of pulse width modulation to achieve the graytone. Binary spatially modulated masks are diffraction limited as their spatial modulation relies on the diffraction limit to be detected by the resist as a graytone. H-PDLC on the other hand, has analog grayscale by adjusting bias on the film eliminating com-

plicated pulse width modulation from the process of obtaining a 3D microstructure.

A final very important potential application of this photomask that has never been seen before is adjustable phase delay lithography. When moving into subwavelength regime, interference from phase shift masks has been used to form these small features [149]. Phase shift can be introduced into a system several ways: phase shift masks typically rely on thickness variation of the glass substrate to precisely delay phase, but index modulation can also be used for phase shifting. We have shown so far that H-PDLC patterning edges cause interference patterns due to the phase delay between the transparent and the attenuating regions simply as a function of how H-PDLC is modulated. Control over transmissive optical phase can be used to pattern subdiffraction limit features or potentially cancel diffraction effects. Electro optic control over the index of transmitted light introduces a new type of phase masking that has never been seen before, that is variable phase masking.

Bibliography

[1] M. J. Madou, *Fundamentals of Microfabrication, 2nd Ed.* Boca Raton, FL.: CRC Press, 2002.

[2] R. Sullivan, "The 100 greatest photographs that changed the world," *The Digital Journalist*, p. 13, 2003.

[3] P. J. Collings, *Liquid Crystals: Nature's Delicate Phase of Matter.* Princeton, NJ.: Princeton University Press, 1990.

[4] S. Chandrasekhar, *Liquid Crystals, 2nd ed.* Cambridge, UK: Cambridge University Press, 1992.

[5] P. G. DeGennes and J. Prost, *The Physics of Liquid Crystals.* Oxford Science Publications, 1993, vol. 2.

[6] M. Nakata, G. Zanchetta, B. D. Chapman, C. D. Jones, J. O. Cross, R. Pindak, T. Bellini, and N. A. Clark, "End-to-end stacking and liquid crystal condensation of 6 to 20 base pair dna duplexes," *Science*, vol. 23, no. 5854, pp. 1276 – 1279, 2007.

[7] T. J. Sluckin, D. A. Dunmur, and H. Stegemeyer, *Crystals That Flow, Classic Papers from the History of Liquid Crystals.* London and New York: Taylor & Francis, 2004.

[8] F. Reinitzer, "Contributions to the understanding of cholesterol," *Monatshefte fur Chemie (Wien)*, vol. 9, pp. 421 – 441, 1888.

[9] O. Lehmann, "On flowing crystals," *Zeitschrift fur Physikalische Chemie*, vol. 4, pp. 462 – 472, 1889.

[10] X.-J. Wang and Q. Zhou, *Liquid Crystalline Polymers.* Singapore: World Scientific, 2004.

[11] I.-C. Khoo, *Liquid Crystals, 2nd ed.* Hoboken, NJ: John Wiley & Sons, Inc., 2007.

[12] G. W. Gray and J. Goodby, *Smectic Liquid Crystals: Textures and Structures.* London, UK: Leonard Hill, 1984.

[13] S. Chandrasekhar, B. K. Sadashiva, and K. A. Suresh, "Liquid crystals of disc-like molecules," *Pramana*, vol. 9, no. 5, pp. 471 – 480, 1977.

[14] L. Schmidt-Mende, A. Fechtenkotter, K. Mullen, E. Moons, R. H. Friend, and J. D. MacKenzie, "Self-Organized Discotic Liquid Crystals for High-Efficiency Organic Photovoltaics," *Science*, vol. 293, no. 5532, pp. 1119–1122, 2001.

[15] S. Moulton, M. Maugey, P. Poulin, and G. Wallace, "Liquid crystal behavior of single-walled carbon nanotubes dispersed in biological hyaluronic acid solutions," *J. Am. Chem. Soc.*, vol. 129, no. 30, pp. 9452 – 9457, 2007.

[16] C. F. Bohren and D. R. Huffman, *Absorption and Scattering of Light by Small Particles*. Weinheim, GER: Wiley-VCH Verlag GmbH & Co. KGaA, 1983.

[17] I.-C. Khoo and S.-T. Wu, *Optics and Nonlinear Optics of Liquid Crystals*. Singapore: World Scientific, 1993.

[18] S.-T. Wu and K.-C. Lim, "Absorption and scattering measurements of nematic liquid crystals," *Appl. Opt.*, vol. 26, no. 9, pp. 1722 – 1727, 1987.

[19] S.-T. Wu, U. Finkenzeller, and V. Reiffenrath, "Physical properties of diphenyldiacetylenic liquid crystals," *J. Appl. Phys.*, vol. 65, no. 11, pp. 4372 – 4376, 1989.

[20] S.-T. Wu, "A semiempirical model for liquid-crystal refractive index dispersions," *J. Appl. Phys.*, vol. 69, no. 4, pp. 2080 – 2087, 1991.

[21] H. Craighead, J. Cheng, and S. Hackwood, "New display based on electrically induced index matching in an inhomogeneous medium," *Appl. Phys. Lett.*, vol. 40, no. 1, pp. 22 – 24, 1982.

[22] J. Doane, N. Vaz, B.-G. Wu, and S. Žumer, "Field controlled light scattering from nematic microdroplets," *Appl. Phys. Lett.*, vol. 48, no. 4, pp. 269 – 271, 1986.

[23] S. Žumer and J. Doane, "Light scattering from a small nematic droplet," *Phys. Rev. A*, vol. 34, no. 4, pp. 3373 – 3386, 1986.

[24] [Online]. Available: http://www.polytronix.com/privacyglass.htm

[25] A. Y.-G. Fuh and T.-H. Lin, "Electrically switchable spatial filter based on polymer-dispersed liquid crystal film," *J. Appl. Phys.*, vol. 96, no. 10, pp. 5402 – 5404, 2004.

[26] H. Kelker and R. Hatz, *Handbook of Liquid Crystals*. Weinheim: Verlag Chemie, 1980.

[27] T. Bunning, L. Natarajan, V. Tondiglia, and R. Sutherland, "Holographic polymer-dispersed liquid crystals (h-pdlcs)," *Annu. Rev. Mater. Sci.*, vol. 30, pp. 83 – 115, 2000.

[28] G. P. Crawford, "Electrically switchable bragg gratings," *Opt. Photonics News*, vol. 14, pp. 54 – 59, 2003.

[29] L. Natarajan, C. Shepherd, D. Brandelik, R. Sutherland, S. Chandra, V. Tondiglia, D. Tomlin, and T. Bunning, "Switchable holographic polymer-dispersed liquid crystal reflection gratings based on thiol-ene photopolymerization," *Chem. Mater.*, vol. 15, no. 12, pp. 2477–2484, 2003.

[30] V. K. S. Hsiao, T.-C. Lin, G. S. He, A. N. Cartwright, P. N. Prasad, L. V. Natarajan, V. P. Tondiglia, and T. J. Bunning, "Optical microfabrication of highly reflective volume bragg gratings," *Appl. Phys. Lett.*, vol. 86, no. 13, p. 131113, 2005.

[31] T. Bunning, L. Natarajan, V. Tondiglia, R. Sutherland, R. Haaga, and W. W. Adams, "Effects of eliminating the chain extender and varying the grating periodicity on the morphology of holographically written bragg gratings," *Proc. SPIE*, vol. 2651, pp. 44 – 51, 1996.

[32] L. Natarajan, R. Sutherland, V. Tondiglia, T. Bunning, and W. W. Adams, "Electro-optical switching characteristics of volume holograms in polymer dispersed liquid crystals," *J. Nonlinear Opt. Phys. Mat.*, vol. 5, pp. 89 – 98, 1996.

[33] R. L. Sutherland, V. P. Tondiglia, L. V. Natarajan, P. F. Lloyd, and T. J. Bunning, "Coherent diffraction and random scattering in thiol-ene–based holographic polymer-dispersed liquid crystal reflection gratings," *J. Appl. Phys.*, vol. 99, no. 12, p. 123104, 2006.

[34] G. Qian, J. K. Colegrove, P.-Y. Liu, and X. Quan, "Organic-based electrically switchable bragg gratings and their applications in photonics and telecommunications," *Proc. SPIE*, vol. 4279, pp. 69 – 77, 2001.

[35] S. Yeralan, J. Gunther, D. L. Ritums, R. Cid, J. Storey, A. C. Ashmead, and M. M. Popovich, "Switchable bragg grating devices for telecommunications applications," *Proc. SPIE*, vol. 4291, pp. 79 – 88, 2001.

[36] S. P. Gorkhali, D. R. Cairns, S. Esmailzadeh, J. Vedrine, and G. P. Crawford, "Conformable-polymer dispersed liquid crystals (c-pdlc) displays with indefinitely captured form," *SID Symposium Digest of Technical Papers XXXIII*, vol. 33, pp. 1004 – 1007, 2002.

[37] D. Cairns, S. Gorkhali, S. Esmailzadeh, J. Vedrine, and G. Crawford, "Conformable displays based on polymer-dispersed liquid-crystal materials on flexible substrates," *J. of the SID*, vol. 11, pp. 289 – 295, 2003.

[38] M. Date, Y. Takeuchi, and K. Kato, "A memory-type holographic polymer dispersed liquid crystal (hpdlc) reflective display device," *J. Phys. D: Appl. Phys.*, vol. 31, pp. 2225 – 2230, 1998.

[39] A. Fontecchio, J. Qi, M. Escuti, I. Amimori, G. Crawford, and S. Faris, "Diffuse renditions of spatially pixelated and temporally multiplexed h-pdlcs for full color reflective displays," *SID Digest of Technical Papers XXXI*, vol. 31, pp. 348 – 351, 2001.

[40] F. Meyer, D. Aleva, S. Longo, T. Trissell, R. Schwartz, and D. Hopper, "Reflective display characterization: temporal and spatial viewability measurements of holographic polymer-dispersed liquid crystal (hpdlc) display samples," *Proc. SPIE*, vol. 4712, pp. 373 – 387, 2002.

[41] T. G. Fiske, J. J. Colegrove, A. Lewis, H. Tran, L. D. Silverstein, G. P. Crawford, and J. R. Kelly, "Advances and applications for color hpdlc reflective technologies," *Proc. SPIE Symposium on Cockpit Displays VII: Displays for Defense Applications*, vol. 4022, pp. 216 – 226, 2000.

[42] G. Saitoh, H. Murai, S. Uehara, T. Gotoh, K. Mimura, T. Nakata, K. Sumiyoshi, and H. Hayama, "Rgb-stacked holographic polymer dispersed liquid crystal device for color reflective display," *SID Digest of Technical Papers XXXII*, vol. 32, pp. 344 – 347, 2001.

[43] J. Colegrove, J. Kelly, T. Fiske, A. Lewis, H. Yuan, H. Tran, G. Crawford, and L. Silverstein, "Technology of stacking hpdlc for higher reflectance," *SID Digest of Technical Papers XXXI*, vol. 31, pp. 770 – 773, 2000.

[44] J. McMurdy, G. Crawford, G. Jay, and S. Suner, "A novel medical diagnostic tool for non-invasively measuring hemoglobin utilizing switchable h-pdlc display technology," *SID Digest of Technical Papers XXXVI*, vol. 36, pp. 364 – 367, 2005.

[45] K. Rai, A. E. Fox, S. Shriyan, B. Pelleg, and A. K. Fontecchio, "Spectrometer applications of hpdlcs fabricated by spatial multiplexing," *Appl. Opt.*, in preparation.

[46] A. E. Fox, K. Rai, and A. K. Fontecchio, "Holographically formed polymer dispersed liquid crystal films for transmission mode spectrometer applications," *Appl. Opt.*, vol. 46, no. 25, pp. 6277 – 6282, 2007.

[47] Y. J. Liu and X. W. Sun, "Holographic polymer-dispersed liquid crystals: Materials, formation, and applications," *Advan. OptoElec.*, 2008, in press.

[48] V. Tondiglia, L. Natarajan, R. Sutherland, D. Tomlin, and T. Bunning, "Holographic formation of electro-optical polymer-liquid crystal photonic crystals," *Adv. Mater.*, vol. 14, no. 3, pp. 187 – 191, 2002.

[49] M. J. Escuti, J. Qi, and G. P. Crawford, "Tunable face-centered-cubic photonic crystal formed in holographic polymer dispersed liquid crystals," *Opt. Lett.*, vol. 28, no. 7, pp. 522 – 524, 2003.

[50] ——, "Two-dimensional tunable photonic crystal formed in a liquid-crystal/polymer composite: Threshold behavior and morphology," *Appl. Phys. Lett.*, vol. 83, no. 7, pp. 1331 – 1333, 2003.

[51] T. Kyu, S. Meng, H. Duran, K. Nanjaundiah, and G. R. Yandek, "Holographic polymer-dispersed liquid crystals and polymeric photonic crystals formed by holographic photolithography," *Macromolecular Research*, vol. 14, no. 2, pp. 155 – 162, 2006.

[52] R. Sutherland, V. Tondiglia, L. Natarajan, S. Chandra, D. Tomlin, and T. Bunning, "Switchable orthorhombic f photonic crystals formed by holographic polymerization-induced phase separation of liquid crystal," *Opt. Express*, vol. 10, no. 20, pp. 1074 – 1082, 2002.

[53] M. J. Escuti and G. P. Crawford, "Mesoscale three dimensional lattices formed in polymer dispersed liquid crystals: A diamond-like face centered cubic," *Mol. Cryst. Liq. Cryst.*, vol. 421, pp. 23 – 36, 2004.

[54] S. P. Gorkhali, J. Qi, and G. P. Crawford, "Electrically switchable mesoscale penrose quasicrystal structure," *Appl. Phys. Lett.*, vol. 86, no. 1, p. 011110, 2005.

[55] M. J. Escuti and G. P. Crawford, "Holographic photonic crystals," *Opt. Eng.*, vol. 43, no. 9, pp. 1973 – 1987, 2004.

[56] R. Jakubiak, T. Bunning, R. Vaia, L. Natarajan, and V. Tondiglia, "Electrically switchable, one-dimensional polymeric resonators from holographic photopolymerization: A new approach for active photonic bandgap materials," *Adv. Mater.*, vol. 15, no. 3, pp. 241 – 244, 2003.

[57] D. E. Lucchetta, L. Criante, O. Francescangeli, and F. Simoni, "Wavelength flipping in laser emission driven by a switchable holographic grating," *Appl. Phys. Lett.*, vol. 84, no. 6, pp. 837 – 839, 2004.

[58] ——, "Light amplification by dye-doped holographic polymer dispersed liquid crystals," *Appl. Phys. Lett.*, vol. 84, no. 24, pp. 4893–4895, 2004.

[59] S. J. Woltman, M. E. Sousa, H. Zhang, and G. P. Crawford, "Survey of switchable lasing configurations using structures of liquid crystal and polymer dispersions," *Proc. SPIE*, vol. 6135, p. 61350B, 2006.

[60] R. Jakubiak, L. V. Natarajan, V. Tondiglia, G. S. He, P. N. Prasad, T. J. Bunning, and R. A. Vaia, "Electrically switchable lasing from pyrromethene 597 embedded holographic-polymer dispersed liquid crystals," *Appl. Phys. Lett.*, vol. 85, no. 25, pp. 6095 – 6097, 2004.

[61] G. S. He, T.-C. Lin, V. K. S. Hsiao, A. N. Cartwright, P. N. Prasad, L. V. Natarajan, V. P. Tondiglia, R. Jakubiak, R. A. Vaia, and T. J. Bunning, "Tunable two-photon pumped lasing using a holographic polymer-dispersed liquid-crystal grating as a distributed feedback element," *Appl. Phys. Lett.*, vol. 83, no. 14, pp. 2733 – 2735, 2003.

[62] D. R. Cairns, C. C. Bowley, S. Danworaphong, A. K. Fontecchio, G. P. Crawford, L. Li, and S. M. Faris, "Optical strain characteristics of holographically formed polymer-dispersed liquid crystal films," *Appl. Phys. Lett.*, vol. 77, no. 17, pp. 2677 – 2679, 2000.

[63] M. L. Ermold, K. Rai, and A. K. Fontecchio, "Hydrostatic pressure response of polymer-dispersed liquid crystal gratings," *J. Appl. Phys.*, vol. 97, no. 10, p. 104905, 2005.

[64] K. Rai and A. K. Fontecchio, "Optimization of pressure response in hpdlc gratings based on polymer composition," *Mol. Cryst. Liq. Cryst.*, vol. 450, pp. 183 – 190, 2006.

[65] V. K. S. Hsiao, W. D. Kirkey, F. Chen, A. N. Cartwright, P. N. Prasad, and T. J. Bunning, "Organic solvent vapor detection using holographic photopolymer reflection gratings," *Adv. Mater.*, vol. 17, no. 18, pp. 2211 – 2214, 2005.

[66] B. White, P. Fremstad, and F. Nogal, "Ibm system z10 enterprise class technical introduction," *IBM International Technical Support Organization*, 2008.

[67] "Intel core i7 processor extreme edition and intel core i7 processor," *Intel Corporation Datasheet*, vol. 1, 2008.

[68] D. Widmann and K. U. Stein, "Semiconductor technologies with reduced dimensions," *European Solid State Circuits Conference*, vol. 2, 1976.

[69] M. J. Comstock, L. F. Thompson, C. G. Willson, and M. J. Bowden, Eds., *Introduction to Microlithography*, ser. 219. Washington, D.C.: ACS Symposium Series, 1983.

[70] E. Hecht, *Optics*, 4th ed. San Francisco, CA: Addison Wesley, 2002.

[71] M. Born and E. Wolf, *Principles of Optics*, 7th ed. Cambridge, UK: Cambridge University Press, 1984.

[72] M. D. Levenson, "Report from spie: Double double, toil and trouble!" *Microlithography World*, 2007.

[73] M. M. Crouse, R. Uchida, Y. van Dommelen, T. Ando, E. Schmitt-Weaver, M. Takeshita, S. Wu, and R. Routh, "Litho-only double patterning approaches: positive–negative versus positive–positive tone," *Journal of Micro/Nanolithography, MEMS and MOEMS*, vol. 8, no. 1, p. 011006, 2009.

[74] K. Bubke, E. Cotte, J. H. Peters, R. deKruif, M. Dusa, J. Fochler, and B. Connolly, "Mask characterization for double patterning lithography," *Proc. SPIE*, vol. 6730, 2007.

[75] A. Kahng, C.-H. Park, X. Xu, and H. Yao, "Layout decomposition for double patterning lithography," in *International Conference on Computer-Aided Design*, Nov. 2008, pp. 465–472.

[76] W. H. Arnold, "Guest editorial: Special section on double-patterning lithography," *Journal of Micro/Nanolithography, MEMS and MOEMS*, vol. 8, no. 1, p. 011001, 2009.

[77] C. P. Ausschnitt and S. D. Halle, "Combinatorial overlay control for double patterning," *Journal of Micro/Nanolithography, MEMS and MOEMS*, vol. 8, no. 1, p. 011008, 2009.

[78] B. E. A. Saleh and S. I. Sayegh, "Reductions of errors of microphotographic reproductions by optical corrections of original masks," *Opt. Eng.*, vol. 20, pp. 781 – 784, 1981.

[79] *Lithography and Level-Sets: Inverse Lithography Technology (ILT) made possible*, Luminescent Technologies, 2471 East Bayshore Road, Suite 600 Palo Alto, CA, 2006.

[80] X. Ma and G. R. Arce, "Generalized inverse lithography methods for phase-shifting mask design," *Opt. Express*, vol. 15, no. 23, pp. 15 066 – 15 079, 2007.

[81] X. Ma and G. Arce, "Binary mask optimization for inverse lithography with partially coherent illumination," *J. Opt. Soc. Am. A*, vol. 25, no. 12, pp. 2960–2970, 2008.

[82] K. Reimer, H. J. Quenzer, M. Jurss, and B. Wagner, "Micro-optic fabrication using one-level gray-tone lithography," *Proc. SPIE: Miniaturized Systems with Microoptics and Micromechanics II*, vol. 3008, pp. 279 – 288, 1997.

[83] Y. Oppliger, P. Sixt, J. M. Stauffer, J. M. Mayor, P. Regnault, and G. Voirin, "One-step 3d shaping using a gray-tone mask for optical and microelectronic applications," *Microelectron. Eng.*, vol. 23, pp. 449 – 454, 1994.

[84] T. J. Suleski and D. C. O'Shea, "Gray-scale masks for diffractive-optics fabrication: I. commercial slide imagers," *Appl. Opt.*, vol. 34, no. 32, pp. 7507 – 7517, 1995.

[85] D. R. Purdy, "Fabrication of complex micro-optic components using photosculpting through halftone transmission masks," *Pure Appl. Opt.*, vol. 3, pp. 167 – 175, 1994.

[86] K. Reimer, R. Engelke, U. Hoffmann, P. Merz, K. K. v. Platen, and B. Wagner, "Progress in graytone lithography and replication techniques for different materials," *Proc. SPIE: Micromachine Technology for Diffractive and Holographic Optics*, vol. 3879, p. 98, 1999.

[87] K. Totsu and M. Esashi, "Gray-scale photolithography using maskless exposure system," *J. Vac. Sci. Technol. B*, vol. 23, no. 4, pp. 1487 – 1490, 2005.

[88] O. J. A. Schueller, D. C. Duffy, J. A. Rogers, S. T. Brittain, and G. M. Whitesides, "Reconfigurable diffraction gratings based on elastomeric microfluidic devices," *Sens. Actuators A: Phys.*, vol. 78, no. 2-3, pp. 149 – 159, 1999.

[89] C. Chen, D. Hirdes, and A. Folch, "Gray-scale photolithography using microfluidic photomasks," *Proc. Natl. Acad. Sci. USA*, vol. 100, no. 4, pp. 1499 – 1504, 2003.

[90] J. McKechnie and D. Sinton, "Dynamic Microfluidic Photomasking," *J. Microelectromech. S.*, vol. 16, no. 5, pp. 1145 – 1151, 2007.

[91] B. B. Yellen, G. Fridman, and G. Friedman, "Ferrofluid lithography," *Nanotechnology*, vol. 15, pp. S562 – S565, 2004.

[92] B. B. Yellen, G. Friedman, and K. A. Barbee, "Programmable self-aligning ferrofluid masks for lithographic applications," *IEEE Transactions on Magnetics*, vol. 40, no. 4, pp. 2994 – 2996, 2004.

[93] M. M. Wefers and K. A. Nelson, "Generation of high-fidelity programmable ultrafast optical waveforms," *Opt. Lett.*, vol. 20, no. 9, p. 1047, 1995.

[94] A. M. Weiner, "Femtosecond pulse shaping using spatial light modulators," *Review of Scientific Instruments*, vol. 71, no. 5, pp. 1929 – 1960, 2000.

[95] C. Dorrer, F. Salin, F. Verluise, and J. P. Huignard, "Programmable phase control of femtosecond pulses by use of a nonpixelated spatial light modulator," *Opt. Lett.*, vol. 23, no. 9, pp. 709–711, 1998.

[96] V. Binjrajka, C.-C. Chang, A. W. R. Emanuel, D. E. Leaird, and A. M. Weiner, "Pulse shaping of incoherent light by use of a liquid-crystal modulator array," *Opt. Lett.*, vol. 21, no. 21, pp. 1756–1758, 1996.

[97] J. L. Pezzaniti and R. A. Chipman, "Phase-only modulation of a twisted nematic liquid-crystal tv by use of the eigenpolarization states," *Opt. Lett.*, vol. 18, no. 18, p. 1567, 1993.

[98] T. Feurer, J. C. Vaughan, R. M. Koehl, and K. A. Nelson, "Multidimensional control of femtosecond pulses by use of a programmable liquid-crystal matrix," *Opt. Lett.*, vol. 27, no. 8, pp. 652–654, 2002.

[99] A. M. Weiner, "Femtosecond optical pulse shaping and processing," *Prog. Quant. Electr.*, vol. 19, pp. 161 – 237, 1995.

[100] K. Lu and B. E. A. Saleh, "Theory and design of the liquid crystal ta as an optical spatial phase modulator," *Opt. Engineering*, vol. 29, no. 3, pp. 240 – 246, 1990.

[101] K. M. Johnson, D. J. McKnight, and I. Underwood, "Smart spatial light modulators using liquid crystals on silicon," *IEEE Journal of Quantum Electronics*, vol. 29, no. 2, pp. 699 – 714, 1993.

[102] N. A. Clark and S. T. Lagerwall, "Submicrosecond bistable electro-optic switching in liquid crystals," *Appl. Phys. Lett.*, vol. 36, no. 11, pp. 899–901, 1980.

[103] J. Funfschilling and M. Schadt, "Fast responding and highly multiplexible distorted helix ferroelectric liquid-crystal displays," *J. Appl. Phys.*, vol. 66, no. 8, pp. 3877 – 3882, 1989.

[104] S. Garoff and R. B. Meyer, "Electroclinic effect at the $a - c$ phase change in a chiral smectic liquid crystal," *Phys. Rev. Lett.*, vol. 38, no. 15, pp. 848–851, Apr 1977.

[105] G. Andersson, I. Dahl, P. Keller, W. Kuczyński, S. T. Lagerwall, K. Skarp, and B. Stebler, "Submicrosecond electro-optic switching in the liquid-crystal smectic a phase: The soft-mode ferroelectric effect," *Appl. Phys. Lett.*, vol. 51, no. 9, pp. 640–642, 1987.

[106] Q. Peng, S. Liu, Y. Guo, B. Chen, J. Du, Y. Zeng, C. Zhou, and Z. Cui, "Real-time photolithographic technique for fabrication of arbitrarily shaped microstructures," *Opt. Engineering*, vol. 42, no. 2, pp. 477 – 481, 2003.

[107] M. V. Kessels, M. E. Bouz, R. Pagan, and K. Heggarty, "Versatile stepper based maskless microlithography using a liquid crystal display for direct write of binary and multilevel microstructures," *Journal of Micro/Nanolithography, MEMS and MOEMS*, vol. 6, no. 3, p. 033002, 2007.

[108] J.-W. Jeon, J.-Y. Choi, J.-B. Yoon, and K. S. Lim, "A new three-dimensional lithography using polymer dispersed liquid crystal (pdlc) films," in *Proc. of MEMs 2006*, Istanbul, Turkey, 2006, pp. 110 – 113.

[109] O. Solgaard, F. S. A. Sandejas, and D. M. Bloom, "Deformable grating optical modulator," *Opt. Lett.*, vol. 17, no. 9, pp. 688–690, 1992.

[110] J. Paufler, S. Brunn, T. Korner, and F. Kuhling, "Continuous image writer with improved critical dimension performance for high-accuracy maskless optical patterning," *Microelectron. Eng.*, vol. 58, pp. 31 – 40, 2001.

[111] K. F. Chan, Z. Feng, R. Yang, A. Ishikawa, and W. Mei, "High resolution maskless lithography," *J. Microlithogr. Microfabr. Microsyst.*, vol. 2, no. 4, pp. 331 – 339, 2003.

[112] T. Sandstrom, A. Bleeker, J. Hintersteiner, K. T. an dJ. Freyer, and K. van der Mast, "Oml: optical maskless lithography for economic design prototyping and small-volume production," *Proc SPIE: Optical Microlithography XVII*, vol. 5377, pp. 777 – 787, 2004.

[113] M. Klosner and K. Jain, "Massively parallel, large-area maskless lithography," *Appl. Phys. Lett.*, vol. 84, no. 15, pp. 2880 – 2882, 2004.

[114] Y. Gao, T. Shen, J. Chen, N. Luo, X. Qi, and Q. Jin, "Research on high-quality projecting reduction lithography system based on digital mask technique," *Optik - International Journal for Light and Electron Optics*, vol. 116, no. 7, pp. 303 – 310, 2005.

[115] M. Seo, H. Kim, and M. Park, "Maskless lithographic pattern generation system upon micromirrors," *Computer-Aided Design & Applications*, vol. 3, no. 1 – 4, pp. 185 – 192, 2006.

[116] G. P. Watson, V. Aksyuk, M. E. Simon, D. M. Tennant, R. A. Cirelli, W. M. Mansfield, F. Pardo, D. O. Lopez, C. A. Bolle, A. R. Papazian, N. Basavanhally, J. Lee, R. Fullowan, F. Klemens, J. Miner, A. Kornblit, T. Sorsch, L. Fetter, M. Peabody, J. E. Bower, J. S. Weiner, and Y. L. Low, "Spatial light modulator for maskless optical projection lithography," *J. Vac. Sci. Technol. B*, vol. 24, no. 6, pp. 2852 – 2856, 2006.

[117] I. W. Jung, J.-S. Wang, and O. Solgaard, "Spatial light modulators for maskless lithography," in *Proc. IEEE: Optical MEMS and their Applications*. Big Sky MT: IEEE/LEOS, August 2006, pp. 150 – 151.

[118] Y.-H. Jang, K.-N. Lee, and Y.-K. Kim, "Characterization of a single-crystal silicon micromirror array for maskless uv lithography in biochip applications," *J. Micromech. Microeng*, vol. 16, pp. 2360 – 2368, 2006.

[119] T. Naiser, T. Mai, W. Michel, and A. Ott, "A versatile maskless microscope projection photolithography system and its application in light-directed fabrication of dna microarrays," *Rev. of Sci. Instr.*, vol. 77, p. 063711, 2006.

[120] X. Guo, J. Du, Y. Guo, C. Du, Z. Cui, and J. Yao, "Simulation of doe fabrication using dmd-based gray-tone lithography," *Microelectronic Engineering*, vol. 83, no. 4-9, pp. 1012 – 1016, 2006.

[121] H. Martinsson, T. Sandstrom, A. Bleeker, and J. D. Hintersteiner, "Current status of optical maskless lithography," *J. Microlithogr. Microfabr. Microsyst.*, vol. 4, no. 1, p. 011003, 2005.

[122] D. Gil, R. Menon, X. Tang, H. I. Smith, and D. J. D. Carter, "Paralled maskless optical lithography for prototyping, low-volume production, and research," *J. Vac. Sci. Technol. B*, vol. 20, no. 6, pp. 2597 – 2601, 2002.

[123] R. L. Sutherland, "Polarization and switching properties of holographic polymer-dispersed liquid-crystal gratings. i. theoretical model," *J. Opt. Soc. Am. B*, vol. 19, no. 12, pp. 2995 – 3003, 2002.

[124] J. Qi, L. Li, M. D. Sarkar, and G. P. Crawford, "Nonlocal photopolymerization effect in the formation of reflective holographic polymer-dispersed liquid crystals," *J. Appl. Phys.*, vol. 96, no. 5, pp. 2443 – 2450, 2004.

[125] M. A. Matin, T. M. Benson, L. R. Chen, and P. W. E. Smith, "Analysis of distributed bragg reflectors using thin-film optics," *Microwave and Optical Tech. Lett.*, vol. 21, no. 1, pp. 11 – 15, 1999.

[126] L. Solymar and D. J. Cooke, *Volume Holography and Volume Gratings*. New York, NY: Academic Press, 1981.

[127] D. J. McCartney, "The analysis of volume reflection gratings using optical thin-film techniques," *Opt. and Quant. Elect.*, vol. 21, pp. 93 – 107, 1989.

[128] H. Kogelnik, "Coupled wave theory for thick hologram gratings," *The Bell System Technical Journal*, vol. 48, no. 9, pp. 2909 – 2947, 1969.

[129] P. Yeh, A. Yariv, and C.-S. Hong, "Electromagnetic propagation in periodic stratified media. i. general theory," *J. Opt. Soc. Am.*, vol. 67, no. 4, pp. 423 – 438, 1977.

[130] R. L. Sutherland, V. P. Tondiglia, L. V. Natarajan, and T. J. Bunning, "Phenomenological model of anisotropic volume hologram formation in liquid-crystal-photopolymer mixtures," *J. Appl. Phys.*, vol. 96, no. 2, pp. 951 – 965, 2004.

[131] *Oriel Product Training: Spectral Irradiance*, Newport Corporation, Startford, CT, http://www.newport.com/oriel.

[132] D. C. Peters, "A comparison of mercury arc lamp and laser illumination for flow cytometers," *J. Histochemistry and Cytochemistry*, vol. 27, no. 1, pp. 241 – 245, 1979.

[133] S. K. Shriyan, K. K. Rai, A. Bellingham, and A. K. Fontecchio, "Multilayer stacking technique for holographic polymer dispersed liquid crystals," *Appl. Phys. Lett.*, vol. 93, no. 26, p. 261113, 2008.

[134] A. E. Fox and A. K. Fontecchio, "Liquid crystal polymer composite films for reconfigurable photomasking applications," *Appl. Phys. Lett.*, vol. 91, no. 15, p. 141119, 2007.

[135] ——, "Lineshape and morphology study of structures formed using a reconfigurable photomasking element," *J. Micro/Nanolithography, MEMs, and MOEMs*, vol. 7, no. 3, pp. 0 330 071 – 6, 2008.

[136] ——, "Reconfigurable lithographic applications using polymer liquid crystal composite films," *Proc. SPIE Symposium on Photomask Technology*, vol. 6730, 2007.

[137] ——, "Applications of liquid crystal polymer composite films for photolithographic fabrication of 3d structures," *Proc. SPIE Symposium on Integrated Optoelectronic Devices, Practical Holography XXII: Materials and Applications*, vol. 6912, 2008.

[138] ——, "Wet and dry etch comparison of silicon patterned using a thin-film photomask," *J. Micro/Nanolithography, MEMs, and MOEMs*, 2009, submitted for Publication.

[139] K. M. Abedin, M. R. Islam, and A. F. M. Y. Haider, "Computer simulation of fresnel diffraction from rectangular apertures and obstacles using the fresnel integrals approach," *Optics and Laser Technology*, vol. 39, pp. 237 – 246, 2005.

[140] A. E. Fox, M. Cosgrove-Davies, and A. K. Fontecchio, "Gap material study for holographically formed polymer dispersed liquid crystal composite film stacks," *Mol. Crys. Liq. Crys.*, vol. 478, pp. 151 – 162, 2007.

[141] B. C. Platt and R. Shack, "History and principles of shack-hartmann wavefront sensing," *J. Refractive Surgery*, vol. 17, p. S573, 2001.

[142] D. Malacara, *Optical Shop Testing*. New York, NY: John Wiley & Sons, Inc., 1992.

[143] V. N. Mahajan, "Strehl ratio for primary aberrations: some analytical results for circular and annular pupils," *J. Opt. Soc. Am*, vol. 72, pp. 1258 – 1266, 1982.

[144] J. C. Wyant and K. Creath, "Basic wavefront aberration theory for optical metrology," *Appl. Opt. and Opt. Engineering*, vol. 11, pp. 27 – 39, 1992.

[145] D. Cheng, *Field and Wave Electromagnetics*, 2nd ed. Reading, MA: Addison Wesley, 1992.

[146] G. W. Parker, "Electric field outside a parallel plate capacitor," *Am. J. Phys.*, vol. 70, no. 5, pp. 502 – 507, 2002.

[147] G. J. Sloggett, N. G. Barton, and S. J. Spencer, "Fringing fields in disc capacitors," *J. Phys. A: Math. Gen.*, vol. 19, pp. 2725 – 2736, 1986.

[148] L. D. Sio, N. Tabiryan, R. Caputo, A. Veltri, and C. Umeton, "Policryps structures as switchable opticalphase modulators," *Opt. Express*, vol. 16, no. 11, pp. 7619–7624, 2008.

[149] M. Fritze, B. M. Tyrrell, D. K. Astolfi, R. D. Lambert, D.-R. W. Yost, A. R. Forte, S. G. Cann, and B. D. Wheeler, "Subwavelength optical lithography with phase-shift photomasks," *Lincoln Laboratory Journal*, vol. 14, no. 2, pp. 237 –250, 2003.

Appendix A. Ideal Bragg Reflector Simulation Code

```
clear

n1=1.524;
n2=1.6227;

a=200E-9;
b=210E-9;

N=50;
Gamma=a+b;

for n=1:9
    theta(n)=5*n*pi/90-5*pi/90;
    cos_thetat=sqrt(1-(n1/n2)^2*(sin(theta(n)))^2);
    r1=((n1*cos(theta(n))-n2*cos_thetat)/(n1*cos(theta(n))+n2*cos_thetat));
    Csq=abs(r1)^2/(1-abs(r1)^2);

    for l=1:300
        lambda=400e-9+l*1E-9;
        yvar(l)=lambda;

        k2x(l)=((2*pi*n2/lambda)^2-((2*pi*theta(l)/lambda))^2)^(1/2);
        k1x(l)=((2*pi*n1/lambda)^2-(2*pi*theta(l)/lambda)^2)^(1/2);

        K(l)=(1/Gamma)*acos((1/2)*(2*cos(k2x(l)*b+sin(theta(n)/(2*pi)))));

        R(n,l)=Csq/(Csq+((sin(K(l)*Gamma))/(sin(N*K(l)*Gamma)))^2);
        T(n,l)=1-R(n,l);

    end
end
```

Appendix B. H-PDLC Reflector Simulation Code

```
clear

D=100E-9;
alpha=0.4;
L=13.4E-6;
Fls=0.19;
F0=0.35;
Fhs=0.165
Beta_e=2/3;
Beta_o=-1/3;

S=1/3;

Fd=(F0-(1-alpha)*Fls-alpha*Fhs)/alpha;

for i=1:65
    lambda=400E-9+i*1E-9;
    ne_1(i)=-9.23E5*lambda+2.23;
    no_1(i)=-3.07E5*lambda+1.68;
end

for i=1:40
    lambda=465E-9+i*1E-9;
    ne_2(i)=-6.25E5*lambda+2.09;
    no_2(i)=-3.25E5*lambda+1.69;
end

for i=1:75
    lambda=505E-9+i*1E-9;
    ne_3(i)=-2E5*lambda+1.876;
    no_3(i)=-4E4*lambda+1.5472;
end

for i=1:120
    lambda=580E-9+i*1E-9;
    ne_4(i)=-2.5E5*lambda+1.905;
    no_4(i)=-3.33E4*lambda+1.5433;
end


ne=[ne_1,ne_2,ne_3,ne_4];
no=[no_1,no_2,no_3,no_4];

np=1.524;

alpha_0=5.26E8;
```

```
lambda_star=300E-9;

a=100E-9;
b=169E-9;

N=60;
Gamma=a+b;

   for  l=1:300
       lambda=400e-9+l*1E-9;
       yvar(l)=lambda;

       abscoef(l)=(alpha_0*lambda^2)/((lambda/lambda_star)^2-1)^2;
       ni(l)=sqrt((1/3)*(2*no(l)^2+ne(l)^2));
       nm(l)=sqrt((Fhs*ni(l)^2+(1-Fhs-Fd)*np^2)/(1-Fd));

           %nm(l)=1.524;
           %nd(l)=sqrt(ni(l)^2+S*(Beta_e*ne(l)^2-Beta_o*no(l)^2));

       nd(l)=ni(l);


       theta=0;

       cos_thetat=sqrt(1-(nd/nm)^2*(sin(theta))^2);
       r1(l)=((nd*cos(theta)-nm*cos_thetat)/(nd*cos(theta)+nm*cos_thetat));


      % r1(l)=(nd(l)-nm(l))/(nd(l)+nm(l));
       Csq(l)=abs(r1(l))^2/(1-abs(r1(l))^2);


       k2x(l)=((2*pi*nd(l)/lambda)^2-((2*pi*theta/lambda))^2)^(1/2);
       k1x(l)=((2*pi*nm(l)/lambda)^2-(2*pi*theta/lambda)^2)^(1/2);

       K(l)=(1/Gamma)*acos((1/2)*(2*cos(k2x(l)*b)));

       R(l)=(Csq(l)/(Csq(l)+((sin(K(l)*Gamma))/(sin(N*K(l)*Gamma)))^2))*1.04;

       d=N*Gamma;
       absc(l)=exp(-abscoef(l)*d);

       T(l)=((1-R(l))*absc(l))*0.96;

     end

plot(yvar,T)
```

Appendix C. Mask Design

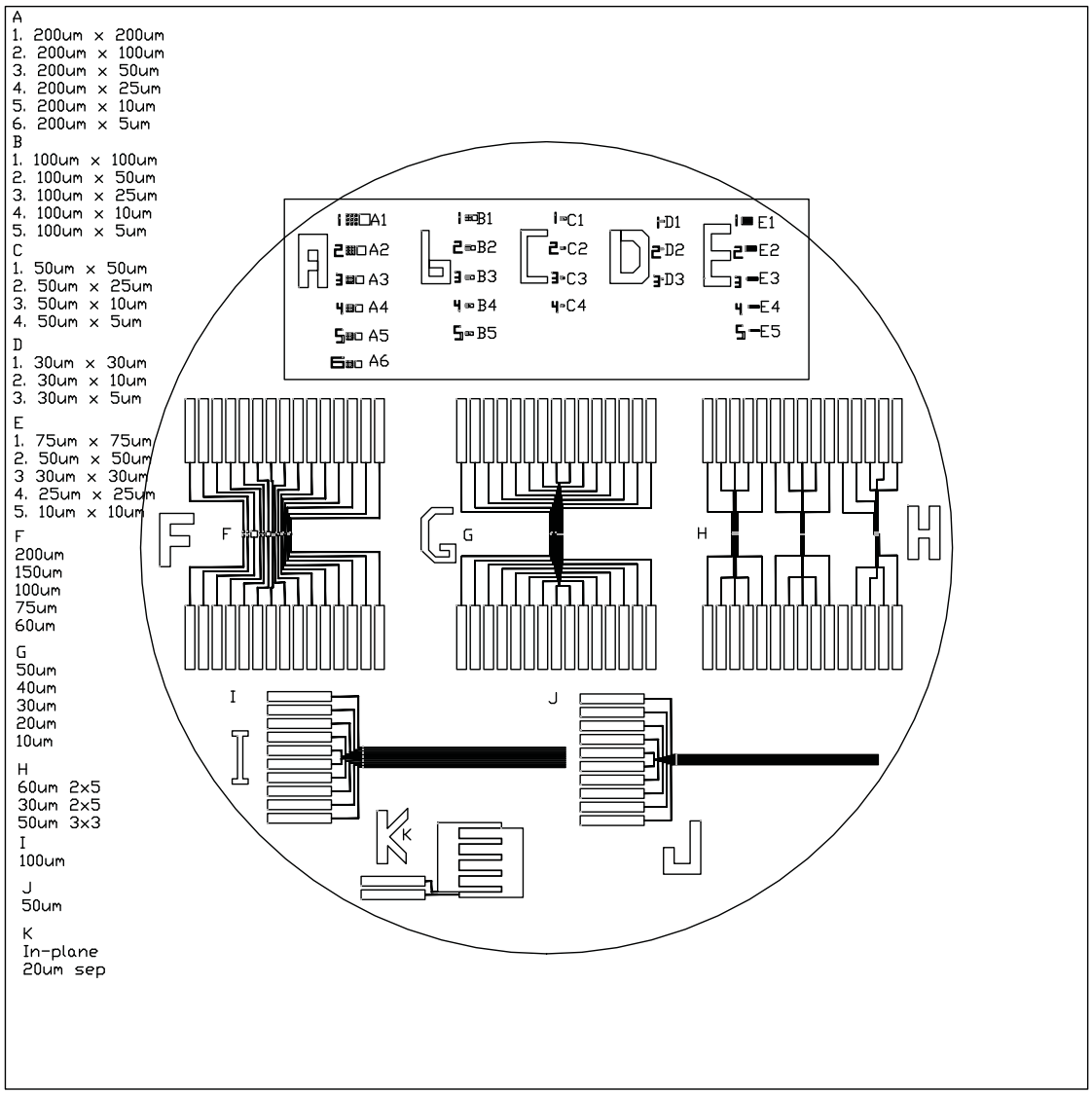

Appendix D. Patterning Procedure

The standard procedure for fabricating H-PDLC masks is detailed here.

Necessary Items:

- 3"x3" Corning 1737 coated with 30 nm indium-tin-oxide
- Shipley 1813 positive photoresist
- Microposit 351 metal-ion-free developer
- HCl 12M

Etch of ITO Substrates:

1. Clean Corning 1737 glass substrates using acetone and measure ITO conductivity.
2. Heat substrates at 200C for 20 minutes to evaporate surface solvents.
3. Spincoat substrates with 1813 at 4000 RPM for 30 seconds. The resulting resist thickness will be approximately 1.4 μm.
4. Softbake substrates for 2 minutes at 100C.
5. Exposure using a Suss MA6 for 15 seconds at 10 mW/cm^2.
6. Develop resist in a 5:1 solution of deionized water to 351 solution for 30 seconds. Rinse in DI water for 30 seconds.
7. Hardbake resist for 3 minutes at 100C.
8. Etch ITO in a warm 50:50 solution of DI:HCl for 3 minutes stirring constantly. Increase etch time 5 seconds for each additional sample.
9. Rinse well in DI water.
10. Strip resist using acetone and examine etched ITO in the profilometer.
11. Dice glass substrates into appropriate pieced for fabricating H-PDLC.

Fabrication of UV H-PDLC for thin film masks:

1. Make a UV thiolene prepolymer syrup of NOA65, BL038, and Darocure 4265.
2. Space cleaned and etched ITO glass using 20 μm spacers.
3. Prepare samples and press for 5 minutes.
4. Measure output power of Ar:Ion laser to verify it is greater than 40mW/cm^2 and align it into the prism.
5. Use an index card to observe the beam reflected off the front surface of the prism. It should point directly back to the expansion lens aperture. Set the rotation stage to zero degrees.
6. The angle of rotation of the rotation stage in which the prism is situated will determine the pitch of the fabricated grating and therefore the center wavelength of the stop-band. Rotate the rotation stage about 1/2 a degree clockwise from the zero position and make a test sample to see if it is greater than or less than

436 nm center wavelength. It is best to use a rotation stage with a micrometer on it

7. The target is of course 436 nm, based on the center wavelength on the stop-band of the test sample rotate the stage counter clockwise to lower the wavelength or clockwise to increase it.
8. Once the ideal angle is determined for stop-bands at 436 nm, exposure the remainder of samples at 45 seconds at a power between 50 and 60mW/cm^2 remembering to index match the samples to the prism.
9. Clean index matching fluid from samples and characterize their wavelengths.
10. Solder leads to the switchable areas remembering to connect the ground plane.

Patterning with H-PDLC masks:

1. Clean and prebake 1"x1" microscope glass slides.
2. Spin slides with 1813 at 4000 RPM for 30 seconds to achieve 1.4 μm resist coating.
3. Softbake for 2 minutes at 100C.
4. Set the adaptable mask up in the mask aligner by removing conventional mask holder and substrate plate. Set mask aligner to contact. Place coated glass with the adaptable mask about it. Since the mask aligner was not designed for 1"x1" samples, its vacuum chucks may not hold the sample and adaptable mask. Tape in to hold steady. Bias the H-PDLC into the appropriate pattern and place the 436 nm spectral filter atop of the stack.
5. Expose at 10 mW/cm^2 for approximately 30 seconds. For 20 μm thick H-PDLC, this exposure dose is approximately the ideal, but it can vary between samples.
6. Develop in 5:1 solution of DI:351 for 30 seconds.
7. Hardbake for 3 minutes at 100C and examine patterns

Patterning chrome H-PDLC

1. Pattern 3"x3" ITO glass as detailed above, but do not etch
2. After resist hardbake, clean and dry with nitrogen
3. Secure in electron beam deposition tool and pump down
4. Deposit chrome at 80 mW for 3 minutes to achieve approximately a 100 nm layer.
5. Liftoff resist using acetone. The result is glass with ITO patterned with chrome.
6. Dice glass into H-PDLC sized pieces and fabricate H-PDLC using the chrome/glass as one of the electrodes. Use clear glass/ITO as the inside electrode for prism fabrication.
7. Use chrome/glass H-PDLC masks to test patterning through nanostructure

Appendix E. Near Field Diffraction Simulation Code

```
clear;
a=2E-3;
b=2E-3;%aperture length and width
lambda=632E-9; %incident wavelength
d=400E-3; %mask distance

points=500;

x=linspace(-a/2,a/2,points);
y=linspace(-b/2,b/2,points);


u1=-sqrt(2/(lambda*d)).*x;
u2=sqrt(2/(lambda*d)).*x;

Cu1 = mfun('FresnelC',u1);
Cu2 = mfun('FresnelC',u2);
Su1 = mfun('FresnelS',u1);
Su2 = mfun('FresnelS',u2);

Ix=(1/4)*(((Cu2-Cu1).^2)+((Su2-Su1).^2));

v1=-sqrt(2/(lambda*d)).*y;
v2=sqrt(2/(lambda*d)).*y;

Cv1 = mfun('FresnelC',v1);
Cv2 = mfun('FresnelC',v2);
Sv1 = mfun('FresnelS',v1);
Sv2 = mfun('FresnelS',v2);

Iy=(1/4)*(((Cv2-Cv1).^2)+((Sv2-Sv1).^2));

intensity=Ix'*Iy;

intensity=fftshift(intensity);
Ix=fftshift(Ix);

figure(1)
        surf(x*1E6,y*1E6,intensity,'LineStyle','none')
        xlabel('microns')
        ylabel('microns')
        zlabel('Intensity')

figure(2)
        plot(x*1E6,Ix)
        xlabel('microns')
```

```
        ylabel('Intensity')

figure(3)
        image(x*1E6,y*1E6,intensity,'CDataMapping','scaled')
        axis image
        xlabel('microns')
        ylabel('microns')
        colormap('gray')
```

Appendix F. Field Fringing Landscapes

Landscape figures illustrating the results from a finite element simulation of field fringing around the edges of adjacent ITO regions at 50 μm and 100 μm regions.

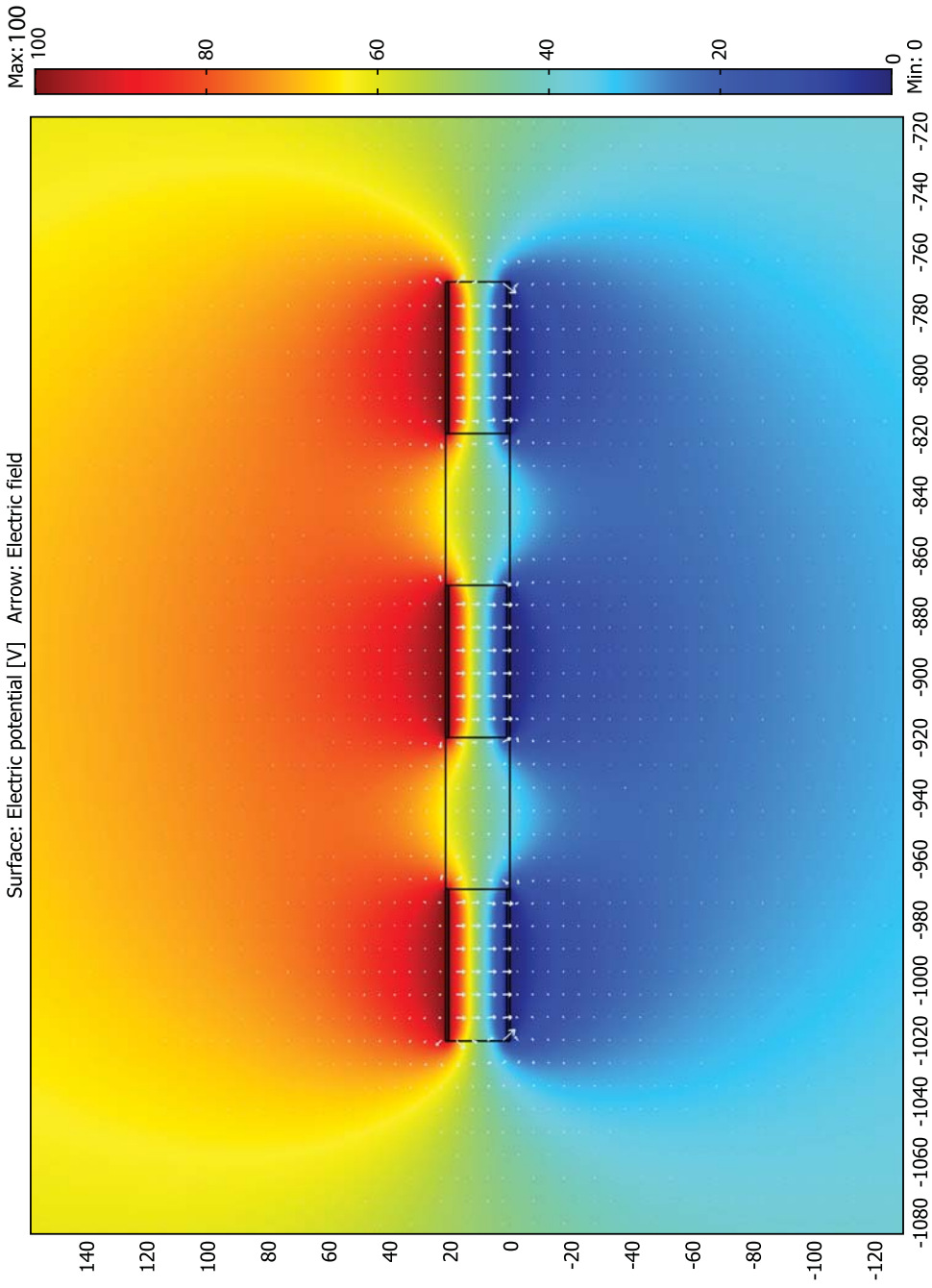

Figure F.1: Field fringing around 50 μm area.

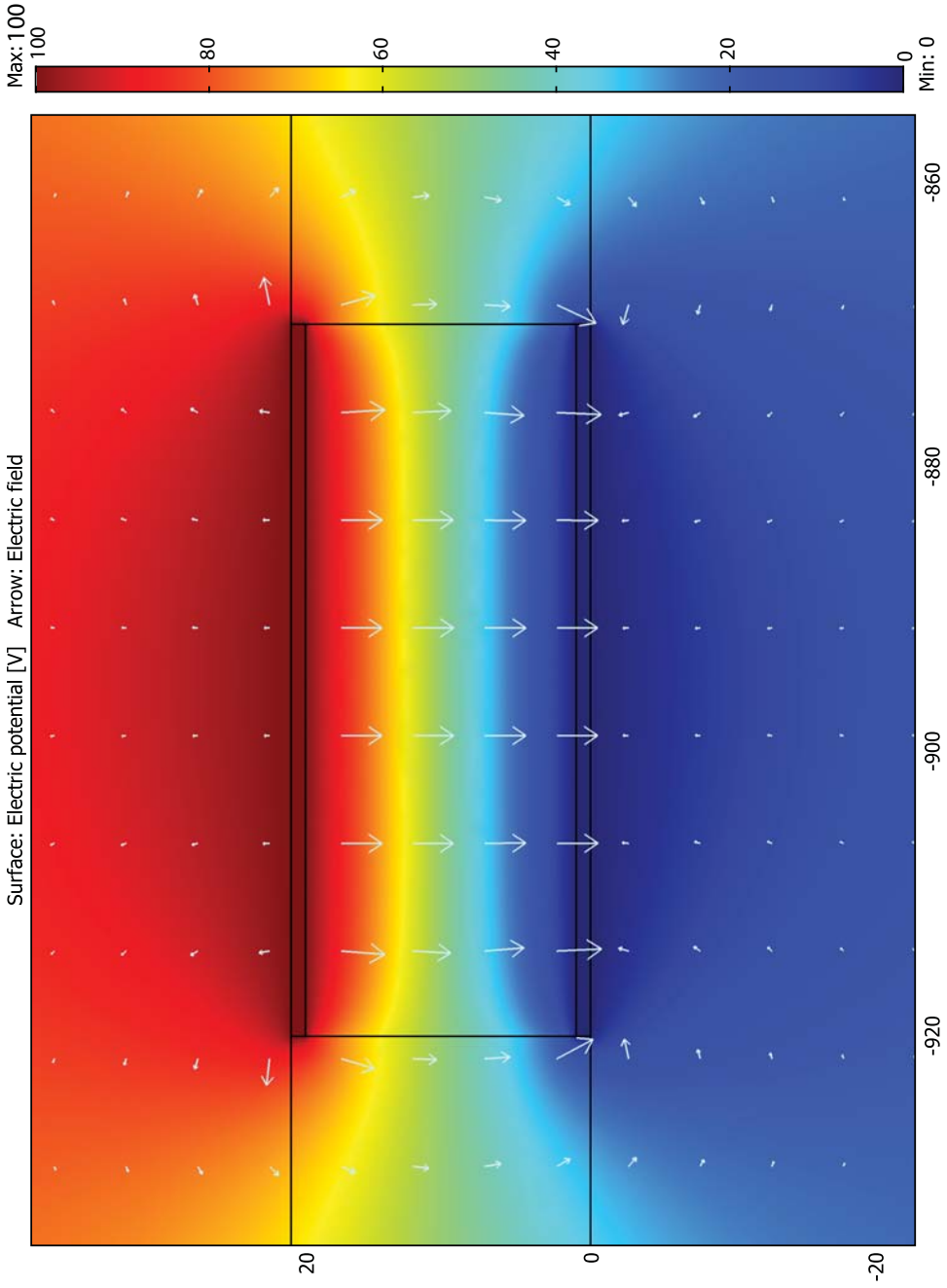

Figure F.2: Field fringing around 50 μm area.

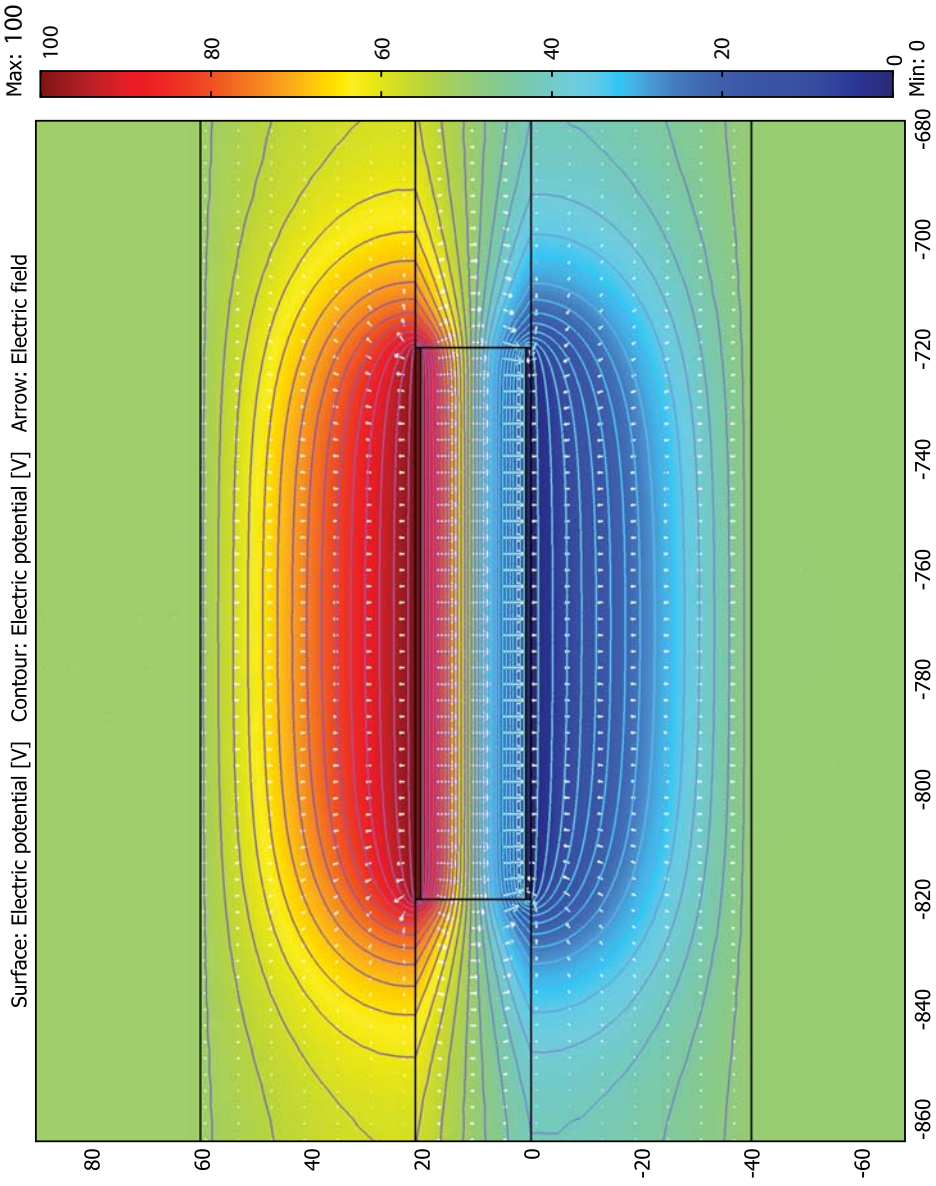

Figure F.3: Field fringing around 100 μm area

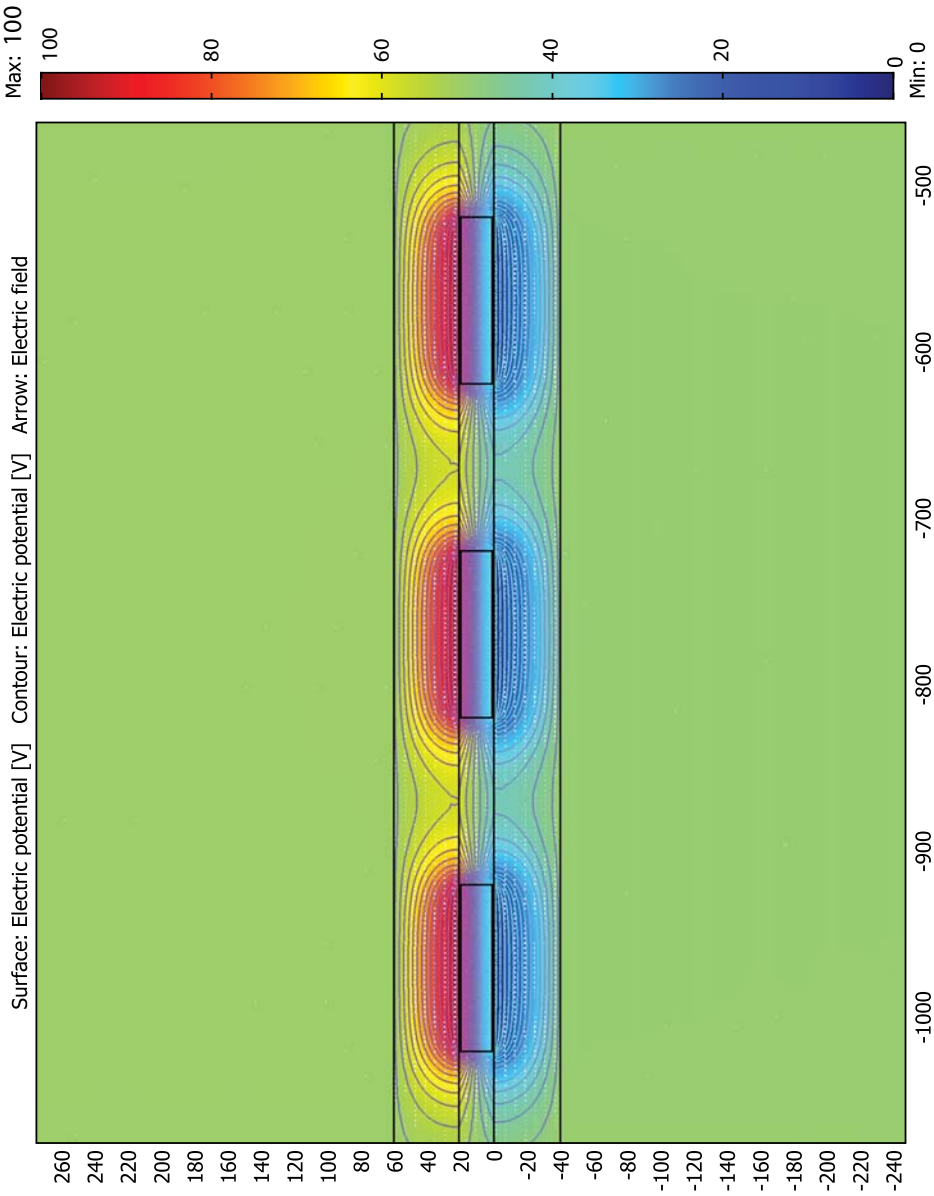

Figure F.4: Field fringing around 100 μm area

Vita

Anna E. Fox

Education

Ph.D. Electrical Engineering, Drexel University, Philadelphia, PA 2009
M.S. Engineering Science, Dartmouth College, Hanover, NH 2005
B.S. Electrical Engineering, Columbia University, New York, NY 2001
B.S. Physics, Bates College, Lewiston, ME 2000

Professional Experience

- **National Science Foundation Graduate Research Fellow**, 06/2006 - 06/2009
- **Graduate Research Fellow**, Drexel University, 09/2005 - 05/2006
- **Graduate Research Fellow**, Dartmouth College, 09/2004 - 08/2005
- **Course Designer and Instructor**, Drexel University, 04/2007 - 06/2009
- **Senior Optical Systems Engineer**, Internet Photonics, Inc., 01/2001 - 08/2004

Awards

- National Research Council Postdoctoral Fellowship, 2009
- National Science Foundation Graduate Research Fellowship, 2006 - 2009
- Chairman's Fund - Gordon Research Conference on Liquid Crystals, 2009
- Drexel University College of Engineering Graduate Student Research Award, 2008
- Chairman's Fund - Gordon Research Conference on Liquid Crystals, 2007
- NASA Graduate Student Research Fellowship, Awarded 2006

Selected Publications

- A.E. Fox and A.K. Fontecchio, *J. Micro/Nanolithography, MEMs, and MOEMs*, Vol. 7, No. 3, 033007-1-6 (2008).
- A.E. Fox and A.K. Fontecchio, *Proceedings of the SPIE Symposium on Integrated Optoelectronic Devices, Practical Holography XXII: Materials and Applications*, Vol. 6912 (2008).
- A.E. Fox and A.K. Fontecchio,*Applied Physics Letters*, Vol. 91, No. 15, 141119 (2007).
- A.E. Fox, K.K. Rai., A.K. Fontecchio, *Applied Optics*, Vol. 46, No. 27, 6277-6282 (2007).
- A.E. Fox, M. Cosgrove-Davies, A.K. Fontecchio,*Molecular Crystals Liquid Crystals*, Vol. 478, 151-162 (2007)
- A.E. Fox and A.K. Fontecchio,*Proceedings of the SPIE Symposium on Photomask Technology*, Vol. 6730 (2007).
- A.E. Fox and U.Österberg,*Optics Express*, Vol. 14, No. 8, 3688-3693 (2006).
- A.E. Fox, U. Österberg, X. Gu, R. Trebino, *Progress in Electromagnetic Research Symposium Proceedings* (2006).